Springer Series in Materials Science 162

Vladimir G. Plekhanov

Isotopes in Condensed Matter

Springer

Springer Series in Materials Science

Volume 162

For further volumes:
http://www.springer.com/series/856

The Springer Series in Materials Science covers the complete spectrum of materials physics, including fundamental principles, physical properties, materials theory and design. Recognizing the increasing importance of materials science in future device technologies, the book titles in this series reflect the state-of-the-art in understanding and controlling the structure and properties of all important classes of materials.

Vladimir G. Plekhanov

Isotopes in Condensed Matter

Springer

Vladimir G. Plekhanov
Mathematics and Physics Department
Computer Science College
Tallinn
Estonia

ISSN 0933-033X
ISBN 978-3-642-28722-0 ISBN 978-3-642-28723-7 (eBook)
DOI 10.1007/978-3-642-28723-7
Springer Heidelberg New York Dordrecht London

Library of Congress Control Number: 2012936960

Printed on acid-free paper

Springer is part of Springer Science+Business Media (www.springer.com)

To my kids and grandchildren

Preface

This book describes the manifestations of the isotope effect in all branches of physics: nuclear, atomic and molecular as well as condensed matter and its applications in *human health* and *medicine*, *geochronology*, industry, research in academic and applied fields. This book is intended both as a tutorial and as a reference. It is a concise introduction to isotopetronics, developing the basic elements of this new branch of nanoscience. The problem of the enigma mass in microphysics is briefly discussed.

The science of the nuclear, atoms and simple molecules and the science of matter from microstructures to larger scales, are well established. A remaining, extremely important, size—related challenge is at the atomic scale—roughly the dimensional scales between 1 and 10 molecular sizes—where the fundamental properties of materials are determined and can be engineered. This field of science—isotopetronics—is a broad and interdisciplinary field of emerging research and development. Isotopetronics technology is concerned with materials, structures and systems whose components, as in nanoscience, exhibit novel and significantly modified physical, chemical and biological properties due to their small sizes. A principal goal of isotopetronics technology is to control and exploit these properties in structures and devices at atomic and molecular levels. To realise this goal, it is essential to learn how to fabricate and use these devices efficiently. Practical implementations of isotopetronics science and technology have great importance, and they depend critically on training people in these fields. Thus, modern education needs to address the rapidly evolving facets of isotopetronics science and applications. With the purpose of contributing to education in the *isotopetronics* as a new branch of *nanoscience* I present this book providing a unifying framework for the basic ideas needed to understand recent developments underlying isotopetronics science and technology, as applied to nanoelectronics and quantum information. Quantum information is a field which at present is undergoing intensive development and, owing to the novelty of the concepts involved, it seems to me it should be as interest to a broad range of scientists beyond those actually working in the field. I have tried to present a simple and

systematic treatment of the isotopetronics, such that the reader might understand the material presented without the need for consulting other books.

With numerous illustrations, this book will be of great interest to undergraduate and graduate students taking courses in mesoscopic physics or nanoelectronics as well as quantum information, and academic and industrial researches working in this field.

The references I cite are those with which I am most familiar and which have helped us understand the subject as presented here. While there has been no attempt to give credit to each contributor, I have tried to cite the original papers, which brought new and important results (methods) to the isotope effect applications in all branches of microphysics.

Tallinn *Vladimir G. Plekhanov*

Acknowledgments

Many thanks are due to Prof. W. Reder for carefully reading the manuscript as well as Dr. N. Write for improving my English. Again it is a pleasure to thank the Staff of Springer, in particular Dr. C. Ascheron and Elke Sauer, for the continued excellent cooperation. I deeply thank the authors and publishers who have kindly permitted us to reproduce figures and tables from their papers and books. In a few cases I have been unable to contact the authors, and I would be grateful if they would nevertheless retrospectively give me the necessary permission. I wish to express my deep gratitude to my kids and grandchildren for their patience during the long preparation of this book.

Tallinn *Vladimir G. Plekhanov*

Contents

Chapter 1
Introduction

The aim of this book is to outline the basic physical concepts and device applications related to isotope effect in all the branches of *microphysics* [1]—new direction of nanoscience (subnanoscience). The experience of the past shows that throughout constant technology improvement microelectronics has become more reliable, faster, more powerful and less expensive by reducing the dimensions of integrated circuits. As demonstrated in this book, when the dimensions of a solid are reduced to the atomic size, new physical properties due to quantum effects become apparent. These novel properties are manifestated in various ways, first we should indicate low-dimensional structures in isotope-mixed solids (*quantum wells, wires, dots*). Besides that we should underline the specific dependence of elastic thermal and vibrational properties of bulk isotope-mixed materials as well as low-dimensional structures from such materials. In the last two decades the unique properties of isotopes are used in the quantum information processing devices as well as in developing of processors of the quantum computers [2].

In the last four decades we have witnessed a remarkable progress in the development of *epitaxial crystal growth* techniques such as molecular beam epitaxy (MBE), metal-organic chemical vapor deposition (MOCVD) and their various variations such as chemical beam epitaxy (CBE), atomic layer epitaxy (ALE), etc. which have allowed the growth of quality semiconductors (insulators), their alloy and heterostructures (see, e.g. [5, 6]). A variety of interesting structures, such as quantum wells, quantum wires and quantum dots, has been fabricated with abrupt changes in composition and/or doping characteristics and their structural, electronic and optical properties have been investigated in considerable detail (see, e.g. [3–12]). Many of these structures, especially those based on quantum wells, have found important applications in a number of electronic and *opto-electronic* devices such as high-electron mobility transistors, lasers, light-emitting diodes (LEDs), photodetectors, spatial light modulators [5, 8, 12]. The use of these devices in opto-electronics, quantum information, for example, has literally revolutionized these fields during the last two decades. Before we study the effects of reduced size and dimensionality on the properties of solids, we review in first chapters those

V. G. Plekhanov, *Isotopes in Condensed Matter*, Springer Series in Materials Science 162,
DOI: 10.1007/978-3-642-28723-7_1,

concepts of isotopes and solids which are essential for understanding the behaviour of quantum nanostructures. For instance, the behaviour of electrons in a quantum well is very different from the case of bulk solids if their motion is across the potential barriers confining the quantum well, but is very similar if the motion is parallel to the interfaces [3, 4, 7].

It is increasingly clear that quantum mechanical principles are not just exotic theoretical statements but fundamental for a new technology of practical information processing [2, 13]. *Quantum communication, quantum cryptography* as well as *quantum teleportation* represent exciting new arenas which exploit intrinsic quantum mechanical correlations [14–16]. In the first step we should analyse the exciton in *quantum dot*, it possible as *qubit* in assembly of quantum dots in isotope-mixed crystals [2].

As we know, at present time only three particles, the proton, the electron and the photon, are stable. Another particle, the neutron, is stable when it is bound within a nucleus, and is unstable with life time of $887 \pm 2\,\mathrm{s}$ when it is free. Since nuclei are involved in a wide variety of applied and pure research, nuclear physics overlaps with a number of other fields of physics: particles; astrophysics; stellar evolution, etc. Therefore, the primary aim of nuclear physics is to understand the force between nucleons, the structure of nuclei and how nuclei interact with each other and with other subatomic particles. These three questions are, to a large extent, related with each other. Modern experimenters can create such nuclei using artificially induced fusion or nucleon transfer reactions, employing ion beams from different sources. Beams with even higher energies (e.g. from accelerator) can be used to create nuclei at very high temperatures, and there are signs that these experiments have produced phase transition from normal nuclear matter to a new state, the *quarks condensate*, the *quark-gluonplasma*, in which the quarks mingle with one another, rather than being segregated in triplets as they are in neutrons and protons. If in the nuclear physics the meaning of isotope is establishing [1] then application isotope effect in atomic and molecular physics allows to get the results, which are difficult to overestimate so far as owing to this results it was to construct the "building" of the science of the twentieth century the quantum mechanics. In the last fifty years the isotope effect is one of the modern and power methods to investigation of structure and properties of solids. This conclusion supports the numerous reviews and first monographs dedicated to isotope effect of stable and *radioactive isotopes*. Moreover, it is obviously a leading role of the isotope physics in the study of the nature-nuclear interactions and reconstruction of *nucleogenesys* process in the *Universe* which could be explained as the observable in nature relative to spreading of chemical elements. Such wide field of isotope applications stimulates necessity for examination and critical analysis from one point of view the microscopical nature of isotope effect. Such approach to isotope physics allows to make known not only the intrinsic contradiction inherent in this area of physics but also determine the borders of the effect.

It is well known [17] that reflectance and absorption spectra of different solids often show structure for photon energies just below the *energy gap*, where we might expect the crystal to be transparent. This structure is caused by the *absorption* of photon with the creation of a bound electron - hole pair. An electron and a hole may

be bound together by their attractive *Coulomb interaction* [18–20], just as an electron is bound to a proton to form a neutral hydrogen atom. The bound electron–hole pair is called by exciton [17]. An *exciton* can move through the crystal and transport energy; it does not transport charge because it is electrically neutral. This task was first studied by Wannier–Mott [18, 19] and later by Slater [20] who showed that if one assumes that the electron and hole wavefunctions are extended over many lattice constants, the exciton can be described as consisting an electron and a hole with effective band masses m_e^* and m_h^*, respectively, coupled together with coulomb potential screened by the static dielectric constant ε_0 [21]. In the *Wannier–Mott model*, the Schrödinger equation for the exciton is resolved into the function of a hydrogen-like atom whose effective charge is $Z_e = \mathrm{e}/\varepsilon_0$ (ε_0 being the dielectric constant of medium), and the energies of the exciton states are described by the hydrogen-like expression of the form (see, e.g. [22])

$$E(\overrightarrow{k}) = E_g - \frac{\mu \mathrm{e}^4}{2\hbar\varepsilon_0^2 \mathrm{n}^2} + \frac{\hbar^2 \overrightarrow{k}^2}{2(m_e^* + m_h^*)}, \tag{1.1}$$

where $\overrightarrow{k}$ is the quasi-momentum of the exciton; μ, n are its reduced mass and principal quantum number and the translational mass of the exciton (M) is equal to the sum of the effective masses of electron (m_e^*) and hole (m_h^*). By analogy with formula of the binding energy of an electron in a hydrogen atom on the nuclear mass (M_N)(Ryd $= 2\pi^2 \frac{me^4}{\hbar^3 c(1+m/M_N)}$), the binding energy of exciton $E_b = -\frac{\mu \mathrm{e}^4}{2\hbar\varepsilon_0^2 n^2}$ is practically independent of the nuclear mass. Hence, we come to the natural conclusion that there is no isotopic effect in a frozen crystal lattice on the levels of the Wannier–Mott exciton [23]. This simplified treatment, however, does not take into account the exciton–phonon interaction, which to a certain extent is nonadiabatic (see, for example [24]). The constant of exciton–phonon interaction depends on the frequency of phonons and hence on the mass of isotopes [1]. The isotopic dependence of the binding energy of large-radius exciton was observed experimentally with LiH and LiD crystals in Ref. [25], where the reflection spectra of these crystals at low temperature were measured for the first time (see, also [25]). As will be shown below, the discovered dependence of E_b on the isotopic composition of the lattice has opened unique opportunities for the use of excitons in the characterisation of bulk isotope mixed crystals as well as quantum low-dimensional structures in such systems [2].

This book comprises of six chapters. Chapter 2 begins by reviewing the present state of the modern picture of isotopes. This chapter introduces the reader with physical base of isotopes and describes its manifestations in nuclear physics. The origin of the *mass* is briefly discussed in this chapter too. Chapters 3 and 4 are devoted to description of the manifestations of the isotope effect in atomic and molecular physics as well as in condensed matter. Although these manifestations vary, they have one common feature—all depend on mass. Such view allows to see the success and failure as well as the borders of the isotope effect. Chapter 5 describes the effects related to isotopic disorder in solids: diffusion and thermal properties.

The objective of the second part (Chap. 6) is to expose the reader to the traditional applications of stable and *radioactive isotopes*. In the first part of this chapter we describe stable isotope applications in neutron transmutative doping (NTD) of semiconductors as well as in optical fibre. There is a brief description about the new nuclear technology for the preparation of the fibre. In the second part of this chapter, the reader can find description of the applications of radiactive isotopes: human health and medicine, geochronometry, solid state, etc. Throughout this book, the author interweaves experimental results with the appropriate theoretical formalism.

From the immense volume of the literature concerned with isotopes in condensed matter and their applications, we primarily selected those reviews and monographs which contain extensive references.

References

1. V.G. Plekhanov, Manifestation and origin of the isotope effect, ArXiv: gen. phys/ 0907.2024
2. V.G. Plekhanov, Isotope-based quantum information, ArXiv:quant-ph/ 0909.0820
3. M.J. Kelly, *Low-Dimemsional Semiconductors* (Clarendon Press, Oxford, 1995)
4. J.H. Davies, *The Physics of Low-Dimensional Semiconductors* (Cambridge University Press, Cambridge, 1998)
5. V.V. Mitin, V.A. Kochelap, M.A. Stroscio, *Quantum Heterostructures* (Cambridge University Press, Cambridge, 1999)
6. L. Jacak, P. Hawrylak, A. Wojs, *Quantum Dots* (Springer, Berlin, 1998)
7. P. Harrison, *Quantum Wells, Wires and Dots* (Wiley, New York, 2001)
8. D. Bimberg, D. Grundman, N.N. Ledentsov, *Quantum Dot Heterostructures* (Wiley, Chichester, 2001)
9. K. Goser, P. Glösekötter, J. Dienstuhl, *Nanoelectronics and Nanosystems* (Springer, Berlin, 2004)
10. S.M. Reiman, M. Mannines, Electronic structure of quantum dots. Rev. Mod. Phys. **74**, 1283–1343 (2002)
11. R. Hanson, L.P. Kowenhoven, J.R. Petta, et al., Spins in few-electron quantum dots, ibid, **79**, 1217–1265 (2007)
12. J.M. Martinez-Duart, R.J. Martin-Palma, F. Agullo-Rueda, *Nanotechnology for Microelectronics and Optoelectronics* (Elsevier, Amsterdam, 2006)
13. See, e.g. the articles in March 1998 issue of Physical World
14. E. Schrödinger, Naturwissenschaften **23**, 807 (1935)
15. E. Schrödinger, *The Present Situation in Quantum Mechanics*, ed by J.A. Wheeler, W.H. Zurek, Translation in Quantum Theory and Measurement (Princeton University Press, Princeton, 1983) pp. 152–167
16. J.S. Bell, *Speakable and Unspeakable in Quantum Mechanics* (Cambridge University Press, Cambridge, 1987)
17. R.S. Knox, *Theory of Excitons* (Academic Press, New York, 1963)
18. G.H. Wannier, The structure of electronic excitation levels in insulating crystals. Phys. Rev. **52**, 191–197 (1937)
19. N.F. Mott, On the absorption light by crystals. Proc. R. Soc. (London) **A167**, 384–391 (1938)
20. J.C. Slater, Electrons in perturbed periodic lattices. Phys. Rev. **76**, 1592–1601 (1949)
21. H. Haken, Die Theorie des Exzitons in Festen Korper. Fortsch. Phys. **6**, 271–314 (1958)
22. V.G. Plekhanov, Isotope effects in lattice dynamics. Physics-Uspekhi **46**, 689–715 (2003)

23. V.G. Plekhanov, T.A. Betenekova, V.A. Pustovarov, Excitons and some peculiarities of exciton-phonon interactions. Sov. Phys. Solid State **18**, 1422–1424 (1976)
24. S.I. Pekar, *Untersuchungen über die Elektronen Theorie der Kristall* (Akademik-Verlag, Berlin, 1954)
25. V.G. Plekhanov, Elementary excitations in isotope-mixed crystals. Phys. Reports **410**, 1–235 (2005)

Chapter 2
Sub-Nucleonic Structure and the Modern Picture of Isotopes

2.1 History and Overview

Investigations of the *atomic nucleus*, and the fundamental forces that determine *nuclear* structure as is well known offer fascinating insights into the nature of the physical world [1–10]. We all known well that the history of the nuclear physics dates from the latter years of the nineteenth century when Henry Becqeurel in 1896 discovered the radioactivity. He was working with compounds containing the element uranium. Becqeurel found that photographic plates covered to keep out light became fogged, or partially exposed, when these uranium compounds were anywhere near the plates. Two years after Becquerel's discovery, Pierre and Marie Curie in France and Rutherford in England succeeded in separating a naturally occurring radioactive element, radium ($Z = 88$), from the ore. It was soon revealed that there are three, distinctly different types of radiation emitted by radioactive substances. They were called *alpha* (α), *beta* (β) and *gamma* (γ) rays—terms which have been retained in ours days. When a radioactive source was placed in a magnetic field, it was found that there were three different activities, as the trajectories of some of the rays emitted were deflected to one direction, some to the opposite direction and some not affected at all. Subsequently it was found that α-rays consist of positively charged ^{4}He nuclei, β-rays are made of electrons (positrons) and γ-rays are nothing but electromagnetic radiation that carries no net charge. The existence of the nucleus as the small central part of an atom was first proposed by Rutherford in 1911. Rutherford proposed that the atom does consist of a small, heavy positively charged centre surrounded by orbiting electrons which occupy the vast bulk of the atoms volume. The simplest atom—hydrogen—consisted of a proton and a single orbital electron. Later, in 1920, the radii of a few heavy nuclei were measured by Chadwick and were found to be in the order of 10^{-14} m, much smaller than the order of 10^{-10} m for atomic radii (for details, see e.g. [4–9]).

The building blocks of nuclei are *neutrons* and *protons*, two aspects, or quantum states, of the same particle, the *nucleon*. Since a neutron does not carry any net electric charge and is unstable as an isolated particle (see, below), it was not discovered

V. G. Plekhanov, *Isotopes in Condensed Matter*, Springer Series in Materials Science 162,
DOI: 10.1007/978-3-642-28723-7_2, © Springer-Verlag Berlin Heidelberg 2013

Table 2.1 Fundamental interactions

Interaction	FQ	Mass	Range (m)	RS	Spin	T C-S (m^2)	TTS (s)
Strong	Gluon	0	10^{-15}	1	1	10^{-30}	10^{-23}
Weak	$W^{\mp}$; Z	81; 93 GeV/c^2	10^{-18}	10^{-5}	1;1	10^{-44}	10^{-8}
Electromagnetic	Photon	0	∞	$\alpha = 1/137$	1	10^{-33}	10^{-20}
Gravity	Graviton	0	∞	10^{-30}	2	–	–

Here *FQ* field quant, *RS* relative strength, *TC-S* typical cross-section, *TTS* typical time scale

until 1932 by Chadwick, whose existence has been anticipated by Rutherford as early as 1920. Since only positive charges (protons) are present in nucleus, the electromagnetic force inside a nucleus is repulsive and the nucleons cannot be held together unless there is another source of force that is attractive and stronger than Coulomb's (see, also [10]). Here we have our first encounter with *strong interaction* (see, also Table 2.1). In 1934 Hideki Yukawa proposed the first significant theory of the *strong force* to explain how the nucleus holds together. As we know, with Fermi and Yukawa's papers the modern model of the atom was complete [2–6].

Studies of the structure of the nucleus have shown that it is composed of protons and neutrons, and more recently studies [11–14] of very high energy collisions have shown that these protons and neutrons are themselves composed of elusive particles called *quarks*. Particle physics deals with the world of the quarks and all other particles still thought to be fundamental. One may argue that, since nuclear force is only one aspect of the strong interaction between quarks, all we need therefore to do is to understand *quantum chromodynamics* (QCD)[1] (for details see [12–15] and below). The structure of neutrons and protons is discerned only at very high energies (see, e.g. [15]) and, for all practical purpose concerning nuclear structure, research and nuclear physics applications in the modern world, the neutron–proton model of the nucleus is entirely adequate.

Thus, our present knowledge of physical phenomena suggests that there are four types of forces between physical objects:

1. Gravitational;
2. Electromagnetic;
3. Strong and
4. Weak.

Both *gravitational* and *electromagnetic* forces are infinite in range and their interaction strength diminishes with the square of the distance of separation. Clearly, nuclear force cannot follow the same radial dependence. Being much stronger, it would have pulled the nucleons in different nuclei together into a single unit and destroy all the atomic structure we are familiar with. In fact, *nuclear force* has a

[1] QCD is the modern theory of the strong interaction. QCD, the theory of quarks, gluons and their interactions, is a self-contained part of the Standard Model (see below) of elementary particles. Historically its route is in nuclear physics and the description of ordinary matter—understanding what protons and neutrons are (and their structure) and how they interact. Nowadays QCD is used to describe most of what goes at high-energy accelerators.

very short distance. As we know at present time, only three particles, the proton, the electron and the photon, are stable. Another particle, the neutron, is stable when it is bound within a nucleus, and is unstable with life time of 887 ± 2 s when it is free (for details see, also [11–14]). Since nuclei are involved in a wide variety of applied and pure research, nuclear physics overlaps with a number of other fields of physics: particles; astrophysics; stellar evolution, etc. Therefore, the primary aim of nuclear physics is to understand the force between nucleons, the structure of nuclei and how nuclei interact with each other and with other *subatomic particles*. These three questions are, to a large extent, related with each other. Much of the current research in nuclear physics (see, e.g. [1–10]) relates to the study of nuclei under extreme conditions such as high spin and excitation energy. Nuclei may also have extreme shapes (for instance similar to that American footballs) or extreme neutron-to-proton ratios. Modern experimenters can create such nuclei using artificially induced fusion or nucleon transfer reactions, employing ion beams from different sources. Beams with even higher energies (e.g. from accelerator) can be used to create nuclei at very high temperatures, and there are signs that these experiments have produced phase transition from normal nuclear matter to a new state, the quarks condensate, the quark-gluon plasma, in which the quarks mingle with one another, rather than being segregated in triplets as they are in neutrons and protons.

If in the nuclear physics the meaning of isotope is establishing one [7, 9, 10, 15], then application of isotope effect in atomic [16–19] and molecular [20–22] physics allows to get the results, which are difficult to overestimate so far as owing to this results it was to construct the "building" of the science of the twentieth century—the quantum mechanics. In the last 50 years the isotope effect is one of the modern and power methods used in investigation of structure and properties of solids. This conclusion supports the numerous reviews (see, e.g. [23–25]) and first monographs [26, 27, 29] dedicated to isotope effect of stable isotopes. In the last years, more and more investigations of solid-state physics are conducted by using *radioactive isotopes*, which give evidence of already comprehensive list of references (see, for instance [28, 30, 31]). It is a well known fact that large and successful application of the radioactive elements in medicine [32–35], the direction in isotope physics, is more finance supportive in different states (see, for example, [36] and references therein). Moreover, it is obviously a leading role of the isotope physics in the study of the nature–nuclear interactions and reconstruction of nucleogenesys process in the Universe [37–40] which could be explained as the observable in nature relative to spreading of chemical elements.

Such wide field of isotope applications stimulate necessity for examination and critical analysis from point of view of the microscopical nature of isotope effect.[2]

[2] With the aim of the ground of nature of isotope effect, a detailed analysis of the neutron and proton structure and their mutual transformation in the *weak interaction* process was conducted. Note that the main characteristics of isotope effect—the mass of free particles (proton and neutron)—does not conserve in the weak interaction process. This contradiction is removed although partly if we take into account the modern presentation [42–44] that the mass of proton (neutron) is created from quark condensate (not from constituent quarks [15, 44]) which is the coherent superposition of the states with different chirality. Thus the elucidation of the reason of origin of the nucleon

Table 2.2 The basic properties of the atomic constituents

Particle	Charge	Mass (u)	Spin ($\hbar$)	Magnetic moment (JT^{-1})
Proton	e	1.007276	1/2	1.411×10^{-26}
Neutron	0	1.008665	1/2	-9.66×10^{-27}
Electron	$-$e	0.000549	1/2	9.28×10^{-24}

Such approach to isotope physics allows to make known not only the intrinsic contradiction inherent this area of physics but also determine the borders of the effect. A step-by-step comparison with existing theoretical models not only reveals the degree of agreement (or disagreement) but also provides a new impulse for both the development of new theoretical ideas and for conducting new experiments (see, also [41]).

2.2 The Structure of Atomic Nucleus

An atom consists of an extremely small, positively charged nucleus (see Fig. 2.1) surrounded by a cloud of negatively charged electrons. Although typically the nucleus is less than one ten-thousandth the size of the atom, the nucleus contains more than 99.9% of the mass of the atom. Atomic nucleus is the small, central part of an atom consisting of A-nucleons, Z-protons and N-neutrons (Fig. 2.2). The atomic mass of the nucleus, A, is equal to Z+N. A given element can have many different isotopes, which differ from one another by the number of neutrons contained in the nuclei [58, 59]. In a neutral atom, the number of electrons orbiting the nucleus equals the number of protons in the nucleus. As usual, *nuclear size* is measured in fermis ($1\text{fm} = 10^{-15}$ m, also called femtometers). The basic properties of the atomic constituents can be read in Table 2.2.

As we can see from this table, protons have a positive charge of magnitude $e = 1.6022 \times 10^{-19}$ C (Coulomb's) equal and opposite to that of the electrons. Neutrons are uncharged. Thus a neutral atom (A, Z) contains Z electrons and can be written symbolically as ${}^{A}_{Z}X_{N}$ (see also Fig. 2.2). Here X is chemical symbol and N is neutron number and is equal $\text{N} = \text{A} - \text{Z}$.[3] The masses of proton and neutron are almost the same, approximately 1836 and 1839 electron masses (m_e), respectively. Apart from electric charge, the proton and neutron have almost the same properties. This is why there is a common name of them: *nucleon*. Both the proton and neutron are nucleons.

(Footnote 2 continued)
mass is taken down to elucidation of the reason to break down the chiral symmetry in *Quantum Chromodynamics* [45–56].

[3] Nuclei with the same N and different Z are called *isotones*, and *nuclides* with the same mass number A are known as *isobars*. In a symbolic representation of a nuclear specie or nuclide, it is usual to omit the N and Z subscripts and include only the mass number as a superscript, since A = N+Z and the symbol X represents the chemical elements.

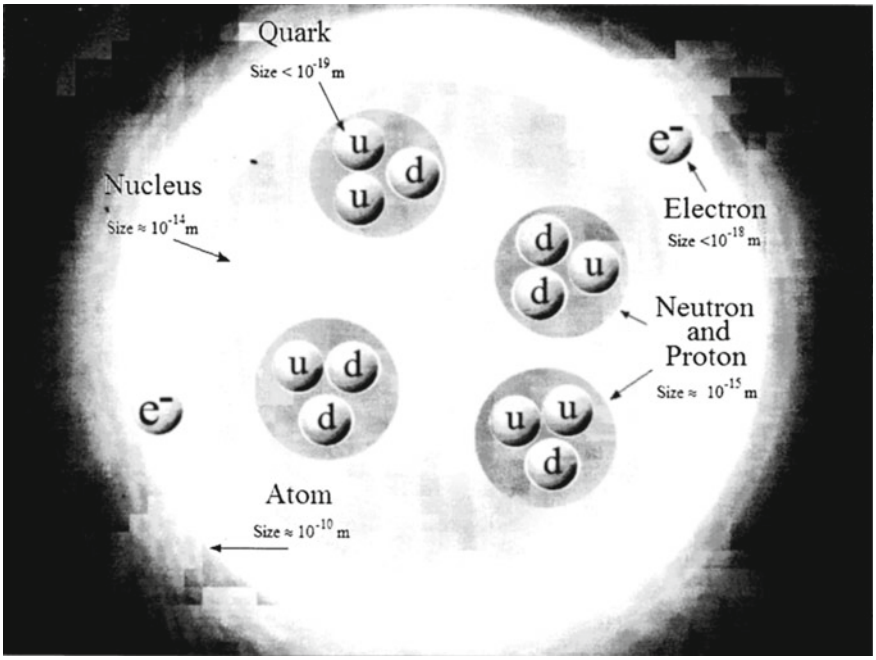

Fig. 2.1 Structure within the atom. If the protons and neutrons in this picture were 10 cm across, then the quarks and electrons would be less than 0.1 mm in size and the entire atom would be about 10 km across (after http://www.lbl.gov/abc/wallchart/)

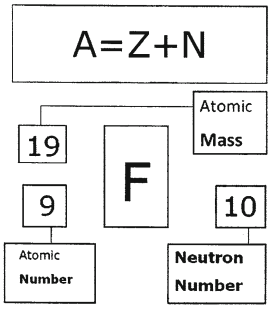

Fig. 2.2 Atomic nomenclature

We know well that the proton is denoted by letter p and the neutron by n. Chemical properties of an element are determined by the charge of its atomic nucleus, i.e. by the number of protons (electrons). It should be added that although it is true that the neutron has zero net charge, it is nonetheless composed of electrically charged quarks (see below), in the same way that a neutral atom is nonetheless composed of protons and electrons. As such, the neutron experiences the electromagnetic interaction. The net charge is zero, so if we are far enough away from the neutron that it appears to occupy no volume, then the total effect of the electric force will add up to zero. The

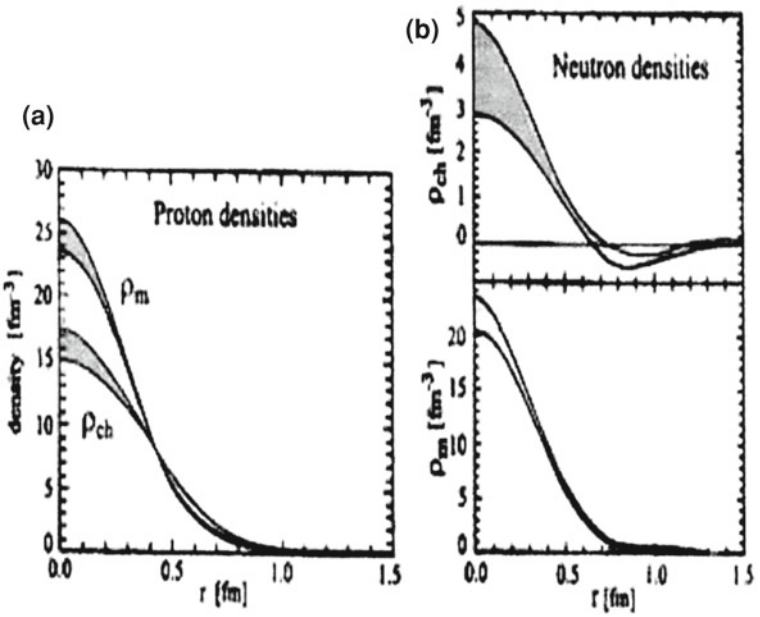

Fig. 2.3 Comparison between charge (ρ_{ch}) and magnetization (ρ_m) for the proton (**a**) and neutron (**b**). Both densities are normalized to $\int \mathrm{drr}^2\rho = 1(\mathrm{r})$ (after [62–64])

movement of the charges inside the neutrons does not cancel, however, and this is what gives the neutron its non-zero magnetic moment.

Each of the atomic constituencies, a spin 1/2 in units of $\hbar(=h/2\pi)$ and is an example of the class of particles of half-integer spin known as fermions. Fermions obey the exclusion principle of Pauli (see, e.g. [9]), which determines the way electrons can occupy atomic energy states. The same rule applies, as will be shown below, to nucleons in nuclei. Associated with the spin is a magnetic dipole moment. Compared with the magnetic moment of electron, nuclear moment is very small. However, they play an important role in the theory of nuclear structure. It may be surprising that the uncharged neutron has a magnetic moment. This reflects the fact that it has an underlying *quark substructure* (see, e.g. [60]), consisting of charged components. Electron scattering off these basic nuclear constituents (proton and neutron) makes up for the ideal probe to obtain a detailed view of the internal structure. A very detailed analysis using the best available data has been carried out recently by Kelly [61]. These data originate from recoil or target polarizations experiments (see, also [62–64]). In Fig. 2.3, the proton charge and magnetization distribution are given. What should be noted is the softer charge distribution compared to the magnetic one for proton. These resulting densities are quite similar to Gaussian density distributions that can be expected starting from quark picture (for details, see below) and, at the same time more realistic than the exponential density distributions [61]. The neutron charge and magnetization are also given in Fig. 2.3. What is striking is that

Table 2.3 Sample values of nuclear magnetic dipole moments (after [65])

Nuclide	$\mu(\mu_N)$
n	− 1.9130418
p	+ 2.7928456
^{2}H(D)	+ 0.8574376
^{17}O	− 1.89379
^{57}Fe	+ 0.09062293
^{57}Co	+ 4.733
^{93}Nb	+ 6.1705

magnetization distribution resembles very closely the corresponding proton distribution. Since scattering on neutrons normally carries the larger error (see, e.g. [6, 7]), the neutron charge distribution is not precisely fixed. Nonetheless, one notices that the interior charge density is balanced by a negative charge density, situated at the neutron surface region, thereby making up for the integral vanishing of the total charge of the neutron.

We may recall from atomic physics that the quantity e$\hbar$/2m is called *magneton*. For atomic motion we use the electron mass and obtain the Bohr magneton $\mu_{\mathrm{B}} = 5.7884\times10^{-5}$ eV/T. Putting in the proton mass we have the nuclear magneton $\mu_{\mathrm{N}} = 3.1525\times10^{-8}$ eV/T. Note that $\mu_N \ll \mu_B$ owing to the difference in the masses, thus, under most circumstances atomic magnetism has much larger effects than *nuclear* magnetism. Ordinary magnetic interactions of matter (ferromagnetism, for example) are determined by *atomic magnetism*.

We can write

$$\mu = \mathrm{g}_l l \mu_N, \tag{2.1}$$

where g_l is the *g-factor* associated with the orbital angular momentum l. For protons $g_l = 1$, because neutrons have no electric charge; we can use Eq. (2.1) to describe the orbital motion of neutrons if we put $g_l = 0$. We have thus been considering only the orbital motion of nucleons. Protons and neutrons, like electrons, as above mentioned above also have intrinsic or spin magnetic moments, which have no classical analog but which we write in the same form as Eq (2.1):

$$\mu = g_s s \mu_N, \tag{2.2}$$

where $s = 1/2$ for protons, neutrons and electrons (see Table 2.2). The quantity g_s is known as the spin *g-factor* and is calculated by solving a relativistic quantum mechanics equation (see, also [9]). For free nucleons, the experimental values are far from the expected value for point particles: proton—$g_s = 5.5856912 \pm 0.0000022$ and neutron—$g_s = 3.8260837 \pm 0.0000018$. Table 2.3 gives some representative values of nuclear magnetic dipole moments according [65]. The next non-vanishing moment is the electric quadrupole moment. The *quadrupole moment* eQ of a classical point charge e is of the form $e(3z^2 - r^2)$. If the particle moves with spherical symmetry, then (on the average) $z^2 = x^2 = y^2 = r^2/3$ and the

Table 2.4 Some values of nuclear electric quadrupole moments (after [65])

^{2}H(D)	+ 0.00288
^{17}O	− 0.02578
^{59}Co	+ 0.40
^{63}Cu	− 0.209
^{133}Cs	− 0.003
^{161}Dy	+ 2.4
^{176}Lu	+ 8.0
^{209}Bi	− 0.37

quadrupole moment vanishes (for details, see [8]). Some examples of the values of *nuclear electric quadrupole moments* are presented in Table 2.4.

Inside a nucleus, neutrons and protons interact with each other and are bound within (as mentioned above) the nuclear volume under the competing influences of attractive nuclear and repulsive electromagnetic forces. This binding energy has a direct effect on the mass of an atom. It is therefore not possible to separate a discussion of nuclear binding energy; if it were, then nucleon would have masses given by $Z_{m_p} + Z_{m_n}$ and the subject would hardly be of interest.

As it is well known, in 1905, Einstein presented the equivalence relationship between mass and energy: $E = mc^2$. From this formula, we see that the speed of light c is very large and so even a small mass is equivalent to a large amount of energy. This is why in nuclear physics it is more convenient to use a much smaller unit called *mega electron volt* ($1\ \text{MeV} = 1.602 \times 10^{-13}$ J). On the atomic scale, 1u is equivalent to 931.5 MeV/c^2, which is why energy changes in atoms of a few electron-volt cause insignificant changes in the mass of atom. Nuclear energies, on the other hand, are millions of electron-volts and their effects on atomic mass are easily detectable. For example, the theoretical mass of $^{35}_{17}$Cl is $17 \times 1.00782503 + 18 \times\ 1.00866491 = 35.28899389$ amu. Its measured (see below) mass is only 34.96995 amu. Therefore, the mass defect and binding energy of $^{35}_{17}$Cl are

$$\begin{aligned} \Delta &= 0.32014389\ \text{amu.} \\ E_B &= \frac{0.32014389 \times 931.5}{35} = 8.520\ \text{MeV/nucleon} \end{aligned} \tag{2.3}$$

and in common sense the binding energy is determined by next relation

$$E_B = Zm_p + Nm_n - B/c^2, \tag{2.4}$$

where B/c^2 is the actual nuclear mass.

As we can see below, the *binding energy* of the atoms of most elements have values ranging from about 7.5 to 8.8 MeV [2–5]. The binding energy per nucleon rises slightly with increasing mass number and reaches a maximum value for ^{62}Ni. Thereafter the binding energies decline slowly with increasing mass number. The

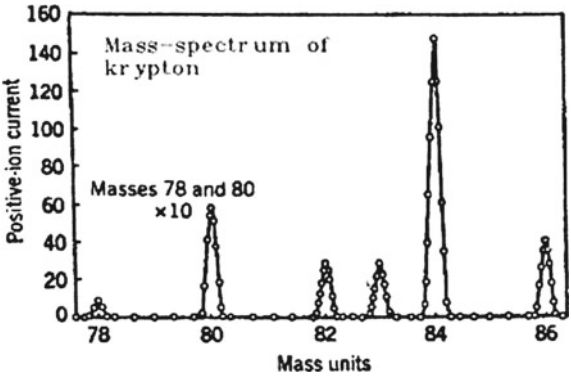

Fig. 2.4 A mass-spectrum analysis of krypton. The ordinates for the peaks at mass positions 78 and 80 should be divided by 10 to show these peaks in their true relation to the others (after [5])

binding energies of the atoms of H, He, Li and Be are lower than the binding energies of the other elements (see, also Fig. 2.5 below).

The measurement of nuclear masses occupies an extremely important place in the development of nuclear physics. Mass spectrometry (see, e.g. [66, 67]) was the first technique of high precision available to the experimenter, and since the mass of a nucleus increases in a regular way with the addition of one proton or neutron. In mass spectrometers, a flux of identical nuclei (ions), accelerated (see, e.g. Fig. 3.13 in [14]) to a certain energy, is directed to a screen (photoplate) where it makes a visible mark. Before striking the screen, this flux passes through magnetic field, which is perpendicular to velocity of the nuclei. As a result, the flux is deflected to certain angle. The greater mass, the smaller is the angle. Thus, measuring the displacement of the mark from the center of the screen, we can find the deflection angle and then calculate the mass. The example of a *mass-spectrum* of a different isotopes of krypton is shown in Fig. 2.4. From the relative areas of the peaks it can be determine the abundance of the stable isotopes of krypton (for details see [65]).

Relative masses of nuclei can also be determined from the results of nuclear reactions or nuclear decay. For example, if a nucleus is *radioactive* and emits an *α-particle*, we know from energy conservation that it mass must be greater than that of decay products by the amount of energy released in the decay. Therefore, if we measure the latter, we can determine either of the initial or final nuclear masses if one of them is unknown. An example of this is presented briefly below. At present we shall illustrate some typical reactions, bridging the gap between "classical" methods and the more advanced "high-energy" types of experiments (see, also [7, 61]).

The possible, natural *decay processes* can also be brought into the class of reaction processes with the conditions: no incoming light particle α and $Q > 0$. We list them in the following sequence:

α - decay:

$$ {}^{A}_{Z}X_{N} \rightarrow {}^{A-4}_{Z-2}Y_{N-2} + {}^{4}_{2}He_{2}. \tag{2.5} $$

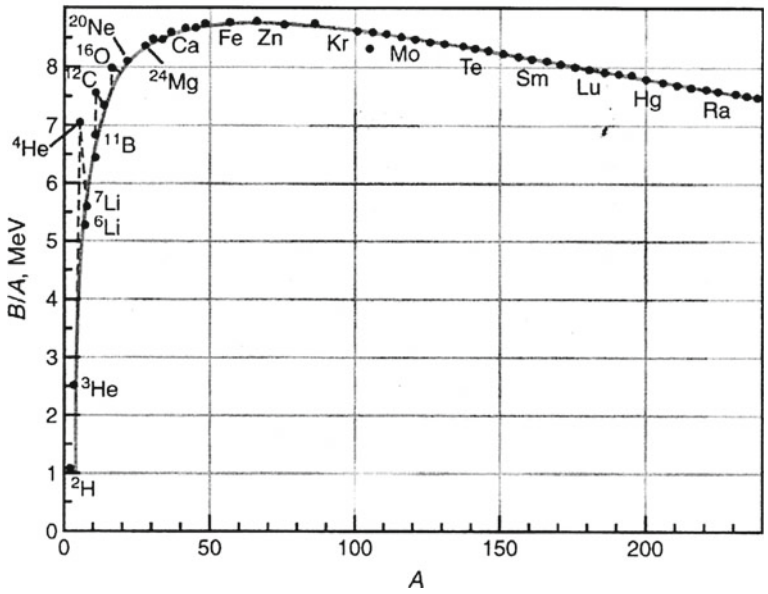

Fig. 2.5 The binding energy per nucleon B/A as a function of the nuclear mass number A (after [41])

β - decay:

$$^{A}_{Z}\mathrm{X}_{N} \rightarrow ^{A}_{Z-1}\mathrm{Y}_{N+1} + \mathrm{e}^{+} + \nu_e \quad (p \rightarrow n\text{-}type) \tag{2.6}$$

$$^{A}_{Z}\mathrm{X}_{N} \rightarrow ^{A}_{Z+1}\mathrm{Y}_{N-1} + e^{-} + \overline{\nu}_e \quad (n \rightarrow p\text{-}type) \tag{2.6'}$$

$$^{A}_{Z}\mathrm{X}_{N+\mathrm{e}^{-}} + \mathrm{e}^{-} \rightarrow ^{A}_{Z-1}\mathrm{Y}_{N+1} + \nu_e \quad (\mathrm{e}^{-}\text{-capture}). \tag{2.6''}$$

Here e^{-}, e^{+}, ν_e and $\overline{\nu}_e$ are electron, positron, neutrino and antineutrino.

γ - decay:

$$^{A}_{Z}\mathrm{X}^{*}_{N} \rightarrow ^{A}_{Z}\mathrm{X}_{N} + h\nu. \tag{2.7}$$

Here X* is excited nuclei.

Nuclear fission:

$$^{A}_{Z}\mathrm{X}_{N} \rightarrow ^{A_1}_{Z_1}\mathrm{Y}_{N_1} + ^{A_2}_{Z_2}\mathrm{U}_{N_2} + x \times n. \tag{2.8}$$

Table 2.5 Masses of electron, nucleons and some nuclei (after [41])

Particle	Number of Protons	Number of Neutrons	Mass (MeV)
e	0	0	0.511
p	1	0	938.2796
n	0	1	939.5731
$^{2}_{1}$H	1	1	1876.14
$^{3}_{1}$H	1	2	2808.920
$^{3}_{2}$He	2	1	2808.391
$^{4}_{2}$He	2	2	3728.44
$^{7}_{3}$Li	3	4	6533.832
$^{9}_{4}$Be	4	5	8392.748
$^{12}_{6}$C	6	6	11174.860
$^{16}_{8}$O	8	8	14895.077
$^{238}_{92}$U	92	146	221695.831

Since mass and energy are equivalent (see Einstein formula above), in nuclear physics it is customary to measure masses of all particles in the units of energy (MeV). Examples of masses of subatomic particles are given in Table 2.5.

As it was noted above, nuclear binding energy increases with the total number of nucleons A and, therefore, it is common to quote the average *binding energy* per nucleon (B/A) The variation of B/A with A is shown in Fig. 2.5. Several remarkable features are immediately apparent. First of all, the curve is relatively constant except for the very light nuclei. The average binding energy of most nuclei is, to within 10%, about 8 MeV per nucleon. Second, we note that the curve reaches peak near A = 60, where the nuclei are most tightly bound and light and very heavy nuclei contain less bound nucleons. Thus, the source of energy production in fusion of light nuclei or fission of very heavy nuclei can be a source of energy [13, 14].

While concluding this paragraph we should remember that it is often stated ^{56}Fe is the most tightly bound nucleus, but this is not correct since ^{62} Ni is more bound by a difference of 0.005 MeV/nucleon (for details see [68, 69] and references therein). In conclusion, it is very interesting to note that one cubic millimeter of *nuclear material*, if compressed together, would have a mass around 200,000 tonnes. *Neutron stars* are composed of such material.

As shown above nuclei vary from about one to a few fermis in radius. Recall that the Bohr radius of hydrogen is in the order 10^{-10} meters , so the nucleus at present time, despite its small size the nucleus has about, as was noted above, 99.9% of the mass of the atom (see, also [2, 3]). Electron scattering off nuclei is, for example, one of the most appropriate methods to deduce radii. The results of this procedure for several different nuclei are shown in Fig. 2.6. One remarkable conclusion is obvious—the central nuclear charge density is nearly the same for all nuclei. *Nucleons* do not congregate near the center of the nucleus, but instead have a fairly constant distribution out to the surface. The conclusion from measurements of the nuclear matter distribution is the same [70, 71]. Under this assumptions of saturation and

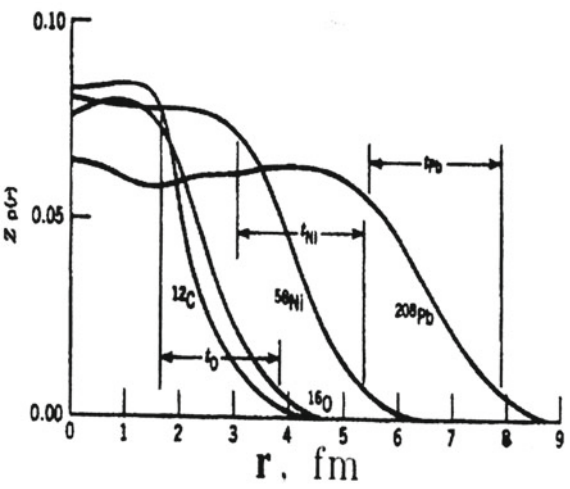

Fig. 2.6 The radial charge distribution of several nuclei determined from electron scattering. The skin thickness value t is roughly constant at 2.3 fm. The central density changes very little from the lightest nuclei to the heaviest (after [70, 71])

charge independence each nucleon occupies an almost equal size within the nucleus. Calling r_0 an elementary radius for a nucleon in the nucleus, a most naive estimate gives for the nuclear volume

$$\mathrm{V} = 4/3\pi r_0^3 \mathrm{A} \tag{2.9}$$

or

$$\mathrm{R} = r_0 \mathrm{A}^{1/3}. \tag{2.10}$$

This relation describes the variation of the nuclear radius, with value of $r_0 \simeq 1.2$ fm when deducing a "charge" radius and a "value of $r_0 \simeq 1.4$ fm for the full matter" radius (see also Figs. 3.5 and 3.9 in [5]). In a simple way the nuclear radius is defined as the distance at which the effect of the nuclear potential is comparable to that of the Coulomb's potential (see Fig. 2.7).

We should indicate another way to determine the nuclear charge radius from direct measurement of the Coulomb's energy differences of nuclei. Consider, for example, ${}^3_1\mathrm{H}_2$ and ${}^3_2\mathrm{He}_1$. To get from ${}^3\mathrm{He}_1$ to ${}^3\mathrm{H}_1$ we must change a proton into a neutron. As we know, there is strong a evidence which suggests that the nuclear force does not distinguish between protons and neutrons. Changing proton into a neutron should therefore not affect the nuclear energy of the three nucleon system: only the Coulomb's energy should change, because the two protons in ${}^3\mathrm{He}_1$ expexperience a repulsion that is not present in ${}^3\mathrm{H}$. The energy difference between ${}^3\mathrm{He}$ and ${}^3\mathrm{H}$ is thus a measure of the Coulomb's energy of the second proton, and the usual formula for the Coulomb's repulsion energy can be used to calculate the distance between the protons and thus the size of the nucleus.

The interactions between two nucleons (NN) is one of the central questions in physics and its importance goes beyond the properties of nuclei. Nucleons can combine to make four different few-nucleon systems, the deuteron $(p + n)$, the triton

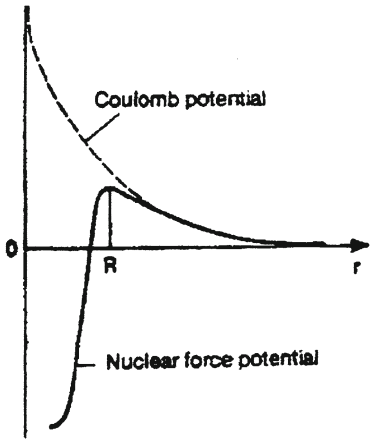

Fig. 2.7 Coulomb's potential used for defining the nuclear radius R

$(p + 2n)$, the helion $(2p + n)$ and the α-particle $(2p + 2n)$ (see, e.g. [72–75]). These particles are grouped together because they are stable (excluding from the radioactive triton which has a half-life of about 12 years and so may be treated as a stable entity for most practical purpose), have no bound excited states (except the α-particles which has two excited states at about 20 and 22 MeV) and are frequently used as projectiles in nuclear investigations. The absence of stable particles of mass of five provides a natural boundary between few-nucleon systems and heavier nuclei [38–40, 74]. Few nucleon systems provide the simplest systems to study nuclear structure. The *deuteron* provides important information about the nucleon–nucleon interaction.

Even before describing any further experimental and theoretical results to study the force between two nucleons, we can already guess at a few of the properties of the N–N force:

1. At short distances it is stronger than the *Coulomb's force*; the nuclear force can overcome the Coulomb's repulsion (see also Fig. 2.7) of protons in the nucleus.
2. At long distances, of the order of atomic sizes, the nuclear force is negligibly feeble. The interaction among nuclei in a molecule can be understood based only on the Coulomb's force.
3. Some fundamental particles are immune from the nuclear force. At present time we have not any evidence from atomic structure, for example, that electrons feel the nuclear force at all.
4. The N–N force seems to be nearly independent of whether the nucleons are neutrons or protons. As is well known this property is called *charge independence*.
5. The N–N force depends on whether the spins of the nucleons are parallel or antiparallel.
6. The N–N force includes a repulsive term, which keeps the nucleons at a certain average separation.

Table 2.6 Table of main families of particles

Family	Particle	Fundamental
Lepton	Electron	Yes
Lepton	Neutrino	Yes
Hadron	Proton	No
Hadron	Neutron	No
Hadron	Delta	No
Hadron	Sigma	No
Hadron	Many	More

7. The N–N force has a noncentral or *tensor component*. This part of the force does not conserve orbital angular momentum, which is a constant of the motion under central forces.

We should add that with knowledge of the N–N interaction provided by *p–p* and *p–n* scattering and by the deuteron [76–78] one can try to calculate the properties of the triton and the helion. The principal properties of few-nucleon systems are summarized in Table 2.6.

Deuteron. The *deuteron* is a very unique nucleus in many respects. It is only loosely bound, having a binding energy much less than the average value ($\leq$8 Mev [38–40]) between a pair of nucleons in all other stable nuclei. We have seen in Eq. (2.4) that the binding energy E_B of a nucleus is given by the mass difference between the neutral atom and the sum of the masses of free neutrons and protons in the form of hydrogen atoms. For a deuteron, as we can see from Table 2.5, the mass M_d is 1876.1244 Mev/c^2. The binding energy is then the difference between M_d and the sum of those for a neutron m_n and a hydrogen atom $m_H (=m_p)$: $m_n c^2 = 939.565$; $m_H c^{2=938.7833}$ MeV and $m_n + m_H = 1878.3489$ MeV. We can write according Eq. (2.4): $E_B = m_n + m_H - M_d = 2.224$ MeV. A more precise value, $E_B = 2.22457312$ MeV is obtained from radioactive capture of a neutron by hydrogen. In this reaction $p(n, \gamma)d$, a slow neutron is captured by a hydrogen atom followed by the emission of a γ-ray (for details see [79]).

To simplify the analysis of the deuteron *binding energy*, we will assume that we can represent the N–N potential of 3-D square well, as shown in Fig. 2.8

$$\begin{aligned} V(r) &= -V_0, \quad \text{for } r < R \quad (=2.1\text{fm}) \\ &= 0, \quad \text{for } r > R. \end{aligned} \tag{2.11}$$

This is of course an oversimplification, but is sufficient for at least some qualitative conclusions. In Eq. (2.11) r represents the separation between the proton and the neutron, so R is in effect a measure of the diameter of the deuteron (Fig. 2.9). If we express the energy, corresponding to the ground state value $E = -E_B$, the Schrodinger equation becomes for the 1-D, radial problem with zero angular moment, just like the lowest energy state of hydrogen atom.

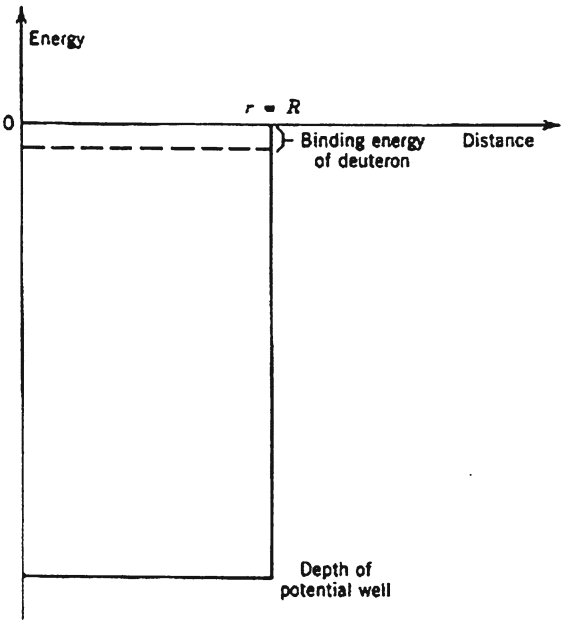

Fig. 2.8 The spherical square-well potential, adjusted to describe correctly the binding energy E_B of the deuteron. The full depth is also given and amounts to $V_0 = U = 38.5$ MeV (after [41])

$$\begin{aligned} &\frac{d^2u}{dr^2} + k^2u = 0, \quad r < R \text{ (see, Fig. 2.8)} \\ &\frac{d^2u}{dr^2} - \alpha^2 u = 0, \quad r > b, \end{aligned} \tag{2.12}$$

defining

$$k^2 = \frac{m_n}{\hbar^2}(u - E_B), \quad \alpha^2 = \frac{m_n}{\hbar^2}E_B \tag{2.13}$$

and using the radial solution

$$u(r) = rR(r). \tag{2.14}$$

Approximate solutions in the two regions became

$$\begin{aligned} u(r) &= A\sin kr, \quad r < R \quad \text{and} \\ u(r) &= Be^{-\alpha(r-R)} \quad r > b. \end{aligned} \tag{2.15}$$

Matching the logarithmic derivatives at $r = R$ gives

$$k\cot ankr = -\alpha \tag{2.16}$$

and matching the wave functions at $r = R$ gives

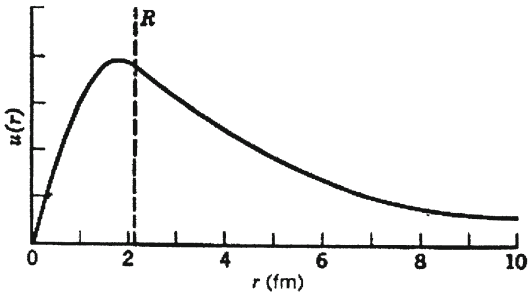

Fig. 2.9 The deuteron wave function for R = 2.1 fm (after [5])

$$\mathrm{AsinkR} = B. \tag{2.17}$$

These two relations lead to the condition

$$k^2\mathrm{A}^2 = (k^2 + \alpha^2)\mathrm{B}^2. \tag{2.18}$$

The normalization of the wave function $4\pi \int u^2(r)\mathrm{dr} = 1$ becomes

$$\frac{\mathrm{A}^2}{2k}(2kR - \sin 2kR) + \frac{\mathrm{B}^2}{\alpha} = \frac{1}{2\pi}. \tag{2.19}$$

Eliminating A^2 from the last two equations, gives the value for B as

$$B \simeq \sqrt{\frac{\alpha}{2\pi}}\mathrm{e}^{-\alpha \mathrm{R}/2}. \tag{2.20}$$

Knowing the *binding energy* E_B [see, Eq. (2.13)], we can determine the value $\alpha = 0.232\ \mathrm{fm}^{-1}$. A best value for R can be determined from proton–neutron scattering (see, e.g. [72–74]) as $R = 1.93$ fm. This then gives u = 38.5 MeV. One can show that this value of u and the value for R just give rise to a single, bound $1s$ state, all other higher-lying $1p$, $1d$, $2s$ being unbound. Since we also have

$$\mathrm{A} \simeq \mathrm{B} \tag{2.21}$$

we obtain the final wave functions

$$\begin{aligned} u(r) &= \sqrt{\tfrac{\alpha}{2\pi}}\mathrm{e}^{-\alpha \mathrm{R}/2}\mathrm{sinkr}, \quad r < \mathrm{R} \quad \text{and} \\ u(r) &= \sqrt{\tfrac{\alpha}{2\pi}}\mathrm{e}^{-\alpha \mathrm{R}/2}\mathrm{e}^{-\alpha \mathrm{r}} \quad r > \mathrm{b} \end{aligned} \tag{2.22}$$

A potential which gives a satisfactory account of the properties of the deuteron given in Table 2.7 is shown in Fig. 2.10. We should add that in all deuteron potentials the *tensor term* is a very sizeable part of the two-nucleon potential, and is charac-

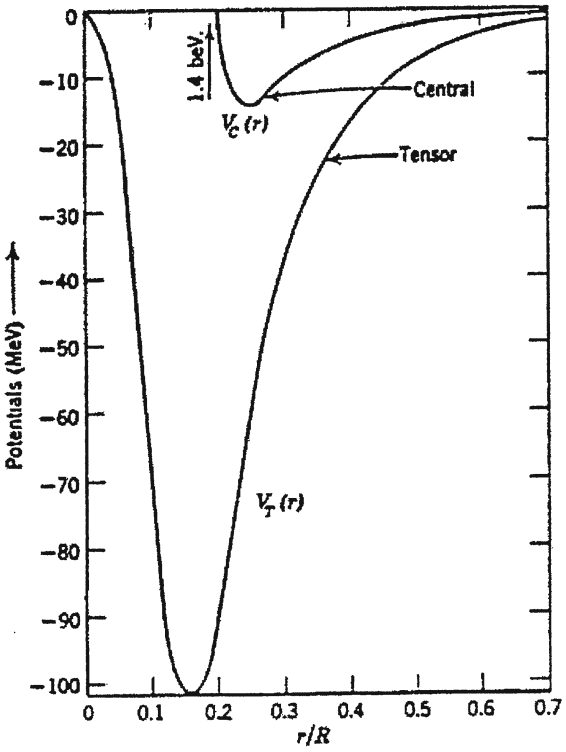

Fig. 2.10 The potential for deuteron triplet states with even L. the distance is in units of deuteron radius R = 4.31 fm (after [80])

terised by a somewhat larger range than the central potential (see Fig. 2.10) being appreciably different from zero even when the central potential is already negligible.

Proton–proton and proton–neutron interactions. Most of the present theories (see, also [74] and references therein) of *nuclear structure* and nuclear reactions are based on the assumption that nuclear properties depend mainly on *two-body interactions* between its constituents. Three-body forces or many-body forces are expected to play only a minor role.[4] It is thus of paramount importance to describe as accurately as possible the two-nucleon interaction. At the fundamental level this interaction is a consequence of the quark structure of the nucleons and should be described by QCD [75] in terms of the quark-gluon field (see, also [54–56, 72, 82]).

However this approach is still in its infancy and therefore we are still far from solution. There are also many indications [72, 73] that at interaction energies below a few hundred MeV it is possible to describe the N–N interaction in terms of the exchange of various types of mesons [83–86].

[4] If the two-body potential has an average strength of 20 MeV, then the three-body one would have a strength of about 1 MeV. We should add that all models have a one-pion exchange character at long range, which gives rise to a spin–spin central potential and a tensor term (for details see [60, 81]).

In principle there are four types of scattering measurements involving two nucleons that can be carried out. The scattering of an incident proton off a proton (*pp-scattering*) is the simplest one of the four from an experimental point of view, as it is relatively easy to accelerate protons and to construct targets containing hydrogen. For *neutron scattering*, there are two major sources for incident beam. At low energies, neutrons from nuclear reactors may be used. At higher energies, one can make use of neutrons produced by a beam of protons, for instance, through a (*p, n*) reaction on a ^{7}Li target. However, both the intensity and the energy resolution of neutron beams obtained in these ways are much more limited than those for proton beams. As a result, neutron scattering is, in general, a more difficult experiment than those with protons. In addition to *pp*- and *np*-measurements, one can, in principle, carry out *pn*- and *nn*-scattering experiments as well. Here, instead of using protons as the target, a neutron target is used. As we know, free neutrons are unstable (see above), with a half-life in the order of 10 min. It is therefore impossible to construct a fixed neutron target, in contrast to protons where material consisting of hydrogen may used. There are, in principle [84, 85], two methods of getting around this limitations. One way is to carry out a colliding beam experiment. In place of a target fixed in the laboratory, a second neutron beam is used and, instead of having an incident beam scattering from a fixed target, two beams of particles are directed towards each other. Scattering takes place when the particles in the two beam collide. To be practical, such an experiment requires high intensities in both beams, and currently highly intense beams of neutrons are not easily available. The other way is to simulate a fixed neutron target using deuterium. Since the deuteron is a loosely bound system of a neutron and a proton, the desired *pn*- or *nn-scattering* results can be obtained by carrying out the corresponding *pd*- or *nd*-scattering experiments. The contribution due to protons in the deuterium target may be removed by subtracting from the measured values the corresponding results obtained in *pp*- or *np*-scattering. The information obtained from *pn*- and *nn*-scattering may not be different from that in *np*- and *pp*-scattering. For example, the only difference between *pn*- and *np*-scattering is whether the neutron or the proton is the target. Under time-reversal invariance, these two arrangements are expected to give identical results. As early to simplify the notation, we shall use the symbol NN from now on to represent a system of two nucleons, as early, when there is no need to differentiate between neutrons and protons and the symbol *np* to represent both *np*- and *pn*-unless further distinction is required by the occasion. Futhermore, we shall assume that *Coulomb's contribution* where present, has already been taken out and we can therefore ignore it in the discussion.

The quantity measured in a scattering experiment is the number of counts registered by a *detector* (θ, φ) (see, e.g. [68]). The counting rate depends on the solid angle subtended by the detector at the scattering centre, the intensity of the incident beam, the number of target nuclei involved and the differential cross-section $\mathrm{d}\sigma/\mathrm{d}\Omega$. Naturally, our primary interest is in $\mathrm{d}\sigma/\mathrm{d}\Omega$, a function of the bombarding energy as well as the scattering angle. For simplicity we shall consider first only *elastic scattering*, and as a result, the wave number k in the centre of mass of the two particles has the same magnitude before and after the scattering. The differential scattering *cross-section* at angles (θ, φ) is given by next equation

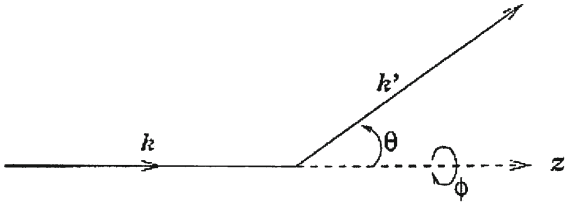

Fig. 2.11 Schematic diagram of a scattering arrangement. The scattering angle θ is between wave vector $\overrightarrow{k}$, along the direction of the projectile, and $\overrightarrow{k}'$, that of the scattered particle. The result is independent of the azimuthal angle Φ unless the orientation of the spin of one of the particles involve d is known (details see in text)

$$\frac{\mathrm{d}\sigma}{\mathrm{d}\Omega}(\theta, \varphi) = |f(\theta, \varphi)|^2 . \tag{2.23}$$

Here $f(\theta, \varphi)$ is the *scattering amplitude*. As shown in Fig. 2.11 the geometry of 0-scattering arrangement is such that it is coordinate system at the centre of the scattering region and takes the direction of the incident beam as the positive direction along the z-axis. The incident wave vector $\overrightarrow{k}$ and the scattered vector $\overrightarrow{k}'$ define a plane, the scattering plane.

For a *central potential*, the relative angular momentum $\overrightarrow{l}$ between the two scattering nucleons is a conserved quantity. Under such conditions, it is useful to expand the wave function as a sum over the contributions from different partial waves, each with a definite l-value

$$\Psi(r, \theta) = \sum_{l=0}^{\infty} a_l Y_{l0}(\theta) \mathrm{R}_l(k,\ r). \tag{2.24}$$

Here a_l is the expansion coefficients. Only spherical harmonics $\mathrm{Y}_{lm}(\theta, \varphi)$ with $\mathrm{m} = 0$ appears in the expansion since, in the absence of polarization, the wave functions is independent of the azimuthal angle Φ. We have explicitly included the wave number k in the arrangement of the radial wave function $\mathrm{R}_l(k,\ r)$ so as to emphasise the dependence of energy.

For a free particle, $V = 0$, and the radial wave function reduces to

$$\mathrm{R}_l(k,\ r) \to \frac{1}{kr} \sin\left(kr - \frac{1}{2} l\pi\right), \tag{2.25}$$

where $k = \sqrt{2\mu \mathrm{E}}/\hbar$ and $\mathrm{j}_l(\rho)$ is the spherical Bessel function of the order l. If only elastic scattering is allowed by the potential, the probability current density in each partial-wave channel is conserved. The only effect the potential can have on the wave

function is a change in the phase angle. In other words

$$\mathrm{R}_l(k,\ r)(\mathrm{scatt/r} \to \infty) \to \frac{1}{\mathrm{kr}} \sin\left(\mathrm{kr} - \frac{1}{2}\mathrm{l}\pi + \delta_\mathrm{l}\right), \tag{2.26}$$

where δ_l is the phase shift in the lth partial-wave channel.

After that, the scattering amplitude may be expressed in terms of δ_l as

$$f(0) = \frac{\sqrt{4\pi}}{k} \sum_{l=0}^{\infty} \sqrt{2l+1}\mathrm{e}^{i\,\delta_i} \sin\delta_l \mathrm{Y}_{l0}(\theta). \tag{2.27}$$

In such case the differential scattering cross-section may be written in terms of the phase shift

$$\frac{\mathrm{d}\sigma}{\mathrm{d}\Omega} = \frac{4\pi}{k^2} \left| \sum_{l=0}^{\infty} \sqrt{2l+1}\mathrm{e}^{i\,\delta_i} \sin\delta_l \mathrm{Y}_{l0}(\theta) \right|^2. \tag{2.28}$$

The scattering cross-section, the integral of $\frac{\mathrm{d}\sigma}{\mathrm{d}\Omega}$ over all solid angles, becomes

$$\sigma = \int \frac{\mathrm{d}\sigma}{\mathrm{d}\Omega} d\Omega = \frac{4\pi}{k^2} \sum_{l=0}^{\infty} (2l+1)\sin^2\delta_l(k). \tag{2.29}$$

Decomposition into partial waves is a useful way to analyse the scattering results for a given bombarding energy. In particular, only a few of the low-order partial waves can contribute to the scattering at low energies, as shown in Fig. 2.12. For realistic *nuclear potential*, the orbital angular momentum is not conserved.

Since we are dealing with identical fermions, the scattering of two nucleons can take place only in a state that is totally *antisymmetric* with respect to a *permutation* of the two particles, in the same way as for deuteron. For *pp*-sattering, we have $\mathrm{T} = 1$ [5] and the two nucleons are symmetric, as for their total isospin wave function [60] is concerned. If the intrinsic spins of the two protons are coupled together to $\mathrm{S} = 0$ (antisymmetric state) and, as a result only even l-values are allowed. For $\mathrm{S} = 0$, we have $\mathrm{J} = \mathrm{l}$ (we remind that $\vec{J} = \vec{l} + \vec{S}$), and the partial waves for the lowest two orders of *pp*-scattering are $^1\mathrm{S}_0$ ($\mathrm{l} = 0$) and $^1\mathrm{D}_2$ ($\mathrm{l} = 2$). The phase shifts extracted from measured *pp*-scattering data for these two partial waves of bombarding energy less than 300 MeV, in the laboratory are shown in Fig. 2.13 as illustrative examples (for details see [87]). Only the real part of the phase shift is given. At laboratory energy less than 300 MeV, contributions from inelastic scattering are still relatively

[5] In 1932 Heisenberg suggested [90] on the basis of the approximate of the proton and neutron mass (see also Table 2.2) that these particles might be considered as two different charge states of a single entity, the *nucleon*, formally equivalent to the up and down states of a spin 1/2 particle. To exploit this hypothesis the nucleon wave function in addition to a space and a spin component also has an isotopic spin (isospin) component (see, also e.g. [7]).

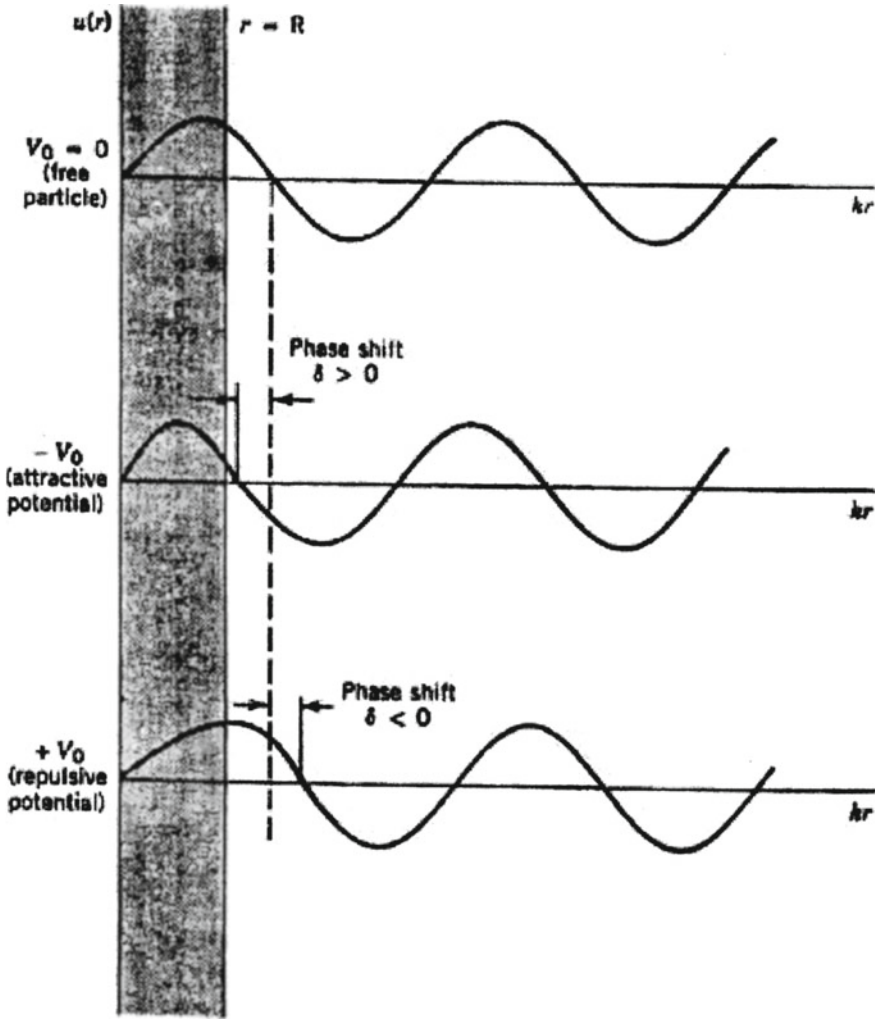

Fig. 2.12 The effect of a scattering potential is to shift the phase of the scattered wave at points beyond the scattering regions, where the wave function is that of a free particle (after [6])

unimportant and the imaginary parts of the phase shifts extracted from measured scattering cross-section are small (see Table 2.8).

By the same token, partial waves for triplet (S = 1) *pp-scattering* have odd l-values. The lowest order in this case is a p-wave ($l = 1$). When $l = 1$ is coupled with S = 1, three states with J = 0, 1, 2 are produced. The phase shifts for two of the triplet of states, $^3P_0$ and $^3P_1$, are also shown in Fig. 2.13a. There is no admixture between the two J = 0 states $^3P_0$ and $^1S_0$, as they are of different parity. As a result

Table 2.7 Properties of nucleons and few-nucleons systems

Particle	Symbol	Spin	Parity	BE(MeV)	MM (μ_0)	QM(fm^2)	RMS CR(fm)
Proton	p	1/2	+		$2.79284739\pm6\times10^{-8}$		0.88
Neutron	n	1/2	+		$-1.9130428\pm5\times10^{-7}$		
Deuteron	^{2}H	1	+	2.2246	$0.8574376\pm4\times10^{-7}$	0.288 ± 10^{-3}	1.963
Triton	^{3}H	1/2	+	8.482	2.978960 ± 10^{-6}		1.63±0.03
Helion	^{3}He	1/2	+	7.718	$-2.127624\pm1.12\times10^{-6}$		1.97±0.0015
Alpha	^{4}He	0	+	28.28			1.671±0.014

Here *BE* binding energy, *MM* magnetic moment, *QM* quadrupole moment; *RMS CR* RMS charge radius

Table 2.8 Nucleon–nucleon scattering length (a) and effective range (r_e)

	$s=0; T=1$ (fm)	$s=1; T=0$ (fm)
pp: a	−17.1±0.2	
pp: r_e	2.794±0.015	
nn: a	−16.6±0.6	
nn: r_e	2.84±0.03	
np: a	−23.715±0.15	5.423±0.005
np: r_e	2.73±0.03	1.73±0.02

we find that both l and S are good quantum numbers here by default (for details see [89] and references therein and Table 2.8).

The *np*-system may be coupled together to either isospin T = 0 or T = 1. For T = 0 the two nucleons are antisymmetric in *isospin*. In this case the S = 0 states must have odd l-values in order to be antisymmetric in the total wave function. The lowest order partial wave here is l = 1 and the phase shifts for ^{1}P$_1$-scattering extracted from experimental data are shown in Fig. 2.13c. In order for p-wave *np*-scattering to be in the S = 1 state, it is necessary for the total isospin to be T = 1. The phase shift in this case is expected to be identical to those found in *pp*-scattering, if nuclear force is charge independent and *Coulomb's* effects are removed. An examination of the two sets of empirical *p*-wave phase shifts, ^{3}P$_0$ and ^{3}P$_1$ given in Fig. 2.13b, shows that they are only slightly different from corresponding values given in Fig. 2.13a for *pp*-scattering. It is not clear whether the small differences come from the way the phase shifts are extracted from experimental scattering cross-section or they are indications of a weak charge dependence in the nuclear force (see, also Fig. 2.14).

The other T = 0 phase shift in the *np*-system, shown in Fig. 2.13c, is for triplet (S = 1), even *l*-scattering. This is the first time we encounter a mixing of different *l*-partial waves. Until now, each phase shift has been characterised by a definite *l*-value (as well as J- and S-values) even though the orbital angular momentum is not fundamentally a good quantum number. Mixing of different *l*-partial waves has not taken place because of parity and other invariance conditions; however, the tensor force can mix two triplet of the same J but different in l by two units ($l = J\pm1$) (see also [89]).

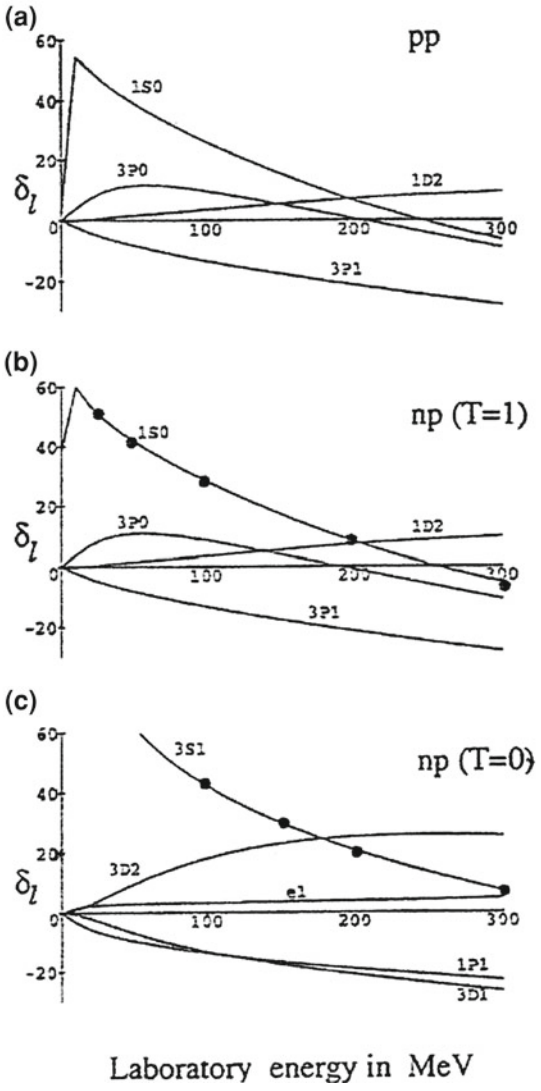

Fig. 2.13 Real part of NN-scattering phase shifts in degrees for low-order partial waves [87]: **a** *pp*-scattering with contribution from the Coulomb's potential removed. **b** isovector *np*-scattering, and **c** isoscalar *np* scattering. *Filled circles* in the $^1S_0$ and $^3S_1$ phase shifts of *np*-scattering are the calculated results using a Paris potential (after [88])

Our present knowledge of *nuclear physics* suggests that there are two main families of particles *leptons* and *hadrons* (*baryons* and *mesons*). The hadrons were first thought to be elementary like the leptons, but soon a very large number of hadrons were discovered, which suggest that they are not elementary (see, also [5, 70, 71, 91–93]). As we can see from Table 2.6 the leptons are fundamental particles, but hadrons are not. They are made up of *quarks* [94, 95] (for details see below). The hadron found in normal matter are the proton and the neutron. Quarks are one of the two basic constituents of matter which is described *QCD*. QCD [54–56, 96, 97] is

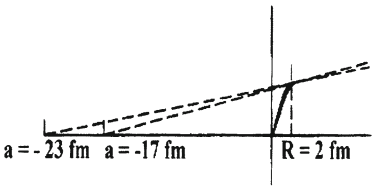

Fig. 2.14 Very small changes in the NN wave function near r = R can lead to substantial differences in the scattering length when the extrapolation is made (after [10])

Table 2.9 Characteristics of the quarks

Flavor	Electric charge (e)	Mass (GeV/c^2)
u—up	+ 2/3	0.004
d—down	− 1/3	0.008
c—charm	+ 2/3	1.5
s—strange	− 1/3	0.15
t—top	+ 2/3	176
b—beaty (bottom)	− 1/3	4.7

the theory of the strong interaction, a fundamental force describing the interactions of the quarks and gluons found in nucleons such as the proton and the neutron. QCD is an important part of the *Standard Model* (SM)[6] of particle physics (see, also [96, 97]). In the present SM [54–56] there are six "flowers" of quarks (see, below Table 2.9) most familiar baryons are the proton and neutron, which are each constructed up and down quarks [82, 98, 91]. Quarks are observed to occur only in combination of two quarks (mesons), three quarks (baryons), and the recently discovered with five quarks (pentiquarks [82]).

(a) *Quarks.* We now know that all the known properties of the hadrons (their quantum numbers, mass, charge, magnetic moment), their excited states and their decay properties (see, also below) may be explained by assuming that the mesons are made of quark–antiquark pairs, the baryons of three quarks and the antibaryons of three antiquarks [82, 96, 97]. To obtain this picture we need six quarks: *up*(u), *down* (d), *charm* (c), *strange* (s), *top* (t) and *bottom* (*beauty*) (b) (see Table 2.9). These six particles may be arranged according to their masses into three pairs, with one number of each pair having a charge +2/3e and the other −1/3e as shown in Table 2.9.Since quarks have not been observed in isolation, they appear either as bound quark–antiquark[7] pairs in the form of mesons or bound groups in the form of

[6] As is well known, the Standard Model [48–52, 54–56, 97, 81, 100] is a unified gauge theory of the *strong*, *weak* and *electromagnetic interactions*, the content of which is summarised by the group structure SU(3)× SU(2)× U(1), where SU(3) refers to the theory of strong interactions,QCD, and latter two factors [SU(2)× U(1)] describe the theory of electroweak interactions. Although the theory remains incomplete, its development represents a triumph for modern physics (for details see [100] and below).

[7] The first question that occurs is whether the quarks actually exist inside the hadrons or whether they are merely a convenient mathematical ingredient leading to the geometrical symmetry [7]. A substantial clue in this direction is obtained in deep inelastic scattering from nucleons [11–13]. The

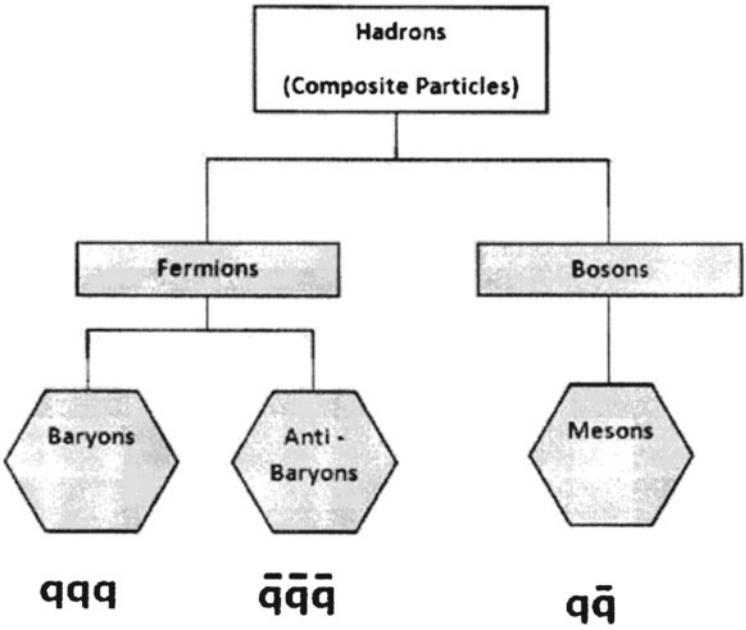

Fig. 2.15 Building blocks of matter, fermions have three quarks qqq and antiquarks $\overline{q}\overline{q}\overline{q}$ as well as bosons are quarks and antiquarks

baryons (see, also Fig. 2.15)—the name assigned to them, up, down, strange, etc., are only mnemonic symbols to identify of different species. The word "flavour" is used, for convenience, to distinguish between different types of quark. Besides flavour, quarks also come in three different colours, for example, red, green and blue. Colour and flavour are quantum-mechanical labels, or in other words, quantum numbers, very similar to spin and parity. Since there are no classical analogous to flavour and colour degrees of freedom, there are no observables that can be directly associated with them. In this respect, they are similar to the parity label of a state which must be observed through indirect evidence.

Now we know that colour charge is the charge associated with *strong interaction*. Colour is whimsically named attribute of *quarks* and *gluons* [109] that cannot be seen. Gluons have one colour and one anticolour [110, 111]. There are, however, only eight types of gluons [5], not nine as we might expect. Quarks and gluons are only found inside hadrons. The quarks inside a hadron are bathed in a sea of gluons

nucleon appears to be made up of to regions in the asymptotic-free regime [100–102] and the outer region of the meson cloud where pions and other heavy mesons can exist (see, also [103–108]). A number of early results on the internal proton structure became accessible through highly inelastic electron scattering carried out at the Stanford Linear Accelerator centre (SLAC). Later work of Kendell et al. [11–13] helped to identify these structures with quarks inside the proton (for details see also [109]).

(and additional quark–antiquark pairs) that are responsible for the binding forces in the hadron. Quarks continually emit and absorb gluons. Colour charge is conserved in every such process. The colour mathematics always work out so that at any instant the entire hadron system is colour neutral.

For quarks, the interaction is very strong at low energies where nuclear physics operates and where most of the experimental observations are made. Because of what is generally known as asymptotic freedom [100, 102], the quark–quark interaction is weak only at extremely high energies. As a result, perturbational techniques apply to *QCD* only at such extremes, far beyond the realm of nuclear physics and low-lying hadron spectroscopy. Since quarks are not observed in isolation, their mutual interaction must have a component that grows stronger as the distance of separation between them increases. This is opposite to our experience in the macroscopic world, where interactions, such as gravitational and electromagnetic, grow weaker as the distance of separation between the interacting objects is increased (and the relation is given by the inverse square low).

From the above text it has become clear that protons and neutrons are no longer considered as elementary (see, also Fig. 2.15) but are composed of quarks in a *bound state*. The binding forces are quite distinct from electromagnetic, gravitational forces: at very short distance, the quarks appear to move freely but, with increasing separation, the binding forces increase in strength too. So it is not possible to separate the nucleon into its constituent quarks.[8] From this picture is followed that quarks are to be able to exist only in combination with other quarks (baryons) or with antiquarks (mesons) [60, 109]. This picture has also modified our ultimate view of a system of densely packed nucleons. For composite nucleons, interpenetration will occur if the density is increased high enough and each quark will find many other quarks in its immediate vicinity (see Fig. 2.16). The concepts of a nucleon and of nuclear matter become ill-defined at this high-energy limit and a new state of matter might eventually be formed: a quark plasma whose basic constituents are unbound quarks [81, 110, 111]. Starting with the matter of vanishing baryon density, the energy density of a non-interacting gas of massless quarks and gluons is (see, also [118, 119])

$$\mathrm{E} \simeq 12\mathrm{T}^4, \tag{2.30}$$

Where T is temperature. Just like in the Stefan–Boltzman for a proton gas, the numerical factor in (2.30) is determined by the number of degrees of freedom of the constituent particles: their spins, colours and flavours. The energy density for quarks plasma via computer simulations is obtained in [81]. The transition temperature from the mesonic regime to the plasma regime is around 200 MeV which means an energy density of at least $2.5\,\mathrm{GeV\,fm^{-3}}$ in order to create a quark-gluon plasma.

As is well known, the neutron decay was thus written

[8] As we know, nonrelativistic quark model use *constituent quark* masses, which are of order 350 MeV for u- and d-quarks. Constituent quark masses model the effect of dynamical chiral symmetry breaking are not related to the quark mass parameters m_q of the *QCD* Lagrangian.

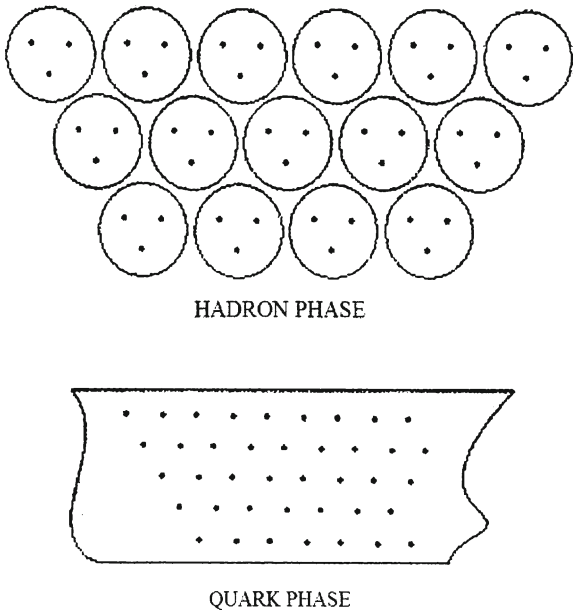

Fig. 2.16 Comparison of a collection in hadronic or nuclear matter phase and within quark-gluon plasma description (after [110, 111])

$$n \rightarrow p + e^{-} + \widetilde{\nu}_e, \tag{2.31}$$

where $\widetilde{\nu}_e$ is an electron antineutrino. This decay illustrates some of this conservation lows which govern particle decays.

The proton in the product satisfies the conservation of *baryon number*, not the emergence of the electron unaccompanied would violate conservation of lepton number. The third particle must be an electron antineutrino to allow the decay to satisfy lepton number conservation The electron has lepton number 1 and the antineutrino has lepton number -1. However, a proton bound in a nucleus may also transform into neutron by emitting a positron and a neutrino. This process is a bound as β^{+}-decay and discussed in any textbooks (see, e.g. [6, 7]). Also for this transformation the above consideration holds and the proton transformation into a neutron was written

$$p_{\text{bound}} \rightarrow n + e^{+} + \nu_e, \tag{2.32}$$

where ν_e is an *electron neutrino*. In conclusion of this part, we should note, that the *lepton number* conservation rule is applied to all cases it is found to work.

As we known well, at present time all *hadrons* are subdivided into two classes *baryons* and *mesons* (see Fig. 2.15). Baryons are distinguished by the fact that they are fermions, particles that obey Fermi-Dirac statistics. Because of this property, two baryons cannot occupy the same quantum-mechanical state. The fact that baryons are fermions implies that quarks must also be fermions, as it is impossible to construct fermions except from odd numbers of fermions. Furthermore, if we accept that a

quark cannot exist as a free particle, the lightest fermion in the hadron family must be made of three quarks (see also Fig. 2.15). Among the baryons, we are mostly concerned with the lightest pair, the neutron and the proton. From charge conservation alone, it can be deduced that a proton carrying a charge +e, must be made of two u-quarks, each having a charge of 2/3e (Table 2.9), and one d-quark, having a charge of −1/3e. The *quark wave function* of a proton may be represented as

$$| p >=| \text{uud} >. \tag{2.33}$$

Similarly, the quark wave function of a neutron is

$$| n >=| \text{udd} > \tag{2.34}$$

so that the total charge of a neutron in units of e is $2/3 - 1/3 - 1/3 = 0$.

Boson particles obeying Bose–Einstein statistics may be made from even number of fermions. This means that mesons are constructed of an even of quarks. Since, on the one hand, bosons can be created or annihilated under suitable conditions and, on the other hand, the number of quarks is conserved in *strong interaction* processes, a meson must be made of an equal number of *quarks* (see, also Fig. 2.15). The simplest meson is, therefore made of quark–antiquark. For example, pions (π), the lightest members among the mesons, are made of a quark, either u or d and an *antiquark*, either $\overline{u}$ or $\overline{d}$ (see, e.g. [109]).

2.3 Big Bang and Stellar Nucleosynthesis: Origin of Elements

The nuclear and particle physicists, the early *Universe*, represents the ultimate particle accelerator in which energies and densities of particles were beyond what we can ever hope to achieve with artificially constructed accelerators. Most modern views of cosmology are in agreement with the idea that the Universe began with an explosion, or "*Big Bang*" some 10–20 billions years ago. The uncertainties in the models are connected mostly with the very beginning of time, within the first fraction of a second or so. At the end of approximately the first 3 min. [112], and three-fourth of the baryon mass in the Universe is in the form of protons and the rest in the form of ^{4}He (see, e.g. [38–40]) Traces of deuteron, ^{3}He, and ^{7}Li are also present but their abundances are down by several orders for deuteron and ^{3}He and 10 orders for ^{7}Li (see, also Fig. 2.17).

Gamow [114–116] and Alpher and others [117] attempted to explain the relative abundance of all elements and isotopes from neutrons, following the hypothetical explosion which marked the beginning of the Universe (see, also [118, 119]). We now place this event $\sim 1.5 \times 10^{10}$ years ago. After that a number of modifications were made to the original theory. The first was made by Hayashi [120], who noted that at the high temperatures in the very early Universe, ther should be an equilibrium between protons and neutrons. The second modification was suggested by Fermi and

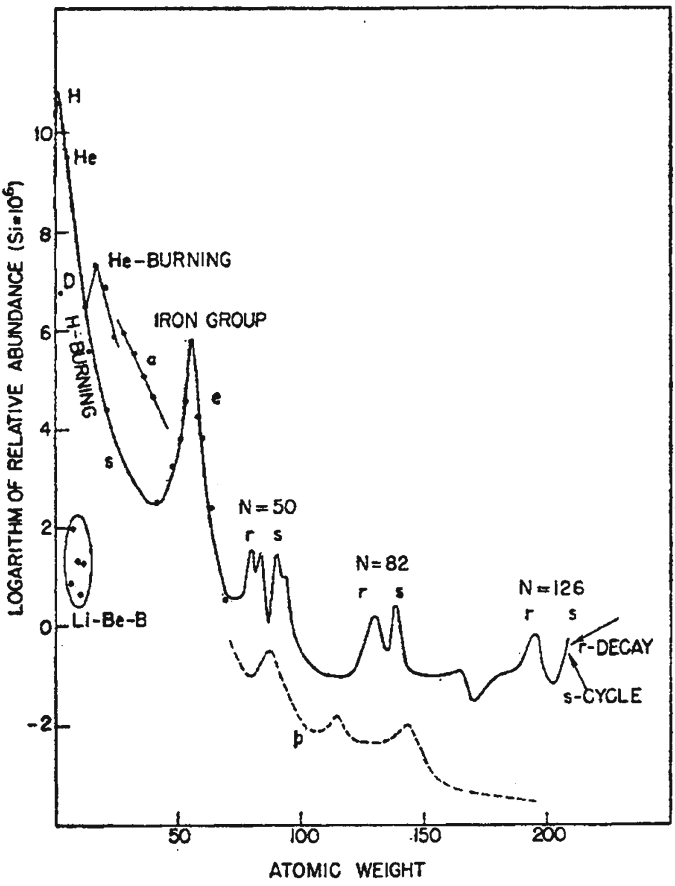

Fig. 2.17 Schematic curve of atomic abundance as a function of atomic weight based on data of Sues and Urey [113]. This author have employed relative isotopic abundance to determine the slope and general trend of the curve (after [113])

Turkevich [118, 119], who noted that lack of stable nuclei at mass 8 prevented the formation of carbon. As a result, this theory was neglected until the mid 1960s. Today the picture of the Big Bang is generally accepted, and forms on essential part of our understanding of the abundance of the elements (see [38]). The strongest facts in favour of the Big Bang theory are:

1. The relative abundance of the light elements [74].
2. The microwave background, which is remnant of the photon field of the Big Bang [121, 122].
3. The agreement of the ages of the oldest stars with the age of Universe.

The most convincing evidence for the Big Bang was provided by the discovery of the microwave background [121, 122]. Strong additional support for the *Big Bang*

model came from the conclusion by authors [124]. For review and history of this question see [125].

Temperature and densities in the Big Bang model are shown in Fig. 2.18. As the expansion began, temperature was too high to allow complex nuclei to survive. About 100s after the start of the Big Bang, T $\langle 1.3\times 10^9$ K (equivalent to an energy of 110 keV) (see, also [5, 8]). Then complex nuclei could survive, so the nucleosynthesis of light elements occur [74]; this is sometimes referred to as the era of nucleosynthesis. The modern theory of this process is referred to as standard Big Bang nucleosynthesis. About 3,000 years later, the expanding material cooled below $\sim 10^3$ K, so that hydrogen ions could recombine.

As was shown above, free *neutrons decay* into protons with a half-life of about 10 min. For a neutron to survive much longer time periods, it must be captured by other nucleons to form a bound nucleus. Since most of the nucleons in the *Universe* are in the form of free protons and neutrons at this stage, the most likely candidate to be formed is the deuteron, a bound nucleus made of a proton and a neutron. Unfortunately the binding energy of a deuteron is very small and this constitutes the major bottleneck in preserving primordial neutrons from β-decay. Because of the short range of nuclear force, bound nuclei can be made from free neutrons and protons only through random collisions that bring some of them into close contact with each other. The probability of such encounters drops drastically for three or more particles. This leaves us with deuteron as the only likely bound system that can be made in any significant amount. On the other hand, the small binding energy means that deuterons can also be destroyed easily in random collisions with other particles. The most likely event is with photons, as there is something like 10^9 for each nucleon. For this reason, photodisintegration constitutes an important sink for any deuterons created when the temperature is still sufficiently high. On further cooling, some deuterons can exist long enough to capture a proton to form ^{3}He. In turn, ^{3}He can capture a neutron and transform it into ^{4}He. When we see that one temperature is sufficiently low for deuterons to last long enough to undergo proton and neutron captures, free neutrons are transformed into bound ones and the total number in the Universe stays more or less constant until start of stellar nucleosynthesis at much later stages in the evolution of our Universe.

As we know, nuclei of mass 8 are a *bottleneck* [126]. Two helium nuclei fuse to form ^{8}Be, but the next step, the fusion of ^{8}Be with a third helium nucleus is rare, since ^{8}Be is unstable with a half-life of $\simeq 10^{-16}$ s. Thus to form carbon, three helium nuclei must react [41]. This is not possible in the Big Bang because of rapid expansion [39, 40]. Thus because of the instability of ^{8}Be, all nuclei heavier than ^{7}Li must have been produced in stars. As will be shown below, carbon is formed from three helium nuclei (α-particles) in the interior of higher-mass stars, where high densities and temperatures are present for $\sim 10^6$ years. Von Weizsäcker [127] and Bethe [128] proposed a quantitative scheme by which the Sun produced energy. This process is the so-called *CNO* (carbon–nitrogen–oxygen) cycle (see, also [129, 130]). In this process, carbon acts as a catalyst; in equilibrium the net effect is the conversion of hydrogen into helium. Later a cycle involving the fusion of protons to produce helium, the *p–p* cycle [38] was found to be effective in lower-mass stars [39, 40]

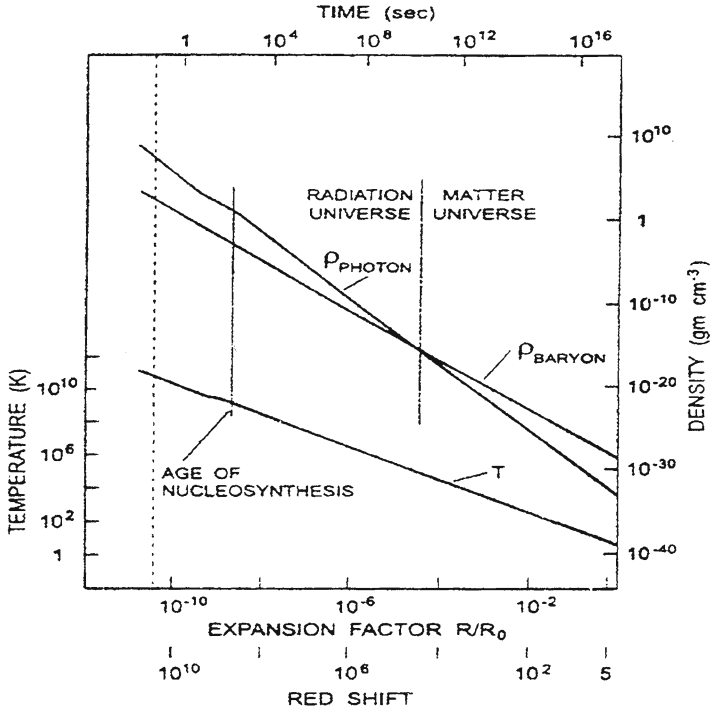

Fig. 2.18 A simplified presentation of the temperature and density relations in the homogenous Big Bang. The scale on the right vertical axis refers to the two upper curves for the photon and matter densities. The scale on the left vertical axis refers to the lowermost curve, which describes the temperature of the photon field. The remnant photon field of the Big Bang is a black body characterised by $T_{BG} = 2.75(1 + z)$. The production of the light elements occurred when the temperature fell below 2×10^9 K. This was the age of nucleosynthesis in the Big Bang. Following this time, the expansion allowed further cooling so that Big Bang nucleosynthesis came to an end. Matter continued to be ionized until the temperature fell below $\sim 10^3$ K. When the ions recombined matter became neutral and photons and matter decoupled. Following this was a period before stars and galaxies formed, the so-called 'dark age'. It is currently believed that star formation began at $z \sim 5$. The temperature contribution shown is the result of only the Big Bang contribution. Star formation will raise the temperature and perhaps re-ionize the Universe at $z \sim 5$ (after [129, 130]

In stars, the material becomes inhomogeneous since deeper in the interior the pressures and temperatures must be larger. In a similar way, the centres of stars more massive than the Sun must be hotter than the centre of the Sun; heavier elements are produced in higher-mass stars which have larger central temperature [39, 40, 125, 126]. To produce the nuclei of heavier elements by fusion, the larger *Coulomb's* repulsive forces must be overcome. These can only be produced in the centres of larger mass stars. Thus, only higher-mass stars can enrich the interstellar medium with nucleosynthesis products such as carbon, oxygen, neon or silicon. The exact yields of such

Table 2.10 Characteristics of the leptons

Flavor	Electric charge (e)	Spin	Mass (Gev/c^2)
ν_e—electron neutrino	0	1/2	$<7\times10^{-9}$
e^-—electron	−1	1/2	0.000511
ν_μ—muon neutrino	0	1/2	<0.00027
μ^-—muon (mu - minus)	−1	1/2	0.106
ν_τ—tau neutrino	0	1/2	<0.03
τ^-—tau (tau - minus)	−1	1/2	1.771

material are not certain since the product yields of such explosive processes depend on many details (for details, see [39, 40]).

When the hydrogen fuel is used up in a star, production of nuclear energy from fusing protons into ^{4}He stops and the temperature drops [129, 130]. Helium burning requires a temperature in the order of 10^8 K. Since ^{8}Be is unstable and lives only $\sim10^{-16}$ s, the conversation takes place mainly through the triple-α reaction

$$^4\text{He} +^4 \text{He} +^4 \text{He} \longrightarrow {}^{12}C + \gamma. \tag{2.35}$$

The ^{12}C produced can capture another α-particle to make ^{16}O,

$$^4\text{He} +^{12} \text{C} \longrightarrow {}^{16}\text{O} + \gamma. \tag{2.36}$$

In (2.35) and (2.36) γ is a electromagnetic radiation. Further α-particle capture produces even heavier nuclei. However, as we move to heavier and heavier nuclei, the *Coulomb's barrier* increases in height. This calls for higher temperatures that can come only from further gravitational contraction, as shown in Table 2.10. Since this is more likely to take place first at the centre, the inner parts of the star go to higher temperatures and densities, and evolve faster through different stages, than those outside.

The release of fusion energy stops at A $\approx$ 56, where the *binding energy* per nucleon peaks in value (see above). This takes place first in the stellar core and most of the nuclei are in the form of ^{56}Fe and ^{56}Ni the two most stable A = 56 *isobars*. Further evolution of the star depends even more critically on its total mass than any of its early stages. If the value is more than 8 times the solar mass [39, 40] there is enough gravitational energy left in the core in the core at the end of fusion to turn the star into a supernova.

When all the available ^{4}He in the central part of a star is used up, the core goes through another stage of gravitational contraction and rise in temperature. When $T \sim 10^9$ K, corresponding $kT \sim 100$ keV, reactions involving the conversion of any ^{12}C remaining after helium burning become possible, such as

$$
\begin{aligned}
{}^{12}\mathrm{C} + {}^{12}\mathrm{C} &\longrightarrow {}^{24}\mathrm{Mg} + \gamma \\
&\longrightarrow {}^{23}\mathrm{Na} + \mathrm{p} \\
&\longrightarrow {}^{23}\mathrm{Mg} + \mathrm{n} \\
&\longrightarrow {}^{20}\mathrm{Ne} + \alpha \\
&\longrightarrow {}^{16}\mathrm{O} + \alpha + \alpha. \qquad (2.37)
\end{aligned}
$$

The time span for the carbon *burning phase* is several orders of magnitude shorter than that for helium.

At even higher temperature, 2 to 3 $\times 10^9$ K, it is possible to convert ^{16}O into heavier elements, for example.

$$
\begin{aligned}
{}^{16}\mathrm{O} + {}^{16}\mathrm{O} &\longrightarrow {}^{32}\mathrm{S} + \gamma, \\
&\longrightarrow {}^{31}\mathrm{P} + \mathrm{p} \\
&\longrightarrow {}^{31}\mathrm{S} + \mathrm{n} \\
&\longrightarrow {}^{28}\mathrm{Si} + \alpha \\
&\longrightarrow {}^{24}\mathrm{Mg} + \alpha + \alpha. \qquad (2.38)
\end{aligned}
$$

When the temperature is between 3 and 4 $\times 10^9$ K, conversion of two ^{29}Si to one ^{56}Ni becomes possible.

Supernovas hold a special place in nucleosynthesis because of the heavy elements they produce. Since binding energy per nucleon decreases beyond A $\sim$ 56, it takes energy to create elements that are heavier (for details see [39, 129, 130]).

2.4 Isotope Effect in Nuclear Physics

In this section we will describe the influence of neutrons on the charge distribution. This influence has been studied using isotopic shift, the difference in the charge distributions of nuclei with the same number of protons but a different number of neutrons. If charge distribution in a nucleus is independent of neutrons, we expect the isotopic difference to be negligible. The measured results (see, e.g. [131–138]) indicate that, in general, the shifts are small but nonzero. Isotope shift (of spectral lines) can be divided into two classes that caused by the mass effect and that resulting from the field effect–volume effect. The mass effect consists of two parts, normal and specific, and results from the nucleus having a finite mass (see, also [41]). The *normal mass effect* can be calculated exactly, while the specific (for details see, also Chap. 4) mass effect present in spectra of atoms with more than one electron is very difficult to calculate precisely. Both of this effects decrease with increasing Z. The *field effect*, which increases with increasing Z, arises because of the deviation of the nuclear electric field from a Coulomb's field and can be used to study details of

Table 2.11 The root-mean-square radius ($\langle r^2 \rangle^{1/2}$) for detailed calcium isotopes

Nucleus	^{40}Ca	^{42}Ca	^{44}Ca	^{48}Ca
$\langle r^2 \rangle^{1/2}$ (fm)	3.4869	3.5166	3.5149	3.4762

nuclear structure. This is probably the most important consequence of isotope shift studies.

Thus in the very light elements the mass effect dominates and can account qualitatively for the observed shifts. In the heaviest elements the mass effect is negligible and the field effect can roughly account for the observed shift. In the element of intermediate mass the two effects are comparable. As a result, the shifts observed are small because the mass and field effects within the levels are often in such a direction as to oppose one another. In order to use the field effect in the demonstration of nuclear properties, it is necessary that the contribution of the mass and field effects to be observed shifts be known.

Isotope effect in calcium isotopes. The isotopic shift data [131], obtained from electron scattering, are summarized in Table 2.11. As we can see, the difference in the *root-mean-square radius* $\langle r^2 \rangle^{1/2}$ between the isotopes given in Table 2.11 are quite small. However, the good accuracies achieved in the measured values indicate a genuine difference among them. Since the radius decreases by 0.01 fm in going from ^{40}Ca to ^{48}Ca, it means that the addition of neutrons to calcium isotopes reduces the size of the charge distribution of the same 20 protons when neutron number is increased from 20 to 28. If we take the simple view that charges were distributed evenly throughout the nuclear volume, the charge radius should have increased by 6% based on simple $R = r_0 A^{1/3}$ relation. This is found to be true in the case of ^{48}Ti [131], a nucleus with two more protons and six more neutrons than ^{40}Ca. Here, the size of the charge distribution in increased by 0.1 fm for ^{48}Ti not far from the expectation of an $A^{1/3}$ dependence, instead of decreasing for ^{48}Ca. There are two possible explanations for the decrease in the charge radius with increasing neutron number among even calcium isotopes. The first is that addition of neutrons makes the protons more tightly bound and, hence, the charge radius is smaller. This is, however, not true for nuclei in general (see, e.g. [5, 9]). A second explanation is based on the charge distribution within a neutron (see, Fig. 2.3). One possible model for the charge distribution in a neutron is that the central part is positive and the region near the surface is negative, as shown in Fig. 2.3. The detailed charge distribution is not well known, because of the difficulty in measuring the small charge form-factor (see, also [132–134]). However, a small excess of negative charge in the surface region can produce about a third of decrease in the charge radius in going from ^{40}Ca to ^{48}Ca, as suggested by the authors of paper [142]. The other two-thirds may be attributed to the spin dependence in interactions of protons with other nucleons in the nucleus (see, e.g. [72, 73, 84, 85]). Regardless of the exact cause of the isotopic shift among calcium isotopes, it is clear that neutrons have a definite influence on the measured charge distribution of a nucleus (for details see [131–137]). The same effect can also

observed in other measurement, for example, such as the energy scattering of X-rays from muonic atoms [139–141].

Isotopic shift in muonic atoms. As was shown above, a muon is a lepton with properties very similar to an electron. For this reason, it is possible to replace one of the electrons on an atom by a (negative) muon to form muonic atom. However, since the mass of a muon is 209 times larger than that of an electron, the radii of the muonic orbits are much smaller than those of electrons.

According atomic physics (see, e.g. [139]) hydrogen-like atom with Z *protons* in the nucleus and only a single electron outside, the radius of the *n*th orbit is given by

$$r_n(e^-) = \frac{n^2\hbar^2}{\alpha\hbar c Z m_e} \tag{2.39}$$

Here, m_e is the mass of an electron, α is the fine structure constant. For hydrogen atom (Z = 1), the ground state (n = 1) radius is well known *Bohr radius* (see, also [139]);

$$a_0 = \frac{\hbar}{\alpha \mathrm{c} m_e} = 5.29\times10^{-11}\,\mathrm{m}. \tag{2.40}$$

Using (2.40), we can obtain the analogous results for a muonic atom by replacing m_e by m_μ

$$r_n(\mu^-) = a_0 \frac{n^2 m_e}{Z m_\mu}. \tag{2.41}$$

Using a muon mass $m_\mu = 106\,\mathrm{MeV/c^2}$, we obtain for a heavy nucleus, such as ^{208}Pb (Z = 82) the radius of the lowest muonic orbit

$$r_1(\mu^-) \simeq 3.1\times10^{-15}\,\mathrm{m} \tag{2.42}$$

or 3.1 fm. This is actually smaller than the value of 7.1 fm for the radius of ^{208}Pb, estimated using $\mathrm{R} = \mathrm{r_0 A^{1/3}}$ with $\mathrm{r_0} = 1.2$ fm [8]. A more elaborate calculation [140] shows that the muon spends inside a heavy nucleus. Being very close to the nuclear surface, the low-lying muonic orbits are sensitive to the detailed charge distribution of the different isotopes. The resulting changes in the energy levels may be observed as shifts in position of lines. Detailed investigation of isotopic shift was done on the different isotopes of Fe in paper by Shera et al. [140]. Muonic X-ray spectra from three isotopes of Fe obtained in this chapter are shown in Fig. 2.19. The isotope shift is large compared with isotope shift of electronic X-rays, which is typically 10^{-2} eV per unit change in A.

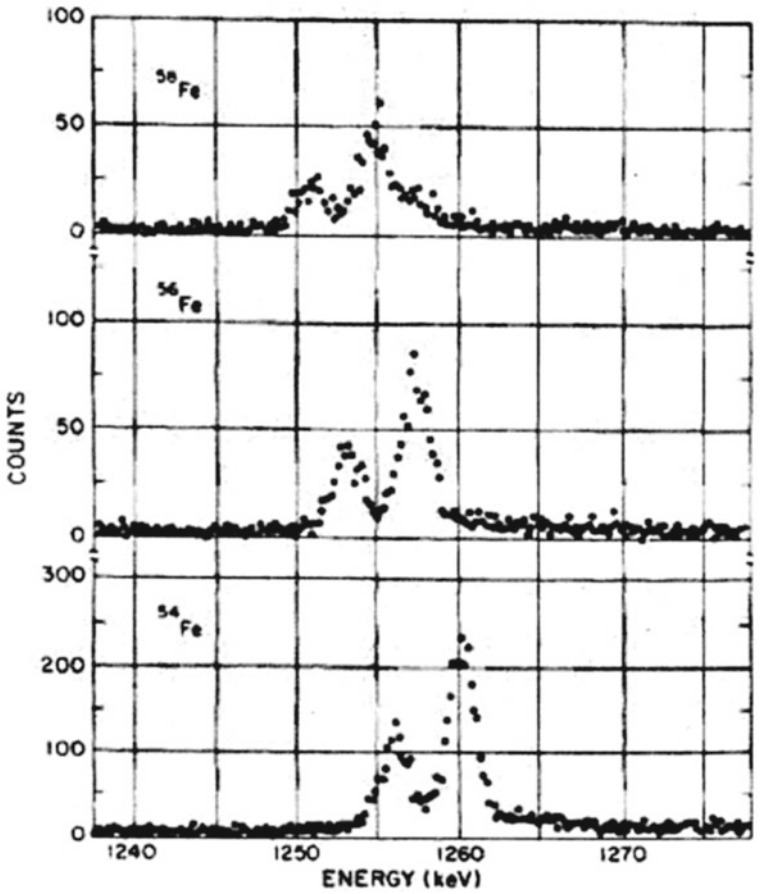

Fig. 2.19 Typical spectra showing the muonic $2p$–$1s$ X-ray doublet for three isotopes of Fe. The two peaks show the $2p_{3/2} \rightarrow 1s_{1/2}$ and $2p_{1/2} \rightarrow 1s_{1/2}$ transitions in the ratio 2:1 determined by the the statistical weight $(2j + 1)$ of the initial initial state. The isotope shift can clearly be seen as the change in energy of the transitions (after [140])

2.5 The Origin of the Mass

As we know well, that in a nucleus the protons and neutrons, collectively known as *nucleons*, are bound together by the strong nuclear force. At a fundamental level these interactions are described by Quantum Chromodynamics (*QCD*), a theory of quarks and gluons carrying colour charges that are asymptotically free at short distances. However, the quarks and gluons in a nucleus are very far from being asymptotically-free. Instead they comprise individual, colourless nucleons, which largely retain their identity in the many-body system. The colour-singlet nucleons are then bound to each other by what can be thought of as 'residual' QCD strong interactions. This sketch

of nuclear dynamics from the QCD point of view—brief as it is—makes it clear that from this standpoint the nucleus is an incredibly complicated, nonperturbative, quantum-field-theoretic, infinite-body problem.

Understanding the nucleon mass and its dependence of light *quark masses* is clearly one of the most fundamental issues [43, 47, 140] in nuclear and particle physics (see, also [143–152]). A key question concerns the origin of the nucleon mass: how do almost massless u and d quarks and massless gluons cooperate dynamically to form a localized baryonic compound with a mass of almost 1 GeV? An equally fundamental issue is the origin of the nucleon spin: how is the total angular momentum of the nucleon in its rest frame distributed between its quarks and gluons and in turn between their spin and orbital angular momentum? We will not discuss the last question here further (for details, see e.g. [152, 153]).

As we all know, almost all of the mass of the visible *Universe* is determined by the mass of the sum of the masses of nucleons in the cosmos. The *gluonic energy density* in the presence of three localized valence quarks obviously plays a decisive role in generating the nucleon mass [47, 149]. Basic *QCD* symmetries and the corresponding conserved currents as a guiding principle to construct effective Lagrangians which represent QCD at low energies and momenta. A rapidly advancing approach to deal with non-perturbative QCD is Lattice Gauge Field Theory (see, e.g. [154–160]). Considerable progress is being made solving QCD on a discretised Euclidean space–time lattice using powerful computers (for details, see [150, 151] and references therein). Lattice QCD has progressed to the joint that it can give reliable results concerning this issue, but with input quark masses still typically in order of magnitude larger than the actual current quark masses entering the QCD Lagrangian. Combining CHPT with lattice QCD has thus become a widely used routine in recent years (see, e.g. Fig. 2.1 in [150, 151]).

To better understand the origin of the mass we should analyse the *QCD condensates*. In QCD by condensates there are the vacuum mean values $< 0 \mid \mathbb{Q} \mid 0 >$ of the local (i.e. taken at a single point of space-time) operator $\mathbb{Q}_i(x)$ which are due to *non-perturbative effects*. When determining vacuum condensates one implies the averaging only over non-perturbative fluctuations. If for some operator $\mathbb{Q}_i$ the non-zero vacuum mean value appears also in the perturbation theory, it should not be taken into account in determination of the condensate. In other words when determining condensates the perturbative vacuum mean values should be substracted in calculation of the vacuum averages. As we know, the *perturbation theory* series in QCD is asymptotic series. So, vacuum mean operator values appear due to one or another summing of asymptotic series. The vacuum mean values of such kind are commonly to be referred as vacuum condensates [161]. The non-zero value of *quark condensate* means the transition of left-hand quark fields into right-hand ones and is not small value would mean to chiral symmetry violation in QCD. Quark condensate may be considered as an order parameter in QCD corresponding to spontaneous violation of the chiral symmetry [154–160].

For quark condensate $<0 \mid \overline{q}q \mid 0>$ ($q = u, d$ are the fields of u and d quarks) there holds the Gell-Mann-Oakes-Renner (GMOR) relation [162]

$$< 0 \mid \overline{q}\mathrm{q} \mid 0 >= -\frac{1}{2}\frac{m_\pi^2 f_\pi^2}{m_u + m_d}. \tag{2.43}$$

Here m_π, f_π are the mass and constant of π^+-meson decay ($m_\pi = 140\,\mathrm{MeV}$, $f_\pi =$ 92–131 MeV for different authors), m_u and m_d are the masses of u- and d-quarks. Relation (2.43) is obtained in the first order of m_u, m_d, m_s (for its derivation see, e.g. [45]). To estimate the value of quark condensate one may use the values of quark masses $m_u + m_d = 13$ MeV [163]. Substituting these values into (2.43) we get for quark condensate

$$< 0 \mid \overline{q}\mathrm{q} \mid 0 >= -(0.23\,\mathrm{GeV})^3 \simeq -1.6\,\mathrm{fm}^{-3}, \tag{2.44}$$

This condensate is a measure, as note above, of spontaneous chiral symmetry breaking. The non-zero pion mass, on the other hand, reflects the explicit symmetry breaking by the small quark masses, with $m_\pi^2 \sim m_q$. It is important to note that m_q and $< 0 \mid \overline{q}\mathrm{q} \mid 0 >$ are both scale-dependent quantities. Only their product $\mathrm{m}_q < 0 \mid \overline{q}\mathrm{q} \mid 0 >$ is scale independent, i.e. invariant under the renormalisation group.

The appearance of the mass gap $\Gamma \sim 1$ GeV in the *hadron* spectrum is thought to be closely linked to the presence of chiral condensate $< 0 \mid \overline{q}\mathrm{q} \mid 0 >$ in the QCD ground state. Ioffe formula [164], based on QCD sum rules, connects the nucleon mass M_N directly with quark condensate in leading order

$$\mathrm{M}_N = -\left[\frac{8\pi^2}{\Lambda_B^2} < 0 \mid \overline{q}q \mid 0 >\right]^{1/3} + \cdots \tag{2.45}$$

where $\Delta_B \sim 1\,\mathrm{GeV}$ is an auxiliary scale (the Borel mass [150, 151]) which separates "short" and "long" distance in the QCD sum rule analysis. While Ioffe's formula needs to be improved by including condensates of higher dimensions, it nevertheless demonstrates the close connection between dynamical mass generation and spontaneous chiral symmetry breaking n QCD. Taking into account the value of quark condensate from Eq. (2.44) we get for M_N

$$\mathrm{M}_N = 986.4\,\mathrm{MeV} \tag{2.46}$$

The obtained value of M_N differs from experimental meaning of $\mathrm{M}_N = 940$ MeV on the 5%. For nuclear physics, Eqs. (2.45–2.46) give important hint: the change of the quark condensate with increasing baryon density implies a significant reduction of the nucleon mass in the nuclear medium.

In the *chiral effective theory*, the *quark mass* dependence of M_N translates into dependence on the pion mass at leading order. The systematic chiral expansion [155–160] of the nucleon mass gives an expression of the form

$$\mathrm{M}_N = \mathrm{M}_0 + c\mathrm{m}_\pi^2 + d\mathrm{m}_\pi^4 - \frac{3\pi}{2} g_A^2 m_\pi \left(\frac{\mathrm{m}_\pi}{4\pi f_\pi}\right)^2 \left(1 - \frac{m_\pi^2}{8\mathrm{M}_0^2}\right) + \cdots \tag{2.47}$$

where the coefficients c and d multiplying even powers of the pion mass include low-energy constants constrained by *pion-nucleon scattering*. Note that the coefficient d also involves a $\log \mathrm{m}_\pi$ term.

In conclusion of this section we should note the fact m_d is larger than m_u by a few MeV implies that the neutron is heavier than the proton by a few MeV. As is well known, the experimental neutron–proton mass difference of $\mathrm{M}_n - \mathrm{M}_p = 1.2933317 \pm 0.0000005$ MeV [68, 94] receives an estimated electromagnetic contribution of [143] $\mathrm{M}_n - \mathrm{M}_p \mid^{em} = -0.76 \pm 0.30$ MeV and the remaining mass difference is due to a strong isospin breaking contribution $\mathrm{M}_n - \mathrm{M}_\mathrm{p} \mid^{d-\mathrm{u}} = 2.05 \pm 0.30$ MeV. Recently Bean et al. [152] have performed the first lattice calculation of the neutron–proton mass difference arising from the difference between the mass of the up and down quarks (see, also [165–168] and find $\mathrm{M}_n - \mathrm{M}_p \mid^{d-\mathrm{u}} = 2.26 \pm 0.57$ MeV). This value is in good agreement with the experimental result quoted. Concluding we should note, that we do not know why the observed mass pattern ($\mathrm{M}_n, \mathrm{M}_p, \mathrm{m}_u, \mathrm{m}_d$ etc.) looks like this, but nuclear physics can analyse the consequence of this empirical fact.

2.6 New Physics Beyond the Standard Model

A major challenge for physics today is to find the fundamental theory beyond the *Standard Model* [47] (the "Theory of everything"). In a nutshell, the standard model (SM) is a unified gauge theory of the strong, weak and electromagnetic interactions, the content which is summarised by the group theory

$$\mathrm{SU}(3)_C \times \mathrm{SU}(2)_L \times \mathrm{U}(1)_Y \tag{2.48}$$

where the first factor refers to the theory of strong interactions, or Quantum Chromodynamics (*QCD*) [149, 155–160], and the latter two factors describe the theory of electroweak interactions (see, also [42, 48–52, 99, 169]). However, we have the difficulty that the vast majority of the available experimental information, at least in principle [170–174], explained by the SM (see, also [175]. Also, until now, there has been no convincing evidence for existence of any particles other than those of the SM and states composed of SM particles. All accelerator physics seems to fit well with the SM, except for *neutrino* oscillations [42]. Apart from neutrino masses and mixing angles the only phenological evidence for going beyond the SM comes from cosmology and astrophysics [176–182]. It is well known that the pure SM predicts a too low value for the baryon number resulting from the Big Bang [1]. Apart from these astrophysical problems, there is only very weak experimental evidence for effects which do not match the SM extended to include neutrino mass as well

as hierarchy of elementary particles mass, etc. From these standpoints, the SM has been an enormously successful theory. Nevertheless, there exist many reasons for believing that the SM is not the end of the story. Perhaps the most obvious is the number of independent parameters that must be put in by hand. For example, the minimal version of the SM has 21 free parameters, assuming massless neutrinos and not accounting electric charge assignments [48–52]. Most physicists believe that this is just too much for the fundamental theory. The complications of the SM can also be described in terms of a number of problems, which we list briefly below.

1. Coupling Unification.
   There exists a strongly held belief among particle physicists and cosmologists that in the first moments of the life of the *Universe*, all forces of nature were "unified", that is they all fit into a single gauge group structure whose interaction strengths were described by a single coupling parameter, g_u (see, Fig. 2.2. in [43]). As we can see from this figure, that the three SM coupling almost meet at a common point around 3×10^{16} GeV.
2. The Hierarchy Problem.
   As we know, all matter under ordinary terrestial conditions can be constructed on the fermions (ν_e, e^-, u, d) of the first family (see Table 2.9). Yet we also know from laboratory studies that there are two families $(\nu_{\mu,}\mu^-, c, s)$ and (ν_τ, τ^-, t, b) that are heavier copies of the first family with no obvious role in nature. The SM gives no explanation for the existence of these heavies families. Futhermore, there is no explanation or prediction of the fermion masses, which over at least five orders of magnitude:

$$\mathrm{M}_{W,Z} \sim \mathrm{m}_{top} \gg \mathrm{m}_b \gg \mathrm{m}_\tau \gg \mathrm{m}_e \gg \mathrm{m}_\nu. \tag{2.49}$$

   How does one explain this hierarchy of masses? The SM gives us no clue as to how to explain the hierarchy problem. Really, the problem is just too complicated. Simple grand unified theory (*GUT*) does not help very much with this (for details see e.g. [48–52] and references therein). We should repeat that the non-vanishing neutrino masses and mixings are direct evidence for new physics beyond the SM.
3. Discrete Symmetry Violation.
   By construction, the SM is maximally parity-violating, it was built to account for observations that weak c.c. processes involve left-handed particles (or right-handed antiparticles). But why this mismatch between right-handness and left-handness? Again no deeper reason for the violation of parity is apparent from the SM. It would be desirable to have answer to this question, but it will take some new framework to provide them.
4. *Baryon* Asymmetry of the *Universe*.
   Why do we observe more matter than antimatter? This is problem for both cosmology and the SM.
5. Graviton Problem.
   Gravity is not fundamentally unified with other interactions in the SM, although it is possible to graft on classical general relativity by hand. However, this is not

a quantum theory, and there is no obvious way to generate one within the *SM* context. In addition to the fact that gravity is not unified and not quantised there is another difficulty, namely the cosmological constant (for details, see [176–182] and references therein). The cosmological constant can be thought of as energy of the vacuum. The energy density induced by spontaneous symmetry breaking is some $\sim$120 orders of magnitude larger than the observational upper limit. This implies the necessity of severe fine-tuning between the generated and bare pieces, which do not have any a priori reason to be related (see, also [183–185]).

6. Quantisation of Electric Charge.
   The SM does not motivate electromagnetic charge quantisation (for example, for quarks), but simply takes it as an input. The deeper origin of charge quantisation is not apparent from the SM (for the details, see also [185, 186]).

To summarize, despite the triumphant success of the SM, there exist conceptual motivations for believing that there is something more that the high energy desert is not so barren after all.

References

1. M. Gell-Mann, *The Quark and the Jaguar* (W.H. Freeman and Co., Adventures in the Simple and the Complex) (New York, 1997)
2. A.E.S. Green, *Nuclear physics* (McCraw-Hill, New York, 1955)
3. I. Kaplan, *Nuclear Physics*, 2nd ed. (Addison-Wesley, New York, 2002)
4. W.E. Burcham, 1973, Nuclear Physics. An Introduction. 2nd ed. (New York, Longman)
5. K.S. Krane, *Introductory Nuclear Physics* (Wiley and Sons, New York-Chichester, 1988)
6. J. Lilley, *Nuclear Physics* (Wiley and Sons, Chichester, 2001)
7. S.M. Wong, *Introductory Nuclear Physics* (Wiley and Sons, Chichester, 1998)
8. P.E. Hodgston, E. Gadioli, E. Gadioli-Erba, *Introductory Nuclear Physics* (Oxford University Press, Oxford-New York, 2000)
9. K. Heyde, *Basic Ideas and Concepts in Nuclear Physics* (Bristol-Philadelphia, IOP, 2004)
10. Ju.M. Schirokov and N.P. Judin, Nuclear Physics (Moscow, Science, 1980) (in Russian)
11. R.E. Taylor, Deep inelastic scattering: the early years. Rev. Mod. Phys. **63**, 573–585 (1991)
12. H.W. Kendall, Deep inelastic scattering: experiments on the proton and the observation of scattering, ibid, 63, 597–614 (1991).
13. J.I. Friedman, Deep inelastic scattering: comparison with quark model, ibid, 63, 615–627 (1991).
14. F.A. Wilczek, The cosmic assymmetry between matter and antimatter, Uspekhi Fiz. Nauk 175, 149–165 (2005) (in Russian).
15. F. Halzen, D. Martin, *Quarks and Leptons* (Wiley, New York, 1984)
16. A.P. Striganov and Ju.P. Donzov, Isotope effect in atomic spectra, Usp. Fiz. Nauk 55, 315–330 (1955) (in Russian).
17. S.E. Frish, Optical Spectra of Atoms (Moscow-Leningrad, Fizmatgiz, 1963) (in Russian)
18. I.I. Sobel'man, Itroduction in Theory of Atomic Spectra, 2nd edn (Moscow, Science, 1977) (in Russian)
19. W.H. King, *Isotope Shift in Atomic Spectra* (Plenum Press, New York, 1984)
20. M.A. Eliashevich, Atomic and Molecular Spectroscopy (Moscow, Fizmatgiz, 1962) (in Russian)
21. G. Herzberg, *Molecular Spectra and Molecular Structure* (D. van Nostrand, New York, 1951)

22. E.B. Wilson Jr, J.C. Decius, P.C. Gross, *Molecular Vibrations* (McGraw-Hill, The Theory of Infrared and Raman Vibrational Spectra (New York, 1955)
23. V.G. Plekhanov, Elementary excitation in isotope—mixed crystals. Phys. Reports **410**, 1–235 (2005)
24. M. Cardona, M.L.W. Thewalt, Isotope effect on optical spectra of semiconductors. Rev. Mod. Phys. **77**, 1173–1224 (2005)
25. V.G. Plekhanov, Fundamentals and applications of isotope effect in solids. Progr. Mat. Science **51**, 287–426 (2006)
26. V.G. Plekhanov, *Giant Isotope Effect in Solids* (Stefan University Press, La Jola, 2004). (USA)
27. V.G. Plekhanov, Applications of isotope effect in solids. J. Mater. Science **38**, 3341–3429 (2003)
28. G. Schatz, A. Weidinger, A. Gardener, *Nuclear Condensed Matter Physics*, 2nd edn. (Wiley, New York, 1996)
29. V.G. Plekhanov, *Applications of the Isotopic Effect in Solids* (Springer, Berlin, 2004)
30. D. Forkel - Wirth, Exploring solid state physics properties with radioactive isotopes, Rep. Progr. Phys. 62, 527–597 (1999).
31. M. Deicher, *Radioactive ion beams: applications to semiconductor physics* (Analysis in Materials Science, Freiberg, June, 2005), pp. 15–17
32. S.I. Adelstein, F.Y. Manning (eds.), *Isotopes for Medicine and Life Science* (National Academy Press, Washington, 1995)
33. L.L. Gol'din, M.F. Lomanov, V.B. Savchenko et al., Uspekhi-Phys (Moscow) 110, 77–100 (1973) (in Russian).
34. U. Amaldi, G. Kraft, Radiotherapy with beams of carbon ions. Rep. Progr. Phys. **68**, 1861–1883 (2005)
35. M.M. Ter-Pogossian, in Positron Emission Tomography, ed. by I. Reivich, A. Alovi (New York, Alan R. Press, 1985)
36. V.Ju. Baranov, (Ed.) Isotopes, Vol. 1 and 2 (Moscow, Fizmatlit, 2005) (in Russian)
37. O. Manuel, *Origins of Elements in the Solar Systems* (Kluwer Academic Press, New York, 2001)
38. E.M. Burbidge, G.R. Burbidge, W.A. Fowler, F. Hoyle, Synthesis of the elements in stars. Rev. Mod. Phys. **29**, 547–652 (1957)
39. G. Wallerstein, I. Jhen, Jr, P. Parker et al., Synthesis of the elements in stars: forty years in progress, ibid, 69, 995–1084 (1997).
40. S. Esposito, Primordial Nucleosynthesis: Accurate Prediction for Light Element Abundances, ArXiv:astro-ph/ 990441
41. V.G. Plekhanov, Manifestation and Origin of the Isotope Effect, ArXiv: gen. phys/0907.2024
42. E.H. Simmons, Top Physics, ArXiv, hep-ph/0011244
43. V.G. Plekhanov, *Isotope Low-Dimensional Structures* (Springer, Heidelberg-Berlin, 2012)
44. B.L. Ioffe, The origin of mass, Usp. Fiz. Nauk (Moscow) **176**, 1103–1104 (2006) (in Russian)
45. A.D. Dolgov and Ja.B. Zel'dovich, Cosmology and elementary particles, Rev. Mod. Phys. **53**, 1–41 (1981)
46. A.D. Linde, The inflated Universe, Usp. Fiz. Nauk **144**, 177–214 (1984) (in Russian)
47. B.L. Ioffe, Chiral effecrive theory of strong interactions, Usp. Fiz. Nauk **171**, 1273–1290 (2001) (in Russian)
48. P. Langacker, Structure of the Standard Model, ArXiv: hep-ph. 0304186
49. S. F. Novaes, Standart Model: An Introduction, ArXiv: hep-ph/00012839
50. C.D. Froggatt, H.B. Nielsen, Trying to Understand the Standard Model Parameters, ArXiv: hep-ph/0308144
51. J.F. Donoghue, E. Golowich, B.R. Holstein, *Dynamics of Standard Model* (Cambridge University Press, Cambridge, 1992)
52. C. Burgess, G. Moore, *Standard Model—A Primer* (Cambridge University Press, Cambridge, 2006)
53. I.I. Royzen, E.L. Feinberg, E.L. Chernavskaya, Color deconfinment and subhadronic matter: phase states and the role of constituent quarks, Usp. Fiz. Nauk **174**, 473–503 (2004) (in Russian)

54. W. Marciano, H. Pagels, Quantum chromodynamics. Phys. Reports **36**, 137–276 (1978)
55. D.W. Lee, *Chiral Dynamics* (Gordon and Breach, New York, 1972)
56. S. Coleman, *Aspects of Symmetry* (Cambridge University Press, Cambridge, 1985)
57. http://www.lbl.gov./abc/wallchart
58. F. Soddy, Intra—atomic charge. Nature (London) **92**, 399–400 (1913)
59. F. Soddy, The structure of the atom, Nature (London) **92**, 452–452 (1913)
60. H. Frauenfelder, E.M. Henley, *Subatomic Physics* (Prentice Hall, New York, 1991)
61. J.J. Kelly, Nucleon charge and magnerization densities from Sachs form factors. Phys. Rev. **C66**, 065203–065206 (2002)
62. G.A. Miller, A.K. Opper, E.J. Stephenson, Charge symmetry breaking and QCD, ArXiv: nucl.- ex/0602021
63. G.A. Miller, Charge densities of the neutron and proton. Phys. Rev. Lett. **99**, 112001–112004 (2007)
64. G.A. Miller, J. Arringfton, The neutron negative central charge density: an inclusive–exclusive connection, ArXiv: nucl-th/0903.1617.
65. C.M. Lederer, V.S. Shirley, *Table of Isotopes* (Wiley, New York, 1978)
66. F.W. Aston, Isotopes and atomic weights. Nature **105**, 617–619 (1921)
67. F.W. Aston, *Mass-Spectra and Isotopes*, (Science, Moscow, 1948) (in Russian)
68. R.N. Cahn, G.G. Goldhater, *The Experimental Foundations of Particle Physics* (Camdridge University Press, Camdridge, 1989)
69. R. Shurtleft, E. Derringh, Am. J. Phys. **47**, 552 (1989), cited in [68]
70. R.C. Barrett, D.F. Jackson, *Nuclear Sizes and Structure* (Clarendon Press, Oxford, 1977)
71. M. Waraquier, J. Morean, K. Heyde et al., Rearrangement effects in shell-model calculations using density—dependent interactions. Phys. Reports **148**, 249–291 (1987)
72. W.F. Hornyack, *Nuclear Structurs* (Academic, New York, 1975)
73. B.M. Brink, *Nuclear Forces* (Pergamon, New York, 1965)
74. J. Carlson, R. Schiavilla, Structure and dynamics of few—nucleon systems. Rev. Mod. Phys. **70**, 743–841 (1998)
75. C. Davies, S. Collins, *Physics* (World, August, 2000), pp. 35–40
76. L.I. Schiff, Scattering of neutrons by deuterons. Phys. Rev. **52**, 149–154 (1937)
77. S.S. Share, J.R. Stehn, Effect of long range forces on neutron–proton scattering. Phys. Rev. **52**, 48–52 (1937)
78. J. Schwinger, E. Teller, The scattering of neutrons by ortho–parahydrogen, Phys. Rev. **52**, 286–295 (1937)
79. G.L. Greene, E.G. Kessler, New determination binding energy and the neutron mass. Phys. Rev. Lett. **56**, 819–822 (1986)
80. S. Gartenhaus, Two-nucleon potential from the cut-off Yukawa theory. Phys. Rev. **100**, 900–905 (1955)
81. J.D. Walecka, *Theoretical Nuclear and Subnuclear Physics* (Oxford University Press Inc, New York, 1995)
82. D.J. Griffiths, *Introduction to Elementary Partcles* (Wiley, New York, 1987)
83. R.K. Adair, Neutron cross-sections of the elements. Rev. Mod. Phys. **22**, 249–298 (1950)
84. R. Wilson, *The Nucleon–Nucleon Interaction* (Wiley, New York, 1963)
85. E.M. Henley, J.P. Schiffer, Nuclear Physics, ArXiv: nucl-th / 9807041
86. E. Segre, *Nuclei and Particles* (Reading MA, Benjamin, New York, 1982)
87. R.A. Arndt, L.D. Roper, Nucleon–nucleon partiale-wave analysis to 1100 MeV. Phys. Rev. **D35**, 128–144 (1987)
88. R. Vinh Mau, in *Mesons in Nuclei*, ed. by M. Rho, D.H. Wilkinson, (North-Holland, Amsterdam, 1979)
89. R. Machleidt, K. Holinde, Ch. Elster, Phys. Rev. **149**, 1 (1987), cited in [88]
90. W. Heisenberg, Über den anschaulichen Inhalt der quantentheoretischen Kinematik und Mechanik. Zs. Physik **77**, 172–198 (1932)
91. P. Renton, *Electroweak Interactions: An Introduction to the Physics of Quarks and Leptons* (Cambridge University Press, Cambridge, 1990)

92. B.R. Holstein, *Weak Interactions in Nuclei* (Princeton University Press, Princeton, 1989)
93. E.A. Paschoes, *Electroweak Theory* (Cambridge University Press, Cambridge, 2007)
94. S. Edelman, Particle physics summary. Phys. Lett. B **592**, 1–101 (2004)
95. D.P. Roy, Basic constituents of matter and their interactions—A progress report: ArXiv: hep-ph/9912523
96. F. Wilczek, The Universe is a strange place, ArXiv: astro - ph/0401347
97. I.J.R. Aitchison, A.J.G. Hey, *Gauge Theories in Particle Physics: A Practical Introduction* (Adam Hilger, Bristol, 1990)
98. A. Volcarce, A. Fernandez, P. Gonzalez, Quark—model study of few—baryon systems. Rep. Progr. Phys. **68**, 965–1041 (2005)
99. W. Wagner, The quarks physics in hadron collisions, Rep. Progr. Phys. **68**, 2409–2494 (2005)
100. D.J. Gross, The discovery of asymptotic freedom and the emergance of QCD. Rev. Mod. Phys. **77**, 837–851 (2005)
101. D. Politzer, The dilemma of attribution, ibid, **77**, 851–857 (2005)
102. F. Wilczek, Asymptotic freedom: from paradox to paradigm, ibid, **77**, 857–871 (2005)
103. S.L. Glashow, Partial-symmetries of weak interactions. Nucl. Phys. **22**, 579–588 (1995)
104. S. Weinberg, A model of leptons. Phys. Rev. Lett. **19**, 1264–1267 (1967)
105. A. Salam, Elementary Particle Theory, in *Proceedings of the Eigth Nobel Symposium*, p. 367, 1968, ed. by N. Svartholm
106. S. Weinberg, The Making of the Standard Model, ArXiv: hep-ph /0401010
107. A. Abbas, Quarks and neutrons halo nuclei, nuclear clusters and nuclear molecules. Mod. Phys. Lett. **A16**, 755–761 (2001)
108. A. Abbas, Structure of A=6 nuclei ^{6}He, ^{6}Li and ^{6}Be, Mod. Phys. Lett. **A19**, 2365–2370 (2004)
109. F.I. Yndurain, *The Theory of Quark and Gluon Interactions* (Springer, Berlin, 1999)
110. H. Satz, The transition from hadron matter to quark-gluon plasma. Ann. Rev. Nucl. Sci. **35**, 245 (1985)
111. T. Celik, J. Engles, H. Satz, Finite temperature lattice QCD with Wilson fermions. Nucl. Phys. **B256**, 670–686 (1985)
112. S. Weinberg, *The First Three Minutes* (Basic Books, New York, 1993)
113. H.E. Suess, H.C. Urey, Abundances of the elements. Rev. Mod. Phys. **28**, 53–74 (1956)
114. G. Gamow, *One, Two, Three Infinity* (Viking Press, New York, 1947)
115. G. Gamow, Expanding Universe and the origin of elements, Phys. Rev. **70**, 572–573 (1946)
116. G. Gamow, The origin of elements and the separation Galaxes, Phys. Rev. **74**, 505–506 (1948)
117. R.A. Alpher, H.A. Bethe, G. Gamow, The origin of chemical elements. Phys. Rev. **73**, 803–804 (1948)
118. R.A. Alpher, R.C. Herman, Theory of the origin of relative abundance. Rev. Mod. Phys. **22**, 153–212 (1950)
119. Refelections on early work on "big-bang" cosmology, Phys. Today **41**, (No 8) 24–33 (1988)
120. C. Hayashi, Prog. Theor. Phys. 5, 224 (1950), cited in [101]
121. A.A. Penzias, R.W. Wilson, A measurements of excess antenna temperature at 4080 ms/c. Astrophys. J. **142**, 419–421 (1965)
122. A.A. Penzias, The Origin of the Elements, Nobel Lecture, December 8, 1978
123. J.C. Mather, Measurement of the cosmic microwave background spectrum by the COBE FIRAS instrument. Astrophys. J. **420**, 439–444 (1994)
124. F. Hoyle, R. Taylor, The mystery of the cosmic abundance. Nature **203**, 1108–1109 (1964)
125. D.N. Schramm, *Primordial Nuclei and Their Galactic Evolution*, ed. by N. Prantzos, M. Tosi, R. von Steiger (Kluwer, Dodrecht, 1998) p. 3
126. M. Arnould, K. Takahashi, Nuclear astrophysics. Rep. Prog. Phys. **62**, 395–464 (1999)
127. C.F. von Weizsacker, Zs. phys. **39**, 633 (1938) cited in [114–116]
128. H.A. Bethe, Energy production in stars. Phys. Rev. **55**, 434–456 (1939)
129. T.L. Wilson, Isotopes in the interstellar medium and circumstellar envelopes. Rep. Prog. Phys. **62**, 143–185 (1999)

130. K. Langanke and M. Wiescher, Nuclear reaction and stellar processes, ibid 64, 1657–1691 (2001)
131. R.F. Frosch, R. Hofstadter, J.R. McCarthy et al., Electron scattering studies of calcium and titanium isotopes. Phys. Rev. **174**, 1380–1389 (1968)
132. K. Heilig, A. Steudel, Changes in mean square nuclear charge radii from optical isotope shift. At. Data Nucl. Data Tables **14**, 613 (1974)
133. H.W. Brandt, K. Heilig, A. Steudel, Optical isotope shift measurements of ^{40,42,43,44,48}Ca by use of enriched isotopes in atomic beam. Phys. Lett. **A64**, 29–30 (1977)
134. F. Aufmuth, K. Heilig, A. Steudel, Changes in mean square nuclear charge radii from optical isotope shift. At. Data Nucl. Data Tables **37**, 455–490 (1987)
135. K. Blaum, High accuracy mass spectrometry with stored ions. Phys. Reports **425**, 1–783 (2006)
136. K. Blaum, W. Geithnar, J. Lassen. Nuclear moments and charge radii of argon isotopes between the neutron—shell closures N=20 and N=28, Nucl. Physics **799**, 30–45 (2008)
137. M. Glaser, M. Borys, Precision mass measurements. Rep. Prog. Phys. **72**, 126101–126131 (2009)
138. A. Kelic, K.-H. Schmidt, T. Enqvist, Isotopic and velocity distributions of ^{83}Bi produced in charge - pickup reactions of ^{82}Pb $_{208}$ at 1 GeV. Phys. Rev. **C70**, 064608–064612 (2004)
139. E.V. Shpol'sky, *Atomic Physics*, Part One. (Fiz-Mat Lit, Moscow, 1974) (in Russian)
140. E.B. Shera, E.T. Ritter, R.B. Perkins, Systematics of nuclear charge distributions in Fe, Co, Ni, Cu, and Zn fom muonic x-ray measurements. Phys. Rev. **C14**, 731–747 (1976)
141. P.L. Lee, F. Boehm, A.A. Hahn, Variations of nuclear charge radii in mercury isotopes with A = 198, 199, 200, 201, 202, and 204 from X-ray isotope shifts. Phys. Rev. **C17**, 1859–1861 (1978)
142. W. Bertolozii, J. Friar, J. Heisenberg, Contributions of neutrons to elastic electron scattering from nuclei. Phys. Lett. **B41**, 408–414 (1972)
143. The prehistory of quark masses is reviewed in J. Grasser, H. Leutwyller, Quark masses, Phys. Rep. **87**, 77–169 (1982)
144. H. Leutwyller, Masses of the light quarks, ArXiv: hep-ph/9405330
145. H. Leutwyller, ArXiv: hep-ph/ 9602255
146. H. Leutwyller, Insights and puzzles in light quark physics, ArXiv:hep-ph/ 07063138
147. C.D. Froggatt, The origin of mass. Surveys High Energy Phys. **18**, 77–99 (2003)
148. C.D. Froggatt, The Problem of mass, ArXiv: hep-ph/0312220
149. S. Narison, *in, QCD as a Theory of Hadrons: from Partons to Confinment* (Cambridge University Press, Cambridge, 2002)
150. M. Procura, B.U. Nusch, W. Weise, Nucleon mass: from lattice QCD to the chiral limit. Phys. Rev. **D73**, 114510–16 (2006)
151. B. Musch, Hadron masses, ArXiv: hep-ph/0602029
152. S.R. Beane, K. Orginos, M.J. Savage, Strong—isospin violation in the neutron–proton mass difference from fully—dynamical lattice QCD and PQQCD. Nucl. Phys. **B768**, 38–50 (2007)
153. B.L. Ioffe, Nucleon Spin Structure: Sum Rules, Arxiv:hep-ph/9511401
154. S. Scherer, M.R. Schindler, Chiral Perturbation Theory Primer, ArXiv:hep-ph/0505265
155. G. Ecker, Chiral Perturbation Theory, ArXiv:hep-ph/9501357
156. A. Pich, Chiral Perturbation Theory, ArXiv:hep-ph/9502366
157. S.R. Bean, P.F. Bedaque, W.C. Haxton., in "*At the Frontier of Particle Handbook of QCD*", ed. by M. Shifman (World Scientific, Singapoure, 2001), pp. 1–140
158. W. Weise, Yukawa's Pion, Low-Energy QCD and Nuclear Chiral Dynamics, ArXiv: nucl-th/ 0704.1992
159. J. Bijens, Chiral Perturbation Theory Beyon One Loop, ArXiv: hep-ph/0604043
160. J. Bijens, Progr. Part. Nucl. Phys. **58**, 521 (2007)
161. B.L. Ioffe, QCD at low energies. Progr. Part. Nucl. Phys. **56**, 232–277 (2006)
162. M. Gell-Mann, R.J. Oakes, B. Renner, Behavior of current divergences under SU_3 X SU_3 Phys. Rev. **175**, 2195–2199 (1968)

163. A. Pich, J. Prades, Tau - decay determination of the strange quark mass. Nucl. Phys. Proc. Suppl. **86**, 236–241 (2000)
164. B.L. Ioffe, Calculation of baryon masses in quantum chromodynamics. Nucl. Phys. **B188**, 317–341 (1981)
165. E. Epelbaum, U.-G. Meissner, W. Glöckle, Nucl. Phys. **A714**, 535 (2003)
166. U.-G. Meissner, Quark mass dependence of baryon properties, ArXiv: hep-ph/0509029
167. Müller B., 2007, From Quark-Gluon plasma to the perfect liquid, ArXiv: nucl-th/ 0710.3366
168. W. Weise, Overview and perspectives in nuclear physics, ArXiv: nucl-th/ 0801.1619
169. G. Altarelli, States of the Standard model and beyond. Nucl. Instr. and Methods **A518**, 1–8 (2004)
170. M. Pospelov, A. Ritz, Electric dipole moment as probes of new physics, ArXiv: hep-ph/0504231
171. M. Pospelov, A. Ritz, Annal. Phys. (NY) **318**, 119 (2005 (cited in [170]))
172. I.B. Khriplovich, S.K. Lamoreaux, *CP Violation Without Strangeness: Electric Dipole Moments of Particles, Atoms and Molecules* (Springer, Berlin, 1997)
173. A. Djouadi, The dichotomy of electroweak symmetry breaking: The Higgs boson and Standard model, Phys. Rep. **457**, 1–216 (2008)
174. M.J. Ramsey-Musolf, S. Su, Low-energy precision tests of supersymmetry, Phys. Rep., **456**, 1–137 (2008)
175. V.G. Plekhanov, The Enigma of the mass, ArXiv:gen. phys/0906.4408
176. C.S. Weinberg, The cosmological constant problem. Rev. Mod. Phys. **61**, 1–23 (1989)
177. C.S. Weinberg, The Cosmological constant problems, ArXiv:astro-ph/0005265
178. M. Tegmark, M.J. Rees, F. Wilczek, Dimensionless constants cosmology and other dark matters, ArXiv:astro-ph/0511774
179. A.D. Dolgov, Cosmology and new physics, ArXiv:hep-ph/0606230
180. T. Padmanabhan, Cosmological constant the weight of the vacuum. Phys. Rep. **380**, 235–320 (2003)
181. T. Padmanabhan, Dark energy: mystery of the millenium, ArXiv:astro-ph/0603114
182. G. Fuller, A. Hime, M. Ramsey-Musolf, Dark matter in, nuclear physics, ArXiv:nucl-ex/0702031
183. K.A. Milton, The Casimir effect: recent controversis and progress. J. Phys. A: Math. Gen. **37**, R209–R277 (2004)
184. S.K. Lamoreaux, The Casimir force: background, experiments and applications. Rep. Prog. Phys. **68**, 201–236 (2005)
185. S.K. Lamoreaux, The Casimir Force: Background, Experiments and Applications. Rep. Prog. Phys. **68**, 201–236 (2005)
186. M. Levin, X.-G. Wen, Photons and electrons as emergent phenomena. Rev. Mod. Phys. **77**, 871–897 (2005)

Chapter 3
Early Spectroscopic Studies of Isotopes

3.1 Some General Remarks

The interpretation of *atomic isotope shifts* relies partly on the knowledge of nuclear structure. Conversely it can provide some information on the structure *nuclei*. This relation between the two fields has been for many years the main reason for the interest in *isotope shifts* of optical (electronic) transition (see, e.g. reviews and monographs [1–14]).

The word "atom" introduced by Democritus more than 2,400 years ago in Greek means "inseparable". The discovery in the twentieth century of complex inner structure of an atom, in fact, has led to emergence of the main branch of physics describing the structure of a *microscopic world*, i.e. *quantum mechanics*, which, in its turn has stimulated the development of many other domains of physics, neighbouring sciences and technologies. Atomism as understood by modern science was first discovered for matter, then for electricity and finally for energies. The atomism of matter, the recognition of the fact that all the chemical elements are composed of atoms, followed from chemical investigations. Only whole atoms react with one another. The first atomic model (at the beginning of nineteenth century) assumed that the atoms of all elements are put together out of hydrogen atoms. As a heuristic principle this hypothesis finally led to a scheme for ordering the elements based on their chemical properties, the *periodic system* of D.I. Mendeleev. More about this subject may be found in introductory textbooks on chemistry [15]. Continuous investigations of gases in the course of the nineteenth century led to the atomism of heat, that is, to the explanation of heat in general and of the thermodynamic laws in particular as consequences of atomic motion and collisions. The atomism of electricity was discovered in nineteenth century by the English scientist M. Faraday. Based on the quantitative evaluation of exceedingly careful measurements of the electrolysis of liquid, M. Faraday concluded "There are 'atoms' of electricity". These "atoms" of electricity—the electrons are bound to atoms in matter.

The discovery of the atomism of energy can be dated exactly: on December 14, 1900 (see, e.g. [16]) M. Planck announced the derivation of his laws for black body

V. G. Plekhanov, *Isotopes in Condensed Matter*, Springer Series in Materials Science 162,
DOI: 10.1007/978-3-642-28723-7_3, © Springer-Verlag Berlin Heidelberg 2013

radiation in a lecture before the Physical Society in Berlin. In order to derive these laws, M. Planck assumed that the energy of *harmonic oscillators* can only take on discrete values—quite contradictory to the classical view, in which the energy values form a continuum. This date can be called the birth date of quantum theory .

Our knowledge of the structure of atoms was influenced strongly by the investigation of optical spectra [17, 18]. The most important sources of information about the electronic structure and composition of atoms are spectra in the visible, infrared (IR), ultraviolet (UV) frequency ranges [19]. Optical spectra are further categorised as line, band and continuous spectra [17]. Continuous spectra are emitted by radiant solids or high-density gases. Band spectra consist of groups of large numbers of spectral lines which are very close to one another. They are generally associated with molecules [20–22]. Line spectra, on the other hand, are typical of atoms [2–4]. They consist of single lines, which can be ordered in characteristic series.

The founders of spectroscopic analysis, Kirchhoff and Bunsen, were the first to discover in the mid-nineteenth century that each elements possesses its own characteristic spectrum. Hydrogen is the lightest element, and the hydrogen atom is the simplest atom, consisting of a proton and an electron. The spectra of hydrogen atom have played an important role again and again over the last (twentieth) century in the development of our understanding of the laws of atomic structure and the structure of matter.

The *emission spectrum* of atomic hydrogen (Fig. 3.1) shows three characteristic lines in the visible region at 6,563, 4,861 and 4,340 Å (H_α, H_β, H_γ, respectively). As we can see from Fig. 3.1, the most intense of these lines was discovered in 1853 by Angström; it is now called the H_α line. In the near UV region, these three lines are followed by a whole series of further lines, which fall closer together in a regular way as they approach a short-wavelength limit (H_∞). During this period empirical regularities in line spectra were being found. The best known of these was Balmer's simple formula (1885) for the wavelengths of the visible lines of the hydrogen spectrum. For the wavenumbers ($\nu = 1/\lambda$) of the lines we write the Balmer formula

$$\nu = R_H \left(\frac{1}{2^2} - \frac{1}{n^2} \right) \tag{3.1}$$

where n-integer and equals $n = 3, 4, 5, \ldots$. The quantity R_H is called the Rydberg constant and has the numerical value $R_H = 109677.581\,\mathrm{cm}^{-1}$ [19]. The series limit is found for $n \longrightarrow \infty$ to be $\nu = R_H/4$. This empirical discoveries of spectral regularities reach their culmination in the clear establishment of the Ritz combination principle. This came in 1898 after a decade of important work on the study of spectral series [18]. According to this result each atom may be characterised by a set of numbers called terms ($R_H/4$), dimensionally like *wavenumbers*, such that the actual wavenumbers of the spectral lines are given by the differences between these terms. A comparison of the calculated obtained from the Balmer formula (Eq. 3.1) with the observed lines [18] shows that the formula is not just a good approximation: the series is described with great precision. The *combination principle* suggests the existence of lines given more generally by

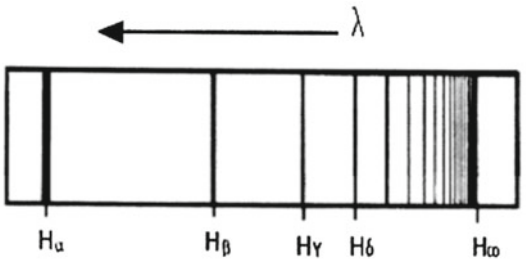

Fig. 3.1 Balmer series in the hydrogen emission spectrum. The convergence of the lines to the series limit H_∞ is clearly seen

$$\nu = R_H\left(\frac{1}{m^2} - \frac{1}{n^2}\right), \tag{3.2}$$

where $m < n$ being integer. The numbers m and n are called principal quantum numbers. For $m = 3$ and $n = 4, 5, 6, \ldots$ the lines fall in the IR. Paschen found them at the predicted places. Lyman also found in the UV three lines corresponding to $m = 1$ and $n = 2, 3, 4, \ldots$. Table 3.1 contains some of the lines from the first four series and thus illustrates the Ritz Combination Principle. As we can see, the difference of the frequencies of two lines in a spectral series is equal to the frequency of a spectral line which actually occurs in another series from the same atomic spectrum. For example, the frequency difference of the first two terms in the Lyman series is equal to the frequency of the first line of the Balmer series. To concluding this paragraph we should repeat that the frequencies (or wavenumbers) of all spectral lines can be represented as differences of two terms of form R/n^2. These are just the energy levels of the electron in a hydrogen atom. The model of the hydrogen atom consisted of an electron and proton describing orbits about their centre of mass according to classical mechanics under their mutual attraction as given by the *Coulomb* inverse-square law. The allowed circular orbits were determined simply by the requirement (an additional postulate of quantum theory [25]) that the angular momentum of the system be an integral multiple of $\hbar = \mathrm{h}/2\pi$. This condition yields an equation from which R_∞ can be calculated (for details see [19])

$$R_\infty = \frac{\mathrm{m_0 e^4}}{8\varepsilon_0^2 \hbar^3 \mathrm{c}}. \tag{3.3}$$

From (3.3) we can find for the Rydberg constant R_∞ the numerical value

$$R_\infty = (109737.318 \pm 0.012)\mathrm{cm}^{-1}. \tag{3.4}$$

This may be compared with empirical value in (3.1). In hydrogen model R is just the *ionisation energy* of the ground state of the atom with $n = 1$. Next part of our review gives an account of what can be understood in experimental isotope shifts before (or without) separating the two types of contributions (*mass*- and *field-shift*), in

Table 3.1 The wavelength of some lines of the various spectral series in hydrogen

n/m	Lyman	Balmer	Paschen	Bracket
2	1,216 Å			
3	1,026Å	6,563Å		
4	973Å	4,861Å	18,751Å	
5	950Å	4,340Å	12,818Å	40,500Å
Year of discovery	1906	1885	1908	1922

The series with $m = 3$ was observed in 1924 by Pfund; it begins with a line of $\lambda = 74,000$ Å , but is not shown in the table

other words, the way in which the isotopes shift changes from one level to the other in a given spectrum. As will be shown below the latter problem is purely problem of atomic structure.

3.2 Motion of the Nucleus: Atomic Isotope Shift

The spectroscopically measured quantity R_H (Sect. 3.1) does not agree exactly with the theoretical quantity R_∞ [23]. The difference is about $60\,\mathrm{cm}^{-1}$ [18]. The reason for this is the motion of the nucleus during revolution of the electron, which was neglected in the above model calculation. As we remember, this calculation was made on the basis of an infinitely massive nucleus. Now we must take the finite mass of nucleus into account [17].

As we know from classical mechanics, the motion of two particles, of masses m and M and at distance r from one another, takes place around the common centre of gravity. If the centre of gravity is at rest, the total energy of both particles is that of a fictitious particle which orbits about the centre of gravity at a distance r and has the mass

$$\frac{1}{\mu} = \frac{1}{m} + \frac{1}{M}; \quad \mu = \frac{mM}{m+M} \tag{3.5}$$

referred to as the *reduced mass*. Replace the mass of the orbiting electron, m_0 by μ and obtain, in agreement with experiment

$$R = R_\infty \left(\frac{1}{1 + m/M}\right) \tag{3.6}$$

Here $m = m_0$—the mass of the orbiting electron, and M, the mass of the nucleus. The energy corrections due to motion of the nucleus decrease rapidly with increasing nuclear mass (Table 3.2). This observation makes possible a spectroscopic determination of the mass ratio M/m_0

$$M_{\text{proton}}/m_{\text{electron}} = 1836.15. \tag{3.7}$$

Table 3.2 Energy corrections for motion of the nucleus for the Rydberg numbers of several one-electron atoms

Atom	H(^{1}H)	D(^{2}H)	T(^{3}H)	He^+	Li^{2+}
A	1	2	3	4	7
$-\frac{\Delta E}{E} \cdot 10^4$	5.45	2.75	1.82	1.36	0.78

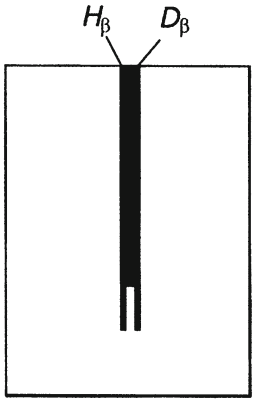

Fig. 3.2 β lines of the Balmer series in a mixture of equal parts hydrogen and deuterium. One sees the isotope effect, which is explained by motion of the nucleus

Due to the motion of the nucleus, different isotopes of the same element have slightly different the frequency of spectral line. This so-called isotope displacement to the discovery of heavy hydrogen with the mass number $A = 2$ (deuterium). It was found that each line in the spectrum of hydrogen was actually double. The intensity of the second line of each pair was proportional to the content of *deuterium* [1, 24]. Figure 3.2 shows the H_β line with the accompanying D_β at a distance of about 1 Å in a 1:1 mixture of the two gases. The nucleus of deuterium contains a neutron in addition to the proton. There are easily measurable differences in the corresponding lines of the H and D Lyman series:

$$R_H = 109677.584\text{cm}^{-1}; \quad R_D = 109707.419\text{cm}^{-1}. \tag{3.8}$$

The more precisely the differences in hydrogen–deuterium 1s–2s isotope shift was done recently by Huber et al. [26]. These authors exceeds the accuracy of earlier experiment by more than 2 orders of magnitude. Figure 3.3 shows the frequency chain that has been described in part in [27], where an absolute measurement of the 1s–2s frequency has been reported. Authors [26, 27] determine the isotope shift by fitting a pair of parallel lines to the hydrogen and deuterium data, thus accounting for a linear frequency drift of the standard. After averaging of 10 measurements line the one shown in Fig. 3.4, these authors obtained the experimental result for the 1s–2s *H–D isotope shift*

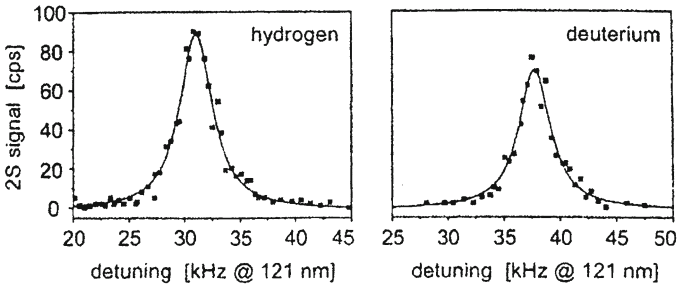

Fig. 3.3 Experimental 1s–2s spectra in hydrogen and deuterium as measured relatively to selected modes of the optical comb generator (after [27])

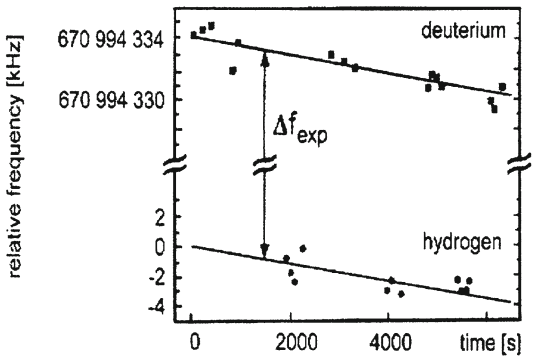

Fig. 3.4 Alternating measurements of the 1s–2s transition frequency in hydrogen and deuterium (after [27])

$$\Delta f_{\text{exp}} = 670994334.64\ (15)\ \text{kHz} \tag{3.9}$$

The uncertainty of 150 kHz is dominated by the frequency fluctuations of the CH_4-stabilised He–Ne standard. At the precision level the theoretical contributions to the isotope shift must be reanalysed. Most of the H–D isotope shift of the 1s–2s interval is caused by the different masses of the nuclei (for details see, also [26]).

3.3 Separation of Mass- and Field-Shift Contributions

Before the early 1960s, for scientists interested in atomic isotope shift, the *Periodic Table* was implicitly divided into three regions (see, e.g. [1, 4]):

(1) The light elements, with approximately $Z \leq 30$, where mass isotope shift only was considered to be present;
(2) The heavy elements ($Z \geq 58$), with field isotope shift only, and;

(3) Between these two regions, namely, beyond the 3d series and before the 4f series, medium-weight elements with small isotope shifts, difficult to measure accurately.

Thus *mass-* and *field-shift* effects were considered almost independently. For mass-shift effects, the paper by Vinti [29] was a reference: it essentially indicates the formal way in which the mass isotope shift changes from one pure Russel - Saunders (RS) term to another [17]. For *field isotope shift* , the basic papers were by Rosenthal and Breit [30] and Racah [31], both of which considered the case of multielectronic atom: in the case of multielectronic spectra, the field-shift was considered inside a given configuration, and the way it changes from one configuration to another was described through the use of "screening factor" introduced by authors of paper [32].

So, the isotope shift of an optical transition is the sum of two terms: the mass effect and the field effect. If only one isotope pair is available, the experiment only yields this sum but not the respective contributions of the two effects. The situation is then much less favourable than for hyperfine structure (see, e.g. [2, 3]), because, in this latter case, the Casimir formula allows a separation of the magnetic-dipole and electric-quadrupole contributions [33, 34]. Unfortunately, if the mass effect and field effect contributions cannot be separated, the theoretical interpretations of experimental result necessary remain rather crude (please compare [35]).

3.3.1 Mass Isotope Shift

The theory for a nucleus of finite mass in an N-electrons has been considered for the first time by Hughes and Eckart [28]. The correction to the atomic energy levels due to the *nuclear mass* motion is given in the non-relativistic limit by the kinetic energy of the nucleus due to its motion about the centre of mass of the atom [17]

$$\Delta \mathrm{E} = \frac{1}{2M}\left(\sum_i \vec{p_i}^{\,2} + \sum_{i \neq \mathrm{j}} \vec{p_i} \cdot \vec{p_j}\right) \tag{3.10}$$

Here M is the nuclear mass and $\vec{p_i}$—the momentum of the ith electron. The sum is over all the electrons in the atom. The effect of the square terms on the *total energy* can be evaluated exactly by taking them together with the corresponding kinetic energy terms of the electrons, giving the well-known reduced mass correction (see Eq. (3.5). The consequent term and line shifts can be simply calculated, and are referred to as "normal mass shifts" (NMS) [1]. Usually it will be assumed that the normal effect has been allowed for in all shifts discussed (see, e.g. [5–7]). Shifts arising from the second term are called "specific mass shifts" (SMS) [28]. The term contains cross products of the momenta of different electrons and is not susceptible of exact calculation, though in light elements results in moderate agreement with experiment have been obtained [1, 4]. For the heavier elements, many electrons are involved and the calculations become rapidly more complex [14]; no simple

rules appear to exist which would allow even the crudest estimates of SMS for such elements. Generally, therefore plausibility arguments or semi-empirical methods are used [4].

In the region of the medium-heavy elements, semi-empirical methods for SMS have been applied, though it appears that such allowance should often be made also in heavier elements [14]. The total observed shift can be written

$$\Delta E_{\text{total}} = \Delta E_{\text{NMS}} = \Delta E_{\text{SMS}} + \Delta E_{\text{FS}}, \tag{3.11}$$

where the values of ΔE apply to the differences in the upper and lower levels involved in a transition, i.e. they refer to line shifts. From (3.11), a relation between the mass shifts in different lines of an element may be obtained. We use the symbol m for the SMS in a line on the addition of one neutron and put $\Delta E_{\text{total}} - \Delta E_{\text{NMS}} = T$. Then the values of T between two isotopes with neutron numbers N and N' for two spectral lines (suffixes 1 and 2) are given by

$$\begin{aligned} T_1^{N,N'} &= (N' - N)m_1 + F_1 C^{N,N'}; \\ T_2^{N,N''} &= (N' - N)m_2 + F_2 C^{\text{N,N'}}. \end{aligned} \tag{3.12}$$

Here F, C are positive constant and functions of size and shape of the nucleus [5–7]. In the last equations it was assumed that m for a heavy elements independent of N. We should not, that the slight dependence can, of course, be taken into account, but (3.12) is sufficiently accurate for most purposes [14]. The superscript N, N; denotes dependence on these quantities, the Z dependence has been omitted to make the formulae less cumbersome, since the argument concerns only one element. From (3.12) we have

$$T_1^{N,N'} = T_2^{N,N'} \frac{\text{F}_1}{\text{F}_2} + (N' - N)(m_1 - m_2 \frac{\text{F}_1}{\text{F}_2}). \tag{3.13}$$

Thus, if two or more corresponding shifts are measured in each of two lines of an element, F_1/F_2 can be found and also $(N' - N)(m_1 - m_2 \frac{\text{F}_1}{\text{F}_2})$. King [4] suggested simply plotting the shifts in one line against the corresponding shifts in another, first dividing each shift by $(N' - N)$. Then the points should lie on a straight line (Figs. 2, 3 in [14]), and the slope and intercept are F_1/F_2 and $(m_1 - m_2 \frac{\text{F}_1}{\text{F}_2})$ respectively. Whatever the number of lines for which results are available, it is, of course, impossible by this method to determine any of the *mass shift* uniquely, however, plausibility arguments based on the nature of the *specific mass effect* can be used to make estimates, and the greater the number of lines for which the total shifts are known, the more restricted becomes the range of reasonable values of the contributions of the *specific shifts*. Further, as King [4] pointed out, if the mass shift could be computed for one line, the procedure described enables it to be found for the others from the experimental results (for details see [14]).

3.3.2 Field Isotope Shift

In optical and electronic X-ray transitions the field shift is very nearly proportional[1] $\langle r^2\rangle^{1/2}$ and it is convenient to express this in terms of a "*standard shift*" based on an equivalent uniform charge density of radius $R_{eq} = r_0 A^{1/3}$ fm. This standard unit of isotope shift does not have a fundamental significance but does represent approximately the overall variation of R_{eq} for stable nuclei. Because a change in neutron number is either a more towards or away from the region of stability there is no reason to expect *isotope shifts* to be the same as the standard shift and in fact they are usually smaller [5–7].

a) *Isotope shift in optical spectra.* The nuclear electrostatic potential acting on the electron depends on the nuclear charge distribution; if this changes from one isotope to another, the energy of an electron which penetrates the nucleus will also change in the two cases. In the early works [30, 31], spherically symmetrical nuclear charge distributions of simple form were assumed, and the values E_{field} and ΔE_{field} were calculated by perturbation treatment, recognised and allowed for to some extent the results of [30], led to evaluation of ΔE_{field} by more rigorous methods [1]. The foundation for this latter work was laid by the author of paper [37]. He considered the solutions to the *radial Dirac equation* for the electron: (1) with the nuclear charge assumed concentrated at a point, and (2) with extended nuclear charge distribution (for details see [18]). The modern description of the field isotope shift have the next form:

$$\Delta E_{field}^{N,N'} = F_i \lambda^{N,N'}. \tag{3.14}$$

and

$$\lambda^{N,N'} = \delta\langle r^2\rangle^{N,N'} + \frac{C_2}{C_1}\delta\langle r^4\rangle^{N,N'} + \frac{C_3}{C_1}\delta\langle r^6\rangle^{N,N'} + \ldots \tag{3.15}$$

λ is the nuclear parameter [9–11] and $F_i = E_i f(z)$-electronic factor. Values of f(z) calculated from the isotope shift constants are given in Table II of [9–11]. The ratios C_n/C_1 have been calculated by Seltzer [36]. The procedure of the evaluation of λ was as follows [9–11]: first the SMS were estimated, either according to above formula of from King plots [4] of the optical isotope versus results from muonic isotope shifts [38] or electronic X-ray shifts [1, 13, 14].

b) *X-ray isotope shift.* As was shown above, *atomic isotope shifts* are measured in both optical and X-ray spectra (Fig. 2.19 of Chap. 2). Since the *Coulomb* potential at the nucleus is so much larger than the binding energy, the *s*-wave function is largely independent of the principal quantum number. For instance, as was shown by Seltzer [36], the change in C_2/C_1 [Eq. (3.15)] is going from 1s to 2s amounts to only a few tenths of percent. Beyond the 2s level, there is very little

[1] The standard shift calculated on the basis of $\langle r^2\rangle^{1/2}$ dependence can be corrected by dividing by the quantity $[1 + 1.2 \cdot 10^{-5} Z^2]$. This correction takes into account the effect of $\langle r^4\rangle$ and $\langle r^6\rangle$ terms and is based on the results of Seltzer [36].

further change. C_2/C_1 for a $p_{1/2}$ level is within a few percent of C_2/C_1 for a $s_{1/2}$ level (4% for Z = 80 [36]). This means that both atomic optical and X-ray *isotope shifts* measure the same parameter λ. Moreover, the largest contributions in heavy atoms to the energy shift observed on going from one isotope to another comes from the modification of the nuclear charge distribution. The total mass shift for K X-ray transitions is usually less than a few percent of the total isotope shift [39, 40]. The *SMS* for optical transitions in heavy atoms is usually neglected. Unlike the X-ray case, the SMS in optical transitions can be a large part of the total isotope shift (for details see [39–41]).

3.4 Vibrations in a Diatomic Molecule

Since a *diatomic molecule* has two atoms and must be linear, it has one degree of vibrational freedom. By convention the z- axis is placed coincident with the molecular axis. Movement of the atoms in the x- and y-directions can then be dismissed as molecule rotations. Let us choose a diatomic molecule AB whose atoms have mass m_A (coordinate z_A) and m_B (z_B). Moreover, let us now suppose that the atoms are like metal balls and the bond between them is like a simple spiral spring (see, e.g. Fig. 27 of [42]). If we then allow the distance between A and B to change by a quantity $q = (z_A^{'} - z_B^{'}) - (z_A - z_B)$, while keeping the centre of mass at the origin of axes, we could say that the force (F) exerted by the spring on the particles is related to q by (see, e.g. [43])

$$F = fq \tag{3.16}$$

This is to say the spring obeys *Hook's law* (*linear approximation*), and we shall see that this analogy is a good one. The force exerted by the spring will cause the atoms to return to their original positions. If we denote the velocity with which do so by dq/dt and the acceleration by d^2q/dt^2 we may apply Newton's second law of motion and equate the force with mass times an acceleration. At this point we shall write the *reduced mass* M ($M = \frac{m_A m_B}{m_A + m_B}$)

$$-fq = M\frac{d^2q}{dt^2} \tag{3.17}$$

This is a second order differential equation which may be solved by making the substitution

$$q = A\cos(2\pi\nu t + \rho), \tag{3.18}$$

where ν is a frequency, ρ is a phase factor and A - a maximum vibration amplitude. Then we have

$$\frac{d^2q}{dt^2} = -4A\pi^2\nu^2\cos(2\pi\nu t + \rho) = -4\pi^2\nu^2 q. \tag{3.19}$$

Substituting this back into Eq. (3.17) we obtain

$$(-4\pi^2\nu^2 M + f)q = 0 \tag{3.20}$$

and assuming $q \neq 0$, we have

$$\nu = \frac{1}{2\pi}\sqrt{\frac{f}{M}} \tag{3.21}$$

This equation is the equations of simple *harmonic oscillators*.

In the last Eq. (3.21) f is proportionality constant. This proportionality constant is known as a *force constant*. It could be defined in terms of Hook's law (Eq. (3.16)), but this is not convenient. Alternatively it may be defined in terms of the vibrational potential energy [19]. Before considering the quantum mechanics of the vibrations in a diatomic molecule, we must first discuss two assumptions that are implicit in the treatment so far: that classical mechanics provides an adequate description of a vibrating molecule, and that Hook's law is valid. The term molecular coordinate is one which we shall meet below in various forms. Unlike the Cartesian coordinates a molecular coordinate does not define the position of the atoms absolutely, but defines the change in coordinates from some initial position. Thus, q defined the change in bond length in the diatomic molecule, but did not define the actual bond length. The term coordinate will be understood to define some change in the molecular configuration. The origin of this coordinate system is given by the average or equilibrium position of the atoms in the molecule, ignoring translation and rotation (for details see, e.g. [21]).

Perhaps the most surprising thing about *molecular vibrations* is that the frequencies of vibration may be correctly calculated by means of classical mechanics. Intuitively one feels that this is due to the wave nature of the vibrations. However, *quantum mechanics* does provide greater inside into aspect other than the frequencies. To simplify our discussion we will only consider the simplest case, the harmonic oscillator [43].

The wave equation for a one-dimensional oscillator such as a *diatomic molecule* is [44]

$$\frac{\mathrm{d}^2\Psi}{\mathrm{d}q^2} + \frac{8\pi^2 M}{h^2}(E - V)\Psi = 0, \tag{3.22}$$

where E is the total vibration energy. In the *harmonic oscillator* the potential energy V is given as $\frac{1}{2}\mathrm{fq}^2$ and the wave equation becomes

$$\frac{\mathrm{d}^2\Psi}{\mathrm{d}q^2} + \frac{8\pi^2 M}{h^2}(E - \frac{1}{2}fq1^2)\Psi = 0. \tag{3.23}$$

The solution of this equation is given in most texts on quantum mechanics (see, e.g. [25]). Thus the energy E is given as

$$E = (n + \frac{1}{2})\frac{h}{2\pi}\sqrt{\frac{f}{M}} \tag{3.24}$$

where n is a quantum number that may take the values 0, 1, 2, 3,. . . . Therefore when the molecule changes from one *vibrational state* to the next nearest by one the change in energy is given by

$$\Delta E = \frac{h}{2\pi}\sqrt{\frac{f}{M}}, \tag{3.25}$$

and since $\Delta E = h\nu$, the frequency of a photon associated with this change is

$$\nu = \frac{1}{2\pi}\sqrt{\frac{f}{M}}, \tag{3.26}$$

which is the same result as given by classical mechanics. It can then be shown that in the general case classical and quantum mechanics give the same answer for the vibration frequencies; hence we are fully justified in using classical mechanics to calculate them [20]. If $n = 0$ in Eq. (3.24) the molecule has an energy of $\frac{h}{4\pi}\sqrt{\frac{f}{M}}$. This energy is known as the *zero point energy* and has no counterpart in classical mechanics [25].

For a diatomic molecule we may expand the vibrational potential energy as a Maclaurin series about the position of minimum energy, V_0 [45, 46]

$$V = V_0 + (\frac{dV}{dq})_0 q + \frac{1}{2}(\frac{d^2V}{dq^2})_0 q^2 + \frac{1}{6}(\frac{d^3V}{dq^3})_0 q^3 + \frac{1}{24}(\frac{d^4V}{dq^4})_0 q^4 + \cdots \tag{3.27}$$

The subsript zero indicates the position of minimum potential energy, so that $(\frac{dV}{dq})_0 = 0$. The quantity V_0 is a constant independent of q and may be ignored since it does not affect the vibrational frequencies. We have already met the *force constant* definition $f = \frac{d^2V}{dq^2}$, so we may rewrite the potential energy as

$$V = \frac{1}{2}fq^2 + \frac{1}{6}\left(\frac{d^3V}{dq^3}\right)_0 q^3 + \frac{1}{24}\left(\frac{d^4V}{dq^4}\right)_0 q^4 + \cdots \tag{3.28}$$

The calculations in the previous text were based on the approximation that the terms in power of q higher than two may be ignored. Of course the true potential energy of a molecule must be more complex, if only because for large values of q the molecules must dissociate. Figure 3.5 shows scheme of the potential energy of typical *diatomic molecule* as a function of q, while the dotted line is the parabola calculated for $V = \frac{1}{2}fq^2$. The true curve is steeper than the parabola at small internuclear distances, because of the interatomic repulsion energy, but at large internuclear distance the true potential energy tends asymptotically to a constant value, the dissociation energy Q. Near the equilibrium internuclear separation (q = 0) the parabola is quite a good approximation to the potential energy. For this reason,the approximation

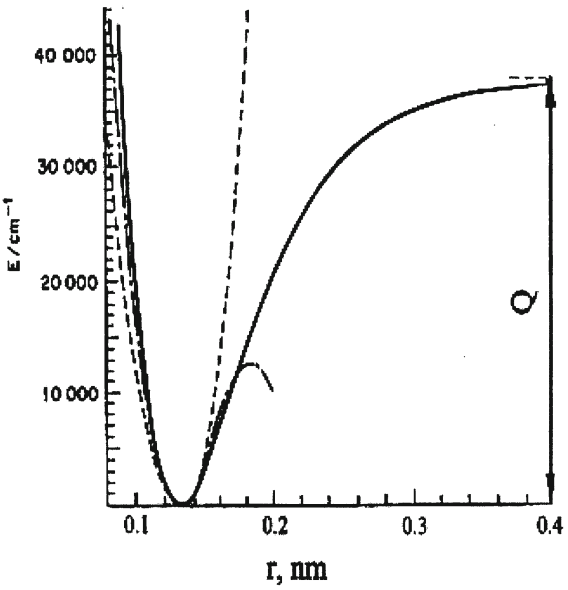

Fig. 3.5 The potential energy curve of typical diatomic molecule (*solid line*) as a function of internuclear distance. The *broken line* and *dotted curves* are those of the quadratic and cubic functions that give the best approximation to the curve at the minimum

$V = \frac{1}{2}\mathrm{fq}^2$ is quite good. Taking $V = \frac{1}{2}\mathrm{fq}^2$ is known as the *harmonic approximation* [20], and the potential energy is said to be quadratic. The *force constant* f defined as $\frac{\mathrm{d}^2 V}{\mathrm{d}q^2}$ is said to be quadratic force constant. The addition of the cubic term in Eq. (3.27) gives a better fit with the true potential energy curve at the minimum and may be used in accurate work. However, the equations of motion obtained by using a cubic term in potential energy are not easy to handle.

One approximate solution to the Schrödinger equation that may be found to express the energy in terms of the harmonic frequency ν_e and an *anharmonic constant* x_e, thus (see, e.g [46])

$$E = h\nu_e(n + \frac{1}{2}) - h\nu_e X_e(n + \frac{1}{2})^2 \tag{3.29}$$

Therefore, if two transitions corresponding, to $\Delta n = 1$ and $\Delta n = 2$, can be observed both ν_e and x_e may be calculated. The quantity ν_e may be regarded as the frequency the molecule would have if it was a *harmonic oscillator*, so that x_e supplies a means of adjusting the observed frequency. In practice, then, the observed frequencies are adjusted to give the harmonic frequencies and the theory of the harmonic oscillator is then applied [22, 45]. It is conventional to express harmonic frequencies cm^{-1}, and to give them the symbol ω_e, where $\omega_e = \nu_e/\mathrm{c}$ and c is the velocity of light. Anharmonic affects molecular vibrations in two important ways [20]. Firstly, the selection rule (see, also below) derived for the harmonic oscillator, $\Delta\mathrm{n} = \pm 1$, ceases to be a rigorous selection rule, and transitions with, for example, $\Delta n = \pm 2$ become allowed. Secondly, the vibrational energy levels are not spaced apart equally

by the quantity $h\nu$. Thus, not only may it be possible to observe a transition with $\Delta n = \pm 2$, but this transition will not have exactly double the frequency of the transition for which $\Delta n = \pm 1$ (see, e.g. Fig. 48 in [20]).

3.4.1 Raman and IR Spectra of Molecules

Vibrational spectroscopy involves the use of light to probe the vibrational behavior of molecular systems, usually via an *absorption* and *light scattering* experiment. When light interacts with matter, the photons which make up the light may be absorbed or scattered, or may not interact with the material and may pass straight through it. If the energy of an incident photon corresponds to the energy gap between the ground state of a molecule and an excited state, the photon may be absorbed and the molecule promoted to the higher energy excited state. It is this change which is measured in absorption spectroscopy by the detection of the loss of that energy of radiation from the light. However, it is also possible for the *photon* to interact with the *molecule* and scatter from it. In this case there is no need for the photon to have an energy which matches the difference between two energy levels of the molecule. The scattered photons can be observed by collecting light at an angle to the incident light beam, and provided there is no absorption from any electronic transitions which we have similar energies to that of the incident light. This process is called the process of Raman scattering.

Figure 3.6 illustrates one key difference between IR and *Raman scattering*. As described above, IR absorption would involve direct excitation of the molecule from state m to state n by a photon of exactly the energy difference between them. In contrast, Raman scattering uses much higher energy radiation and measures the difference in energy between n and m by subtracting the energy of the scattered photon from that of the beam.

Before it will demonstrate IR and Raman spectra of some molecules, we should say about *selection rule* for these processes. As we all know, a triatomic molecule will have three modes of vibrations. They are symmetrical stretch, a bending or deformation mode and an asymmetrical of water (H_2O) shown in Fig. 3.7. These diagrams use spring and ball models. The spring represents the bond or bonds between the atoms. The stronger the bond has the higher frequency. The balls represent the atoms and the heavier they are the lower the frequency [see Eq. (3.21)]. Thus, it is clear that strong bonds and light atoms will give higher frequencies of vibration and heavy atoms and weak bonds will give lower ones. This simple model is widely used to interpret *vibrational spectra*. If either molecule vibrates, the electron cloud will alter as the positive nuclei change position and depending on the nature of the change, this can cause a change of dipole moment or polarisation. In these triatomic molecules, the symmetrical stretch causes large polarisation changes and hence strong Raman scattering with weak or no dipole change and hence weak or no IR absorption. The deformation mode cause a dipole change but little polarisation change and hence strong IR absorption and weak or nonexistent Raman scattering.

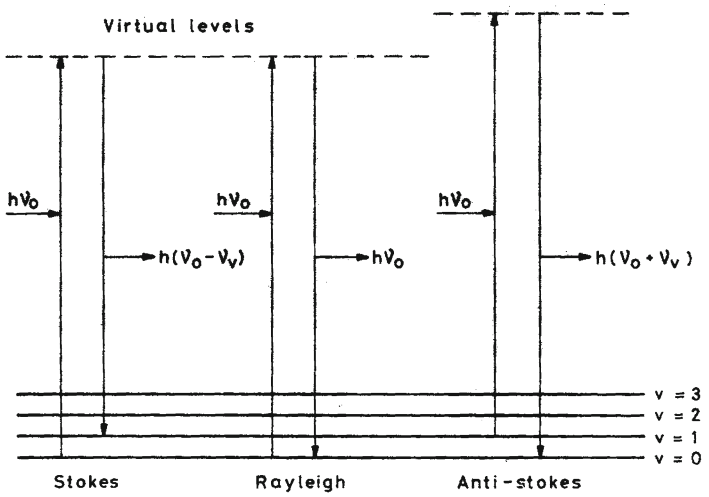

Fig. 3.6 Idealised model of Rayleigh scattering and Stokes and anti-Stokes Raman scattering. Here ν_V is vibration frequency of molecule

Fig. 3.7 Spring and ball model—three modes of vibration for H_2O

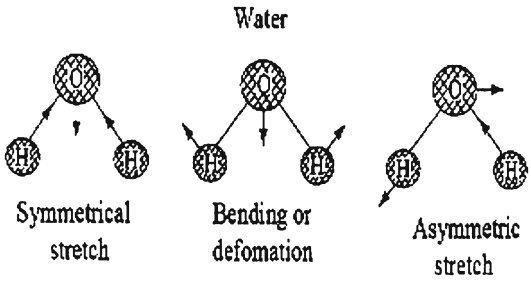

Figure 3.8 shows a comparison of the IR and Raman spectra for benzoic acid (see, e.g. [47] and references therein). The x-axis is given in *wavenumbers* for which the unit is cm^{-1}. For IR absorption each peak represents an energy of radiation absorbed by the molecule. The y-axis gives the amount of the light absorbed (% - unit) and is usually shown with the maximum absorbance as the lowest point on the trace. Raman scattering is presented only as the *Stokes spectrum* and is given as a shift in energy from the energy of the laser beam. This is obtained by subtracting the scattered energy from the laser energy. In this way the difference in energy corresponding to the ground and excited vibrational states (n and m in Fig. 3.6). This energy difference is what is measured directly by infrared. The scattering is measured as light detected by the spectrometer and the maximum amount of light detected is the highest point on the trace. Strictly speaking, Raman scattering should be expressed as a shift in energy from that of the exciting radiation and should be referred to as $\Delta\ cm^{-1}$ but it is often expressed simply as cm^{-1}.

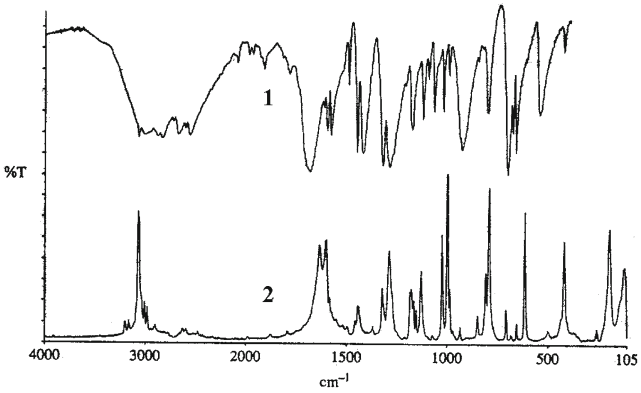

Fig. 3.8 IR *1* and Raman spectra *2* of benzoic acid

3.4.2 Isotope Shift in Molecular Frequencies

The study of the spectra of molecules in which one or more of their atoms are substituted by the corresponding *isotope* can often furnish information about the structure of the molecule which cannot at all, or only with difficulty, be obtained in any other way. This is especially true for those molecules in which a hydrogen atom is replaced by its heavy isotope *deuterium*, because for this substitution the relative change in the masses is so much greater than for all other isotopic substitutions. In order to make full use of the material which can be obtained in this way it is necessary to know exactly the changes which must be expected in the structure of the corresponding energy levels and wave functions.

When an atom of a molecule is replaced by an *isotopic atom* of the same element, it is assumed that the potential energy function and configuration of the molecule are changed by negligible amount (see, e.g. [28]). The frequencies of vibration may, however, be appreciably altered because of the change in mass involved (Eq. (3.21)). This especially, as defined above, true if hydrogen is the atom in question because of the large percentage change in mass. This shift or isotopic effect is very useful for several purposes. In the first place it may be used to help assign spectral lines to modes of vibration. Thus a normal mode of vibration in which the hydrogen atom in question is oscillating with a large relative amplitude will suffer a greater isotopic change in frequency then a normal mode in which a small relative amplitude. In the limiting case in which only hydrogen atoms are moving, replacement of all of them by deuterium atoms should decrease the corresponding fundamental frequency by the factor $1/\sqrt{2}$, this being the square root of the ratio of masses. The totally symmetric (A_1) vibration of methane [47] is an example of this situation [46]. For CH_4, the frequency is $2914.2\,\mathrm{cm}^{-1}$ which decrease to $2084.2\,\mathrm{cm}^{-1}$ for the case CD_4. The ratio $\omega_{CD_4}/\omega_{CH_4}$ thus has experimental value of $\rho = \nu^i/\nu = \sqrt{\mu/\mu^i} = 0.715$, compared to a theoretically expected value of 0.707 [49]. The discrepancy is attributed to the

fact that the observed frequencies are influenced by cubic and quartic terms in the potential energy (see above Eq. 3.27), so that the vibration is nor strictly harmonic as has been assumed in the theoretical development (for details, see [48]).

As was pointed out above, the potential energy functions of two isotopic molecules are identical to a high degree of approximation since they depend only on the motions of the electrons and the *Coulomb* repulsion of the nuclei [29]. The latter, of course, is entirely independent of these masses (see below). Not only the form of the potential curves, but also the relative positions of the potential curves of different electronic energies E_e are the same for two isotopic molecules [50]. The mass difference affects only, as noted above, the vibrational and rotational energy of the molecule in each electronic state. Restricting our considerations to the non-rotating molecule, we have for the band systems of two isotopic molecules, neglecting cubic and higher terms (in Eq. (3.27))

$$\nu = \nu_e + \omega'(v' + \frac{1}{2}) - \omega'_e x'_e (v' + \frac{1}{2})^2 - [\omega''_e (v" + \frac{1}{2}) - \omega''_e x"_e (v" + \frac{1}{2})^2 \quad (3.30)$$

and for isotope molecule

$$\begin{aligned} \nu' = \nu_e + \rho\omega'(v' + \frac{1}{2}) - \rho^2 \omega'_e x'_e (v' + \frac{1}{2})^2 \\ -[\rho\omega''_e (v" + \frac{1}{2}) - \rho^2 \omega''_e x"_e (v" + \frac{1}{2})^2]. \end{aligned} \quad (3.31)$$

Here ν_e is the difference in energy of the minima of the potential curves of the two electronic states involved which is the same to a very good approximation for the two isotopic molecules (see, however [32]). In the last two formula (3.30) and (3.31) one and two stroke label the upper and lower states. The Eqs. (3.30) and (3.31) can be written in the approximation form

$$\nu = \nu_e + \nu_v; \quad \nu^i = \nu_e + \rho\nu_v \quad (3.32)$$

Following to the quantum mechanical formulae (3.30, 3.31) do give a shift for the 0–0 band, owing to the fact that the zero-point vibration energies in the upper and lower states, in general, have different magnitudes and are different for the two isotopic molecules. A shift of the 0–0 band is directly observed in many isotope molecules (see, e.g. [29, 50]). Thus the existence of *zero-point vibration* is proved.

a)*Isotope effect in water molecule.* Before to describing this effect we should remind the symmetry of the vibrations of water (see Fig. 3.7). We reproduce the C_{2v} point group (see, e.g. [52]) in Table 3.3 which would be correct point group for a single molecule of water. In this table, the symmetry elements are shown across the top. The first column contains a series of letters and numbers. The first one we see is A_1. This is a way of describing a vibration, or for that matter an electronic function. It describes what happens to the vibration with each symmetry element of the molecule. These symbols are called irreducible representations and the top line always contains

Table 3.3 The symmetry elements of the C_{2V} point group (see, e.g. [46])

C_{2V}	E	C_2	σ_V(xz)	σ_V(yz)		
A_1	1	1	1	1	z	x^2; y^2z^2
A_2	1	1	-1	-1	R_z	xy
B_1	1	-1	1	-1	x, R_y	xz
B_2	1	-1	-1	1	y,R_x	yz

the one which refers to the most symmetrical vibration in terms of its behavior when it is rotated or reflected by the symmetry operations. In higher symmetry point groups [52] where there is a centre of symmetry, there would also be a g or a u subscript. There are four possible letters, A,B, E and T. A and B mean that the vibration is singly degenerate. E means it is doubly degenerate and T means it is triply degenerate. In the C_{2v} point group all vibrations are singly degenerate. A is more symmetric than B. Across the line from the symbols representing the irreducible representations, there are a series of numbers for each. The numbers are either 1 or -1 and 1 is more symmetric than -1. For example, in the Table 3.3, an A_1irreducible representation gives the value of 1 for every symmetry element. Figure 27 of [23] shows three vibrations of water. For the stretching vibration, when the molecule is rotated about C_2 axis, the direction of the arrow representing a vibration does not change. This is the highest symmetry and is denoted as 1. In the asymmetric stretching vibration the sign of the arrow is reversed for C_2 and one plane. When this happens this is given the number -1. Thus, this last vibration belongs to a lower symmetry representation. It is conventionally given the *irreducible representation* B_1. The main advantage of this assignment is that these tables also contain information that enables us to work on whether the vibration will be allowed by symmetry or not. For IR, this is done by multiplying the irreducible representation of the vibration by the irreducible representation of x,y or z which is given in the end column of the point group Table 3.3 in most, but not all, layouts. These correspond to three Cartesian coordinates of the molecule and are irreducible representation of the dipole operator. A similar approach is adopted for Raman scattering but in this case we look for the more complex quadratic functions x^2,y^2z^2xy, $x^2 - y^2$ etc., in the Table 3.3 and these are multiplied by the symmetry representation of the vibration.

Water is the main absorber of the sunlight. As we can see above, water molecules (with the molecular formula H_2O) are symmetric with two mirror planes of symmetry and a 2-fold rotation axis. Its molecular diameter is about 2.74 Å [53]. The water molecule consists of two light atoms (H) and a relatively heavy atom (O). The approximately 16-fold difference in mass gives rise to its ease of rotation and significant relative movements of the hydrogen *nuclei*, which are in constant and significant movement. As we can see from Fig. 3.7, the water molecule may vibrate in a number of ways. In the gas state the vibrations involve combination of symmetric stretch (ν_1), asymmetric stretch (ν_3) and bending (ν_2) of covalent bonds with absorption intensity ($H_2^{16}O$) $\nu_1{:}\nu_2{:}\nu_3 = 0.07{:}1.47{:}1$ (see [53] and reference therein). The frequencies of the main vibration of water isotopologues are shown in Table 3.4.

Table 3.4 Main vibrations of water isotopologues

Gas	ν_1, cm^{-1}	ν_2, cm^{-1}	ν_3, cm^{-1}
$H_2^{16}O$	3657.05	1594.75	3755.93
$H_2^{17}O$	3653.15	1591.32	3748.32
$H_2^{18}O$	3649.69	1588.26	3741.57
$HD^{16}O$	2723.68	1403.48	3707.47
$D_2^{16}O$	2669.40	1173.38	2787.92
$T_2^{16}O$	2233.9	995.37	2366.61

Table 3.5 Main vibrations of liquid ordinary and heavy water (cm^{-1})

Vibrations	H_2O	D_2O
Combination of ν_2 + libration	2127.5	1555
ν_2	1643	1209.4
ν_1, ν_2 and overtone of ν_2	3404	2504

The *dipole moments* of the molecule of water change in the direction of the movement of the oxygen atoms as shown by the arrows on the Fig. 3.7. As the H atoms are light, the vibrations have large amplitudes. The water molecule has a very small inertia on rotation which gives to rich combined vibrational - rotational spectra in vapour containing tens of thousands to millions of absorption lines [22, 52]. In the liquid rotations tend to be restricted by hydrogen bonds, giving the librations. Also, spectral lines are broader causing overlap of many of the absorption peaks. The main stretching band in liquid water is shifted to a lower frequency ($\nu_3 = 3,490\,cm^{-1}$ and $\nu_1 = 3,280\,cm^{-1}$) and the bending frequency increased $\nu_2 = 1644\,cm^{-1}$ by hydrogen bonding (see, e.g. [53]). Isotope shift of molecular frequencies is shown in Table 3.5. Infrared spectra of ordinary and heavy water are depicted in Fig. 27 of Ref. [19] (see, also [55] and reference therein). In liquid water the IR spectrum is far more complex than the vapour due to vibrational overtones and combinations with librations (see Table 3.5). The librations depend on the movement of inertia such that the almost doubling of the moments of inertia of D_2O, relative to H_2O, reduces the frequencies by about a factor of $\sqrt{2}$ (see, however below).

b) *Isotope effect in "fullerene" molecule*. The discovery [56] of the new *fullerene* allotropes of carbon, exemplified by C_{60} and soon followed by an efficient method for their synthesis [57], led to a burst of theoretical and experimental activity on their physical properties. Much of this activity concentrated on the vibrational properties of C_{60} and their elucidation by *Raman scattering* (see, review [58]). Comparison between theory and experiment was greatly simplified by the high symmetry (I_h), resulting in only ten Raman active modes for the isolated molecule and the relative weakness of solid state effect [58], causing the crystalline C_{60} (c–C_{60} *Raman spectrum* at low resolution to deviate only slightly from that expected for the isolated molecule. Since the natural abundance of ^{13}C is 1.11% (see [58]), almost half of all C_{60} molecules made from natural graphite contain one or more ^{13}C isotopes. If the squared frequency of a vibrational mode in a C_{60} molecule with n ^{13}C isotopes is written as a series $\omega^2 = \omega_{(0)}^2 + \omega_{(1)}^2 + \omega_{(2)}^2 + \omega_{(3)}^2 + \cdots$ in the mass perturbation

(where $\omega_{(0)}$ is an eigenmode frequency in a C_{60} molecule with 60 ^{12}C atoms), nondegenerate perturbation theory predicts for the two totally symmetric A_g modes a first-order correction given (see, e.g. [58])

$$\frac{\omega^2_{(1)}}{\omega^2_{(0)}} = -\frac{n}{720} \tag{3.33}$$

This remarkable result, independent of the relative position of the isotopes within the molecule and equally independent of the unperturbed eigenvector, is a direct consequence of the equivalence of all carbon atoms in icosahedral C_{60}. To the same order of accuracy within nondegenerate perturbation theory, the Raman polarisability derivatives corresponding to the perturbed modes are equal to their unperturbed counterparts, since the mode eigenvectors remain unchanged. These results lead to the following conclusion [58]: The A_g Raman spectrum from a set of noninteracting C_{60} molecules will mimic their mass spectrum if the isotope effect on these vibrations can be described in terms of first - order nondegenerate perturbation theory. It is no means obvious that C_{60} will meet the requirements for the validity of this simple theorem. A nondegenerate perturbation expansion is only valid if the A_g mode is sufficiently isolated in frequency from its neighboring modes. Such isolation is not, of course, required by symmetry. Even if a perturbation expansion converges, there is no a priory reason why second- and higher order correction to Eq. (3.33) should be negligible. As was shown in paper [58] the experimental Raman spectrum (see below) of C_{60} does agree with the prediction of Eq. (3.33). Moreover, as was shown in quoted paper, experiments with isotopically enriched samples display the striking correlation between mass and Raman spectra predicted by the above simple theorem. Figure 3.9 shows a high-resolution Raman spectrum at 30 K in an energy range close to the high-energy pentagonal-pinch A_g (3.2) vibration according to Menendez and Page [58]. Three peaks are resolved, with integrated intensity of 1.00; 0.95; and 0.35 relative to the strongest peak. The insert of this figure shows the evolution of this spectrum as the sample is heated. The peaks cannot be resolved beyond the melting temperature of CS_2 at 150 K. The theoretical fit [58] yields a separation of $0.98 \pm 0.01 cm^{-1}$ between two main peaks and $1.02 \pm 0.02 \text{cm}^{-1}$ between the second and third peaks. The fit also yields full widths at half maximum (FDWHM) of 0.64; 0.70 and 0.90 cm^{-1}, respectively. The mass spectrum of this solution shows three strong peaks (Fig. 3.9b) corresponding to mass numbers 720; 721 and 722, with intensities of 1.00; 0.67 and 0.22, respectively as predicted from the known isotopic abundance of ^{13}C. The authors [58] assign the highest-energy peak at $1{,}471\,\text{cm}^{-1}$ to the $A_g(2)$ mode of isotopically pure C_{60} (60 ^{12}C atoms). The second peak at $1{,}470\,\text{cm}^{-1}$ is assigned to C_{60} molecules with one ^{13}C isotope, and the third peak at $1, 469\,\text{cm}^{-1}$ to C_{60} molecules with two ^{13}C isotopes. The separation between the peaks is in excellent agreement with the prediction from Eq. (3.33), which gives $1.02\,\text{cm}^{-1}$. In addition, the width of the Raman peak at $1, 469\,\text{cm}^{-1}$, assigned to a C_{60} molecule with two ^{13}C atoms, is only 30% larger than the width of the other peaks. This is consistent with the prediction of Eq. (3.33) too, that the frequency

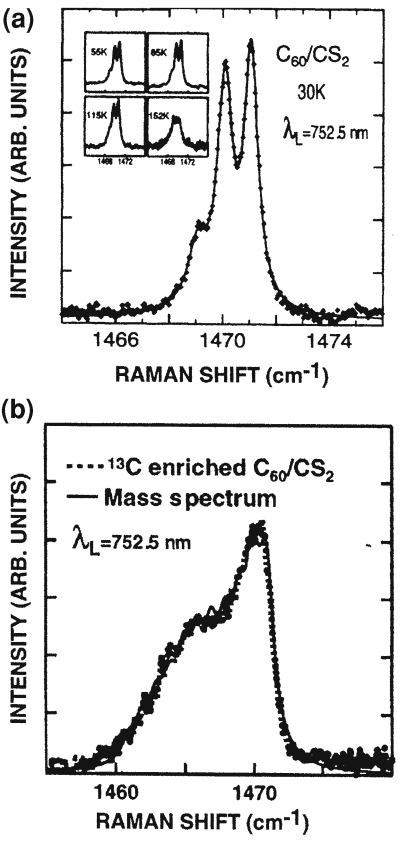

Fig. 3.9 **a** Unpolarised Raman spectrum in the frequency region of the pentagonal-pinch mode, for a frozen sample of nonisotopically enriched C_{60} in CS_2 at 30 K. The points are the experimental data, and the *solid curve* is a three-Lorentzian fit. The highest-frequency peak is assigned to the totally symmetric pentagonal-pinch A_g mode in isotopically pure $^{12}C_{60}$. The other two peaks are assigned to the perturbed pentagonal-pinch mode in molecules having one and two ^{13}C-enriched C_{60}, respectively. The *inset* shows the evolution of these peaks as the solution is heated. **b** The points give the measured unpolarised Raman spectrum in the pentagonal-pinch region for a frozen solution of ^{13}C-enriched C_{60} in CS_2 at 30 K. The *solid line* is a theoretical spectrum computed using the sample's mass spectrum, as described in the text (after [58])

of the mode will be independent of the relative position of the ^{13}C isotopes within the molecule. The relative intensity between two isotope and one isotope Raman lines agrees well with the mass spectrum ratios. Concluding this part we stress that the Raman spectra of C_{60} molecules show remarkable correlation with their mass spectra. Thus the study of *isotope-related shift* offers a sensitive means to probe the vibrational dynamics of C_{60}.

3.5 "Mass-Independent" Isotope Effect

More than the quarter of a century [59] Thiemens and Heidenreich [60] demonstrated essentially equal effects of *isotopic substitution* of ^{18}O and ^{17}O for ^{16}O on the rates [61, 62] of formation of ozone by an electric discharge in oxygen (see, also reviews [63–65]). Thiemens and Heidenreich called this observation a "non-mass dependent" or *"mass-independent"isotopic effect*. The observed non-mass

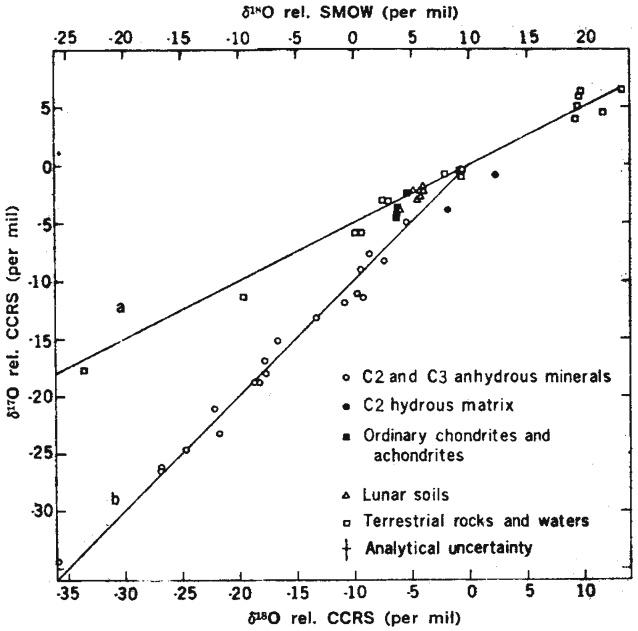

Fig. 3.10 Relationship between $^{17}O/^{18}O$ variations $^{18}O/^{18}O$ variations for terrestrial, lunar, and meteoritic samples. Points lying along *line a*, with a slope of +1/2, define the trend for chemical isotope effects; points lying along *line b* of +1, define a mixing line between "normal" oxygen and an ^{16}O-rich component. The points on *line b* are all from phases in carbonaceous chondrites (after [84])

dependent oxygen isotope formation is a kinetic isotope effect [61]. The observed effect was a remarkable deviation from the accepted theory (see, e.g. [66]) of isotope effects, which would predict that the effect of ^{18}O would be approximately double that of ^{17}O. The mechanism for the effect remains uncertain. Since that first publication, the ozone reaction has been extensively investigated both experimentally and theoretically. A number of other reactions have been labelled "mass-independent" isotope effect [63]. Mass-independent isotopic composition have been observed in O_3, CO_2, N_2O and CO in Earth's atmosphere and in carbonate from a martian meteorite (see Fig. 3.10), which suggests a role for mass-independent processes in the atmosphere of Mars [23]. According to [64], the observed mass-independent meteoritic oxygen and sulphur isotopic (see, also [67]) compositions may derive from chemical processes in the presolar nebula and their distributions could provide insight into early solar system evolution (see, also [68–71]). Although the magnitude and direction of variation of the isotope ratios for these processes vary, they have one common feature—they all depend on mass.

The most complete set of experimental data for oxygen *isotope effects* in the photochemical formation of ozone has been obtained by the Mauersberger group [72–74]. These authors managed to sort out rate constants (see below) for many

reactions of labelled O atoms and/or labelled O_2 molecules providing a severe test for theory (see, also review [65]). At present time, the most successful theory in terms of agreement with experiment is that of Marcus group [75–79], which is based on the RRKM (Rice–Ramsperger–Kessel–Marcus) theory of recombination reactions, and this will be described.

Quantum mechanical resonance calculations as performed by Babikov et al. [80–82] are the ultimate tool for investigating the formation of ozone, but these attempts are the first in the direction of "first-principle" solutions of the ozone isotope effect [67]. Resonance lifetimes for large total angular momenta are required and their determination is a formidable task. What is the impact of the shallow van der Waals-like wells and the long-lived states they support? Do they contribute to the stabilization process or are these states so fragile that the first collision with M (third body) destroys them? What is the role of the excited electronic states which correlate with ground state products? Moreover, how the vibrational energy of the excited complex is removed by the bath atom or molecule is largely not understood.

On the basis of the assumption that any deviation from mass dependence must reflect of a *nuclear* process, Hulston and Thode [83] suggested that deviations from mass-dependent isotopic composition may be used to distinguish nuclear from chemical and physical processes in meteoritic measurements [23].The observation by Clayton et al. [84] of a *non-mass dependent isotopic* composition in meteoritic substances was thus interpreted as indicating that the meteorite contained residual primary grains from a nucleosynthesis process [68–71]. Subsequently, the authors of the paper [60] reported a chemically produced mass-independent isotopic composition in the formation of ozone from molecular oxygen. The observed fractionation pattern was the same as observed in meteoritic substances and thus it was suggested that the observed isotopic composition in a meteoritic material could reflect a chemical instead a nuclear process.

Gellene [85, 86] modelled the isotope fractionation based on nuclear symmetry. In his approach, symmetry restrictions arise for homonuclear diatomic (for example, $^{16}O^{16}O$ and $^{18}O^{18}O$) involved in the $O + O_2$ collision because a fraction of their rotational states (f-parity) correlate with those of the corresponding ozone molecule. In contrast, in the case of heteronuclear oxygen molecules (for example, $^{16}O^{18}O$), all of their rotational states (e and f parity) correlate with those of the resulting ozone molecule. Gellen's model can reproduce the general features of the enrichment pattern quite well. A number of other attempts have been made [87] to find an explanation of the ozone isotope anomaly; none were able to account for the experimental results [65].

The role of *molecular symmetry* was questioned by Anderson et al. [72], who presented rate coefficients of four selected ozone formation channels. Whereas three channels

$$^{16}O + ^{16}O + ^{16}O + M \longrightarrow {}^{16}O + {}^{16}O + {}^{16}O + M \tag{3.34}$$

$$^{18}O + ^{16}O + ^{16}O + M \longrightarrow {}^{18}O + {}^{16}O + {}^{16}O + M \tag{3.35}$$

$$^{18}O + ^{18}O + ^{18}O + M \longrightarrow {}^{18}O + {}^{18}O + {}^{18}O + M \tag{3.36}$$

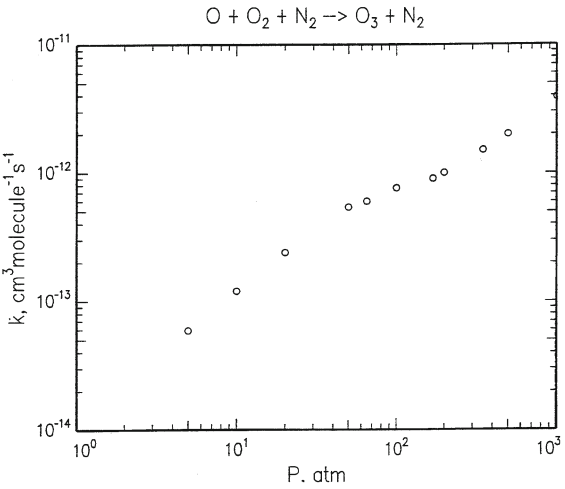

Fig. 3.11 Pressure dependence of the rate constant for the reaction $O + O_2 \longrightarrow O_3$ (after [67])

had similar rates of formation, which were consistent with a value of $\sim 6 \cdot 10^{-34} cm^6 s^{-1}$ [65], the fourth channel

$$^{16}O + ^{18}O + ^{16}O + M \longrightarrow ^{16}O + ^{18}O + ^{16}O + M \tag{3.37}$$

resulted in a rate coefficient that was 50% higher than the other three. Here M represents a third-body molecule as was indicated earlier. The difference in the rate coefficients of reactions 2 and 4 was unexpected. Thus, the difference in the rate coefficients of reactions 2 and 4 does not support an important role of symmetry in the *isotope enrichment process*. Later, a similar conclusion was reached by Sahested et al. [88, 89] who performed rate coefficient studies for the ^{16}O–^{18}O system on dual channel processes, using CO_2 and A as third-body molecules, but without isolating the process contributing to the enrichments.

More detail studies [74] are shown:

(1) Molecular symmetry cannot explain the ozone enrichment process;
(2) A collision between a light oxygen atom and a heavier molecule will result in a rate coefficient that is higher than the coefficient from reactions involving only one isotope.

Thus, experimental results presented provide new insights into the puzzling ozone *isotope effect*.

To conclude this part we should mentioned some theoretical results of Marcus et al. recognised the fact that the ozone isotope effect in this reaction is very pressure dependent (see, Fig. 3.11), as indeed is the rate constant for recombination of an oxygen molecule with an oxygen atom to form ozone. The reaction may be written

$$O + O_2 + M \leftrightarrows O_3^* + M \tag{3.38}$$

$$O_3^* + M \longrightarrow O_3 + M. \tag{3.39}$$

In this reaction mechanism, the *ozonemolecule* initially formed with excess *vibrational energy* (O_3^*) will revert to reactants unless it is stabilised by energy transfer by collision with another molecule (third body), M. This is the source of the pressure dependent of the rate constant. Marcus et al. [75–79] found two factors important in the RKKM analysis of the isotope effect in this pressure-dependent region:

a) *Zero-pointenergy* difference between isotopic species in competing reactions of asymmetrical molecules, such as

$$^{16}O + {}^{16}O{}^{18}O \rightleftarrows {}^{16}O{}^{16}O{}^{18} \rightleftarrows {}^{16}O{}^{16}O + {}^{18}O. \tag{3.40}$$

The lower zero-point energy [61] of the heavier molecule increases the region of phase space accessible to the transition state, favoring this channel.

b) A "non RKKM" effect that precludes certain regions of phase space to a symmetrical transition state, thus preventing the complete randomization of vibrational energy distribution (for details see [64, 65]).

In addition to the formation of ozone, a number of other three-isotope systems involving oxygen or sulphur isotopes have been found to exhibit non - mass dependent *isotope effects* [63, 67]. The bright example of this situation a three-isotope system which have ^{32}S–^{33}S–^{34}S combination (see, also [90]).

Thus, in the formation of ozone from molecular oxygen by photolysis or in an electric discharge, the kinetic isotope effects of ^{17}O and ^{18}O are essentially equal, in spite of the predictions of the accepted theory. This is clearly a *non-mass dependent isotope effect*.

3.6 Laser Isotope Separation

Wide employment of isotopes in such fields as atomic and thermonuclear power, fundamental and applied science, *biology*, *medicine*, *isotopic geochronology* (see Chapter 5), *agriculture*, activations analysis, *ecology* and production of new materials attracts increasing interest in the development of new highly efficient methods for isotope separation. As is well - known, the separation of isotopes requires a physical process that depends on mass. In the electromagnetic method, as used in a mass spectrograph, ions to be separated travel in circles of different radii. In the gaseous diffusion process, light molecules of a gas diffuse through a membrane more readily than do heavy molecules. The amount of enrichment in gaseous diffusion depends on the square root of the ratio of the masses and is small per stage, requiring a large number of stages. An alternative separation device is the gas centrifuge, in which gases diffuse against the centrifugal forces produced by high speeds of rotation.

The primary purposes for which methods of atomic vapour laser isotope separation (*AVLIS*) [91–94] and molecular laser isotope separation (*MLIS* process [95–97]) were

developed are to enrich natural uranium (with 0.7% ^{235}U) for uses as reactor fuel (3% ^{235}U) and to produce isotopically refined plutonium for use in weapons and other applications (see, also [98–100]). Further we briefly describe the AVLIS process as applied to uranium [101–103].

It is well-known that *uranium conversion* to appropriate fission fuel necessitates the concentration of ^{235}U from 0.7 to 3% (natural uranium contains 0.7% ^{235}U, 0.054 % ^{234}U and 99.3 % ^{238}U). In AVLIS technology (see below), atomic vapour that is natural uranium isotope mixture is obtained by electron-vacuum evaporation in a special high-vacuum technological unit (see, Figs. 3.14 and 3.15). Then vapour passes from the evaporation unit to flow former, where it is shaped to required, for example, leaf-like system. Then it comes to an interaction zone with light beams produced by a dye laser system. Usually the *dye-laser* system is pumped by another high-power system of copper-vapour lasers (*CVL*) [98, 99]. The ionisation potential for uranium is $U_{ion} = 6\,\text{eV}$ [1–3]; the *isotopic shift* of uranium levels amounts to 0.08 cm^{-1} [43, 105]. Then uranium atomic vapour is photoionised in the interaction via three-step excitation process. The spectral width of radiation, the operating wavelengths $\lambda_1 = 6,059\,\text{Å}$, $\lambda_2 = 6,046\,\text{Å}$, $\lambda_3 = 5,868\,\text{Å}$ and average power of dye laser beams are matched in such a way that after absorbing three sequenthal quanta of light at special uranium atom transitions, only the required isotope would be excited in cascade and photoionisation processes (see Fig. 3.12). as we can see from Fig. 3.12, quanta of energy for each transition are near 2 eV. The choice of particular levels of uranium is a rather complicated spectroscopic problem [95, 100]. Uranium possesses a branched system of atomic levels and has many valence electrons. The wavelengths of possible laser sources also shown in Fig. 3.12. When a *CVL* pumps *dye lasers*, all three wavelengths of the dye lasers are chosen in the red spectral range because a uranium atom has allowed transitions between suitable for efficient cascade excitation in this range (590–600 nm) [96]. In the three-step scheme, an atom at the upper *autoionisation* level decays into electrons and ions, that is, it is ionised. ^{235}U isotopes ionised in this way are extracted from the interaction zone by an electromagnetic field and are directed to collector plates where they are neutralised and condensed as a final product separation. One important problem with the method considered is the choice of a photoionised scheme. It may be a two-level (Fig. 3.13), three-level (Fig. 3.13) or four-level scheme. The choice is mainly determined by the laser source. In the case of a two-level photoionisation of uranium it usually uses a visible and UV lasers of appropriated wavelengths (see, also Fig. 3.13).

To avoid spontaneous emission of lasers one should employ pulse-periodic sources of laser radiation with the pulse lying in the range 3–200 ns (excluding excitation of metastable or Rydberg levels). The characteristic excitation time for a level is determined by the next formula (see, also Chapter 8 in [97]):

$$\tau = (\sigma\Phi)^{-1}, \tag{3.41}$$

where σ is the absorption *cross-section* and Φ is the *quantum flux*. The energy of the pulse per unit area:

$$W = \text{h}\nu\Phi\tau = \text{h}\nu/\sigma. \tag{3.42}$$

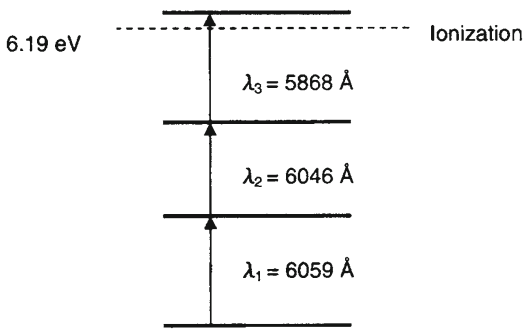

Fig. 3.12 Photoionisation of a uranium atom with three dye lasers (λ_1, λ_2, λ_3)

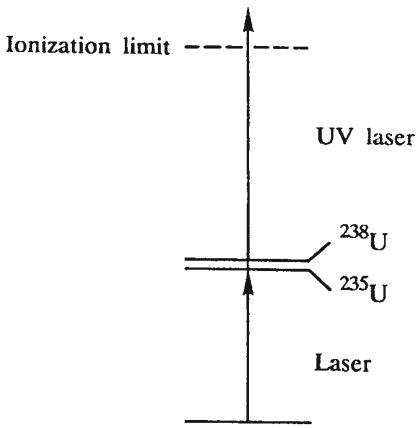

Fig. 3.13 Photoionisation of a uranium atom with two lasers

The magnitude of σ is at least 10^{-15}cm^{-1} even in the case of Doppler broadening. For the characteristic quantum energy of 1 eV we have $W \simeq 160\ \mu\text{Jcm}^{-2}$ [94]. At the pulse repetition of 10 kHz (the typical frequency for pumping pulses) we obtain that the required power in the range 1–2 Wcm^{-2}. The radiation power of modern laser source noticeably exceeds this value in UV, visible and IR spectral ranges (see, e.g. [106, 107]).

Below we consider in more detail the *AVLIS* technology. As we all know the primary goal of the AVLIS program (for instance in USA) is to develop a process that can enrich natural (and/or tails) material at less than half the cost of any other competing technology (in the first step-the gaseous diffusion and gas centrifuge). As we can see from Fig. 3.14, the AVLIS process developed in USA consists of two major subsystems: a laser system and a separator system. In the separator (see, also Fig. 3.15), unenriched metallic uranium is vapourised by an electron beam that creates an atomic $^{235}\text{U}/^{238}\text{U}$ vapour stream that rapidly moves away from the uranium melt. At the same time, dye lasers produce beam of red-orange light precisely tuned to the colours that will selectively photoionize ^{235}U isotopes. Power CVL emit beams of green–yellow light that energize the dye lasers. This configuration produces

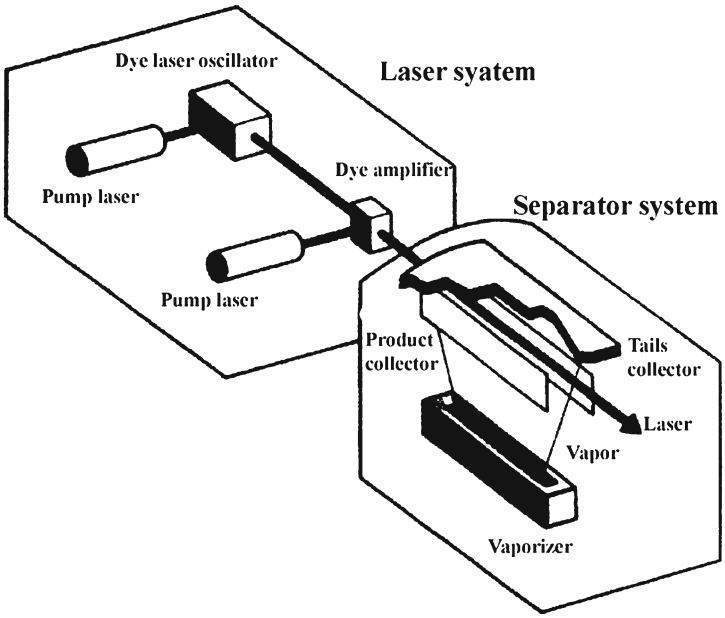

Fig. 3.14 Illustration of the AVLIS process. Metallic uranium is melted and vapourised. The vapour is illuminated by visible laser light that photoionizes the selected isotope. The ion is then electromagnetically extracted

powerful beams of tuned red–orange light to illuminate the uranium atomic vapour inside the separator. ^{235}U isotopes absorb the tuned red–orange light (see Fig. 3.12), but ^{238}U isotopes do not. The ^{235}U ions can then be moved preferentially by an electromagnetic field to condense on the product collector (see, Fig. 3.15). The ^{238}U isotopes, which remain uncharged, pass through the collector sections to condense on the tails collector. The separated uranium condensates are collected in metallic form. Presently, the technology is being developed to convert the AVLIS product to a uranium oxide form suitable for fabricating nuclear reactor fuel elements (for details, see [100, 102]).

The second major subsystem required for the AVLIS process is the separator system, in which the material to be isotopically enriched or purified is vapourised, photoionised and collected separately from the nonionised or tails. vapour flow stream. Both the collected product and tails streams condense as liquids and flow via separate path to product and tails accumulators. To operate for reasonable processing times, a separator system must also have provisions to continuously feed material as it vapourised. Typically the separator system manufactured from stainless steel, the vessel provides a high-vacuum envelope for the vapourization and collection process. Sattelite subvessels at each end house the optical system to insert and control the *AVLIS* process laser beams, which interact with the vapour stream. Since a loss of vacuum or a water leak can generate a vigorous reaction with liquids metals, the vessel

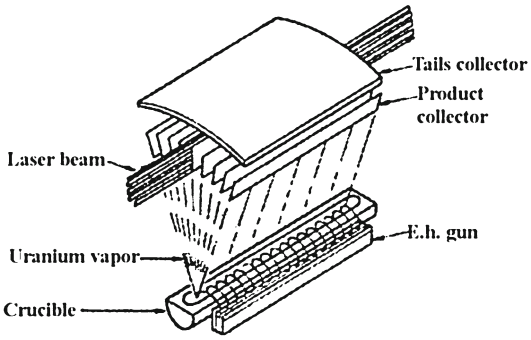

Fig. 3.15 A conceptual separator module. The uranium is evaporated by electron beam heating at the bottom of the sector, and flows past the collector near the top. The vapour is irradiated between the plates and the ^{235}U is extracted electromagnetically. It is deposited on the collector plates. The ^{238}U tails are collected on the roof

must also be designed to withstand moderate overpressure and release safely above a defined pressure limit. Because the near-term applications involve *radioactive* and/or *toxic* metals, all operations must be engineered to prevent any material release that could be harmful or hazardous to the workers and surrounding community. Highly engineered airflow and control systems integrated with a redundant high-efficiency particulate filter system are a significant part of the separation system.

Most of the discussion above is very general since the geometry, materials, many critical dimensions, and operating points for the electron gun, vapourizer evaporation rate, extractor voltage and any other parameters needed to design an AVLIS process separator are classified. Those having appropriate clearances to obtain more specific information may find novel applications for the vapouriser and or material systems developed for AVLIS (for more details see, also [102, 103].

In conclusion in this paragraph we briefly considered *MLIS* process. MLIS [95, 96] has two subapproches CO_2 laser-based approach and UF_6 molecule-based approach. The basic motivation of this approach was to take advantage of the high-power CO_2 laser technology developed for other applications, like metal cutting and welding. The first scientific challenge here was to synthesise a uranium-bearing compound having absorption features in the region 9.5–10.5 μm, where CO_2 lasers have several lines. First materials were $U(BH)_4$ and $UO_2[(CF_3CO)_2CH]_2$ [95]. The next step in MLIS process was connected with using UF_6. The rationale of this approach was to take advantage of the fact that UF_6 had been produced and handled on an industrial scale, and a large amount of scientific and engineering data on UF_6 were available. The difficult engineering problems are to supercool huge amount of UF_6 (up to 30 K) and build 16 micron lasers operating for long durations at kilowatts of power [96, 97].

Among the six fundamental vibrations of UF_6 ν_1 to ν_6 only ν_3 at 625.5 cm^{-1} and ν_4 at 186.2 cm^{-1} are IR active (absorbing) vibrations, which can be used for selective excitation [100]. Of these, ν_3 is a better choice because of its larger *isotope shift* (0.65 cm^{-1}) and more frequency location. Sensitised multiphoton dissociation of UF_6 in SF_6-UF_6 mixtures was studied using *TEA* CO_2 laser. The ν_3 mode of SF_6 absorbed the resonant CO_2 laser photons, and the vibrational energy thus gained was redistributed between different modes of SF_6. Since ν_4 mode of SF_6 is close to the

ν_3 mode of UF_6, rapid vibrational energy exchange took place between vibrationally excited SF_6 and UF_6 molecules, and the latter got excited to the vibrational quasi-continuum by sequential absorption of CO_2 laser photons by SF_6 molecules and vibrational energy transfer. From the quasi-continuum, the UF_6 molecules, by further direct sequential absorption of CO_2 laser photons got dissociated. We should add that recently it was observed direct isotopic enrichment ^{10}B as well ^{11}B in the laser ablation of B_4C (BN and GaN [108]) target using nanosecond (femtosecond [108]) wide 532 nm laser beam of a Nd-YAG laser [108, 109].

On the example of the separation of uranium isotopes we described two methods laser *isotope* separation: *AVLIS* and *MLIS*. In the AVLIS method, uranium vapour was produced around 2800 K and the uranium atoms ionised using three CVL pumped three *dye-lasers*. MLIS method used 16 micron *TEA* CO_2 laser and UF_6 molecules. The former method is more effective and uses in industrial manufacture of ^{235}U isotopes.

References

1. A.P. Striganov, Ju.P. Donzov, Isotope effect in atomic spectra, Usp. Fiz. Nauk 55, 315–330 (1955) (in Russian)
2. I.I. Sobel'man, Introduction in Theory of Atomic Spectra, 2nd edn. (Science, Moscow, 1977) (in Russian)
3. S.E. Frish, Optical Spectra of Atoms (Moscow - Leningrad, Fizmatgiz, 1963). (in Russian)
4. W.H. King, Isotope Shift in Atomic Spectra (Plenum Press, New York, 1984)
5. R.C. Barrett, Nuclear charge distributions. Rep. Prog. Phys. **37**, 1–54 (1974)
6. D.F. Jackson, Nuclear sizes and the optical model, Rep. Prog. Phys., 37, 55–146 (1974)
7. R.C. Barrettt, D.C. Jackson, *Nuclear Sizes and Structure* (Clarendon Press, Oxford, 1977)
8. M. Waraquier, J. Morean, K. Heyde et al., Rearrangement effects in shell model calculations using density - dependent interactions. Phys. Reports **148**, 249–291 (1987)
9. K. Heilig, A. Steudel, Changes in mean square nuclear charge radii from optical isotope shift. At. Data Nucl. Data Tables **14**, 613 (1974)
10. H.W. Brandt, K. Heilig, A. Steudel, Optical isotope shift measurements of $^{40,42,43,44,48}Ca$ by use of enriched isotopes in atomic beam. Phys. Lett. **A64**, 29–30 (1977)
11. F. Aufmuth, K. Heilig, A. Steudel, Changes in mean square nuclear charge radii from optical isotope shift. At. Data Nucl. Data Tables **37**, 455–490 (1987)
12. A. Djouadi, The dichotomy of electroweak symmetry breaking: The Higgs boson and Standard model. Phys. Reports **457**, 1–216 (2008)
13. D.N. Stacey, Isotope shift and nuclear charge distributions. Rep. Prog. Phys. **29**, 171–215 (1966)
14. J. Bausche and R. - J. Champeau, Recent progress in the theory of atomic isotope shift, Adv. At. and Mol. Physics 12, 39–86 (1976)
15. See e.g. E.N. Ramsden, A - Level Chemistry (Hull, Stanley Thornes Publishers, 1985; L.J. Malone, Basic Concepts of Chemistry (New York, Wiley, 2003)
16. V.I. Kogan, The discovery of the Planck constant: "X - ray" analysis of the scientific situation (1900). Overlooked opportunities of choice of the Second Step (to the centenary of the First Step of quantum theory), Usp. Fiz. Nauk 170, 1351–1357 (2000) (in Russian)
17. E.U. Condon, G.H. Shortley, *The Theory of Atomic Spectra* (Cambridge University Press, Cambridge, 1953)
18. Z. Rudzikas, *Theoretical Atomic Spectroscopy* (Cambridge University Press, Cambri dge, 2006)

19. E.V. Shpol'sky, *Atomic Physics* (Fiz. - Mat. Lit, Part One (Moscow, 1974). (in Russian)
20. G. Herzberg, *Molecular Spectra and Molecular Structure* (D. van Nostranr, New York, 1951)
21. E.B. Wilson, Jr, J.C. Decius and P.C. Gross, Molecular Vibrations. The Theory of Infrared and Raman Vibrational Spectra (New York, McGraw-Hill, 1955)
22. M.A. Eliashevich, Atomic and Molecular Spectroscopy (Moscow, Fizmatgiz, 1962). (in Russian)
23. V.G. Plekhanov, Manifestation and Origin of the Isotope Effect, ArXiv:gen. phys/0907.2024
24. A.P. Striganov, Isotope spectral analysis, Usp. Fiz. Nauk 58, 365–414 (1956) (in Russian)
25. L.D. Landau, E.M. Lifshitz, Quantum Mechanics (Nonrelativistic Theory) (New York, Pergamon Press, 1977)
26. A. Huber, Th Udem, B. Gross et al., Hydrogen - deuterium 1s–2s isotope shift and the structure of the deuteron. Phys. Rev. Lett. **80**, 468–471 (1998)
27. Th. Udem, B. Gross, M. Kourogi, et al., Phase coherent measurement of the hydrogen 1s–2s transition frequency with an optical frequency interval divider chain, Phys. Rev. Lett., 79, 2646–2649 (1997)
28. D.S. Hughes, C. Eckart, The effect of the motion of the nucleus on the spectra of Li I and Li II. Phys. Rev. **36**, 694–698 (1930)
29. J.P. Vinti, Isotope shift in magnesium. Phys. Rev. **56**, 1120–1132 (1939)
30. J. Rosenthal, G. Breit, The isotpe shift in hyperfine structure. Phys. Rev. **41**, 459–470 (1932)
31. G. Raxah, Isotopic displacement and hyperfine structure. Nature (London) **129**, 723–724 (1932)
32. P. Brix, H. Kopferman, Isotope shift studies of nuclei. Rev. Mod. Phys. **30**, 517–520 (1958)
33. D. Goorvitch, S.P. Davis, H. Kleinman, Isotope shift and hyperfine structure of the neutron-eficient thallium isotopes. Phys. Rev. **188**, 1897–1904 (1969)
34. A. - M. Martensson - Pendrill, D.S. Gough and P. Hannaford, Isotope shifts and hyperfine structure in the 369.4 nm 6s–$6p_{1/2}$ resonance line of single ionised ytterbium, Phys. Rev. A49, 3351–3365 (1994)
35. U. Bersinsh, M. Gustaffson, D. Hanstrop, Isotope shift in the electron affinity of chlorine, ArXiv, phys/9804028
36. E.C. Seltzer, K X - ray isotope shifts. Phys. Rev. **188**, 1916–1921 (1969)
37. E.K. Broch, Arch. Math. Natur. 48, 25–32 (1945), cited in [36]
38. H. Haken, HCh. Wolf, *The Physics of Atoms and Quanta* (Springer, Berlin, 2005)
39. P.L. Lee and Boehm, X - ray isotope shofts and variations of nuclear charge radii in isotopes, Phys. Rev. C8, 819–826 (1973)
40. P.L. Lee, F. Boehm, A.A. Hahn, Variations of nuclear charge radii in mercury isotopes with A = 198, 199, 200, 201, 202 and 204 from x - ray isotope shifts. Phys. Rev. **C17**, 1859–1861 (1978)
41. V.G. Plekhanov, Isotopetronics—new direction of nanoscience, ArXiv: phys/1007.5386
42. V.G. Plekhanov, Elementary excitations in isotope - mixed crystals. Phys. Reports **410**, 1–235 (2005)
43. M.A. Eliashevich, The mechanics of molecular vibrarions. Usp. Fiz. Nauk **48**, 482–544 (1946)
44. A. Anderson (ed.), *The Raman Effect* (Marcell Dekker Inc., New York, 1973)
45. D.A. Long, *Raman Spectroscopt* (MsGraw-Hill Inc., UK, 1977)
46. J.G. Grasselli, M. Snavely, B.J. Bulkin, *Chemical Application of Raman Spectroscopy* (Wiley, New York, 1981)
47. H.A. Shymanski (ed.), *Raman Spectroscopy* (Plenum Press, New York, 1967)
48. V.G. Plekhanov, Fundamentals and applications of isotope effect in modern technology. J. Nucl. Sci. and Technol. (Japan) **43**, 375–381 (2006)
49. J.G. Valatin, The isotope effect of the potential function of molecular states. Phys. Rev. **73**, 346–347 (1948)
50. C.N. Banwell, *Fundamentala of Molecular Spectroscopy* (McGraw - Hill Inc., New York - London, 1983)
51. V.G. Plekhanov, Fundamentals and applications of isotope effect in solids. Prog. Mater. Sci. **51**, 287–486 (2006)

52. S. Bhagavantam, T. Venkataraudu, *Theory of Groups and its Applications to Physical Problems* (Adha University Press, Waltair, 1951)
53. I. Danielewicz - Ferchmin and A.B. Ferchmin, Water at ions, biomolecules and charged surfaces, Phys. Chem. Liquids 42, 1–36 (2004)
54. G.E. Walrafen, Raman spectral studies of water structure. J. Chem. Phys. **40**, 3249–3256 (1964)
55. M.F. Chaplin, Models of water, see http://www.lsbu.ac.uk/water/models.html; A proposal for the structuring of water, Biophys. Chem. 83, 211–221 (2000)
56. H.W. Kroto, J.R. Heath, S.C. O'Brien et al., C_{60}: Buckminsterfullerene. Nature (London) **318**, 162–163 (1985)
57. W. Kratschmer, B. Fositropolus, D.R. Hoffman, The infrared and ultraviolet absorption spectra of laboratory - produced carbon dust: evidence for the presence of the C_{60} molecule. Chem. Phys. Lett. **170**, 167–170 (1990)
58. J. Menendez and J.B. Page, Vibrational Spectroscopy of C_{60}, in, M. Cardona and G. Guntherodt, eds, Light Scattering in Solids, VIII (Berlin - Heidelberg, Springer, 2000) (Vol. 76 in Topics in Applied Physics)
59. K. Mauersberger, Measurement of heavy ozone in the stratosphere. Geophys. Res. Lett. **8**, 935–937 (1981)
60. M.H. Thiemens, J.E. Heidenreich, The mass - independent fractionation of oxygen: A novell isotope effect and its possible cosmochemical implications. Science **219**, 1073–1075 (1983)
61. E.K. Thornton and E.R. Thornton, Origin and interpretation of isotope effects, in, C.J. Collins and N.S. Bowman, eds, Isotope Effects in Chemical Reactions (New York, van Nostrand Reinhold Co., 1970)
62. J. Biegelsen, M.W. Lee and F, Mandel, Equilibrium isotope effect, Ann. Rev. Phys. Chem. 24, 407–440 (1973)
63. R.E. Weston, Anomalous or mass-independent isotope effect. Chem. Rev. **99**, 2115–2180 (1973)
64. M.H. Thiemens, Mass - independent isotope effects in planetary atmospheres and the early solar system. Science **283**, 341–346 (1999)
65. K. Mauersberger, D. Krankowsky, C. Janssen et al., Assessment of the ozone isotope effect. Adv. At. Mol. and Optical Physics **50**, 1–54 (2005)
66. H.S. Johnston, *Gas Phase Reaction Rate Theory* (The Ronald Press Company, New York, 1966)
67. R.E. Weston Jr, When is an isotope effect non - mass dependent. J. Nucl. Sci. and Technol. (Japan) **43**, 295–299 (2006)
68. E.M. Burbidge, G.R. Burbidge, W.A. Fowler, F. Hoyle, Synthesis of the elements in stars. Rev. Mod. Phys. **29**, 547–652 (1957)
69. T.L. Wilson, Isotopes in the interstellar medium and circumstellar envelopes. Rep. Prog. Phys. **62**, 143–185 (1999)
70. G. Wallerstein, I. Jhen Jr, P. Parker et al., Synthesis of the elements in stars: forty years in progress. Rev. Mod. Phys. **69**, 995–1084 (1997)
71. S. Esposito, Primordial Nucleosynthesis: Accurate Prediction for Light Element Abundances, ArXiv:astro-ph/ 990441
72. S.M. Anderson, D. Hulsebusch, K. Mauersberger, Suprising rate coefficients for four isotopic variants of $O + O_2 + M$. J. Chem. Phys. **107**, 5385–5392 (1997)
73. Ch. Janssen, J. Guenther and K. Mauersberger, Relative formation rates of $^{50}O_3$ and $^{52}O_3$in ^{16}O - ^{18}O, J. Chem. Phys., 111, 7179–7182 (1999)
74. K. Mauersberger, K. Erbacher, D. Krankowsky et al., Ozone isotope enrichment: isotopomer-specific rate coefficients. Science **283**, 370–373 (1999)
75. B.C. Hathorn, R.A. Marcus, An intramolecular theory of the mass - independent isotope effect for ozone. I. J. Chem. Phys. **111**, 4087–4100 (1999)
76. B.C. Hathorn, R.A. Marcus, An intramolecular theory of the mass - independent isotope effect for ozone. II. Numerical implementation at low pressures using a loose transition state. J. Chem. Phys. **113**, 9497–9509 (2000)

77. B.C. Hathorn, R.A. Marcus, Estimation of vibrational frequencies and vibrational densities of states in isotopically substituted nonlinear triatomic molecules. J. Phys. Chem. **A105**, 5586–5589 (2001)
78. Y.Q. GaoMarcus, R.A. Marcus, On the theory of the strange and unconventional isotopic effects in ozone formation. J. Chem. Phys. **116**, 137–154 (2002)
79. Y.Q. Gao, W. - Ch. Chenc and R.A. Marcus, A theoretical study of zone isotopic effects using a modified ab initio potential energy surface. J. Chem. Phys. **117**, 1536–1543 (2002)
80. D. Babikov, B.K. Kendrick, R.B. Walker et al., Quantum origin of an anomalous isotope effect in ozone formation. Chem. Phys. Lett. **272**, 686–691 (2002)
81. D. Babikov, B.K. Kendrick, R.B. Walker et al., Metastable states of ozone calculated on an accurate potential energy surface. J. Chem Phys. **118**, 6298–6307 (2003)
82. D. Babikov, B.K. Kendrick, R.B. Walker, et al., Formation of ozone - metastable states and anomalous isotope effect. J. Chem Phys. 119, 2577–2589 (2003)
83. J.R. Hulston, H.G. Thode, Variations in the S^{33}, S^{34}, and S^{36} contents of meteorities and their relation to chemical and nuclear effects. J. Geophys. Res. **70**, 3475–3484 (1965)
84. R.N. Clayton, L. Grossman, T.K. Mayeda, A component of primitive nuclear composition in carbonaceous meteorites. Science **182**, 485–488 (1973)
85. G.I. Gellene, An explanation for symmetry - induced isotopic fractionation in ozone, Science 274, 1344–1346 (1996)
86. K.S. Grifith and G.I. Gellene, Symmetry restriction in diatom - diatom reactions: II Nonmass dependent isotope effects in the formation of O_4^+, Science, 96, 4403 4411 (1992)
87. J.J. Valentini, Mass-indepenent isotopic fractionation in nonadiabatic molecular collisions. J. Chem Phys. **86**, 6757–6765 (1987)
88. J. Sehested, O.J. Nielsen, H. Egsgaard et al., First kinetic study of isotopic enrichment of ozone. J. Geophys. Res. **100**, 20979–20982 (1995)
89. J. Sehested, O.J. Nielsen, H. Egsgaard, et al., Kinetic study of the formation of isotopically substituted ozone in argon, J. Geophys. Res., 103, 3545–3552 (1998)
90. V.G. Plekhanov, The enigma of the mass, ArXiv, phys./0906.4408
91. R.V. Ambartzumian, V.S. Letokhov, Two - steps selective photoionisation rubidium by laser radiation, JETP Lett. (Moscow) 13, 305–308 (1971) (in Russian)
92. S.A. Tussio, J.W. Durbin, O.G. Peterson, Two-step selective photoionisation of U-235 in uranium vapor. J. Quant. Electron. QE - **10**, 790–797 (1976)
93. J.S. Janes, I. Itzkan, C.T. Pika, Two - photon laser isotope separation of U-235 in uranium vapor. J. Quant. Elextron. QE - **12**, 11–117 (1978)
94. P.T. Greenland, Laser isotope separation. Contemp. Phys. **31**, 405–424 (1990)
95. P.R. Rao, Laser isotope separation of uranium. Current Science **85**, 615–633 (2003)
96. M. Gilbert, J.M. Weulersse, P. Isnard et al., Multiphonon dissociation of UF_6 at 16 μm in supersonic jets. SPIE **669**, 10–17 (1986)
97. V.Ju. Baranov (ed.), Isotopes, Vol I-II, Moscow, Fizmatlit, 2005 (in Russian)
98. Laser Applications: Isotope Separation, Lawrence Livermore National Laboratory, TGB - 067, 1984
99. J.L. Lyman, Laser Spectroscopy and its Applications, L.J. Radziemski (ed.) New York, Marcel Dekker Inc., 1987
100. J.W. Kelly, A review of laser isotope separation of uranium hexafluoride, Australian Atomic Energy Comission, ISBN 0642597723, 1983
101. R.M. Feinberg, R.S. Hargrove, Overview of uranium atomic vapor laser isotope separation, UCRL - ID - 114671, 1993
102. C.B. Moore, *Alternative Applications of Atomic Vapor Laser Isotope Separation Technology* (National Academic Press, Washington D.C., 1991)
103. R.L.R. Murray, *Nuclear Energy: An Introduction and Applications* (Woburn, MA, Butterworth-Heineman, 2001), pp. 99–113
104. P.A. Bokhan, V.V. Buchanov, N.V. Fateev et al., *Laser Isotope Separation in Atomivc Vapor* (Wiley - VCH - Verlag GmbH & Co., Weinheim, 2006)

105. A.R. Striganov, G.A. Odintzova, *Tables of the Spectral Lines of Atoms and Ions* (Energoatomizdat, Moscow, 1982). (in Russian)
106. Dye Lasers, E. - P. Sheffer (ed.), Moscow, MIr, 1976 (in Russian)
107. Handbook of Lasers, A.M. Prokhorov (ed.), Vol. 1, Moscow, Sov'et Radio, 1978 (in Russian)
108. P.P. Pronko, P.A. VanRompay, Z. Zhang et al., Isotope enrichment in laser - ablation plumes and commensurately deposited thin films. Phys. Rev. **83**, 2596–2599 (1999)
109. M. Joseph, P. Monoravi, Boron isotope enrichment in nanosecond pulsed laser-ablation pume. Appl. Phys. **A76**, 153–156 (2003)

Chapter 4
Isotopes in Solids

4.1 Elementary Excitations in *Isotope-Mixed Crystals*

The modern view of solid-state physics is based on the presentation of *elementary excitations*, having mass, quasiimpuls, electrical charge and so on (see, e.g. [1]). According to this presentation the elementary excitations of the non-metallic materials are *electrons* (*holes*), *excitons* (*polaritons* [2]) and *phonons* [3]. The latter are the elementary excitations of the crystal lattice, the *dynamics* of which is described in *harmonic approximation* as is well known, the base of such view on solids is the multiparticle approach. In this view, the *quasiparticles* of solids are ideal gas, which describe the behavior of the system, e.g. noninteracting electrons. We should take into account such an approach to consider the theory of elementary excitations as a suitable model for the application of the common methods of *quantum mechanics* for the solution of the solid-state physics task. In this chapter we consider not only the manifestations of the *isotope effect* on different solids, but also the new accurate results, showing the quantitative changes of different characteristics of phonons and electrons (excitons) in solids with isotopic substitution [4]. The isotopic effect becomes more pronounced when dealing with solids. For example, on substitution of H with D the change in energy of the electron transition in solid state (e.g. LiH) is two orders of magnitude larger than in atomic hydrogen (see, e.g. [5]). Using elementary excitations to describe the complicated motion of many particles has turned out to be an extraordinarily useful device in contemporary physics, and it is the view of a solid which we describe in this chapter.

The basic Hamiltonian of our solid model is of the form [4]

$$\mathrm{H} = \mathrm{H}_{\mathrm{ion}} + \mathrm{H}_{\mathrm{electron}} + \mathrm{H}_{\mathrm{electron-ion}} \tag{4.1}$$

where

$$\mathrm{H}_{\mathrm{ion}} = \sum_i \frac{p_i^2}{2m} + \frac{1}{2}\sum_{i \neq j} V(R_i - R_j), \tag{4.2}$$

V. G. Plekhanov, *Isotopes in Condensed Matter*, Springer Series in Materials Science 162,
DOI: 10.1007/978-3-642-28723-7_4, © Springer-Verlag Berlin Heidelberg 2013

$$\mathrm{H}_{\mathrm{electron}} = \sum_i \frac{p_i^2}{2m} + \frac{1}{2}\sum_{i\neq j} \frac{e^2}{|r_i - r_j|}, \tag{4.3}$$

$$\mathrm{H}_{\mathrm{electron-ion}} = \sum_{i,j} v(r_i - R_j), \tag{4.4}$$

$\mathrm{H}_{\mathrm{ion}}$ describes a collection of ions (of a single species) that interact through a potential $V(R_i - R_j)$ which depends only on the distance between ions. By ion we mean a nucleus plus the closed-shell, or core, electrons, that is, those electrons that are essentially unchanged when the atoms are brought together to make a solid. $\mathrm{H}_{\mathrm{electron}}$ presents the valence electrons (the electrons outside the last closed shell), which are assumed to interact via a Coulomb interaction. Finally, $\mathrm{H}_{\mathrm{electron\text{-}ion}}$ describes the interaction between the electrons (excitons) and the ions, which is again assumed to be represented by a suitable chosen potential.

In adopting Eq. (4.1) as our basic Hamiltonian, we have already made a number of approximations in the treatment of a solid. Thus, in general the interaction between ions is not well—represented by a potential $V(R)$, when the coupling between the closed-shell electrons on different ions begins to play an important role (see, e.g. [6, 7]). Again, in using a potential to represent electron–ion interaction, we have neglected the fact that the ions possess a structure (the core electrons); again, when the Pauli principle plays an important role in the interaction between the valence electrons, that interaction may no longer be represented by a simple potential. It is desirable to consider the validity of these approximations in detail (for detail see, e.g. [7]). In general one studies only selected parts of the Hamiltonian (4.1). Thus, for example, the band theory of solids is based upon the model Hamiltonian [6, 8].

$$\mathrm{H}_B = \sum_i \frac{p_i^2}{2m} + \sum_{i,j} v(r_i - R_{j0}) + V_{\mathrm{H}}(r_i), \tag{4.5}$$

where the R_{j0} represents the fixed equilibrium positions of the ions and the potential V_{H} describes the (periodic) Hartree potential of the electrons. One studies the motion of a single electron in the periodic field of the ions and the Hartree potential, and takes the Pauli principle into account in the assignment of one-electron states. In so doing, one neglects aspects other than the Hartree potential of the interaction between electrons. On the other hand, where one is primarily interested in understanding the interaction between electrons in metals, it is useful to consider only Eq. (4.3), replacing the effect of the ion cores by a uniform distribution of positive charge [9]. In this way one can approximate the role that electron interaction plays without having present the additional complications introduced by the periodic ion potential. Of course one wants finally to keep both the periodic ion potential and the electron interactions, and to include also the effects associated with departure of the ions from the equilibrium positions, since only in this way one does not arrive at a generally adequate description of the solid. Usually for the *elementary excitations* in solids first

consider the various parts of the Hamiltonian Eq. (4.1) and then take into account the remaining terms which act to couple different excitations.

4.2 Electronic Band Structure

The importance of the electronic theory of solids as embodied in band theory is that it provides us with clear means of understanding how solids may be *insulators*, *semiconductors* or *metals*. This depends upon whether or not it is a Fermi surface. The existence of a Fermi surface produces metallic behavior, whereas at 0 K, if the filled electron levels are separated from vacant ones, we have insulating properties. If the separation is large, say ≥5 eV, the substance remains an insulator at temperature above 0 K, whereas semiconducting properties arise if the filled and empty levels lie within 0–2 eV of one another.

(a) LiH: LiH crystal is of NaCl structure type. The simple electronic structure of Li^+ and H^- ions, having $1s^2$ configuration, gives LiH a special place among binary crystals and in many aspects allows it to serve as an ideal model for *ionic compounds*. The spectrum of one-electron states of crystals is determined by the solution of Schrodinger equation for the 'extra' particle (hole or electron) moving in the averaged field created by all the remaining electrons and nuclei [10]:

$$\left[-\frac{\hbar^2}{2m}\Delta + V(\vec{r})\right]\Psi_{\vec{k}}(\vec{r}) = E_n\left(\vec{k}\right)\Psi_{\vec{k}}(\vec{r}), \tag{4.6}$$

where the notation is conventional and $V(\vec{r})$ is the periodic potential. The existing calculation techniques differ in the method of constructing the electron potential $V(\vec{r})$, the approximation of the wave function $\Psi_{\vec{k}}(\vec{r})$, the ways of ensuring self-consistency, the reliance on empirical parameters, etc. In particular, two factors are especially important in case of *ionic crystals*: (1) the inclusion of exchange interaction and (2) the inclusion of polarisation of the electron and ion subsystems of crystal by the extra particle [11].

The one-electron potential of any many-electron system is nonlocal because of the exchange interaction between the electrons. It is difficult to take this interaction into account. Because of this, the exact potential in the band theory is often replaced by the local potential of the form $V_{\text{exchange}}(\vec{r}) \propto \alpha\left[\rho(\vec{r})\right]^{1/3}$, where $\rho(\vec{r})$ is the charge density function, and the constant α is selected in the range from 1 (Slater potential) to 2/3 (Cohn–Sham potential) [12].

Two effects are associated with the local exchange. First, the results of calculation depend strongly on the numerical value of α, and second, this approximation always underestimates the values of E_g and E_v (the width of the valence band). It is the low values of E_v obtained by many authors in the approximation of local exchange that are responsible for the wrong conclusion concerning the inapplicability of band theory to ionic dielectrics. These problems reflect the fundamental drawback of the

one-electron approximation which does not take into account the reciprocal effect of the selected electron (hole) on the rest of the system. This effect consists in the polarisation of the crystal by the particle, and is generally made up of two parts: the electron polarisation (inertialess), and the lattice polarisation (inertial). In the common optical phenomena, related to absorption or scattering of photons, the lattice polarisation is not important, because the frequency of optical transitions is much higher than the average frequencies of phonons. The *electron polarisation* is different. The extra particle (electron, hole) is regarded by this theory as the slowest particle in the system—in other words, all the remaining electrons adiabatically follow it. Hence it follows that the inertialess polarisation must definitely be included in the calculation of energy spectrum. An important feature of *ionic crystals* is that the polarisation energy E_p is of the same order of magnitude as the bandwidth. Such a correction obviously cannot be regarded as small. In the extreme case of particle at rest, the polarisation energy can be calculated by methods of classical electrostatics (the Mott–Littleton method [11]), or by the newer and more accurate technique proposed by Fowler [13]. The value of E_p for AHC found by this method is 2–3 eV for each of the quasi-particles ($E_p > 0$ for electrons, and $E_p < 0$ for holes). This implies that the inclusion of electron polarisation will reduce the magnitude of E_g by 4–5 eV [10]. By assumption, the electron bands are displaced rigidly, without changing the dispersion law $E(\vec{k})$.

The simple electron structure of lithium hydride (combined with the negligibly small *spin-orbital interaction*) is very helpful for calculating the band structure: all electron shells can easily be taken into account in the construction of the electron potential. The first calculations of band structure of lithium hydride were carried out as early as 1936 by Ewing and Seitz [14] using the Wigner–Seitz cell method. This method consists essentially in the following. The straight lattice is divided into polyhedra in such a way that the latter fill the entire space; inside each polyhedron is an atom forming the basis of the lattice (Wigner–Seitz cells). The potential inside each cell is assumed to be spherically symmetrical and coinciding with the potential of free ion. This approximation works well for ions with closed shells. The radial Schrodinger equation in the coordinate function $R_l(\vec{r})$ is solved within each selected cell, the energy being regarded as a parameter. Then the Bloch function is constructed in the form of expansion

$$\Psi_{\vec{k}}(\vec{r}) = \sum_{l=0}^{\infty} \sum_{m=-l}^{l} C_{lm}\left(\vec{k}\right) \mathrm{Y}_{lm}\left(\theta, \varphi\right) R_l\left(\vec{r}, \mathrm{E}\right), \tag{4.7}$$

where $\vec{r}$, θ, φ are the spherical coordinates (with respect to the centre of the cell); Y_{lm} are spherical functions. The coefficients $C_{lm}(\vec{k})$ and the energy $E(\vec{k})$ are found from conditions of periodicity and continuity on the boundaries of the cell. If $\vec{r}_1$ and $\vec{r}_2$ are the coordinates of two points on the surface of Wigner–Seitz cell, linked by the translation vector $\vec{R}_l$, then the boundary conditions are [14]

$$\Psi_{\vec{k}}(\vec{r}_2) = \exp\left(i\vec{k}\vec{R}_l\right)\Psi_{\vec{k}}(\vec{r}_1), \tag{4.8}$$

and

$$\nabla_n \Psi_{\vec{k}}(\vec{r}_2) = \exp\left(-i\vec{k}\vec{R}_l\right)\nabla_n \Psi_{\vec{k}}(\vec{r}_1), \tag{4.9}$$

where ∇_n is the gradient normal to the surface of the cell. We see that the method of cells only differs from the problem of free atom in the *boundary conditions*. Owing to the complex shape of the cell, however, the construction of boundary conditions is a very complicated task, and this method is rarely used nowadays.

The method of plane associated waves (PAW) was used for calculating the band structure and the equation of state for LiH was used in Perrot [15]. According to this method, the crystal potential is assumed to be spherically symmetrical within a sphere of radius $\vec{r}_s$ described around each atom, and constant between the spheres (the so-called cellular muffin-tin (MT) potential). Inside each sphere, like in the Wigner–Seitz method, the solutions of Schrodinger equation have the form of spherical harmonics; outside the spheres they become plane waves. Accordingly, the basis functions have the form

$$\Psi_{\vec{k}}(\vec{r}) = \exp\left(i\vec{k}\vec{r}\right)\theta(\vec{r}-\vec{r}_s) + \sum a_{lm} Y_{lm}(\theta, \varphi) R_l(E, \vec{r})\,\theta(\vec{r}_s - \vec{r}), \tag{4.10}$$

where $\theta(x) = 1$ at $x \geq 0$, and $\theta(x) = 0$ at $x < 0$. The coefficients a_{lm} can be easily found from the condition of sewing on the boundary of the sphere. This is an important advantage of the PAW method over the method of cells. The calculations of Perrot [15] are self-consistent, and the local potential is used in the Cohn-Sham form. The correlation corrections were neglected. The method of Corringi-Cohn-Rostocker (CCR method), or the method of Green's functions, was used for calculating the band structure of LiH in Zavt et al. [16] (only concerned with the valence band) and in Kulikov [17]. Calculation of band structure of LiH in Grosso and Paravicini [18] was based on the wave function used in the method of orthogonalised plane waves (OPW) of the form

$$\Psi_{\vec{k}}(\vec{r}) = \exp\left(i\vec{k}\vec{r}\right) - \sum_c \left\langle \exp\left(i\vec{k}\vec{r}\right) \mid X_c \right\rangle X_c(\vec{r}), \tag{4.11}$$

where X_c are the atomic functions of state of the skeleton; $\left\langle \exp\left(i\vec{k}\vec{r}\right) \mid X_c \right\rangle$ is the integral of overlapping of plane wave with skeleton function [19]. The method of linear combination of local basis functions was applied to the calculation of band structure of LiH in Kunz and Mickish [20]. This method is based on constructing the local orbitals for the occupied atom states, based on certain invariant properties of the Fock operator. The main feature of local orbitals is that they are much less extensive than the atom orbitals. Importantly, the correlation correction is taken into account in Kunz and Mickish [20]. Owing to the high polarizability of hydrogen molecules, the correlation effect in lithium hydride is exceptionally strong. Yet another calculation of

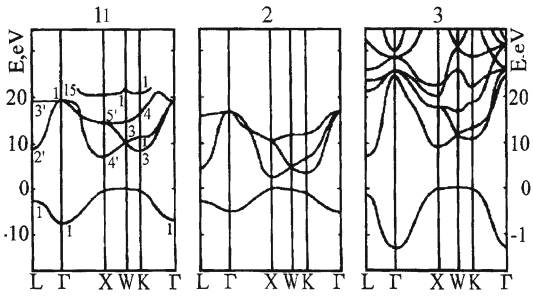

Fig. 4.1 Band structure of LiH crystal as calculated: [20]–*1*; [15]–*2*; [19]–*3*

Table 4.1 Calculated energy values of some direct optical transitions in LiH reduced to the experimental value of $E_g = 5.0\,eV$

Transition	1	2	3,4	5
K_1–K_3	6.9	7.5	6.5	6.4
W_1–W_3	8.0	7.9	7.3	7.4
L_1–L'_2	9.2	9.6	9.0	9.1
W_1–W'_2	12.6	14.9	12.2	–
X_1–X'_5	12.9	13.8	13.6	–
K_1–K_4	14.7	16.1	15.0	–
L_1–L'_3	19.7	20.9	20.7	–
Γ_1–Γ_{15}	24.5	25.3	33.3	–

band structure of LiH was carried out in Zavt et al. [16] using the so-called method of extended elementary cell. This approach is based on the semiempirical techniques of the theory of molecules, and is similar to the cluster calculations. Let us add that the cluster is selected in such a way that the quasi-molecular wave function transforms in accordance with the group symmetry of certain wave vectors in the *Brillouin zone*. This methods only yields the energy values at the points of high symmetry. We ought to mention also Hama and Kawakami [133], where, in connection with the study of high pressure effects on the transition NaCl–CsCI in lithium hydride, the band structure and the equation of state of the latter are analysed in detail. The calculated band structures of LiH are compared in Fig. 4.1. We see that the overall picture given by various methods is generally the same, despite the vast spread of the transition energy values (see Table 4.1). Looking at the structure of the valence band we see that it is very similar to the s-band in the method of strong bond [10]. This is surprising, given the strong overlap of the anion s-functions in lithium hydride. The wave functions in this band are almost entirely composed of the Is states of hydrogen ion. Different authors place the ceiling of the band either at point X or at point W of the Brillouin zone. Although in all cases the energies of the states X_1 and W_1 differ little ($\leq 0.3\,eV$), the question of the actual location of the top of the valence band may be important for the *dynamics* of the hole. Different calculations also disagree on the width of the valence band. For example, the width of the valence band in LiH without correlation is, according to Kunz and Mickish [20], $E_v = 14.5\,eV$, and the value of E_v is reduced to one half of this when correlation is taken into account. This shows

how much the polarisation of crystal by the hole affects the width of the valence band E_v. According to Perrot [15], the width of the valence band in LiH is 5.6 eV. The density of electron states in the valence band of LiH was measured in Betenekova et al. [21] and Ichikava et al. [22]. In Betenekova et al. the measurements were carried out with a magnetic spectrometer having the resolution of 1.5 eV, whereas the resolution of hemispherical analyser used in Ichikawa et al. [22] was 1.1 eV. From experimental data, the width of the valence band is 6 eV according to Betenekova et al., and 6.3 eV according to Ichikawa et al. Observe the good agreement with the calculated value of E_v in this theory. Let us add also that the measured distribution of the electron density of states in the valence band of LiH exhibits asymmetry typical of s-bands (for more details see Betenekova et al. [21] and Ichikawa et al. [22]). The lower part of the conduction band is formed wholly by p-states and displays an absolute minimum at point X which corresponds to the singlet symmetry state X_4. The inversion of order of s and p-states in the spirit of LCAO method may be understood as the result of the *s*-nature of valence band. Mixing of *s*-states of the two bands leads to their hybridisation and spreading, which changes the sequence of levels (see also [10] and references there). If we compare the structure of the conduction band with the p-band of the method of strong bond (see, also [5]), we see that the general structure and the sequence of levels are the same except for some minor details (the location of L_3 level, and the behavior of $E(\vec{k})$ in the neighbourhood of Γ_{15}). In other words, the lower part of the conduction band in lithium hydride is very close to the valence p-band of AHC. The direct optical gap in LiH according to all calculations is located at X point and corresponds to the allowed transition X_1–X_4. The indirect transition W_1–X_4 ought to have a similar energy. According to the above calculations, the energies of these transitions differ by 0.03–0.3 eV. The different values of E_g for LiH obtained by different authors are apparently due to the various methods used for taking into account the exchange and correlation corrections (see above). As follows from Table 4.1, the transitions at critical points in the low-energy region form two groups at 7–9 and 13–15 eV. Measurements of reflection spectra in the 4–25 eV range at 5 K (Kink et al. [23]) and 4–40 eV at 300 K throw new light on the results of calculations (see also review by Plekhanov [5]). The singularities occurring at 7.9 and 12.7 eV in *reflection spectra* are associated in the above papers with the interband transitions W_1–W_4 and X_1–X_5 respectively.

From the standpoint of *dynamics* of quasiparticles, an important consequence of such band structure is the high anisotropy of the *tensor of effective mass* of electrons and (especially) holes. The estimated mass of electron in the neighbourhood of X_4 is, according to Kunz and Mickish [20], $(m_e)_x \simeq 0.3\ m_0$ in the direction X–Γ, and $(m_e)_y = (m_e)_z \simeq 0.8\ m_0$ in the direction X–W. Similarly, the mass of hole in the neighbourhood of X_1 is X–Γ in the direction $(m_e)_x \simeq 0.55\ m_0$ and about the same in the neighbourhood of W_1. It is assumed that the transverse components of m_h are greater by several orders of magnitude (Zavt et al. [16]). Note also that, according to Baroni et al. [19], the estimated masses of carriers are: $m_{el} = 0,121$; $m_{et} = 0,938$; $m_{hl} = 0,150$; $m_{ht} = 4,304\ m_e$, where the subscripts 1 and t denote, respectively, the longitudinal (in the direction Γ–X) and the transverse (in the direction X–W) components. This high anisotropy of masses of electron and hole ought to have resulted

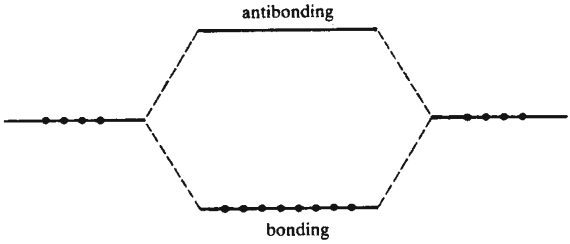

Fig. 4.2 A schematic picture of bonding and antibonding levels in a silicon dimer

in the high anisotropy of the *reduced* ($1/\mu = \mathrm{I}/m_e + 1/m_h$) and the *translation* ($\mathrm{M} = m_e + m_h$) *masses* of *exciton*. This, however, is not the case. Moreover, the study of Plekhanov and Altukhov [24] reveals that with a good degree of confidence one may assume that in the energy range $\mathrm{E} \leq 40\,\mathrm{meV}$ the exciton band is isotropic and exhibits parabolic dispersion ($m_e = 0.04\,\mathrm{m}$ and $m_h = 0.15\,\mathrm{m}$). As was shown below, the studies of exciton–phonon luminescence of free excitons and resonance *Raman scattering* of light in LiH crystals [10] reveal that the kinetic energy of excitons in these crystals is greater than E_b by an order of magnitude exactly because of the very small masses of electron and hole. The latter may indicate that in the metallic phase of hydrogen at the high pressure [10] we can expect the Dirac character of the *electronic excitations* [25].

(b) Si: *Semiconductors* may be pure elements like Si (Ge), but may also be compounds (like LiH), for example Zns, CdS, SiC, Cu_2O and GaAs. Their properties are strongly affected by the presence of impurities, defects or departures from exact stoichiometry. The properties of a perfect crystal of a pure element or perfectly stoichiometric compound are called intrinsic properties, whereas the influences of added impurities or defects give rise to extrinsic properties.

The electronic configuration of a Si atom is $1s^2 2s^2 2p^6 3s^2 3p^2$ (see, e.g. [26]). When Si atoms form a crystal it can divide their electrons into core electrons and valence electrons as pointed out in different textbooks [7, 8, 27]. In crystalline Si 1s, 2s and $2p$ orbitals are completely occupied and form the core shells. The outer 3s and $3p$ shells are only partially filled. Electrons in these shells are called valence electrons because they are involved in bonding with neighbouring Si atoms. The crystal structure of Si at ambient pressure is similar to that of *diamond* [28]. The tetrahedral arrangement of bonds between Si atoms (see, e.g. Fig. 4.18 in [8]) and its four nearest neighbours can be understood if one of the electrons in the 3s shell is promoted to the $3p$ shell so that the four valence electrons form hybridised sp^3 orbitals. It is these valence electrons in the outermost shells of a Si atom that are nearly free. These electrons are not affected by the full *nuclear* charge as a result of screening of the *nucleus* by the filled core shells. In the core region the valence electron wave functions must be orthogonal to those of the core.

Consider further the formation of a Si dimer, i.e. a diatomic molecule. Just as in the formation of the H_2 molecule, we expect the electron states to interact and form bonding and antibonding levels (see, Fig. 4.2). As is well known, the separation into *bonding* and *antibonding* levels is the origin of the energy gap in the band structure of

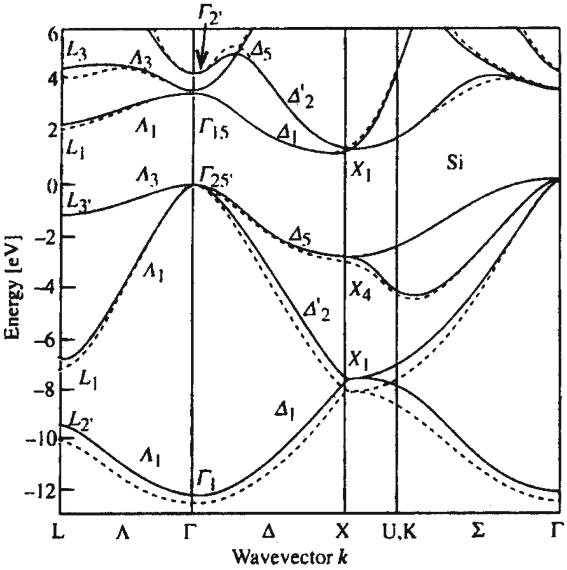

Fig. 4.3 Electronic band structure of Si calculated by pseudopotential technique. The solid and the dotted lines represent calculations with a nonlocal and a local pseudopotential, respectively (after [29])

solid Si. According to this very simple approximation, the lower four bands are filled and the upper four bands are empty [29]. One should not worry about the detailed shapes of these bands but accept them as solutions of the Schrödinger equation in the assumed potential. Using the pseudopotential concept [29], the one-electron Schrödinger equation have the next form

$$\left[\frac{p^2}{2m} + V(\overrightarrow{r_i})\right]\Psi_k(\overrightarrow{r_i}) = \mathrm{E}_k\Psi_k(\overrightarrow{r_i}), \tag{4.12}$$

Here $\Psi_k(\overrightarrow{r_i})$ is the pseudo wave-function and $V(\overrightarrow{r_i})$ is *pseudopotential*. The bringing function is a good approximation to the true wave function outside the core region and therefore can be used to calculate the physical properties of the semiconductors which are dependent on the valence and conduction electrons only. The difference in energy between the highest occupied and lowest unoccupied state is indicated as 1.17 eV at 0 K. It is to be noted, however, that these limiting states lie at different points within the zone, and this minimum excitation of an electron from the valence to the conduction band demands that it be given crystal momentum equivalent to the difference in the $\overrightarrow{k}$ vectors; this is readily obtained in thermal excitation by the crystal momentum available from the phonons (see, Fig. 4.3).

The energy gap characterising an *intrinsic semiconductor* may be determined by *optical absorption*. At low temperatures there are very few carriers and the Drude contribution to the absoptivity is absent [8] in an intrinsic semiconductor. Semiconductors are therefore transparent to infrared radiation and become absorbing only when interband transitions are excited. We might therefore expect the band gap to fix

the threshold for interband transitions and in this way be readily determined experiment [27]. This would be the case if the band gap were determined by filled and empty states with the same reduced value of $\overrightarrow{k}$; the absorption of light would then cause a "vertical" transition and give rise to a sharp edge at $\hbar\omega = \mathrm{E}_g$. This is the case for many semiconductors such as CdS, GaAs, etc.

In Si (and many other semiconductors), we have seen (Fig. 4.3) that excitation across the minimum separation of filled and empty states demands a large change in wave vector, and such a transition cannot be initiated by a photon unless it has access to a source of crystal momentum. We should repeat that it is the phonons that provide the required momentum. We write the conservation laws in the form

$$\begin{aligned} \mathrm{E}_f - \mathrm{E}_i &= h\nu + \hbar\omega_f, \\ \overrightarrow{k}_f - \overrightarrow{k}_i &= 0 + \overrightarrow{q}, \end{aligned} \tag{4.13}$$

where $\overrightarrow{q}$ and ω_f apply to the phonon involved in the transition. Now $\mathrm{E}_f - \mathrm{E}_i = \mathrm{E}_g$ and it is clear that the inclusion of phonons produces an absorption edge at a somewhat lower energy, namely $\mathrm{E}_g - \hbar\omega_f$. These indirect or *phonon-assisted transitions* produce only weak absorption compared with that associated with direct transitions (see, e.g. Fig. 3.25 in [30]).

4.2.1 Phonons

The simplest kind of motion in solids is the vibration of atoms around the equilibrium point. The interaction of the crystalforming particles with one another at the move of the one atom entanglements neighbour atoms [31]. The analysis of this kind of motion shows that the elementary form of motion is the wave of the atom displacement. As is well known, the quantisation of the vibrations of the crystal lattice and after introduction of the *normal coordinates*, the Hamiltonian of our task will be the following relation (see, e.g. [8])

$$\mathrm{H}(Q, P) = \sum_{i,q} \left[-\frac{\hbar^2}{2} \frac{\partial^2}{\partial Q^2(\overrightarrow{q})} + \frac{1}{2}\omega_j^2 Q_j^2(\overrightarrow{q}) \right]. \tag{4.14}$$

In this relation, the sum, where every addend means the Hamiltonian of *linear harmonic oscillator* with coordinate $Q_j(\overrightarrow{q})$, the frequency $\omega_j(\overrightarrow{q})$ and the mass, equals a unit. If the Hamiltonian system consists of the sum, where every addend depends on the coordinate and conjugate its quasiimpuls, then according to quantum mechanics [32] the wave function of the system equals the product of wave functions of every appropriate addend and the energy is equal to the sum of assigned energies. Any separate term of the Hamiltonian Eq. (4.14) corresponds, as indicated above,

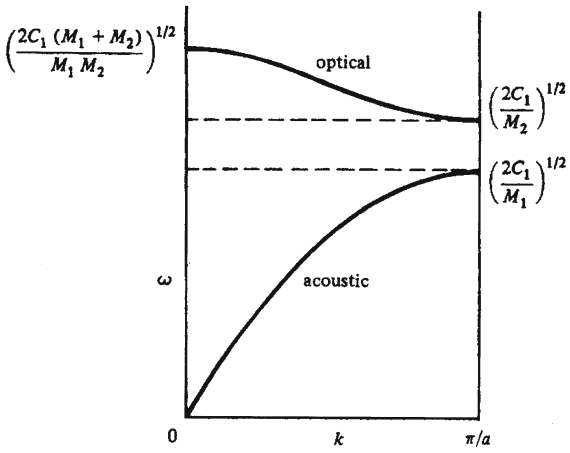

Fig. 4.4 Optical and acoustical modes. The optical modes lie at higher frequencies and show less dispersion than the acoustic modes (for details see text)

to the linear oscillator

$$-\frac{\hbar^2}{2}\frac{\partial^2\Psi}{\partial Q^2}+\frac{1}{2}\omega^2Q^2\Psi=\varepsilon\Psi. \tag{4.15}$$

Solving the last equation and finding the eigenvalues and eigenfunctions and then expressing explicitly the frequency, we will obtain for a model with two atoms in primitive cell (with masses M_1 and M_2) the following equation

$$\omega^2\simeq 2\mathrm{C}\left(\frac{1}{M_1}+\frac{1}{M_2}\right) \tag{4.16}$$

and

$$\omega^2\simeq\frac{C}{2(M_1+M_2)}K^2a^2. \tag{4.17}$$

Taking into account that $\mathrm{K_{max}}=\pm\pi/a$, where a is a period of the crystal lattice, i.e. $\mathrm{K_{max}}$ respond the border of the first *Brillouin zone*

$$\omega^2=\frac{2C}{M_1}\quad\text{and}\quad\omega^2=\frac{2C}{M_2} \tag{4.18}$$

Formula (4.16) describes the optical branch of *vibrations*, whereas Eq. (4.17)—acoustical branch of vibrations (see, e.g. Fig. 4.4). Usually the last formula is written as follows:

$$\omega=\sqrt{\frac{\alpha}{M}}, \tag{4.19}$$

where α is the so-called *force constant* (see, also Chap. 2). Here, early M is the mass of vibrated atom (ion). From the preceding relation it is clear that, as in molecular physics, in solid isotope the effect directly manifests in *vibration spectrum*, which depends on the symmetry [39] measures either in IR-absorption or in *Raman scattering* of light. Before analysing Raman scattering spectra of different solids we briefly consider the classical approximation of the mechanism of Raman effect [33–36].

Historically, Raman scattering denotes inelastic scattering of light by molecular vibrations or by optical phonons in solids. In a macroscopic picture, the Raman effect in crystals is explained in terms of the modulation of polarisability by the quasi particle under consideration. The assumption that the polarisation depends linearly upon the electric field strength [37] is a good approximation and is invariably used when discussing the scattering of light by crystal excited by lasers. However, the approximation is not valid for large strengths such as can be obtained from pulsed lasers [38]. The polarisation may then be expressed as

$$P = \alpha \mathrm{E} + \frac{1}{2}\beta \mathrm{E}^2 + \frac{1}{6}\gamma \mathrm{E}^3 + \frac{1}{24}\delta \mathrm{E}^4 + \ldots\ldots\ldots, \tag{4.20}$$

where β, the first *hyperpolarizability* coefficient, plays an important role for large values of E, since it is responsible for the phenomenon of optical harmonic generation using Q-switched lasers. Isolated atoms have $\beta = 0$, since, like μ the dipole moment, it arises from interactions between atoms. A simplified theory of Rayleigh scattering, the Raman effect, harmonic generation and hyper Raman scattering are obtained by setting ([38])

$$\mathrm{E} = \mathrm{E}_0 \cos \omega_0 t, \tag{4.21}$$

$$\alpha = \alpha_0 + \left(\frac{\partial \alpha}{\partial \mathrm{Q}}\right) \mathrm{Q}, \tag{4.22}$$

$$\beta = \beta_0 + \left(\frac{\partial \beta}{\partial \mathrm{Q}}\right) \mathrm{Q}, \tag{4.23}$$

$$\mathrm{Q} = \mathrm{Q}_0 \cdot \cos \omega_v t. \tag{4.24}$$

Here Q is a normal coordinate, ω_v is the corresponding vibrational frequency and ω_0 is the laser frequency. After that we have

$$\begin{aligned} \mathrm{P} = {} & \alpha_0 \mathrm{E}_0 \cos \omega_0 t + \left(\frac{\partial \alpha}{\partial \mathrm{Q}}\right) \mathrm{Q}_0 \mathrm{E}_0 \cos \omega_0 t \cos \omega_v t \\ & + \frac{1}{2}\beta_0 \mathrm{E}_0^2 \cos^2 \omega_0 t + \frac{1}{2}\left(\frac{\partial \beta}{\partial \mathrm{Q}}\right) \mathrm{Q}_0 \mathrm{E}_0^2 \cos^2 \omega_0 t \cos \omega_v t. \end{aligned} \tag{4.25}$$

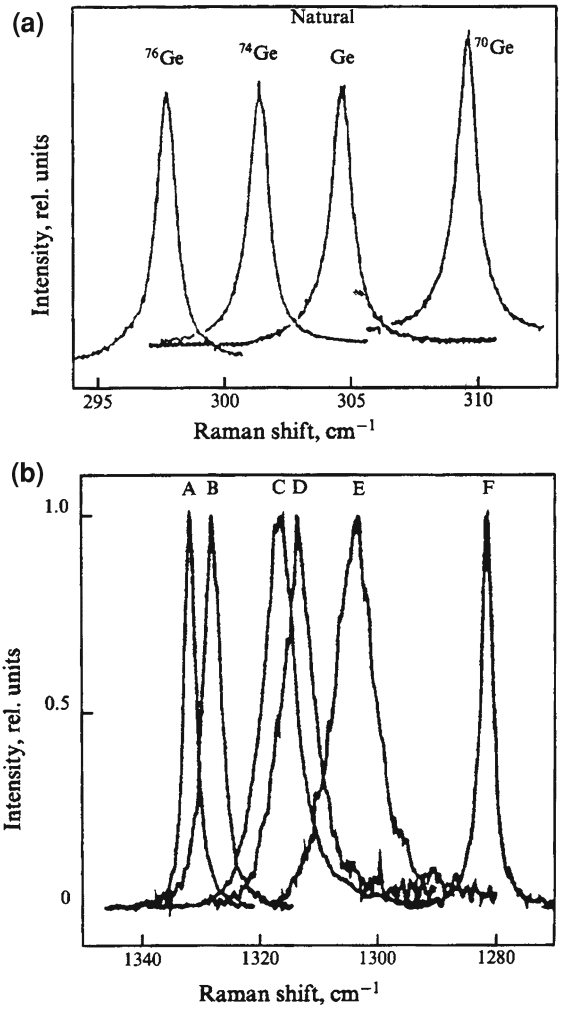

Fig. 4.5 **a** First-order Raman scattering spectra Ge with different isotope contents [40], and **b** first-order Raman scattering in isotopically mixed diamond crystals $^{12}C_x^{13}C_{1-x}$. The peaks *A*, *B*, *C*, *D*, *E* and *F* correspond to $x = 0.989, 0.90, 0.60, 0.50, 0.30$ and 0.001 [44]

Then, after small algebra, we obtain

$$\begin{aligned} P = \alpha_0 E_0 \cos\omega_0 t + \left(\frac{\partial\alpha}{\partial Q}\right) Q_0 E_0 \Big[\cos(\omega_0 - \omega_v)t + \cos(\omega_0 + \omega_v)t\Big] \\ + \frac{1}{4}\beta_0 E_0^2 + \frac{\beta_0}{4} E_0^2 \cos 2\omega_0 t + \frac{\partial\beta}{\partial Q} E_0^2 Q_0 \cos\omega_v t \\ + \frac{1}{2} Q_0 E_0^2 \left(\frac{\partial\beta}{\partial Q}\right) \Big[\cos(2\omega_0 + \omega_v)t + \cos(2\omega_0 - \omega_v)t\Big] \end{aligned} \tag{4.26}$$

In last relation the first term describes the Rayleigh scattering, second—Raman scattering, third—d.c. polarisation, fourth—frequency doubling and the last—hyper

Raman effect. Thus the *hyper Raman effect* is observed with large electric field strength in the vicinity of twice the frequency of the exciting line with separations corresponding to the vibrational frequencies. α and β are actually tensors and β components $\beta_{\alpha\beta\gamma}$ which are symmetrical suffixes [39].

Semiconducting crystals (C, Si, Ge, α-Sn) with diamond-type structure present ideal objects for studying the isotope effect by the Raman light-scattering method. At present time this is facilitated by the availability of high-quality crystals grown from isotopically enriched materials (see, e.g. [40] and references therein). In this part our understanding of first-order Raman light scattering spectra in isotopically mixed elementary and compound (CuCl, GaN, GaAs) semiconductors having a zinc blende structure is described. Isotope effect in light scattering spectra in Ge crystals was first investigated by Agekyan et al. [41]. A more detailed study of Raman light scattering spectra in isotopically mixed Ge crystals has been performed by Cardona et al. [40].

It is known that materials having a *diamond* structure are characterised by the triply degenerate phonon states in the Γ point of the Brillouin zone ($\overrightarrow{k} = 0$). These phonons are active in the Raman scattering spectra, but not in the IR absorption one [42]. Figure 4.5a demonstrates the dependence of the shape and position of the first-order line of optical phonons in germanium crystal on the isotope composition at liquid nitrogen temperature (LNT) [43]. The coordinate of the centre of the scattering line is proportional to the square root of the reduced mass of the unit cell, i.e. $\sqrt{\mathrm{M}}$. It is precisely this dependence that is expected in the harmonic approximation. An additional frequency shift of the line is observed for the natural and enriched germanium specimens and is equal, as shown in Ref. [40] to 0.34 ± 0.04 and $1.06 \pm 0.04\,\mathrm{cm}^{-1}$, respectively (see, e.g. Fig. 7 in Chap. 4 of Ref. [45]).

First-order Raman light-scattering spectrum in diamond crystals also includes one line with maximum at $\omega_{\mathrm{LTO}}(\Gamma) = 1332.5\,\mathrm{cm}^{-1}$. In Fig. 4.5b the first-order scattering spectrum in diamond crystals with different isotope concentration is shown [44]. As shown below, the maximum and the width of the first-order scattering line in isotopically—mixed diamond crystals are nonlinearly dependent on the concentration of isotopes x. The maximum shift of this line is $52.3\,\mathrm{cm}^{-1}$, corresponding to the two limiting values of $x = 0$ and $x = 1$. Analogous structures of first-order light scattering spectra and their dependence on isotope composition has by now been observed many times, not only in elementary Si, and α-Sn, but also in compound CuCl and GaN semiconductors (for more details see reviews [31, 40]). Already a shortlist of data shows a large dependence of the structure of first-order light-scattering spectra in diamond as compared to other crystals (Si, Ge). This is the subject of detailed discussion in [46].

Second-order Raman spectra in natural and isotopically mixed diamond have been studied by Chrenko [47] and Hass et al. [48]. Second-order Raman spectra in a number of synthetic diamond crystals with different isotope compositions shown in Fig. 4.6 are measured with resolution ($\sim 4\,\mathrm{cm}^{-1}$) worse than for first-order scattering spectra. The authors of the cited work explain this fact by the weak signal in the measurement of Second-order Raman scattering spectra. It is appropriate to note

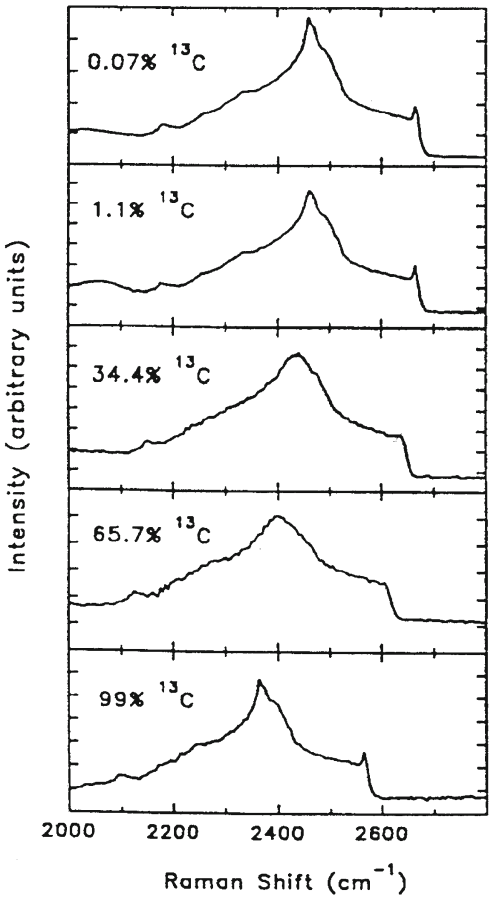

Fig. 4.6 Second-order Raman scattering spectra in synthetic diamond with different isotope concentration at room temperature [48]

that the results obtained in [48] for natural diamond ($C_{13_C} = 1.1\%$), agree well with the preceding comprehensive studies of Raman light-scattering spectra in natural diamond [49]. As is clearly seen from Fig. 4.6 the structure of Second-order light scattering "follows" the concentration of the ^{13}C isotope. It is necessary to add that in the paper by Chrenko [47] one observes a distinct small narrow peak above the high-frequency edge of LO phonons and the concentration of ^{13}C $x = 68\%$. Note in passing that Second-order spectra in isotopically mixed diamond crystals were measured in the work by Chrenko [47] with a better resolution than the spectra shown in Fig. 4.6. Second-order Raman light scattering spectra and IR absorption spectra in crystals of natural and isotopically enriched ^{70}Ge can be found in [31].

A comprehensive interpretation of the whole structure of Second-order Raman light-scattering spectra in pure LiH (LiD) crystals is given in [10, 46, 50]. Leaving this question, let us now analyse the behavior of the highest frequency peak after the substitution of hydrogen for *deuterium* [51].

Absorption behavior of an IR—active phonon in mixed crystals with a change in the concentrations of the components can be classified into two main types: one and two-mode (the review [52]). *Single-mode behavior* means that one always has a band in the spectrum with a maximum gradually drifting from one endpoint to another. *Two-mode behavior* is defined by the presence, in the spectrum, of two bands characteristic of each components leading not only to changes in the frequencies of their maxima, but mainly to a redistribution of their intensities. In principle, one and the same system can show different types of behavior at opposite ends [53]. The described classification is qualitative and is rarely realised in its pure form. The most important necessary condition for the two-mode behavior of phonons (as well as of electrons [54]) is considered to be the appearance of the *localised vibration* in the localised defect limit. In the review [52] a simple qualitative criterion for determining the type of the IR absorption behavior in crystals with an NaCl structure type has been proposed [54]. Since the square of the TO (Γ) phonon frequency is proportional to the reduced mass of the unit cell M, the shift caused by the defect is equal to

$$\Delta = \omega_{\mathrm{TO}}^2 \left(1 - \frac{\overline{M}}{\overline{M'}} \right). \tag{4.27}$$

This quantity is compared in [52] with the width of the optical band of phonons which, neglecting acoustical branches and using the parabolic dispersion approximation, is written as

$$\mathrm{W} = \omega_{\mathrm{TO}}^2 \left(\frac{\varepsilon_0 - \varepsilon_\infty}{\varepsilon_0 + \varepsilon_\infty} \right). \tag{4.28}$$

A local or gap vibration appears, provided the condition $|\Delta| > (1/2)W$ is fulfilled. As mentioned, however, in [55] in order for the two peaks to exist up to concentrations on the order of $\sim$0.5, a stronger condition $|\Delta| > W$ has to met. Substituting the numerical values from Tables 1 and 2 of [46] into formulas (4.27) and (4.28) shows that for LiH (LiD) there holds (since $\Delta = 0.44\omega_{\mathrm{TO}}^2$ and $W = 0.58\omega_{\mathrm{TO}}^2$) the following relation:

$$|\Delta| > (1/2)W. \tag{4.29}$$

Thereby, it follows that at small concentrations the local *vibration* should be observed. This conclusion is in perfect agreement with earlier described experimental data [50]. As to the second theoretical relation $\Delta > \mathrm{W}$, one can see from the above discussion that for LiH (LiD) crystals the opposite relation, i.e. $\mathrm{W} > \Delta$, is observed [55].

Following the results of [56], in Fig. 4.7 we show the Second-order Raman scattering spectra in mixed $\mathrm{LiH}_x\mathrm{D}_{1-x}$ crystals at room temperature. In addition to what has been said on Raman scattering spectra at high concentration [56], we note that as the concentration grows further ($x > 0.15$) one observes in the spectra a decreasing intensity in the maximum of 2LO (Γ) phonons in LiD crystal with a simultaneous growth in intensity of the highest frequency peak in mixed $\mathrm{LiH}_x\mathrm{D}_{1-x}$ crystals. The

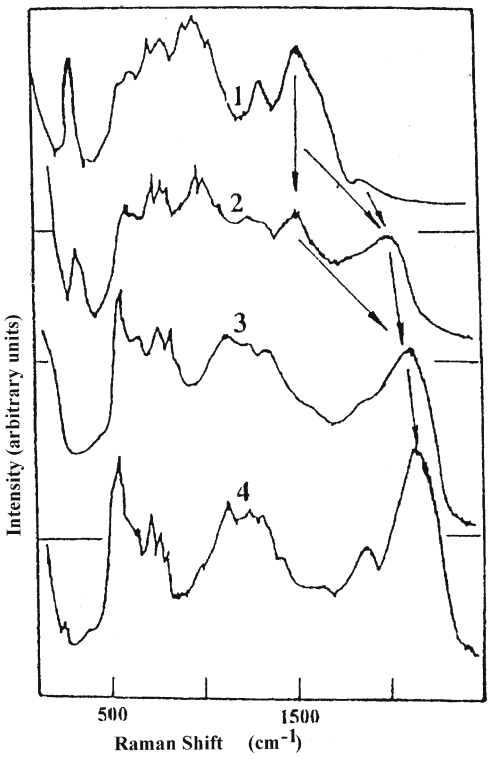

Fig. 4.7 Second-order Raman scattering spectra in the isotopically mixed crystals LiH_xD_{1-x} at room temperature: *1*-$x = 0$; *2*-0.42; *3*-0.76; *4*-1. The arrows point out a shift of LO(Γ) phonons in the mixed crystals [50]

nature of the latter is in the renormalisation of LO(Γ) vibrations in mixed crystal [55]. Comparison of the structure of *Raman scattering* spectra (curves 1 and 2 in Fig. 4.7) allows us, therefore, to conclude that in the concentration range of $0.1 < x < 0.45$ the Raman scattering spectra simultaneously contain peaks of the LO(Γ) phonon of pure LiD and the LO(Γ) phonon of the mixed LiH_xD_{1-x} crystal. For further concentration growth ($x > 0.45$) one could mention two effects in the Raman scattering spectra of mixed crystals. The first is related to an essential reconstruction of the acoustooptical part of the spectrum. This straightforwardly follows from a comparison of the structure of curves 1–3 in Fig. 4.7. The second effect originates from a further shift of the highest frequency peak towards still higher frequencies, related to the excitation of LO(Γ) phonons. The limit of this shift is the spectral location of the highest frequency peak in LiH. Finishing our description of the Raman scattering spectra, it is necessary to note that a resonance intensity growth of the highest frequency peak is observed at $x > 0.15$ in all mixed crystals (for more details see [51]).

One more reason for the discrepancy between the theory and the results of the experiment may be connected with not taking into account in theory the change of the *force-constant* at the isotope substitution of the smaller in size D by H ion [57].

We should stress once more that among the various possible *isotope substitution*, by far the most important in vibrational spectroscopy is the substitution of hydrogen by *deuterium*. As is well known, in the limit of the Born–Oppenheimer approximation the force-constant calculated at the minimum of the total energy depends upon the electronic structure and not upon the mass of the atoms. It is usually assumed that the theoretical values of the phonon frequencies depend upon the force-constants determined at the minimum of the adiabatic potential energy surface. This leads to a theoretical ratio $\omega\,(\mathrm{H})/\omega\,(\mathrm{D})$ of the phonon frequencies that always exceed the experimental data. Very often anharmonicity has been proposed to be responsible for lower value of this ratio. In isotope effect two different species of the same atom will have different vibrational frequencies only because of the difference in isotopic masses. The ratio p of the optical phonon frequencies for LiH and LiD crystals is given in *harmonic approximation* by:

$$p = \frac{\omega\,(\mathrm{H})}{\omega(\mathrm{D})} = \sqrt{\frac{\mathrm{M(LiD)}}{\mathrm{M(LiH)}}} \simeq \sqrt{2} \tag{4.30}$$

while the experimental value (which includes anharmonic effects) is $1.396 \div 1.288$ (see Table 1 in Ref. [57]). In this table there are the experimental and theoretical values of p according to formula (4.30), as well as the deviation $\delta = \frac{P_{\mathrm{Theory}} - p_{\mathrm{exp}}}{p_{\mathrm{theory}}}$ of these values from theoretical ones. Using the least squares method it was found the empirical formula of $\ln(\delta\%) \sim f(\ln[\frac{\partial \mathrm{E}}{\partial \mathrm{M}}])$ which is depicted in Fig. 4.8. As can be seen the indicated dependence has in the first approximation a linear character:

$$\ln(\delta\%) = -7.5 + 2\ln\left(\frac{\partial \mathrm{E}}{\partial \mathrm{M}}\right). \tag{4.31}$$

From the results of Fig. 4.8, it can be concluded that only hydrogen compounds (and its isotope analog-*deuterium*) need to take into account the *force-constant* changes in isotope effect. It is also seen that for semiconductor compounds (in Fig. 4.8-points, which is below Ox line) the isotope effect has only the changes of the *isotope mass* (for details see [57]).

Thus, the experimental results presented in this section provide evidence of, first, strong scattering potential (most importantly, for optical phonons) and second, the insufficiency of CPA model for a consistent description of these results [48].

4.2.2 Electronic Excitations

Isotopic substitution only affects the wavefunction of phonons; therefore, the energy values of electron levels in the Schrödinger equation ought to have remained the same. This, however, is not so, since isotopic substitution modifies not only the phonon spectrum, but also the constant of *electron-phonon interaction* (see above). It is for

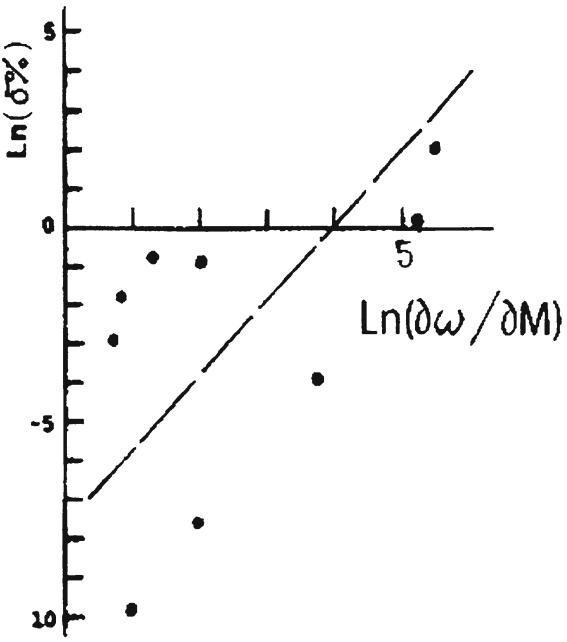

Fig. 4.8 The dependence of $\ln(\delta\%) \sim f[\ln(\frac{\partial\omega}{\partial M})]$: points are experimental values and continuous line-calculation on the formula (4.31) [57]

this reason that the energy values of purely electron transition in *molecules* of hydride and deuteride are found to be different [58]. This effect is even more prominent when we are dealing with a solid [60]. Intercomparison of absorption spectra for thin films of LiH and LiD at room temperature revealed that the longwave maximum (as we know now, the exciton peak [59]) moves 64.5 meV towards the shorter wavelengths when H is replaced with D. For obvious reasons this fundamental result could not then receive consistent and comprehensive interpretation, which does not belittle its importance even today. As will be shown below, this effect becomes even more pronounced at low temperatures [31].

The mirror *reflection spectra* of mixed and pure LiD crystals cleaved in liquid helium are presented in Fig. 4.9. For comparison, in the same diagram we have also plotted the reflection spectrum of LiH crystals with a clean surface. All spectra have been measured with the same apparatus under the same conditions. As the *deuterium* concentration increases, the long-wave maximum broadens and shifts towards the shorter wavelengths. As can clearly be seen in Fig. 4.9, all spectra exhibit a similar long-wave structure. This circumstance allows us to attribute this structure to the excitation of the ground (Is) and the first excited (2s) exciton states. The energy values of exciton maxima for pure and mixed crystals at 2 K are presented in Table 4.2. The binding energies of *excitons* E_b, calculated by the hydrogen-like formula, and the energies of interband transitions E_g are also given in Table 4.2.

Going back to Fig. 4.9, it is hard to miss the growth of Δ_{12}, [61], which in the hydrogen-like model causes an increase of the exciton Rydberg with the replacement

Table 4.2 Values of the energy of maxima (in meV) in exciton reflection spectra of pure and mixed crystals at 2 K, and energies of exciton binding E_b, band-to-band transitions E_g (after [5])

Energy, meV	LiH	$LiH_{0.82}D_{0.18}$	$LiH_{0.40}D_{0.60}$	LiD	^{6}LiH (78 K)
E_{1s}	4950	4967	5003	5043	4939
E_{2s}	4982	5001	5039	5082	4970
E_b	42	45	48	52	41
E_g	4992	5012	5051	5095	4980

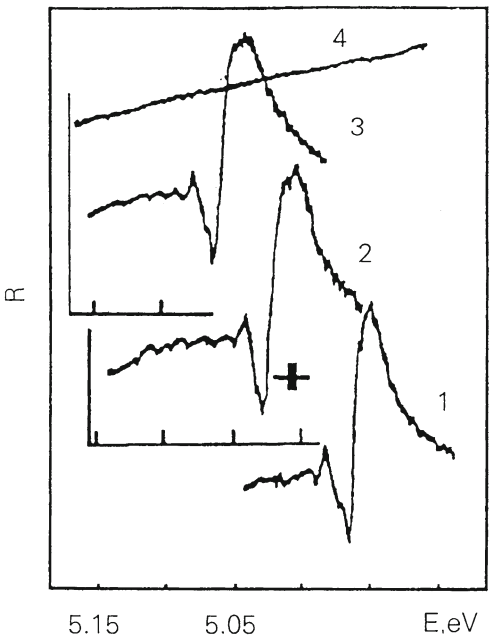

Fig. 4.9 Mirror reflection spectra of crystals: *1*-LiH; *2*-LiH_xD_{1-x}; *3*-LiD; at 4.2 K. *4*-source of light without crystal. Spectral resolution of the instrument is indicated on the diagram (after [61])

of*isotopes* (see Fig. 90 in [31]). When hydrogen is completely replaced with deuterium, the exciton Rydberg (in the Wannier–Mott model) increases by 20% from 40 to 50 meV, whereas E_g exhibits a 2%increase, and at $2 \div 4.2$ K is $\Delta E_g = 103$ meV. This quantity depends on the temperature, and at room temperature it is 73 meV, which agrees well enough with $\Delta E_g = 64.5$ meV as found in the paper by Kapustinsky et al. Isotopic substitution of the light isotope (^{32}S) by the heavy one (^{34}S) in CdS crystals [62] reduces the exciton Rydberg, which was attributed to the tentative contribution from the adjacent electron bands (see also [10] and references therein), which, however, are not present in LiH. The single-mode nature of exciton reflection spectra of mixed crystals LiH_xD_{1-x} agrees qualitatively with the results obtained with the virtual crystal model (Elliott et al. [52]; Onodera and Toyozawa [63]), being at the same time its extreme realisation, since the difference between ionisation potentials ($\Delta\zeta$) for this compound is zero [64]. According to the *virtual*

crystal model, $\Delta\zeta = 0$ implies that $\Delta E_g = 0$, which is in contradiction with the experimental results for LiH_xD_{1-x} crystals. The change in E_g caused by *isotopic substitution* has been observed for many broadgap and narrow-gap semiconductor compounds (see also below).

All these results are documented in Table 22 of Ref. [31], where the variation of E_g, E_b, are shown at the isotope effect. We should highlight here that the most prominent isotope effect is observed in LiH crystals, where the dependence of $E_b = f(C_H)$ is also observed and investigated. To end this section, let us note that E_g decreases by $97\,cm^{-1}$ when ^7Li is replaced with ^6Li.

Further, we will briefly discuss the variation of the electronic gap (E_g) of semiconducting crystals with its isotopic composition. The last time the whole raw semiconducting crystals were grown. These crystals are *diamond*, *copper halides*, *germanium*, *silicon*, CdS and GaAs. All numerated crystals show the dependence of the electronic gap on the *isotope masses* (see, reviews [31, 40]).

Before we complete the analysis of these results we should note that before these investigations, studies were carried out on the isotopic effect on exciton states for a whole range of crystals by Kreingol'd et al. [65]. First, the following are the classic crystals Cu_2O [65, 66] with the substitution $^{16}O \rightarrow {}^{18}O$ and $^{63}Cu \rightarrow {}^{65}Cu$. Moreover, there have been some detailed investigations of the isotopic effect on ZnO crystals, where E_g was seen to increase by $55\,cm^{-1}$ ($^{16}O \rightarrow {}^{18}O$) and $12\,cm^{-1}$ (at $^{64}Zn \rightarrow {}^{68}Zn$) [67, 68]. In [62] it was shown that the substitution of a heavy ^{34}S isotope for a light ^{32}S *isotope* in CdS crystals resulted in a decrease in the exciton Rydberg constant (E_b), which was explained tentatively by the contribution from the nearest electron energy bands, which however are absent in LiH crystals (for details see [10]).

More detailed investigations of the exciton reflectance spectrum in CdS crystals were done by Zhang et al. [69]. Zhang et al. studied only the effects of Cd substitutions, and were able to explain the observed shifts in the band gap energies, together with the overall temperature dependence of the band gap energies in terms of a *two-oscillator model* provided that they interpreted the energy shifts of the bound excitons and $n = 1$ polaritons as a function of average S mass reported as was noted above, earlier by Kreingol'd et al. [62] as shifts in the band gap energies. However, Kreingol'd et al. [62] had interpreted these shifts as resulting from isotopic shifts of the free exciton binding energies (see, also [61]), and not the band gap energies, based on their observation of different energy shifts of features which they identified as the $n = 2$ free exciton states (for details see [62]). The observations and interpretations, according to Meyer at al. [70], presented by Kreingol'd et al. [62] are difficult to understand, since on the one hand a significant band gap shift as a function of the S mass is expected [69], whereas it is difficult to understand the origin of the relatively huge change in the free exciton binding energies which they claimed. Very recently Meyer et al. [70] reexamined the optical spectra of CdS as a function of average S mass, using samples grown with natural Cd and either natural S (~95% ^{32}S), or highly enriched (99% ^{34}S). The authors observed shifts of the bound excitons and the $n = 1$ free exciton edges consistent with those reported by Kreingol'd et al. [62], but, contrary to their results, Meyer et al. observed essentially identical shifts of the

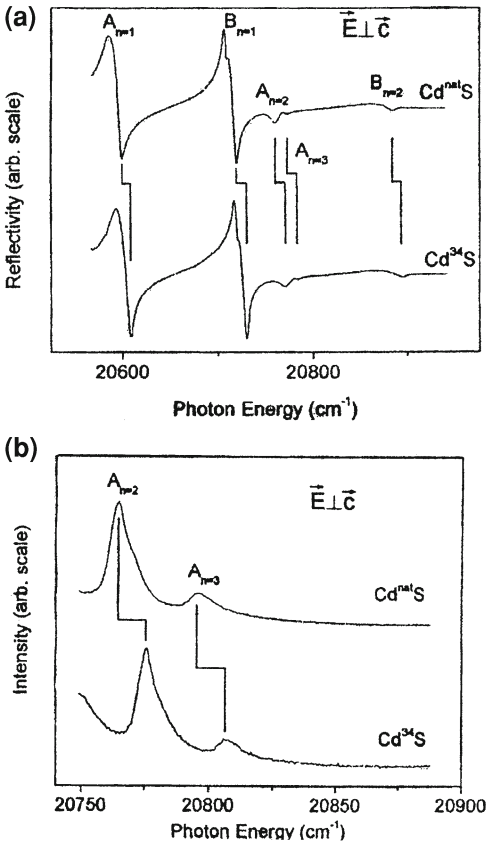

Fig. 4.10 **a** Reflection spectra in the A and B excitonic polaritons region of $Cd^{nat}S$ and $Cd^{34}S$ at 1.3 K with incident light in the $\vec{E} \perp \vec{C}$. The broken vertical lines connecting peaks indicate measured enrgy shifts reported in Table 4.3. In this polarisation, the $n = 2$ and 3 excited states of the A exciton, and the $n = 2$ excited state of the B exciton, can be observed. **b** Polarised photoluminescence spectra in the region of the $A_{n=2}$ and $A_{n=3}$ free exciton recombination lines of $Cd^{nat}S$ and $Cd\ ^{34}S$ taken at 1.3 K with the $\vec{E} \perp \vec{C}$. The broken vertical lines connecting peaks indicate measured enrgy shifts reported in Table 4.3 (after [70])

free exciton excited states, as seen in both reflection and luminescence spectroscopy. The reflectivity and photoluminescence spectra in polarised light ($\vec{E} \perp \vec{C}$) over the A and B exciton energy regions for the two samples are depicted in Fig. 4.10. For the $\vec{E} \perp \vec{C}$ polarisation used in Fig. 4.10 both A and B excitons have allowed transitions, and therefore reflectivity signatures. Figure 4.10 also reveals both reflectivity signatures of the $n = 2$ and 3 states of the A exciton as well that of the $n = 2$ state of the B exciton.

Meyer et al. summarised the energy differences $\Delta E = E(Cd^{34}S) - E(Cd^{nat}S)$, of a large number of bound exciton and free exciton transitions, measured using *photoluminescence*, *absorption* and *reflectivity spectroscopy*, in CdS made from natural S ($Cd^{nat}S$, 95% ^{32}S) and from highly isotopically enriched ^{34}S ($Cd^{34}S$, 99% ^{34}S) (see Table 4.3). As we can see, all of the observed shifts are consistent with a single value, $10.8 \pm 0.2\,cm^{-1}$. Several of the donorbound exciton photoluminescence transitions, which in [70] can be measured with high accuracy, reveal shifts which differ from each other by more than the relevant uncertainties, although all agree

Table 4.3 The energy shifts of all of the transitions studied in [70] are given in terms of the $Cd^{34}S$ minus the $Cd^{nat}S$ energy, ΔE

Transition	Method	ΔE (cm^{-1})
I_2	PL	10.6 ± 0.1
I_2^z	PL	11.1 ± 0.1
I_2^a	PL	10.6 ± 0.1
$A_{n=1}$ (Γ_6)	A$\parallel$	10.8 ± 0.2
$A_{n=1}$ (Γ_5^L)	PL	11.0 ± 0.2
$A_{n=1}$ (Γ_5^L)	R$\perp$	10.9 ± 0.2
$A_{n=2}$	PL$\parallel$	11.3 ± 0.4
$A_{n=2}$	PL$\perp$	11.1 ± 0.4
$A_{n=2}$	R$\perp$	10.2 ± 0.5
$A_{n=3}$	PL$\parallel$	11.8 ± 1.1
$A_{n=3}$	PL$\perp$	10.9 ± 0.6
$A_{n=3}$	R$\perp$	10.7 ± 0.6
$B_{n=1}(\Gamma_1)$	R$\parallel$	10.9 ± 0.3
$B_{n=1}(\Gamma_5^L + \Gamma_5^T)$	R$\perp$	10.6 ± 0.4
$B_{n=2}$	R$\parallel$	9.4 ± 1.2
$B_{n=2}$	R$\perp$	9.8 ± 1.2
$C_{n=1}(\Gamma_1)$	R$\parallel$	15 ± 6
$C_{n=1}(\Gamma_5)$	R$\perp$	14 ± 5

The methods used were photoluminescence spectroscopy (*PL) and reflection spectroscopy (R). For measurements made using polarised light, the $\parallel$ or $\perp$ specifies the orientation of the E vector versus the c axis

with the $10.8 \pm 0.2\,cm^{-1}$ average shift. These small differences in the shift energies for donor bound exciton transitions may reflect a small isotopic dependence of the donor binding energy in CdS. This value of $10.8 \pm 0.2\,cm^{-1}$ shift agrees well with the value of $11.8\,cm^{-1}$ reported early by Kreingol'd et al. [62] for the $B_{n=1}$ transition, particularly when one takes into account the fact that enriched ^{32}S was used in that earlier study, whereas Meyer et al. have used natural S in place of an isotopically enriched $Cd^{32}S$.

The authors of [70] conclude that all of the observed shifts (see Table 4.3) arise predominantly from an *isotopic dependence* of the band gap energies, and that the contribution from any isotopic dependence of the free exciton binding energies is much smaller. On the basis of the observed temperature dependencies of the excitonic transitions energies, together with a simple two-oscillator model, Zhang et al. [69] earlier calculated such a difference, predicting a shift with the S isotopic mass of $950\,\mu eV$/amu for the A exciton and $724\,\mu eV$/amu for the B exciton. Reflectivity and photoluminescence study of $^{nat}Cd^{32}S$ and $^{nat}Cd^{34}S$ performed by Kreingol'd et al. [62] shows that for anion isotope substitution the ground state ($n = 1$) energies of both A and B excitons have a positive energy shift with rate of $\partial E/\partial M_S = 740\,\mu eV$/amu. Results of Meyer et al. [70] are consistent with a shift of $\sim 710\,\mu eV$/amu for both A and B excitons. Finally, it is interesting to note that the shift of the exciton energies

with Cd mass is 56 μeV/amu [69], an order of magnitude less than found for the S mass.

The present knowledge of the electronic band structure of Si stems from experimental observation of electronic transitions in transmission, reflectivity, or cyclotron resonance, on the one hand, and theoretical calculations, e.g. those based on pseudopotential or $\overrightarrow{k} \times \overrightarrow{p}$ methods (for details see [71–77] and references therein). In this manner it has been established that the fundamental, indirect band gap of Si occurs between the Γ_8^+ valence band maximum and the Δ_0 conduction band minima along (100).

Recently, Lastras-Martinez et al. [73] performed ellipsometric measurements on *isotopically enriched* ^{28}Si and ^{30}Si and deduced the isotopic dependence of E_1 from the analysis of the data in reciprocal (Fourier inverse) space. However, these measurements did not resolve [67] the nearly degenerate E_0' and E_1 transitions and the isotopic shift was assigned solely to the stronger E_1 transitions (see, however, Fig. 4.11). We should add that in [75–77] very recently was studied the dependence of indirect band gap in Si on the isotopic mass. Photoluminescence and wavelength-modulated transmission spectra displaying phonon assisted indirect excitonic transitions in isotopically enriched ^{28}Si, ^{29}Si, ^{30}Si as well as in natural Si have yielded the isotopic gap E_{gx} which equals 1213.8 ± 1.2 meV. This is purely an electronic value in the absence of electron–phonon interaction and volume changes associated with anharmonicity (for details see [75–77] and below).

Returning to Fig. 4.11, we can see that the spectrum contains two characteric signatures, attributed to the excitonic transitions across the E_0' and E_1 gaps. Isotopic dependence of the E_0' and E_1 is displayed in Fig. 4.11, where the photomodulated reflectivity spectra of ^{28}Si, ^{29} Si, and ^{30}Si are shown for the spectral range $3.3 \leq E \leq 3.58$ eV. The E_0' and E_1 excitonic band gaps determined in paper [75–77] from the line-shape analysis. Linear least-squares fit yielded the corresponding isotopic dependences $E_0' = (3.4468 - 0.3378 M^{-1/2})$ eV and $E_1 = (3.6120 - 0.6821 M^{-1/2})$ eV. In conclusion, we should note that the spin-orbit interaction depends on Ge in contrast to that in Si [75–77].

As is well known, the fundamental energy gap in *silicon*, *germanium* and *diamond* is indirect (see, e.g. [72] and Fig. 4.3). While the conduction band minima in Si and diamond are located at the Δ point along $\langle 100 \rangle$, with Δ_6 symmetry, those of germanium with L_6^+ symmetry occur at the $\langle 111 \rangle$ zone boundaries [75–77]. The onset of the absorption edge corresponds to optical transition from the Γ_8^+ valence band maximum to the L_6^+ conduction band minima in Ge, and the Δ_6 in Si and diamond; for *wavector conservation*, these indirect transitions require the emission or absorption of the relevant phonons. In Si and C, transverse acoustic (TA), longitudinal acoustic (LA), transverse optic (TO) or longitudinal optic (LO) phonons of Δ symmetry must be simultaneously emitted or absorbed. In Ge (see, also above), the wavector conserving phonons are TA, LA, TO or LO phonons with L symmetry. At low temperatures, these indirect transitions are assisted by phonon emission. In this case we should expect at low temperatures four excitonic derivative signatures at photon energies $E_{gx} + \hbar\omega_{\overrightarrow{q},j}$ in modulated transmission experiments and in

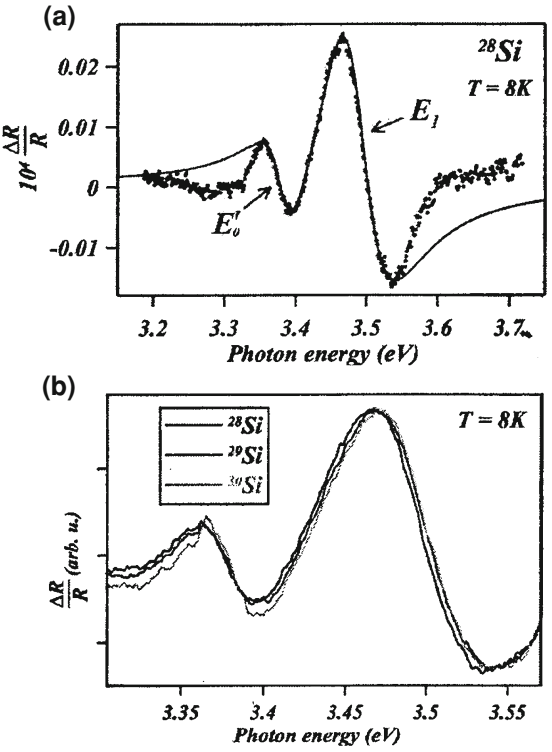

Fig. 4.11 (**a**) Signatures of the E_0' and E_1 excitonic band gaps of ^{28}Si observed (dots) in photomodulated reflectivity. The solid line is a theoretical fit using the excitonic line shape. (**b**) Photomodulated reflectivity spectra of isotopically enriched Si exhibiting isotopic shifts of the E_0' and E_1 gaps (after [75–77])

photoluminescence at the photon energies $E_{gx} - \hbar\omega_{\vec{q},j}$. Here E_{gx} is the excitonic band gap and j corresponds to a wave vector preserving phonon (see, also formula (4.13)). In Fig. 4.12a the photoluminescence and wavelength—modulated spectra of ^{30}Si M = 2.81 amu) are displayed; the labels $n = 1$ and 2 designate the ground and the first excited states of the indirect TA and and TO excitons. From the energies of the photoluminescence and wavelength-modulated excitonic signatures in all isotopic specimens [75–77] cited authors deduce E_{gx} as well as the energies of the participating TO, LO and TA phonons, shown in Fig. 4.12b as function of $M^{-1/2}$. The excitonic band gap data are fitted well with expression $E_{gx}(M) = E_{gx}(\infty) - CM^{-1/2}$, yielding $E_{gx}(\infty) = (1213.8 \pm 1.2)$ meV and $C = (313.7 \pm 5.3)$ meV/amu. A linear fit in M can be made over small range of available masses (see, Fig. 4.12b) with a slope $(\partial E_{gx}/\partial M)_{P,T}\, 1.01 \pm 0.04$ meV/amu, which agrees with the results of bound exciton photoluminescence of Karaiskaj et al. [74]. The experiments in [75–77] also indicate that separation of the $n = 2$ and $n = 1$ excitons is isotope mass independent, implying, according to these authors, the excitonic binding energy is independent on isotope mass within experimental error. In concluding this part we should note that recent high-resolution spectroscopic studies of excitonic and impurity transition in high-quality samples of isotopically enriched Si have discovered the broadening of bound exciton emission (absorption) lines connected with isotope-induced disorder

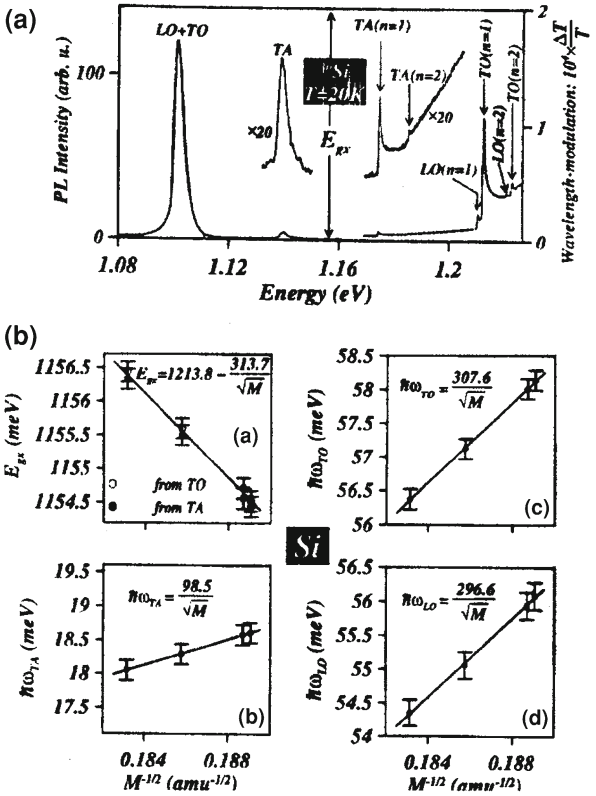

Fig. 4.12 **a** Photoluminescence (PL) and wavelength-modulated transmission (WMT) spectra of isotopically enriched ^{30}Si recorded at 20 K; **b** The excitonic indirect band gap and the associated phonon energies as a function of M (after [75–77])

as well as the dependence of their binding energy on the *isotope mass* [74–77]. The last effect was earlier observed on the bound excitons in diamond [78, 79], and earlier on the *free excitons* [80] in LiH_xD_{1-x} mixed crystals (see, e.g. [81] and references therein).

4.3 Phonon Spectra of Solids: Indicator of their Isotope Purity

4.3.1 Thermal Conductivity

In *insulators* and *semiconductors* (at $T < \theta_D$) the *thermal conduction* is effected by phonons, predominantly acoustic ones [82]. Thermal conductivity of crystals has been the subject of many experimental and theoretical studies (see, e.g. reviews and

monographs [9, 82–88]). The first experimental results (see, e.g. [91]) have already pointed out the existence of maximum of the thermal conductivity coefficient k_m at about $T \approx 0.05\,\theta_D$, where θ_D is the Debye temperature. The growth of k at low temperatures has been related to phonon scattering due to Umklapp (U-)—type processes [31, 87]. In the vicinity of k_m thermal conductivity is quite sensitive to impurities and defects in the specimen. The scattering of phonons dynamic isotope disorder is independent of temperature and lattice anharmonicity. The role of *isotopes* as an additional channel of phonon scattering and their influence on thermal conductivity were first theoretically studied by Pomeranchuk [89] in 1942, and were experimentally studied using Ge in 1958 [90]. According to the results of the latter reference, for a Ge specimen (having 95.8% ^{74}Ge), a 3-fold growth of the thermal conductivity coefficient as compared to the specimen of germanium with natural isotope composition was observed. Later, the influence of isotopes on *diamond* thermal conductivity was studied many times [91–93].

It is generally assumed ([31]) that at not too high temperatures, the dominant interact among phonons involve three phonons. In a "normal" (N-) process the *wave vectors* $\vec{q}$ of the phonons are conserved and such a process tends to restore a disturbed phonon distribution to one which can be described as a displaced Planck distribution (see, e.g. Fig. 5.2 in [83]) which is unaffected by N-processes and corresponds to a heat flow. By themselves, therefore, N-processes would not lead to a thermal resistance.

In Umklapp (U-)—process [87] the wave vectors are not conserved and, as in other resistive processes, they tend to restore a disturbed phonon distribution to the equilibrium Planck distribution which corresponds to zero heat flow, and thus lead to a finite conductivity (for more details, see, review [31]). The Debye expression [94] for the conductivity k(T) is derived from an adoptional of the simple kinetic theory

$$\mathrm{k(T)} = \frac{1}{3}\left\langle \mathrm{v_{ph}} \right\rangle \ell_{\mathrm{ph}}(\mathrm{T}) C_p(\mathrm{T}), \tag{4.32}$$

where $\left\langle \mathrm{v_{ph}} \right\rangle$ is an average phonon velocity, $\ell_{\mathrm{ph}}(\mathrm{T})$ their mean free path and $\mathrm{C}_p(\mathrm{T})$ the corresponding specific heat (for diamond see [95]). A theory of k(T) requires basically the calculation of

$$\ell_{\mathrm{ph}}(\mathrm{T}) = \tau_{\mathrm{ph}}(\mathrm{T})\left\langle \mathrm{v_{ph}} \right\rangle \tag{4.33}$$

a rather formidable task since several scattering mechanisms (*normal-, u- processes*, boundary of sample, isotope scattering) [96] contribute to determining the mean free path. In formula (4.33) $\tau_{\mathrm{ph}}(\mathrm{T})$ is the phonon relaxation time; the simplest of these mechanisms, and the one that can be varied for a given material of the acoustic phonons by isotopic mass fluctuations. This scattering is equivalent to Rayleigh scattering (of photons) at point defect. Within *Debye approximation*, we will have

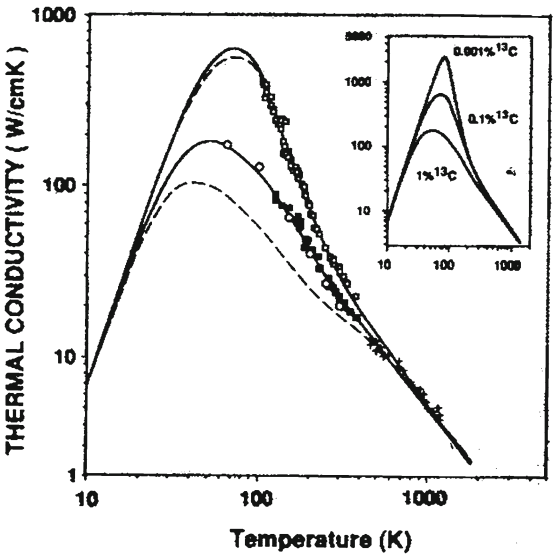

Fig. 4.13 Thermal conductivity of natural abundance (1.1% of ^{13}C) diamons (*lower squares*), isotopically enriched (0.1% ^{13}C) diamond (*upper squares*), together with the low-temperaturw data (*circles*) and high-temperature data. The solid curves are the result of fitting the Callaway theory [86] to the data, using tha same set fitting parameters. The inset shows the calculated thermal conductivity corresponding to 1, 0.1, and 0.001% ^{13}C concentration according to Callaway theory (after [93])

$$k(T) = \frac{k_B}{2\pi\nu}\left(\frac{k_B}{\hbar}\right)^3 T^3 \int_0^{\frac{\theta_D}{T}} \tau(x)\frac{x^4 e^x}{(e^x-1)^2}\mathrm{d}x. \tag{4.34}$$

In the latter expression k_B is the Boltzmann constant. Klemens [82] was the first to try to take the role of N-processes into account. Using *perturbation theory* Klemens [82] developed the following expression for the scattering rate $\tau^{-1}_{\text{isotope}}$:

$$\tau^{-1}_{\text{isotope}} = \frac{x(x-1)V_0}{4\pi\langle v_{ph}\rangle^3}\left(\frac{\Delta M}{M}\right)^2\omega^2, \tag{4.35}$$

where V_0 is a volume per atom (for diamond 5.7×10^{-24} cm^3) and ω is phonon frequency. Callaway approach [86] successfully introduces normal phonon scattering (τ_N^{-1}) and resistive scattering (τ_R^{-1}) (see formula (4.51) in [31]).

Figure 4.13 presents the results of Wei et al. [93]. The solid curves are the result of fitting the Callaway theory [86], using a single set of fitting parameter. In their paper, Wei et al. have measured a record thermal conductivity of 410 Wcm^{-1}K^{-1} at 104 K for a 99.9% ^{12}C enriched diamond. These authors predict that a 99.999% ^{12}C diamond should have a peak value of thermal conductivity exceeding 2,000 Wcm^{-1}K^{-1}, at about 80 K, assuming, of course, that it is not limited by point defect scattering mechanisms other than minority isotopes. Similar results have very recently been reported by Olson et al. [92]. We should stress that none of the currently existing theories accurately takes into account all the possible scattering processes.

Thermal conductivity studies have also been performed on very highly enriched, ultra-pure ^{70}Ge (see, reviews [31, 40]). The maximum value of $k_m = 10.5\,kWm^{-1}K^{-1}$ was observed, in the vicinity of $T = 16.5\,K$, for the ^{70}Ge specimen of 99.99% purity, which is significantly higher than the value for sapphire ($6\,kWm^{-1}K^{-1}$ around $T_m = 35\,K$) and comparable to the value of silver ($11\,kWm^{-1}K^{-1}$ near $T_m = 15.4\,K$). Comparison of experimental results shows [97] that, at its maximum (see, e.g. Fig. 6^a [46]), the thermal conductivity of the $^{70/76}$Ge (91.91%) specimen is 14 times less than that of ^{70}Ge (91.91%). An increase in k reaches, however, only 30% at $T = 300\,K$ (see, also [31, 40]).

The thermal conductivity of *monoisotopic* and *isotopically mixed specimens* of silicon crystals has been studied in [98–101]. Since the most detailed results have been obtained by the authors of [100], we restrict ourselves to their consideration. It is well known that natural silicon consists of three isotopes: ^{28}Si (∼92%), ^{29}Si (∼5%), and ^{30}Si (∼3%). The use of monoisotopic silicon (for example ^{28}Si) can substantially reduce the value of dissipated energy scattered in electronic elements made of silicon (e.g. in the memory of electronic computers [102]). The resulting studies of the thermal conductivity of monoisotopic and isotopically mixed crystals are shown in Fig. 4.14. According to the results presented in Fig. 4.14, for SI284 specimen $k = 237(8)\,Wm^{-1}K^{-1}$ at 300 K, whereas for the SINI (natural Si) specimen it is equal to $150\,Wm^{-1}K^{-1}$. This means that at 300 K the thermal conductivity of a monoisotopic ^{28}Si specimen grows, as compared to the natural silicon, by 60% (later-10%, see, erratum). At the same time, at about 20 K (in the vicinity of the maximum of the silicon thermal conductivity curve) k reaches the value of $30,000 \pm 5,000\,Wm^{-1}K^{-1}$, which is 6 times higher than the value $k = 5140\,Wm^{-1}K^{-1}$ for natural specimen (see, also [84]).

The thin solid and dashed lines in Fig. 4.14 correspond to the results of theoretical computations of thermal conductivity for monoisotopic specimen SI284 and for a specimen with natural silicon *isotope composition*. In these calculations, the model of the Ge thermal conductivity developed in [97] with modified *Debye temperature* and phonon mean free path has been used. For fitting, the authors have used the low-temperature results, where the thermal conductivity is described by the T^3 law. Calculations presented in Fig. 4.14 were performed, for the natural specimen, for free mean path it equals 5.0 mm (dashed line). For comparison, let us point out that in Ref. [98] the analogous quantity was equal to 5.7 mm, and for isotopically pure SI284 specimen the corresponding value was 14.0 mm (thin solid line). As seen from Fig. 4.14, there is agreement between theory and experiment, which has also been mentioned by the authors of [100] themselves. They have also pointed out good agreement between their experimental results and calculations made in [103], except for the domain of *U-processes*. Besides, Ruf et al. have mentioned an unsatisfactory agreement between theory and experiment in the domain of high-temperatures (300–400 K), especially for the specimen with natural isotope composition. They think that this disagreement can occur due to fundamental reasons that require further study. In particular, taking into account the fine structure of the nonequilibrium phonon distribution function could bring theoretical and experimental results much closer.

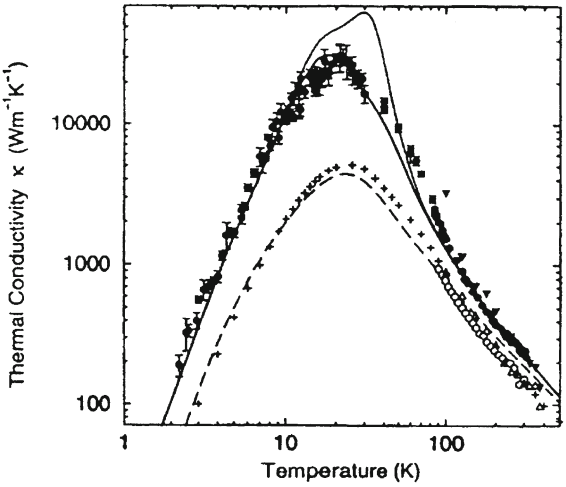

Fig. 4.14 Thermal conductivity of the highly isotopically enriched ^{28}Si sample SI284 (*filled circles*) and the natural Si reference SINI (*open circles*). The filled and open triangles are other measurements for highly isotopically enriched ^{28}Si and natural Si, respectively (from Ref. [84]); "plus" symbols denote the "standard" curve for natural Si (from [84]). The thin solid and dashed lines are the theoretical results of [98] for ^{28}Si and natural Si, respectively. The thick solid line has been calculated with the same theory using the actual mass variance g_2 of sample SI284 (see, also Table 4.4) (after [100])

Table 4.4 Comparison of the effect of isotopic scattering on the thermal conductivity of natural Ge, Si and diamond at 300 K

	% increase in k	θ	$\Gamma \times 10^{-4}$
Ge	30	376	5.80
Si	60	658	2.01
Diamond	50	1860	0.76

The % increase in k is the increase of the thermal conductivity of the nearly isotopically pure sample compared to the natural sample. The isotope is defined as $g = \sum_i f_i \left(\frac{\Delta M_i}{M}\right)^2$ (after Asen-Palmer et al. [97], Capinski et al. [99] and Ruf et al. [100])

A qualitative comparison of the influence of the isotope effect on the thermal of germanium, silicon and diamond is given in Table 4.4.

In conclusion we should remark that until recently all theories on thermal conductivity had a strongly phenomenological flavour, making use of the relaxation time approximation. In recent years, considerable progress towards an ab initio theory has been made [103, 104]. These authors used two- and three-body potentials obtained by fitting phonon dispersion relations and related the anharmonic properties with a single average Grü neisen parameter. In this manner they determined the third-order coupling coefficients for all possible three-phonon combinations. They then solved iteratively the Boltzmann equation for phonon transport without using

the relaxation-time approximation. A scattering time must, however, still be used to describe boundary scattering in the lowest temperature region. In this manner they reproduced rather well the thermal conductivities of Ge, Si and diamond and the observed isotope effects (for details see [103, 104]).

4.3.2 Isotope-Induced-Disorder Raman Scattering

The frequencies of *vibrational modes* in a solid depend on the *interatomic forces* and the atomic masses. By changing the mass of atoms by isotopic substitution the frequencies of modes are changed in a small but characteristic way that can be monitored by *Raman spectroscopy*. In isotopically pure crystals the width Γ_0 of the Raman line is determined—apart from experimental resolution—by the phonon lifetime which is governed by the spontaneous anharmonic decay into phonon of lower energy [82]. In an isotopically disordered material an additional contribution Γ_{isotope} to the linewidth comes from the elastic scattering of phonons via mass fluctuation and has been observed for many semiconductors (see, review [40] and reference therein). Line shift and line broadening are theoretically obtained as real and imaginary parts of a complex self-energy which can be calculated in the framework of a coherent potential approximation (CPA) in the case of weak phonons scattering [31]. This theory describes, for example, frequency shift and line broadening very well in isotopically disordered diamond [105], Ge [106] and α-Sn [107]. A mass *perturbation theory* of the harmonic lattice dynamics for calculating Γ_{isotope} has been developed by Tamura and applied to Ge [108], GaAs and InSb [109]. For the complex self-energy of the Raman phonon of a*semiconductor* with *diamond* structure, the Second-order term (n = 2) contains the real part [110, 31]

$$\Delta_2(\omega, x) = \frac{g_2(x)}{4}\omega\left(\frac{1}{6N_c}\right)\sum_i \omega_i \frac{\omega - \omega_i}{(\omega - \omega_i)^2 + \gamma^2} \tag{4.36}$$

and the imaginary part (see, also [108, 109])

$$\Gamma_2(\omega, x) = \frac{g_2(x)}{4}\omega\left(\frac{1}{6N_c}\right)\sum_i \omega_i \frac{\gamma}{(\omega - \omega_i)^2 + \gamma^2}. \tag{4.37}$$

In the last two formula N_c is the number of unit cells. For $\gamma \to 0$ Eq. (4.36) simplifies to a sum over δ-functions, which represents the one - phonon density of state $\rho(\omega)$ (compare to [109]),

$$\Gamma_2(\omega,x) = \Gamma_{\text{iso}} = \tau_{\text{iso}}^{-1} = \frac{\pi}{6}\omega^2 g \left|\overrightarrow{e}\right| \rho(\omega). \tag{4.38}$$

From this relation we can see, that Γ_{iso} depends on three factors:

(i) the relative mass variance g_2;
(ii) the phonon density of states $\rho(\omega)$ at the frequency ω of the Raman mode, and
(iii) a relevant phonon eigenvector $\overrightarrow{e}$.

In modern language, as above, phonons are referred to as quasiparticles, with a complex self-energy $\Sigma = \Sigma_r + i\Sigma_i$ induced in insulators (semiconductors) by anharmonic phonon–phonon interactions and in crystals with several isotopes of a given element also by isotopic mass disorder. In metals and heavily doped semiconductors one must also take into account the self-energy which corresponds to the interaction of the phonon with the conduction electrons. The purpose of this section is to discuss the isotopic disorder contributions to the self-energy of phonons, in the first step in semiconductors of the tetrahedral variety with special emphasis on the quantum effects observed at low temperatures (especially in diamond—where isotopic effects dominates over the anharmonic ones—as well as in germanium where anharmonic effects are larger [31]).

The definition of the average mass $\overline{m} = \sum_i c_i m_i$ implies that $g_1 = 0$. In further discussion, we display a compilation of the disorder-induced *self-energies* for the Raman phonons of elemental and compound crystals (diamond, Si, Ge, α-Sn and LiH_xD_{1-x}, 6H-Sic polytype) which have been obtained either by *Raman spectroscopy* or from theoretical calculations by several research groups during the last two decades. Raman studies that address the variation of the self-energy with the isotopic composition have been conducted for LiH_xD_{1-x} (see, for example review [55]), diamond [44, 105, 111, 112], and Si [113]. The coherent potential approximation (*CPA*) has been employed for diamond [105, 111] and Si [113], while ab initio electronic structure-based calculations have been performed for diamond and Ge [114].

Figure 4.15 displays the Raman frequencies of diamond versus the ^{13}C concentration. The points (open symbols) represent experimental values. The dashed curve represents the approximately linear dependence expected in the VCA. The upward curvature of the experimental data (with respect to the VCA line) clearly demonstrates the existence of an isotopic-disorder-induced self-energy as emphasised by the solid line, which is a fit with Eq. (2.39) for $n = 2, 3$ of Ref. [31]. It is difficult to see with the naked eye in Fig. 4.16 the asymmetric behavior versus x, which may arise from third-order perturbation terms. The asymmetry appears, however, rather clearly when the difference between the measured (or the calculated) behavior and the VCA line is plotted, as shown in Fig. 4.16. In this figure, the solid line also represents the fit to all experimental data, the dot–dashed line represents CPA calculations while the dotted line is a fit to the asterisks which indicate points obtained in the ab initio calculations [7, 41]. All data in Fig. 4.16 show a similar asymmetric behaviour, with a maximum of $\Delta_{dis}(x)$ at $x \approx 0.6$. These results allow us to conclude that the real part of the self-energy due to isotopic disorder is well understood for these systems, including the superposition of second-order and third-order perturbations terms in the case of the diamond. A Similar degree of understanding has been reached for $\Gamma_{dis}(x)$ as shown in Fig. 4.17. The x position of the maxima of Δ_{dis} and Γ_{dis} determined from the experimental data agree with those obtained by perturbation theory

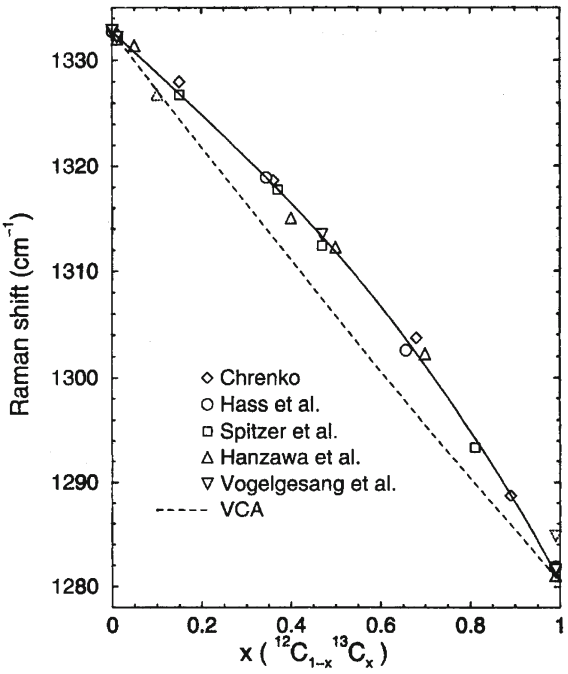

Fig. 4.15 Raman shift of isotopically disordered diamond. The *open symbols* represent experimental values [44, 105, 111, 112]. The *dashed line* indicates the harmonic scaling of the phonon frequency within the VCA ($\omega \sim \overline{m}^{-1/2}$). The *solid line* corresponds to a fit with Eq. (2.40) for n = 2, 3 of Ref. [31] to all experimental data, added to the VCA scaling (after [110])

(Eq. (2.42) of Ref.[31]) and also with the CPA and ab initio calculations (for details see [110]). Concerning the other elemental semiconductors, detailed experimental results with sufficient values of x to reach quantitative conclusions of the type found for diamond, are only available for Si. These data for Si are shown in Figs. 4.18 and 4.19 (filled circles) together with the results of CPA calculations (filled squares). The latter show for Δ_{dis} a clear asymmetry with a maximum at $x_{max,\Delta} \approx 0.56$. The quality and the number of the experimental points are not sufficient to conclude that an asymmetry exists but they cannot exclude it either. The measured absolute values of Δ_{dis} almost (not quite) agree within error bars with the calculated ones. The corresponding experimental; values of Γ_{dis} (x) (see Fig. 4.19) are about a factor of 2 lower than the calculated ones, although both show the asymmetric behavior ($x_{max,\Gamma} \approx 0.62$) predicted by theory. The reason for the discrepancy between the calculated and measured Γ_{dis} is to be sought in the mechanism responsible for it in Si [96]. Within *harmonic approximation* $\Gamma_{dis} = 0$ for Si, Ge and α-Sn, because the Raman frequency is at the maximum of the spectrum and thus corresponds to zero density of one-phonon states. The rather small, but not negligible, observed value of Γ_{dis} results from *DOS* induced at the Γ point by the anharmonic interactions responsible for the linewidths of the isotopically pure crystals. Thus, the widths observed for Si, as well as for Ge and α-Sn, correspond to fourth-order (twice disorder and twice anharmonicity) and higher order terms.

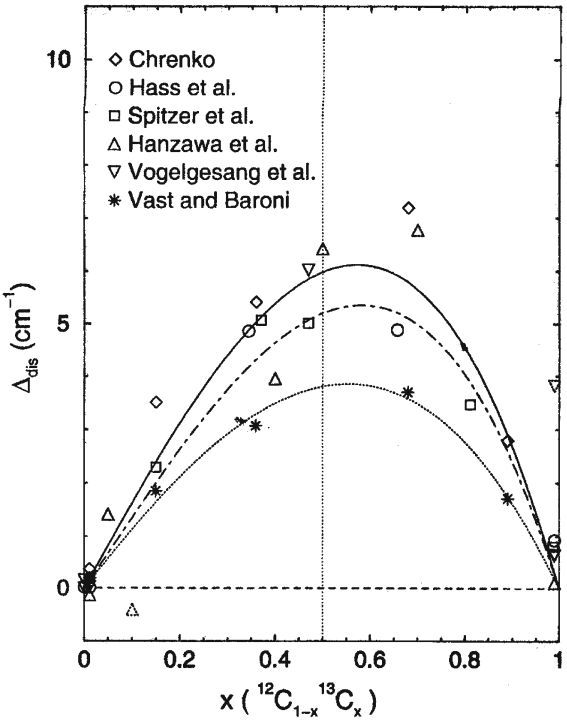

Fig. 4.16 Disorder-induced shift of the Raman phonon of diamond as a function of the ^{13}C concentration. The *open symbols* are Raman experimental data, whereas the *asterisks* correspond to ab initio calculations [40, 114, 115]. The *solid line* is a fit with Eq. (2.40) for $n = 2, 3$ of Ref. [31] to all experimental data. The *dotted* and *dot–dashed lines* represent the fits to theoretical values obtained from ab initio and CPA calculations, respectively (after [110])

As was shown in [109, 110], the *isotope effects* of a disordered sublattice in a compound is different from that for the corresponding monatomic crystal. Widulle et al. apply Eqs. (2.50a) and (2.50b) of Ref. [31] to the Raman spectroscopic results on a variety of $^{nat}Si^{12}C_{1-x}$ $^{13}C_x$ polytypes, recently reported by Rohmfeld et al. [116]. They have performed a fit Eq. (2.40) for $n = 2, 3$ of Ref. [31] to the linewidths of the transverse optic (TO) modes of the 6H-SiC polytype measured in [116] for ^{13}C concentration ranging from x = 0.15 to 0.40 Fig. 4.20). The fit performed in Ref. [116] was based on the asymmetric curve obtained by CPA calculations for diamond [105]. This curve was first fitted to the data points of the TO (2/6) mode and further adjusted to the TO (0) and TO (6/6) modes by multiplication with the constant eigenvectors. Instead, authors [110] have considered each TO mode separately and performed fits with Eq. (2.40) for $n = 2, 3$ of Ref. [31] in the same manner as for elemental semiconductors (see above). Widulle et al. used, however, parameters appropriate to SiC, not to diamond. In this way, they conclude that the behavior of Γ_{dis} versus x is asymmetric (Fig. 4.20). This fact cannot, according to Widulle et al., be derived from the data of the results paper [115]. The latter can be fitted equally with either a symmetric or an asymmetric curve.

As has been mentioned many times, the isotopic disorder in the crystal lattice lifts the forbiddenness imposed by the quasiimpuls conservation law, thus allowing a contribution to the half-width of the scattering line from other phonons from the

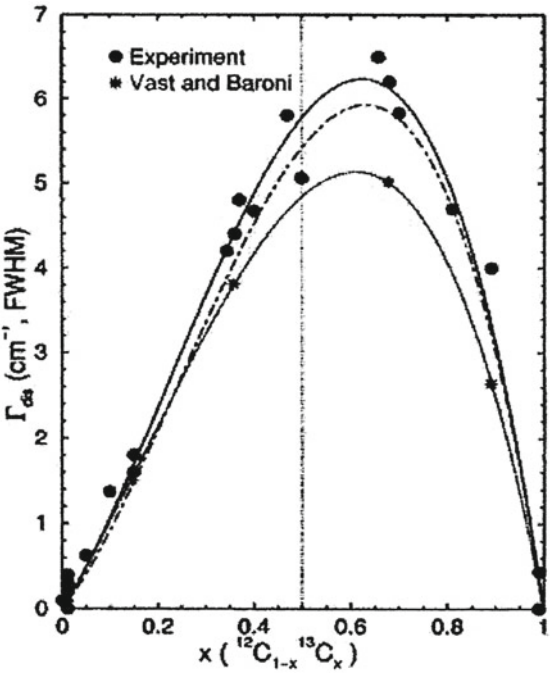

Fig. 4.17 Disorder-induced broadening of the Raman phonon of diamond as a function of the ^{13}C concentration. The *filled circles* have been obtained from the Raman data by taking into account the corresponding instrumental resolutions and substracting the anharmonic broadening $\Gamma_{anh} \approx 2\,cm^{-1}$ (FWHM). The *solid line* is a fit with Eq. (2.40) for $n = 2, 3$ of Ref. [31] to these points. The *dotted* and *dot–dashed lines* are the corresponding fits to the values obtained from ab initio [114, 115] and CPA [105] calculations, respectively (after [110])

domain with the maximum density of states, especially from the TO branches of Ge. The two structures observed in the spectrum of first-order Raman scattering near 275 and 290 cm^{-1} correspond to the maximum of the density of states of TO phonons (see [40] and references therein), which become active because of the violation of the quasi—momentum conservation law by the isotopic disorder in the crystal (see, for instance Fig. 20 in [46]). The effect of the development of an additional structure in Raman scattering spectra was observed relatively long ago [117] in isotopically mixed LiH_xD_{1-x} (Fig. 4.21). The effects caused by isotopic disorder in the crystal lattice in isotopically mixed are analogous to those described above (see, also [46]). There exist, however, principal differences. In contrast to Ge and C, in which the first-order spectra exhibit a one-mode character, the Second-order spectra of LiH_xD_{1-x} crystals have one- and two-mode characters for LO(Γ) phonons, and also contain a contribution from the local excitation at small values of x. Figure 4.21 demonstrates the dependence of the half-width of the line of LO(Γ) phonons in light-scattering spectra on the concentration of isotopes. One clearly sees a substantial growth (by factor 2–4) of the half-width of the line with increasing concentration of isotopes, as well as the existence of a short-wavelength structure that has already been related in Ref. [117] to the excitation of TO phonons in isotopically disordered crystal lattice (for more details see [118]).

To conclude this part of this chapter, we should note that in contrast elemental *semiconductors*, where isotope scattering potential is weak, in the case*isotope-mixed*

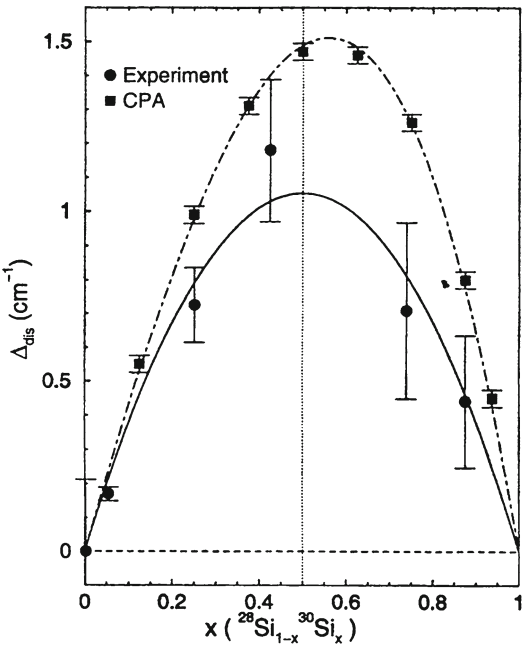

Fig. 4.18 Disorder-induced broadening of the Raman phonon of Si as a function of the ^{30}Si concentration [113]. The *solid line* is a fit with Eq. (2.40) for $n = 2, 3$ of Ref. [31] to the experimental data. The *dot–dashed line* represents the corresponding fit to the values obtained from CPA calculations (after [110])

crystals LiH_xD_{1-x} isotope scattering potential is very strong and *CPA approximation* in such simple version does not describe the Raman spectra of these crystals.

4.4 Effects of Isotope Randomness on Electronic Properties and Exciton Transitions

As follows from Fig. 4.9, *excitons* in LiH_xD_{1-x} crystals display a unimodal character, which facilitates the interpretation of their concentration dependence. Figure 4.22 shows the concentration dependence of the energy of interband transitions E_g. Each value of E_g was found by adding together the energy of the long-wave band in the reflection spectrum and the binding energy of the exciton. The latter was found from the hydrogen-like formula using the experimental values of the energies levels of 1s and 2s exciton states. We see that the 100% replacement of hydrogen with deuterium changes E_g by $\Delta E_g = 103$ meV at $T = 2$ K(see, e.g. [61]). This constitutes 2% of the energy of the electron transition, which is two orders of magnitude greater than the value corresponding to the *isotopic replacement* of atomic hydrogen with *deuterium* reported earlier [119].

The nonlinear concentration dependence of E_g can be sufficiently well approximated with a second order polynomial

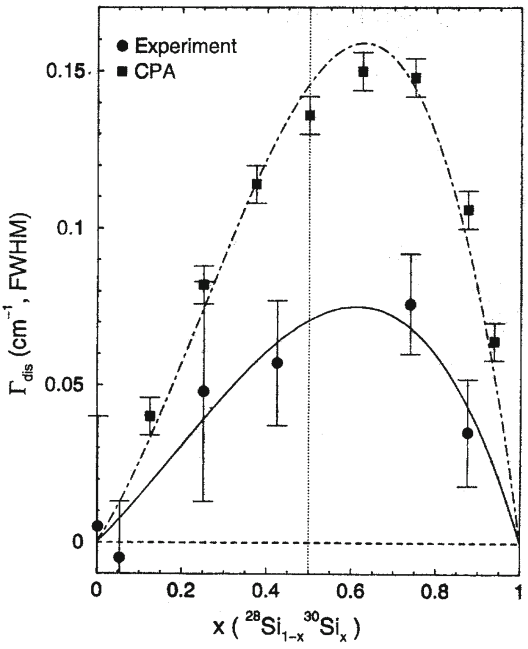

Fig. 4.19 Disorder-induced broadening of the Raman phonon of Si as a function of the ^{30}Si concentration [113]. The *solid line* is a fit with Eq. (2.40) for $n = 2, 3$ of Ref. [31] to the experimental data. The *dot–dashed line* represents the corresponding fit to the values obtained from CPA calculations (after [110])

$$E_g(x) = E_b + (E_a - E_b - b)x - bx^2, \tag{4.39}$$

where E_a, E_b are the values of E_g for LiD and LiH respectively, and b is the curvature parameter equal to 0.046 eV. This result generally agrees with the published data (see also Elliott and Ipatova [120] and references therein). For comparison let us indicate that in the case of isotopic substitution in germanium the energy E_g depends linearly on the isotopic concentration for both direct (E_0, $E_0 + \Delta_0$, $E_1 + \Delta_1$) and indirect electron transitions [121]. Unfortunately, today there is no information about the form of the function $E_g \propto f(x)$ for isotopic substitution in C, ZnO, CdS, CuCl, Cu_2O, GaAs,GaN, Si, etc., crystals, although, as noted above, the values of E_g have been measured for isotopically pure crystals. However, we should add that isotopic substitution in Ge leads not only to the shift of the *luminescence spectrum*, but also to the nonlinear concentration dependence of the emission line half-width, as in the case of lithium hydride (see, below) was attributed to isotopic disordering of the crystal lattice [122].

According to the results depicted in Fig. 4.9, the addition of deuterium leads not only to the short-wave shift of the entire exciton structure (with different rates for Is and 2s states [61]), but also to a significant broadening of the long-wave exciton reflection line. This line is broadened 1.5–3-fold upon transition from pure LiH to pure LiD. The measure of broadening was the halfwidth of the line measured in the standard way [123, 124] as the distance between the maximum and the minimum in the dispersion gap of the reflection spectrum, taken at half-height. The concentration

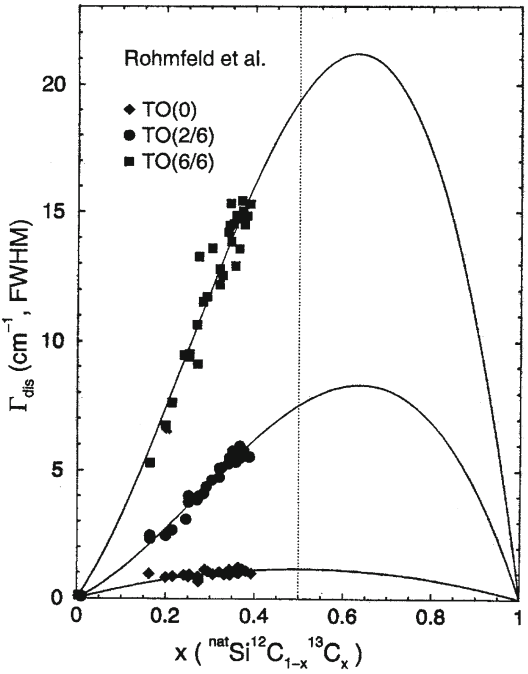

Fig. 4.20 Disorder-induced broadening of the Raman modes of the 6H-SiC polytype versus the ^{13}C concentration of the carbon sublattice. The data are taken from [116] the *solid lines* represent fits with Eq. (2.40) for n = 2, 3 of Ref. [31] to the data points that correspond to the TO(0), TO(2/6) and TO(6/6) phonon modes (after [116])

dependence of the halfwidth (ΔE^R) of the long-wave band in the exciton reflection spectrum at 2 K is shown in Fig. 4.23. Despite the large spread and the very limited number of concentrations used, one immediately recognises the nonlinear growth of ΔE^R with decreasing x. A similar concentration dependence of ΔE^R in the low-temperature reflection spectra of solid solutions of semiconductor compounds A_2B_6 and A_3B_5 has been reported more than once (see e.g. the review [120] and references therein). The observed broadening of exciton lines is caused by the interaction of excitons with the potential of large-scale fluctuations in the composition of the solid solution. Efros and colleagues [125] used the method of optimal fluctuation [126] to express the formula for the concentration dependence of the broadening of exciton reflection lines:

$$\Delta E^R = 0.5\alpha \left[\frac{x\,(1-x)}{N r_{ex}} \right]^{1/2}. \tag{4.40}$$

where $\alpha = dE_g/dx$; r_{ex} is the exciton radius which varies from 47 A to 42 Å upon transition from LiH to LiD [5]. The value of coefficient α was found by differentiating Eq. (4.39) with respect to x—that is, $dE_g/dx = \alpha = E_a - E_b - b + 2bx$. The results of calculation according to Eq. (4.40) are shown in Fig. 4.23 by a full curve.

The experimental results lie much closer to this curve than to the straight line plotted from the *virtual crystal* model. At the same time it is clear that there is only qualitative agreement between theory and experiment at $x > 0.5$. Nevertheless, even

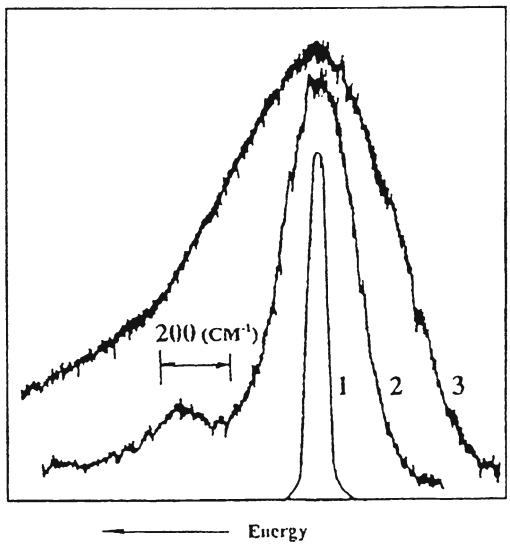

Fig. 4.21 Dependence of the half-width of the line of 2LO(Γ) phonons in Raman scattering spectra of (2) the pure crystal LiH and (3) LiH_xD_{1-x}. Curve (1) shows the profile of the line of exciting light (after [46])

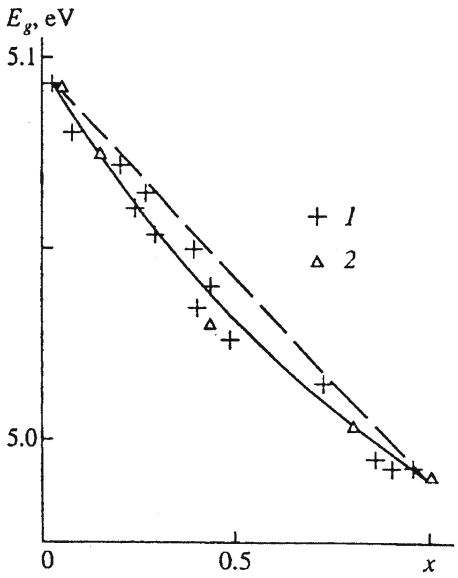

Fig. 4.22 Energy of band-to-band transitions E_g as function of isotope concentration in mixed crystals LiH_xD_{1-x} at 2 K: 1–linear dependence of E_g on x in virtual crystal model; 2–calculation according to Eq. (4.39), points derived from reflection spectra indicated by croses, and those from luminescence spectra by triangles (after [61])

this qualitative analysis clearly points to the nonlinear dependence of broadening on the concentration of isotopes, and hence to the isotopic disordering. Since *isotopic substitution* only affects the energy of optical phonon, and, as a consequence, the constant exciton–phonon interaction (in the first place, the Fröhlich interaction g_F^2), the nonlinearity of functions $\Delta E_g \propto f(x)$, $\Delta E^R \propto f(x)$ is mainly related to the

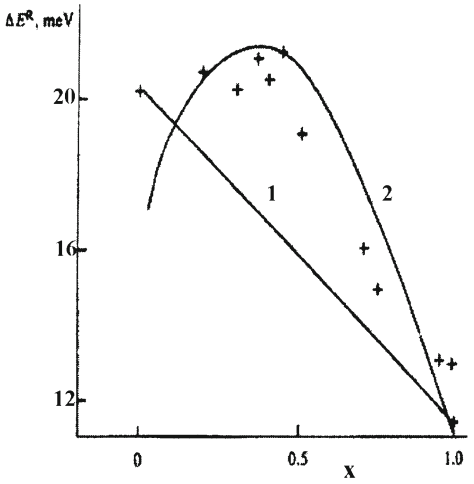

Fig. 4.23 Concentration dependence of half-width of the lineof ground state of exciton in mirror reflection spectra at 2 K: 1–approximation of virtual crystal model; 2–calculation according to Eq. (4.40); experimental points indicated by croses (after [61])

nonlinear behavior of $g_F^2 \propto f(x)$. In this way, the experimental study of the concentration dependence of the exciton–phonon interaction constant may throw light on the nature and mechanism of the large-scale fluctuations of electron potential in isotopically disordered crystals [118].

A principal matter for further theoretical development is the question concerning the effect of crystal lattice disordering on the binding energy E_B of *Wannier-Mott exciton* [81]. This problem has been treated theoretically in the papers of Elliott et al. [127, 128], where they study the effect of weak disordering on E_B (the disordering energy is comparable with E_B). The binding energy indicated in the papers was calculated under the coherent potential approximation by solving the Bethe–Salpeter equation [129] as applied to the problem of Wannier–Mott exciton in disordered medium. One of the principal results of this paper [127] is the nonlinear dependence of E_B on the concentration. As a consequence, the binding energy E_B at half-and-half concentrations is less than the value derived from the virtual crystal model. The exciton binding energy is reduced because the energy E_g is less owing to the fluctuation smearing of the edges of the conduction and valence band. This conclusion is in qualitative agreement (although not in quantitative agreement, the discrepancy being about an order of magnitude [127] with the experimental results for the mixed crystal $GaAs_{1-x}P_x$ with $x = 0.37$, where the reflection spectra exhibited two exciton maxima (see also Fig. 4.9) used for finding the value of E_b (see Nelson et al. [130] and references therein). Let us add that the pivotal feature of the model of Elliott et al. is the short-range nature of the *Coulomb potential* (for more details see [32]).

Before the comparison of our experimental results with the theory developed by Elliott and Kanehisa, it would be prudent to briefly review the main properties of their theoretical model. According to Ref. [127] this model considers an *exciton* with a direct gap of a semiconductor alloy. Such a system consists of an electron (particle 1)

in the conduction band (c) with mass m_c and a hole (particle 2) in the valence band (v) with mass m_v. The problem of the exciton in disordered systems is to solve the Hamiltonian

$$H = \vec{p}^{\,2}/2m_c + \vec{p}^{\,2}/2m_v + u(\vec{r_1} - \vec{r_2}) + V_c(\vec{r_1}) + V_v(\vec{r_2}), \tag{4.41}$$

with both the Coulomb interaction u and the potential V_ν due to disorder ($\nu = c, v$). Reference [127] neglected disorder–induced interband mixing. As it is well known, in place of the electron-hole coordinates, ($\vec{r_1}$, $\vec{p_1}$) and ($\vec{r_2}$, $\vec{p_2}$), one may introduce the centre-of-mass and relative coordinates, ($\vec{R}$, $\vec{P}$) and ($\vec{r}$, $\vec{p}$) to rewrite Eq. (4.41) as

$$H = \vec{p}^{\,2}/2m_r + u(\vec{r}) + \vec{P}^{\,2}/2M + V_c(\vec{R} + m_v\vec{r}/M) + V_v(\vec{R} - m_c\vec{r}/M), \tag{4.42}$$

where m_r and M are the reduced and total masses, respectively. Because of the random potential, the translational and relative degrees of freedom cannot be decoupled. This is essentially difficult when considering the two-body problem in a disordered system [131]. However, when the exciton state in question is well separated from other states so that the energy spacing is much larger than the translational width and disorder, one can forget about the relative motion and just apply any single-particle alloy theory (see, e.g. Ref. [132] and references therein) solely to their translational motion. For each exciton state the translational part of Hamiltonian in this case is

$$\mathrm{H}_t = \vec{\mathrm{P}}^{\,2}/2M + \bar{V}_\mathrm{c}(\vec{\mathrm{R}}) + \bar{V}_\mathrm{v}(\bar{R}). \tag{4.43}$$

Here, $\bar{V}_c$ and $\bar{V}_v$ are averages of V_c and V_v. This approach is very similar to the Born-Oppenheimer adiabatic approximation. Such situations hold in some mixed alkali halide crystals and probably A_2B_6 crystals. On the contrary, when the exciton binding energy is comparable to the disorder energy, the adiabatic approximation breaks down, and it is essential to take into account the effect of disorder on both the translational and relative motions. This is the case with the Wannier-Mott exciton in A_3B_5 alloys, for which the Elliott and Kanehisa model was developed. In this case the solution task is to start from the independent electron and hole by neglecting u in Eq. (4.42) and then to take into consideration the Coulomb interaction between the average electron and average hole. A further simplified approach adopted in the literature [132] in solving the Bethe–Salpeter [129] equation is to suppose a free-electron-like one particle Green's function with a built-in width to allow for the random potential due to disorder. In the cited theoretical model, the average (or "*virtual crystal*") gap is given by

$$\mathrm{E}_g^{vc}(x) = \mathrm{E}_0 + (\delta_\mathrm{c} - \delta_\mathrm{v})(\mathrm{x} - 1/2), \tag{4.44}$$

where E_0 is average gap, δ_c, δ_v are the values of the fluctuation broadening of the conduction and valence bands, respectively. Reference [127] also assumed the Hub-

bard density of states for both the conduction and valence bands with width W_c and W_v, respectively, as well as similar dispersion in both bands. With this assumption the exciton binding energy has been calculated according to the CPA model (see, also [52]). It should be added here that the key feature of the model developed in Ref. [127] is the short-range nature of the *Coulomb potential*.

The data from Table 4.2 and other published sources [32, 61, 118] were used for plotting the energy E_B as a function of isotopic concentration x in Fig. 4.24. The values of binding energy E_B were calculated using the hydrogen-like formula (see below) with the energies of exciton levels of 1s and 2s states being found from the reflection spectra (see Fig. 4.9). Theoretical description of the binding energy of *Wannier–Mott excitons* as a function of x was based on the polynomial derived by Elliott and coworkers [127]:

$$E_b = E_b^{crys} - E_{bow}\left[\frac{1-W}{2U}_0\right] - E_{eff}, \tag{4.45}$$

$$E_{eff} = x(1-x)\frac{\delta_c \delta_v}{W}, \tag{4.46}$$

$$E_b^{crys} = U_0 + \frac{W}{2U_0} - W. \tag{4.47}$$

where $W = W_c + W_v$, and W_c and W_v are the widths of the conduction band and the valence band which are equal to 21 eV [133] and 6 eV [21, 22] respectively. Here E_{bow} is the curvature parameter found from the function $E_g \propto f(x)$; δ_c and δ_v are the magnitudes of the fluctuation smearing of the valence band and the conduction band edges, $\delta_c = 0.103$ eV and $\delta_v = -0.331$ eV. As follows from Fig. 4.24, these values of the parameters give a good enough description of the nonlinear dependence of the binding energy of Wannier-Mott exciton in disordered medium. This agreement between theory and experiment once again proves the inherent consistency of the model proposed by Kanehisa and Elliott, since the *isotopic substitution* affects the short-range part of the interaction potential (see, also [134, 135]).

In this way, the nonlinear dependence of the binding energy of Wannier-Mott exciton is caused by isotopic disordering of the crystal lattice. As is seen from Fig. 4.24 the exciton binding energy decreasing (relative linear law (VCA)-see dashed line in Fig. 4.24) in the vicinity of the middle meaning concentration really calls out the fluctuated broadening of the edge of the conduction and valence bands. In accordance with the theoretical model the last reason gives rise to the reduced E_g and thereby the shallowing of the exciton levels and, respectively, the reduction of E_b (for more details see [81, 118]).

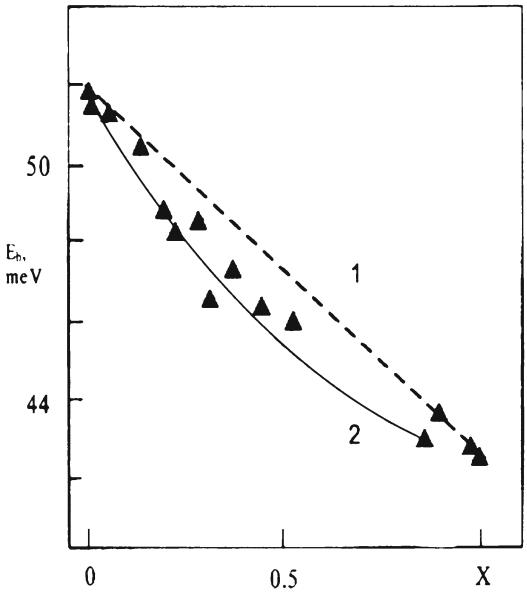

Fig. 4.24 Concentration dependence of binding energy of Wanier–Mott exciton; 1–approximation of vitual crystal model; 2–calculation according to Eq. (4.45): experimental points indicated by triangles (after [118])

4.5 Zero-Point Field Energy

4.5.1 Zero-Phonon Vibration Energy in Solids

The short history of zero-point vibration energy can be found in Rechenberg's paper [136]. According to Rechenberg, M. Planck used this conception at a Berlin meeting of German Physical Society in 1911 [137] after which it was used numerously (see, e.g. [94, 138, 139]). For the first time in solid state physics the conception of zero-point vibration energy probably was used by Fan [140] and for the interpretation of experimental results by Kreingol'd et al. [65, 66, 68], Cardona et al. (see, e.g. [141, 40]) as well as Agekyan et al. [41]. The classical definition of this conception have proposed by Baym [142].... " The minimum amount of kinetic energy coming from the uncertainty principle is called *zero-point energy*" (see, also [143, 144]).

The effect of changing the atomic mass M is to change the phonon frequencies ω according to Eq. (4.19)

$$\omega = \sqrt{\frac{\alpha}{M}}, \tag{4.19′}$$

where α is a force constant characteristic of the phonon under consideration (see above). The change in atomic mass implies, at low temperatures (see below), a change in the average atomic displacement for each phonon mode. In the case of one atom per primitive cell the mean *squared phonon amplitude* $\langle u^2 \rangle$ is given by [126]:

$$\langle u^2\rangle = \left\langle \frac{\hbar^2}{4M\omega}\left[1+2n_B(\omega)\right]\right\rangle = \left\langle \frac{\hbar}{4M^{1/2}\alpha^{1/2}}\left[1+2n_B(\omega)\right]\right\rangle, \tag{4.48}$$

where $n_B(\omega)$ is the Bose–Einstein statistical factor, ω is the frequency of a given phonon and $\langle\ldots\rangle$ represents an average over all phonon modes. The average in r.h.s. of Eq. (4.48) is often simplified by taking the value inside $\langle\ldots\rangle$ at an average frequency ω_D which usually turns out to be close to the Debye frequency. We should distinguish between the low temperature ($\hbar\omega \gg k_B T$) and the high temperature ($\hbar\omega \ll k_B T$) limits and see:

$$\begin{aligned} (\hbar\omega \gg k_B T), \quad \langle u^2\rangle &= \frac{\hbar}{4M\omega_D} \sim M^{-1/2} \quad \text{independent of T and} \\ (\hbar\omega \ll k_B T), \quad \langle u^2\rangle &= \frac{k_B T}{2M\omega^2} \sim T \quad \text{independent of M.} \end{aligned} \tag{4.49}$$

Using Eq. (4.49) we can find from the latter equations that $\langle u^2\rangle$, the *zero-point vibrational amplitude*, is proportional to $M^{-1/2}$ at low temperatures: it thus decreases with increasing M and vanishes for $M \to \infty$. For high T, however, we find that $\langle u^2\rangle$ is independent of M and linear in T (for details see [135] and references therein).

The temperature and isotopic mas dependence of a given energy gap $E_g(T, M_i)$ can be described by average Bose–Einstein statistical factor n_B corresponding to an average phonon frequency θ_i as [73, 141, 145]

$$E_g(T, M_i) = E_{bar} - a_r \left(\frac{M_{nat}}{M_i}\right)^{1/2} [1+2n_B], \tag{4.50}$$

where $n_B = 1/[\exp\left(\frac{\theta_i}{T}\right) - 1]$ and E_{bar} and a_r the unrenormalised (bare) gap and the renormalisation parameter, respectively. In the low-temperature limit, $T \ll \theta_i$, Eq. (4.50) reduces to

$$E_g(T, M_i) = E_{bar} - a_r \left(\frac{M_{nat}}{M_i}\right)^{1/2} \tag{4.51}$$

Here, $E_g(T, M_i)$ is independent of temperature and proportional to $(1/M_i)^{1/2}$, whereas a_r is the energy difference between the unrenormalised gap ($M_i \to \infty$) and the renormalised value [140, 146].

In the high-temperature limit, $T \gg \theta_i$ and Eq. (4.51) can be written as

$$E_g(T, M_i) = E_{bar} - 2T\frac{a_r}{\theta}, \tag{4.52}$$

and $E_g(T, M_i)$ is independent of M_i [31]. The extrapolation of Eq. (4.52) to $T = 0\,K$ can be used to determine the unrenormalised gap energy E_{bar}, i.e. the value that cor-

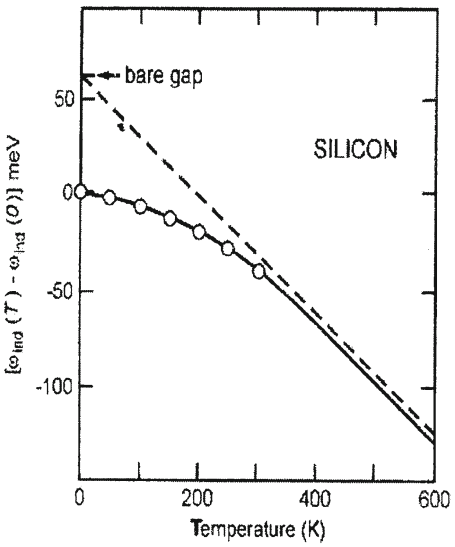

Fig. 4.25 Temperature dependence of the indirect gap of silicon. The points are experimental, the solid curve represents a single Einstein oscillator fit to the experimental points. The dashed line represents the asymptotic behavior at high temperature: its intersept with the vertical axis allows us to estimate the bare gap and thus the zero-point renormalisation due toe electron–phonon interaction (after [40])

responds to atoms in fixed lattice position without vibrations (frozen lattice [119]), from the measured temperature dependence of $E_g(T)$ in the high-temperature (i.e. linear in T) region. Figure 4.25 shows the indirect gap dependence of silicons of the T [96]. It is important to note that the experimental T range of Fig. 4.25 (confined to $T < \theta$) does not suffice to determine the asymptotic behavior for $T \longrightarrow \infty$. The experimental range is usually limited (to 300 K in Fig. 4.25) by the broadening the optical spectra with increasing T. As already mentioned, the *zero-point renormalisation* of a gap can also be estimated from the corresponding isotope effect. In the case of E_{ind} for silicon, a gap shift of -1.04 meV/amu is found for $T \ll \theta$ [40]. On the basis of Eq. (4.52), the isotope effect leads to a renormalisation of 60 ± 1 meV for the E_{ind} in silicon, in reasonable agreement with the value ~ 57 meV found from the E_{ind} (T) asymptote. The isotope shift, and the corresponding zero-point renormalisation, have also been determined for the indirect gap of Ge (see Fig. 4.26). They amount to (at $T \simeq 6$ K): isotope shift equals 0.36 meV/amu, renormalisation equals -53 meV. The value of -370 meV found for the zero-point renormalisation of E_{ind} in diamond (see, Fig. 4.27) can be used to obtain the dependence on isotopic mass by means of the $M^{-1/2}$ rule Eq. (4.51) [40]

$$\frac{dE_{ind}(0)}{dM} = \frac{1}{2} \times 370 \times \frac{1}{13} = 14.2\,\text{meV/amu}. \tag{4.53}$$

The last value is in excellent agreement with the value estimated above. A recent semiempirical LCAO calculation results in a renormalisation of 600 meV [141], even larger than the experimental values. The value of the exciton energy shown in Fig. 4.27, 5.79 eV, can be compared with ab initio calculations of the indirect gap

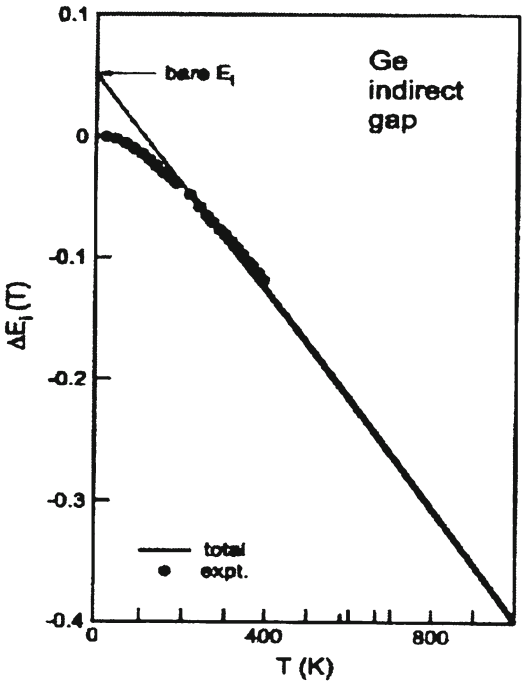

Fig. 4.26 Temperature dependence of the indirect gap measured for Ge (*dots*). The *solid line* (through the points and at higher temperature) represents a fit a single oscillator. The *thin line* below 200 K represents the linear extrapolation of the single-oscillator fit to $T = 0$ K, used to determine the zero-point renormalisaton of −53 meV (after [79])

[40], which yield an indirect gap of 5.76 eV. This value must be compared with that from Fig. 4.27 adding the exciton binding energy (5.79 + 0.07 = 5.86 eV). This experimental gap value according to [27] is in rather good agreement with ab initio calculations. The agreement becomes considerably worse if the zero-point renormalisation of 370 meV is not taken into account (5.48 vs. 5.76) All these arguments support the large zero-point renormalisation found for the indirect gap of diamond.

Using Eq. (4.51) can be written the difference in energy ΔE_g between a given energy gap in isotopically pure material (LiH) and its isotope analogue (LiD)

$$\Delta E_g = E_g(M_i) - E_g(M_{\text{nat}}) = a_r \left[1 - \left(\frac{M_{\text{nat}}}{M_i} \right)^{1/2} \right]. \tag{4.54}$$

As can be seen from Table 4.1 and results of [145] ΔE_g at 2 K equals $\Delta E_g = 0.103$ eV and $E_g(\text{LiH}, T = 0\,K) = 5.004$ eV (linear approximation and $E_g(\text{LiH}, T = 300\,\text{K}) = 4.905$ eV then using Eq. (4.52) we obtain $a_r = 0.196$ eV. This magnitude is very close (approximately 84%) to the value of 0.235 eV of zero (see Fig. 4.28) vibration renormalisation of the energy band gap in LiH crystals (for details see [45, 146]). Using Eq. (4.54) we obtain ΔE_g(theor)= 0.134 eV that is very close, on the other hand, to observed experimental value equals 0.103 eV. The discrepancy between these values may be caused by the negligible contribution of the *isotopic lattice expansion* to the band gap renormalisation as well as small temperature range. We

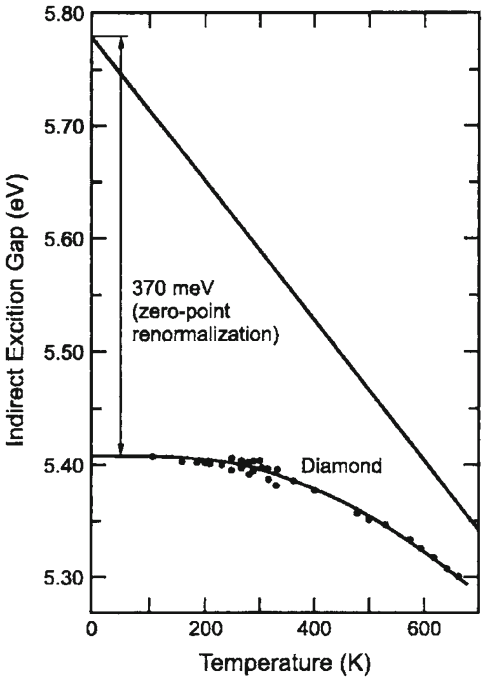

Fig. 4.27 Energy of the indirect exciton of dimond versus temperature. The points are experimental. The extrapolation of the linear behavior of the fitted curve at high T as a straight line to $T = 0\,\mathrm{K}$ leads to a zero-point gap renormalisation of $-370\,\mathrm{meV}$, much larger than the accuracy of 100 meV often claimed for full-blown ab initio calculatuions (after [40])

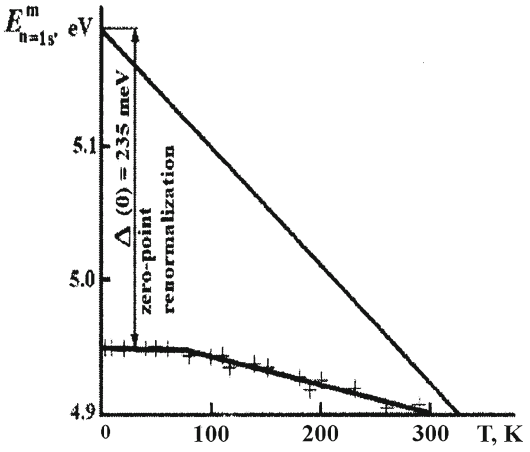

Fig. 4.28 zero-point energy renormalisation of exciton state in LiH crystals (after [96])

should add, so far LiH and LiD have different temperature coefficients $\frac{\mathrm{dE}_{n=1s}}{\mathrm{dT}}(\mathrm{LiH}) = 0.19\,\mathrm{meVK}^{-1}$ and $\frac{\mathrm{dE}_{n=1s}}{\mathrm{dT}}(\mathrm{LiD}) = 0.25\,\mathrm{meVK}^{-1}$ [118], we may conclude that the isotope effect at high temperature is disappeared (Fig. 4.29) (see, also [96]).

Several groups have conducted low-temperature studies of the direct and indirect band gaps of natural and isotopically controlled Ge single crystals. Parks et al. [121]

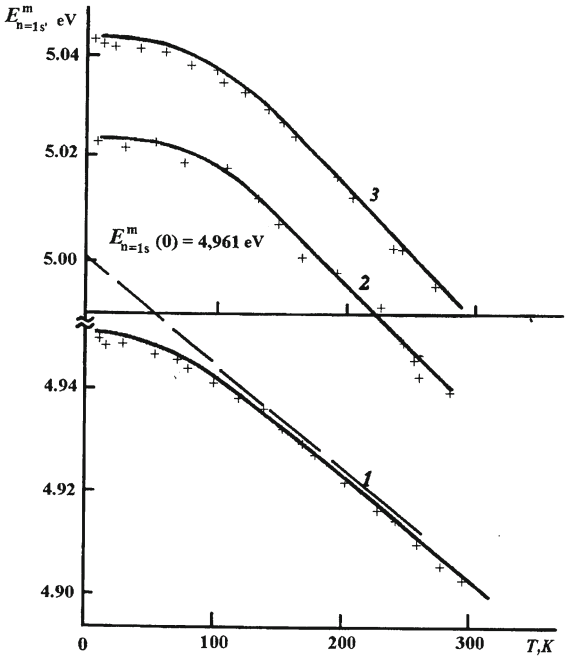

Fig. 4.29 Temperature shift of location of maximum of 1s exciton state in the reflection spectrum of crystals, 1 LiH; 2 $LiH_{0.25}D_{0.75}$; 3 LiD. Experimental values are shown by *points* and the calculated values by *full curves* (after [61])

have used piezo- and photomodulated reflectivity spectra of four *monoisotopic* and one natural Ge crystals. These techniques do not require the extreme sample thinning which is necessary for optical-absorption measurements and the derivative nature of the spectra emphasises the small changes. The excellent signal-to-noise ratio and the superb spectral resolution allowed a very accurate determination of the dependence of E_{DG} on isotopic mass. At very low temperatures an inverse square-root dependence accurately describes band-gap dependence $E_{DG} = E^{\infty}_{DG} + \frac{C}{\sqrt{M}}$.

A fit through five data points yields $E^{\infty}_{DG} = 959\,\text{meV}$ and $C = -606\,\text{meV/amu}^{1/2}$. Written as a linear dependence for the small range of isotopic masses, Parks et al. find $dE_{DG}/dA = 0.49\,\text{meV/amu}$, in perfect agreement with the results of other researchers [40]. Parks et al. also determined the isotope mass dependence of the sum of the direct gap and the split-off valence band (Δ_0) and find $d(E_{DG} + \Delta_0)/dA = 0.74\,\text{meV/amu}$. The experimental results can be compared to the Zollner et al. [141] calculations which are found to be of the correct order of magnitude. The theoretical estimates for the contributions of the linear isotope shifts of the minimum, indirect gaps which are caused by electron-phonon interaction, are too large by a factor of $\sim$1.7 and for the smallest direct gap they are too large by a factor $\sim$3.2. The analogous results were obtained by Zhernov [147], who have criticised the approach of Cardona et al. in estimation of *zero-point renormalisation* of the band gap.

4.5.2 Origin of Zero-Point Field Energy

According to contemporary physics, the Universe is made of matter fields, whose quanta are fermions and force fields, whose quanta are bosons. All these fields have vacuum fluctuations and zero-point energy. Although the concepts of *zero-point energy* arise in introductory courses on quantum mechanics, usually in connection with the *harmonic oscillator*, it is typically brushed aside as one of the formal peculiarities of quantum theory (see, above Chap. 3), and even in advanced treatises there is seldom any discussion of its theoretical significance or experimental relevance [148]. This paragraph is a discussion of the concept of the origin of zero-point energy.

As is well known the quantum theory of physics predicts that the vacuum of space in the Universe is filled with low-energy electromagnetic waves, random in phase and amplitude and propagating in all possible directions. This is different from the cosmic microwave background radiation (see, also above Chap. 2) and it is referred to as the electromagnetic quantum vacuum which is the lowest state of otherwise empty space. When integrated over all frequency modes up to the *Planck frequency*, $\nu_P \sim 10^{43}$ Hz, this represent an enormous potential source of energy with a density of as much as $\sim 10^{111}$ J/cm^3 which is an in excess of any other known energy source, for example, this value is much more than the density of nuclear energy.

As we all know the concept of the zero-point energy was first in 1911 in Planck's so-called second theory [137] for the *blackbody radiation spectrum* (see, also [149]). Planck obtained, for the average energy of an oscillator in equilibrium with radiation field a temperature T,

$$u(\nu) = \frac{h\nu}{e^{h\nu/kT}-1} + \frac{1}{2}h\nu, \tag{4.55}$$

and for the spectral energy density

$$\rho(\nu, T)d\nu = \frac{8\pi\nu^2}{c^3}\left(\frac{h\nu}{e^{h\nu/kT}-1}\right)d\nu. \tag{4.56}$$

It is interesting to note that Planck obtained, in Eq. (4.55) a *temperature-independent term* $\frac{1}{2}h\nu$, suggestive of some residual energy at the temperature of absolute zero for the oscillator energy but failed to obtain in Eq. (4.56) this temperature-independent term for the field, which is now identified as the zero-point field (ZPF) of the fluctuating vacuum field (see, also [150–152]). In 1913, Einstein and Stern [139] published a paper about the interaction of matter with radiation using a sample dipole oscillator model. These authors remarked that if such an oscillator has zero-point energy of $\hbar\omega$ per normal mode, then the equilibrium spectrum of radiation is found to be the *Planck spectrum*

$$\rho(\omega, T)d\omega = \frac{\hbar\omega^3/\pi^2c^3}{e^{h\nu/kT}-1}d\omega. \tag{4.57}$$

It is clear that Einstein and Stern had attributed the sum of the *oscillator ZPF* and the field ZPF solely to that of the oscillator. Had they postulated the correct zero-point energy of $\frac{\hbar\omega}{2}$ to both the oscillator and the field, they would have arrived at the correct Planck spectrum with temperature-independent terms see Eq. (4.55). As this result of Einstein and Stern indicates, there was no concept, at this point, of the ZPF. In 1916, Nernst [153] stated that it is impossible to tell the difference between matter and field oscillators if they are in thermal contact to attain statistical equilibrium, and that Planck equation (4.55) should therefore hold for both matter and field oscillators. This statement of Nernst is generally considered as the birth of the concept of the ZPF [136, 149]).

In traditional quantum theory presented in many textbooks (see, e.g. [32]), the basis of the ZPF is attributed to the so-called *Heisenberg Uncertainty Principle*. According to this principle, A and B are two conjugate observables that we are interested in measuring in a lab experiment and they must obey the commutation relation $[\mathrm{A}, \mathrm{B}] = \mathrm{i}\hbar$ ($\hbar$ is a Planck's reduced constant) [154]. Their corresponding uncertainty relation is

$$\Delta\mathrm{A}\Delta\mathrm{B} \geq \frac{\hbar}{2}, \tag{4.58}$$

where ΔA is the variance (uncertainty) of observable A and ΔB is that of the *conjugate observable* B. The relation Eq. (4.58) states that if one measures observable A with very high precision (i.e. its uncertainty ΔA is very small), then a simultaneous measurement of observable B will be less precise (i.e. its uncertainty ΔB is very large), and vice versa. In other words, it is not possible to simultaneously measure two conjugate observable quantitaties with infinite precision. This minimum uncertainty is not due to any correctable flows in measurement, but rather reflects the intrinsic fuzziriness in the quantum nature of energy and matter. Substantial theoretical and experimental work (see, e.g. [155] and references therein) has shown that in many quantum systems the limits to measurement precision imposed by the *quantum vacuum zero-point fluctuations* (ZPF) embodied within the uncertainty principle. Nowadays, we rather see the *Heisenberg Uncertainty Principle* as a necessary consequence, and therefore, a derived result of the wave nature of quantum phenomena. The uncertainties are just a consequence of the Fourier nature of conjugate pairs of quantities (observables). For example, the two *Fourier-wave-conjugates* time and frequency become the pair of quantum-particle conjugates time and energy and the two Fourier-wave-conjugates displacement and wavenumber become the pair of quantum-particle conjugates position and momentum (for the details, see [153]).

The Heisenberg Uncertainty Principle dictates that a *quantised harmonic oscillator* (a photon state) can never come entirely to rest, since that would be a state of exactly zero energy, which is forbidden. Every mode of the field must have $\frac{\hbar\omega}{2}$ (ω is the mode/photon frequency, $\hbar\omega$ is the energy of a single mode/photon) as its average minimum energy in the vacuum. This is a tiny amount of energy, but the number of modes is enormous, and indeed increases as the square of the frequency. The product of this tiny energy per mode times the huge spatial density of modes

yields a very high theoretical energy density per volume—see above). It is for this reason that a ZPE term is added to the *classical blackbody spectral radiation energy density* $\rho\,(\omega)\mathrm{d}\omega$ (i.e. the energy per unit volume of radiation in the frequency interval $[\omega, \omega + \mathrm{d}\omega]$) for when the absolute temperature T of oscillator system becomes 0 K in the vacuum (see, e.g. [148])

$$\rho\,(\omega)\,\mathrm{d}\omega = \frac{\omega^2}{\pi^2 \mathrm{c}^2}\left(\frac{\hbar\omega}{\mathrm{e}^{\hbar\omega/\mathrm{kT}} - 1} + \frac{\hbar\omega}{2}\right)\mathrm{d}\omega, \tag{4.57′}$$

where, as usually $\omega = 2\pi\nu$. The first term inside the brackets is the standard blackbody radiation energy per mode, and the second term inside brackets is the quantum zero-point energy (ZPE) per mode. This equation is called *zero-point Planck spectral radiation energy density*. From this line of reasoning, quantum physics predicts that all space must be filled with electromagnetic zero-point fluctuation (the zero-point field) creating a universal sea of ZPE. The density of this energy depends critically on where the frequency of the zero-point fluctuations cease (see, e.g. [156]). Since space itself is thought to break up into a kind of quantum foam at a tiny distance scale called the *Planck length*, $l_P \sim 10^{-35}$ m, it is argued that the zero-point fluctuations must cease at the corresponding ν_P. If that is the case, then the ZPE density would be 108 orders of magnitude greater than the radiant energy at the centre of the Sun. That is the extreme limit. Formally, in quantum electrodynamics (QED) the ZPE density is taken as infinite. However, arguments based on quantum gravity considerations yield a finite cutoff at ν_P (see also below). Therefore, the *spectral energy density* is given by $\rho\,(\omega)\mathrm{d}\omega = \left(\hbar\omega^3/2\pi^2\mathrm{c}^3\right)\mathrm{d}\omega$, which integrates to an energy density $\mathrm{u} = \mathrm{h}\nu_P^4/8\pi^2\mathrm{c}^3 \approx 10^{113}$ J/m^3, this value was indicated above. As large as the ZPE is, interactions with it are typically cut off at lower frequencies depending on the particle constants or their structure (see, also, Chap. 2).

In *stochastic electrodynamics (SED)* the origin of the ZPF comes as a direct consequence of the fundamental assumptions. SED is just the ordinary classical electrodynamics of *Maxwell* and *Lorentz*, where instead of taking the homogeneous solutions of the source—free differential wave equations for the electromagnetic potentials, as done in traditional electrodynamics, one considers that (because there are many moving charged particles in the distant Universe) there always is the presence of a random electromagnetic background in the form of a random radiation affecting the particles in our experiment. This new boundary condition replaces the null one of traditional classical electrodynamics. Moreover, as the relative principle dictates that identical experiments performed in different inertial frames and therefore have a Lorentz—invariant energy density spectrum. But the only energy density spectrum that obeys such a condition happens to be one that is proportional to the cubic power of the frequency. Interestingly enough, this is exactly the same frequency dependence as that of the *QED* spectral ZPF energy density presented above when in Eq. (4.57′) we set the temperature T to zero. In SED we can then write this random radiation in the same way as the ZPE of QED and it calls the classical electromagnetic ZPE. Planck's constant appears then in SED as an adjustable parameter that sets the scale

of the ZPE spectral density. Several quantum results have been reproduced by means of the classical SED approach (see, for example, [157–160]).

In his study of the coordinate operator in the *Dirac equation* (see [154] and references therein), *Schrödinger* [161] discovered microscopic oscillatory motion at the speed of light, which he called *Zitterbewengung* [162, 163]). While Dirac*) argued that such motion does not violate relativity or quantum theory, from a "classical particle point of view, these speed of light motions would seem to imply" masslessness of the particle (see, also [160] and references therein). According to the monograph by *de la Pena* and *Cetto* [159] the zittewrbewegung is the result of electromagnetic quantum vacuum fluctuations acting upon a fundamentally point—like *massless charged particle*.

Another curiosity of the SED approach is that it could have provided a different method of attack to the problem of the stability of the ground-state of hydrogen (see, e.g. [164–166]). As is well known [167], *Rutherford*'s discovery of the atomic nucleus in 1911 together with *Thomson*'s previous discovery of the electron in 1897 led to the analogy between atomic structure and planetary orbits about the Sun. In this naive analogy, however, electrons being charged, would radiate away their orbital energy and quickly collapse into the nucleus. Bohr resolved the problem of radiative collapse of the hydrogen atom (see also [167] and references therein). He recognised that Planck's constant, h, could be combined with Rydberg's empirical relationship among the spectral lines of hydrogen to solve the problem of atomic stability by postulating that only discrete transitions are allowed between the states whose angular momenta are multiplies of $\hbar$. The ground state of the hydrogen atom would then have angular momentum $mva_0 = \hbar$, or equivalently $m\omega_0 a_0^2 = \hbar$, and would be forbidden to decay below this orbit by *Bohr*'s fiat. A more complex picture quickly developed from this that substituted wave functions for orbiting point particles, and in that view the orbital angular momentum of the ground state is actually $l = 0$: the wave function is spherically symmetric and has a radial probability distribution whose most probable value is a_0 (the expectation value being $\frac{3a_0}{2}$).

As with classical derivation of the blackbody function made possible by the assumption of a real ZPF, modern SED analysis of the Bohr hydrogen atom has yielded a suggestive insight. A simple argument assuming strictly circular by *Boyer* [157, 158] and *Puthoff* [164] indicated that while a classically circularly orbiting electron would indeed radiate away energy, if one takes into account the ZPF as a source of energy to be absorbed, then it is at the Bohr orbit, a_0, that a condition of balance would take place in absorbed and emitted power such that $\langle P^{abs}\rangle_{circ} = \langle P^{rad}\rangle_{circ}$. In other words, a classicaly orbiting and *radiating electron* would pick up as much energy as it loses, and thus be energetically stabilized [168]. In the analyses a strong assumption was introduced, namely that the electron moves around the nucleus along strictly circular orbit.

Finally, it is seen that a well defined precise quantitative argument can be made that the ground state of the hydrogen atom is defined by a dynamic equilibrium in which collapse of the state is prevented by the presence of zero-point fluctuations of the electromagnetic field. This carrier with it the attendant implication that the stability of matter itself is largely mediated by ZPF phenomena in the manner described in cited

papers, a concept that transcends the usual interpretation of the role and significance of ZPF of the *vacuum electromagnetic field*. We should add that a detailed description of the correspondence between *SED and QED treatments* for linear dipoles-plus-radiation-field systems can be found in Ref. [169].

(*) In the *Dirac theory* of the electron, the velocity operator has eigenvalues of $\pm c$. The motion of an electron thus consists of two components: some average motion-specific physical circustance plus an inherent highly oscillatory component whose instaneous velocity $\pm c$ which *Schrödinger* named *Zitterbewegung* [162, 163]. The amplitude of this zitterbewegung oscillation is on the order of the *Compton* wavelength. From the perspective of ZPF—inertia theory, the ZPF can induce such speed-of-light fluctuations since at this level the electron would be a massless point-charge. It is the Compton wavelength size electron cloud that acquires the measured electron inertial mass of 512 keV in energy units via next relationship $m_{zp} = \frac{\Gamma_z \hbar \omega_C}{2\pi c^2}$, where Γ_z represents a damping constant for zitterbewegung oscillations which is equal $\Gamma_z = 6.25 \times 10^{-24}$s. This is an example of an SED interpretation of an apparent quantum phenomenon. The *quantum size of the electron* is its Compton wavelength. The SED interpretation would be one of a massless point charge driven by the ZPF to oscillate at $\pm c$ within a Compton wavelength-size region of space.

4.5.3 Inertia and Gravitation in the Zero-Point Field Model

Inertia as formulated by *Galileo* (ca 1638) was simply the property of a material object to either remain at rest or in uniform motion in the absence of external forces. In his first law of motion, *Newton* (ca 1687) merely restated the *Galilean* proposition; however, in his second law, Newton expanded the concept of inertia into fundamental quantitative property of matter (see, e.g. [170] and references therein). By proposing a relationship between external force acting upon an object and change in that object's velocity (according the second law), he defined and quantified the property of inertial mass. Since the time of Newton there has been only one noteworthy attempt to associate an underlying origin of inertia of an object with something external to that object: *Mach*'s principle. Since motion would appear to be devoid of meaning in the absence of surrounding matter, it was argued by Mach [171] that the local property of inertia must somehow asymptotically be a function of the cosmic distribution of all other matter. Mach's principle has remained, however, a philosophical statement rather than a testable scientific proposition. Thus apart from Mach's principle, the fact that matter has the property of inertia is a postulate of physics, and while special and general relativity both involve the inertial properties of matter, they provide no deeper insight into an origin of inertia as a fundamental property of matter.

Puthhoff [172] have analysed a hypothesis of *Sakharov* [173] that Newtonian gravity could be interpreted as a van der Waals type of force induced by the electromagnetic fluctuations of the vacuum, the so-called zero-point fluctuations or zero-point field (ZPF). In that analyses ordinary neutral matter is treated as a collection

of electromagneticall interacting polarisable particles made of charged point-mass subparticles (*quarks*). This is a reasonable approach in ZPF analyses in which an ideal Planck oscillator for more detailed representations of matter: or, more specifically, it is a simple model in which at ultrahigh (*Planckian*) energies matter appears as if formed of very small elementary constituents that respond like oscillators characterised by a radiation damping constant Γ and a characteristic frequency ω_0. The effect of the ZPF is to induce a *zitterbewegung* [161–163] motion in the quark in a manner entirely analogous to that of the bound oscillators used to represent the interaction of matter with electromagnetic radiation by *Planck* [174] and others (see, e.g. [170]). This has the consequence that the *van der Waals force* associated with the long-range radiation fields generated by the quark zitterbewegung can be identified with the *Newtonian gravitational field*. In the proposed model, the inertia of matter could be interpreted at least in part as a reaction force originated in interactions between ZPF and the elementary charged constituents (quarks, electrons, etc.) of mater [175, 176]. Indeed, Newton's second law may be most generally written as

$$\overrightarrow{f} = \frac{\mathrm{d}\vec{p}}{\mathrm{dt}} \tag{4.59}$$

which is the limited form of the space part of the relativistic four-force:

$$\overrightarrow{F} = \frac{\mathrm{d}\vec{p}}{\mathrm{d}\tau} = \gamma \frac{\mathrm{d}\vec{p}}{\mathrm{d}t}, \tag{4.60}$$

which for the case when $\beta = \left(\frac{\mathrm{v}}{\mathrm{c}}\right) = 0$ and $\gamma = 1$ becomes Eq. (4.59).

It is seen that the second law is a definition of force as the rate of change of momentum imparted to an object by an agent. Having defined force, Newton's third law states that such a force will result in the creation of an equal and opposite reaction force back upon the accelerating agent. This now makes the concept of inertia a necessity: Inertia must be attributed to the accelerating object in order to generate the equal and opposite reaction force upon the agent required by the third law. According to [175, 176] the resistance from the vacuum is the physical basis of that reaction force. One can interpret this as either the origin of *inertia of matter* or as a substitute for the concept of innate inertia of matter. Inertia, following [175, 176], becomes a placeholder for this heretofore undiscovered vacuum—based force which is a necessary requirement of *Newton's third law*. Force is then seen to be primary concept, inertia is not. The inertia of *protons and neutrons* would arise via ZPF scattering at the level of the individual quarks. Moreover, it appeared that Newton's equation of motion ($\overrightarrow{f} = m\overrightarrow{a}$) could be inferred from Maxwell's equation as applied to the ZPF, i.e. SED version of the quantum. If correct proposed model by Puthoff, Rueda and Haisch, then their concept would substitute for Mach's principle and imply that no further mass-giving Higgs-type fields may be required to explain the inertia of material objects.

If inertia is a electromagnetic phenomenon involving interactions between charge and the ZPF, then gravitation must be a similar phenomenon [175, 176]. The mere

existence of a ZPF would not necessarily generate gravitation or space-time curvature. Indeed, preliminary development of a conjecture of *Sakharov* [173] by *Puthoff* [172] indicates that the ZPF in and of itself cannot be a source of gravitation (for the details see [177]). Expressed in the simplest possible way, all matter at the level of quarks and electrons is driven to oscillate (*zitterbewegung* in the terminology of *Schrödinger*) by the ZPF. But every oscillatimg charge will generate its own minute electromagnetic fields. Thus any particle will experience the ZPF as modified ever so slightly by the fields of adjacent particles and that is gravitation [175, 176]. It is a kind of long-range *van der Waals force*. It should be added, the *Einstein* $E = mc^2$ relationship between mass and energy will also be cast in a different light. As it now stands this formula seems to state that one kind of "thing", namely energy, can mysteriously be transformed into a totally different kind of "thing", namely mass …. and vice versa. It is proposed instead that the $E = mc^2$ relationship is a statement about the kinetic energy that the ZPF fluctuations induce on the quarks and electrons constituting matter [172]. In the *quantum vacuum inertia hypothesis,* inertial and gravitational mass are not merely equal, they prove to be the identical thing. According [175, 176] both mass and wave nature of matter can be traced back to specific interactions with electromagnetic ZPF and possible the other *bosonic vacuum fields*. The Cited authors suggest that it is premature to take a firm stand against the reality of the *zero-point radiation field* and its associated energy on the basis of cosmological arguments, especially given the possible relation between vacuum, or zero-point, radiation and *dark energy*.

4.5.4 Vacuum Energy Extraction

In this paragraph we briefly consider the possible employment of *zero-point field energy*. The concept "engineering the vacuum" was first introduced by Nobel Laureate T.D. *Lee* in his book "Particle Physics and Introduction to Field Theory" (see also [178]). As stated there…. "The experimental method to alter the properties of the vacuum may be called vacuum engineering……If indeed we are able to alter the vacuum, then we may encounter some new phenomena, totally unexpected"……Recent studies have indeed shown this to be the case [179, 180].

As utopian as such a possibility may seem, physicist *Forward* [181] demonstrated prof-of-principle in a paper "Extreme Electrical Energy from the vacuum by Cohesion of Charged Foliated Conductor". His approaches exploited a phenomenon called the *Casimir effect* [182]—an attractive quantum force between closely spaced metal plates. The Casimir force recently measured with high accuracy by *Lamoreaux* (see, review [143, 144]—derives from partial shielding of the interior region of the plates from background ZPF of the vacuum electromagnetic field. As shown by *Milonni* et al. [183], this shielding results in the plates being pushed together by the unbalanced ZPE radiation pressures. The result is a corollary conversion of vacuum energy to some other form such as heat [184]. With regard to the extraction of energy from the vacuum fluctuation energy reservoir, there are no energetic or thermody-

namic constraints preventing such release under certain conditions (see, e.g. [184]). Analyses of the scientific literature suggest that such mechanism are already operative in Nature in the "powering-up" of cosmic rays [185] or as the source of energy release from supernovas [186] and gamma-ray bursts [187].

Below we shall briefly list a few possibilities of the vacuum energy extraction:

(1) An early one of interest is based on the idea of a *Casimir force* pinch effect in non-neutral plasmas.
(2) Another intriguing possibility is provided by the phenomenon of *sonoluminescence*-bubble collapse in an ultrasonically-driven fluid which accompanied by intense, subnanosecond light radiation.
(3) Yet another proposed for ZPE extraction is described in a patent [188]. The approaches proposed the use of resonant dielectric spheres—slightly detuned from each other—to provide a beat frequency downshift of the more energetic high-frequency components of the ZPE to a more easily captured form.
(4) Next approaches utilising microcavity techniques to perturb the *ground state stability of atomic hydrogen*. It is based on the paper by *Puthoff* [164], where he puts forth the hypothesis that the nonradoative nature of the ground state is due to a dynamic equilibrium in which radiation emitted due to accelerated electron ground state motion is compensated by absorption from the ZPE.
(5) *Turtur* ([180] and references therein) have described the mechanical rotor which converts vacuum energy (ZPE) into mechanical energy using an electrostatic principle.
(6) The idea of the vacuum as a quantum state with ZPE and fluctuations of physical consequence is now commonplace, with implications ranging from *optical communications* [31, 148, 189] to *quantum chromodynamics* to inflationary models of the Universe (see, also Chap. 2).

References

1. D. Pines, *Elementary Excitations in Solids* (W.A. Benjamin, Inc., New York, 1963)
2. S.I. Pekar, *Crystaloptics and Addition Waves* (Kiev, Naukova Dumka, 1982) (in Russian)
3. G.P. Srivastava, *The Physics of Phonons* (Hilger, Bristol, 1990)
4. V.G. Plekhanov, *Isotopetronics-New Directions of Nanoscience*, ArXiv, phys./1007.5386
5. V.G. Plekhanov, Isotopic and disorder effects in large exciton spectroscopy. Physcs–Uspekhi (Moscow) **40**, 553–579 (1997)
6. J. Callaway, *Energy Band Structure* (Academic Press, New York, 1964)
7. R.M. Martin, *Electronic Structure—Basic Theory and Practical Methods* (Cambridge University Press, Cambridge, 2004)
8. N.W. Ashcroft, N.D. Mermin, *Solid State Physics* (Holt, Reinhart and Winston, New York, 1976)
9. J.M. Ziman, *Electrons and Phonons* (Oxford University Press, London, 1963)
10. V.G. Plekhanov, *Giant Isotope Effect in Solids* (Stefan University Press, La Jola, 2004)
11. N.F. Mott, R.V. Gurney, *Electron Processes in Ionic Crystals* (Clarendon Press, Oxford, 1948)
12. J. Slater, *The Self-Consistent Field for Molecules and Solids* (McGraw-Hill, New York, 1975)

13. W.B. Fowler, Influence of electronic polarization on the optical properties of insulators. Phys. Rev. **151**, 657–667 (1966)
14. D.H. Ewing, F. Seitz, On the electronic constitution of crystals: LiF and LiH. Phys. Rev. **50**, 760–777 (1936)
15. F. Perrot, Bulk properties of lithium hydride up to 100 Mbar. Phys. Stat. Sol. (b) **77**, 517–525 (1976)
16. G.S. Zavt, K. Kalder et al., Electron excitation and luminescence LiH single crystals, Fiz. Tverd. Tela (St. Petersburg) **18**, 2724–2730 (1976) (in Russian).
17. N.I. Kulikov, Electron structure, state equation and phase transitions insulator—metal in hydride lithium, ibid, **20**, 2027–2035 (1978) (in Russian)
18. G. Grosso, G.P. Parravichini, Hartree-Fock energy bands by the orthogonalized-plane-wave method: lithium hydride results. Phys Rev. **B20**, 2366–2372 (1979)
19. S. Baroni, G.P. Parravichini, G. Pezzica, Quasiparticle band structure of lithium hydride. Phys. Rev. **B32**, 4077–4087 (1985)
20. A.B. Kunz, D.J. Mikish, Electronic structure of LiH and NaH, ibid, **B11**, 1700–1704 (1975)
21. T.A. Betenekova, I.N. Shabanova, F.F. Gavrilov, The structure of valence band in lithium hydride, Fiz. Tverd. Tela **20**, 2470–2477 (1978) (in Russian)
22. K. Ichikawa, N. Susuki, K. Tsutsumi, Photoelectron spectroscopic study of LiH. J. Phys. Soc. Japan **50**, 3650–3654 (1981)
23. R.A. Kink, M.F. Kink, T.A. Soovik, Reflection spectra of lithium hydride crystals in 4–25 eV at 5 K. Nucl. Instrum. Methods Phys. Res. **A261**, 138–140 (1987)
24. V.G. Plekhanov, V.I. Altukhov, Determination of exciton and exciton–phonon interaction parameters via resonant secondary emission of insulators. Sov. Phys. Solid State **23**, 439–447 (1981)
25. V.G. Plekhanov, *Nuclear Technology of the Creation of Quantum Dots in Graphene*, (Science Transactient of SHI, Tallinn, 2011), pp. 66–71
26. A.A. Blistanov, in *Acoustic Crystals: Handbook*, ed. by M.T. Shchaskol'skaya (Nauka, Moscow, 1982) (in Russian)
27. C. Kittel, *Introduction to Solid State Physics* (Wiley, New York, 1986)
28. R. Wyckoff, *Crystal Structures* (Interscience, New York, 1963)
29. M.L. Cohen, J. Chelikowsky, *Electronic Properties and Optical Properties of Semiconductors*, 2nd ed. Springer Series Solid-State Science, Vol. 75 (Springer, Berlin, 1989)
30. J.I. Pankove, *Optical Processes in Semiconductors* (Prentice-Hall Englewood Cliffs, New Jersey, 1971)
31. V.G. Plekhanov, Elementary excitations in isotope mixed crystals. Phys. Reports **410**, 1–235 (2005)
32. L.D. Landau, E.M. Lifshitz, *Quantum Mechanics (Nonrelativistic Theory)* (Pergamon Press, New York, 1977)
33. R. Loudon, The Raman effect in crystals. Adv. Phys. **13**, 423–488 (1964)
34. R.A. Cowley, Anharmonicity, J. Phys. (Paris). **26**, 659–664 (1965)
35. R.A. Cowley, Anharmonic crystals, Rep. Prog. Phys. **31**, 123–166 (1968)
36. R.A. Cowley, in *Anharmonicity*, ed. by A. Anderson. Raman Effect, (Marcel Dekker, New York, 1971)
37. M.A. Eliashevich, Mechanics of the vibrations of molecules, Uspekhi Fiz. Nauk (Moscow) **48**, 482–544 (1946) (in Russian)
38. D.A. Long, *Raman Spectroscopy* (McGraw-Hill Inc., London, 1977)
39. J.L. Birman, in *Space Group Symmetry*, Handbuch fur Physik, vol. 25/2b (Springer, Berlin, 1974)
40. M. Cardona, M.L.W. Thewalt, Isotope effect on the optical spectra of semiconductors. Rev. Mod. Phys. **77**, 1173–1224 (2005)
41. V.F. Agekyan, A.M. Asnin, V.M. Kryukov et al., Isotope effect in germanium, Fiz. Tverd. tela (St. Petersburg) **31**, 101–104 (1989) (in Russian)
42. M. Lax, E. Burstein, Infrared lattice absorption in ionic and homopolar crystals. Phys. Rev. **97**, 39–52 (1955)

43. H.D. Fuchs, P. Etchegoin, M. Cardona et al., Vibrational band modes in germanium: isotopic—disorder induced Raman scattering. Phys. Rev. Let. **70**, 1715–1718 (1993)
44. H. Hanzawa, N. Umemura, Y. Nisida, H. Kanda, Disorder effect of nitrogen impurities, irradiation induced defects and ^{13}C composition on the Raman spectrum in synthetic I^b diamond. Phys. Rev. **B54**, 3793–3799 (1996)
45. V.G. Plekhanov, Isotope Effects in Solid State Physics, in *Semiconductors and Semimetals*, vol. 68, ed. by R.K. Willardson, E. Weber (Academic Press, San Diego, 2001)
46. V.G. Plekhanov, Isotope effect in lattice dynamics. Physics-Uspekhi (Moscow) **46**, 689–715 (2003)
47. R.M. Chrenko, ^{13}C-doped diamond: Raman spectra. Appl. Phys. **63**, 5873–5875 (1988)
48. K.C. Hass, M.A. Tamor, T.R. Anthony, W.F. Banholzer, Effect of isotopic disorder on the phonon spectrum of diamond. Phys. Rev. **B44**, 12046–12053 (1991)
49. S.H. Solin, A.K. Ramdas, Raman spectrum of diamond. Phys. Rev. **B1**, 1687–1699 (1970)
50. V.G. Plekhanov, Isotope effect on the lattice dynamics. Mater. Sci. Eng. **R35**, 139–237 (2001)
51. V.G. Plekhanov, Lattice—dynamics of isotope—mixed crystals, ArXiv cond–mat/1007.5125 (2010).
52. R.J. Elliott, J.A. Krumhansl, P.L. Leath, The thery and properties of randomly disordered crystals and physical systems. Rev. Mod. Phys. **46**, 465–542 (1974)
53. I.F. Chang, S.S. Mitra, Long-wavelength of optical phonons in mixed crystals. Adv. Phys. **20**, 360–404 (1971)
54. I.P. Ipatova, Universal parameters in mixed crystals, in [120] Ch. p. 1–34, 1988
55. V.G. Plekhanov, Lattice dynamics of isotopically mixed crystals, Opt. spectrosc. (St. Petersburg) **82**, 95–24 (1997)
56. V.G. Plekhanov, Experimental evidence of strong phonon scattering in isotopical disordered systems: the case LiH_xD_{1-x}. Phys. Rev. **B51**, 8874–8878 (1995)
57. V.G. Plekhanov, Fundamentals and applications of isotope effect in modern technology, J. Nucl. Sci. Technol. (Japan) **43**, 375–381 (2006). ArXiv: cond–mat/0807.2521 (2008)
58. G. Herzberg, *Molecular Spectra and Molecular Structure* (D. van Nostrand, New York, 1951)
59. A.F. Kapustinsky, L.M. Shamovsky, K.S. Bayushkina, Thermochemistry of isotopes. Acta Physicochim. (USSR) **7**, 799–810 (1937)
60. V.G. Plekhanov, T.A. Betenekova, V.A. Pustovarov et al., Excitons and some peculiarities of exciton–phonon interactions. Sov. Phys. Solid State **18**, 1422–1424 (1976)
61. V.G. Plekhanov, Wannier—Mott excitons in isotope—disordered crystals. Rep. Prog. Phys. **61**, 1045–1095 (1998)
62. F.I. Kreingol'd, K.F. Lider, M.B. Shabaeva, Influence of isotope substitution sulfur on the exciton spectrum in CdS crystal, Fiz. Tverd. Tela (St. Petersburg) **26**, 3940–3941 (1984) (in Russian)
63. Y. Onodera, Y. Toyozawa, Persistence and amalgamation types in the electronic structure of mixed crystals. J. Phys. Soc. Japan **24**, 341–355 (1968)
64. Y. Toyozawa, *Optical Processes in Solids*, (Cambridge University Press, Cambridge, 2003)
65. F.I. Kreingol'd, K.F. Lider, K.I. Solov'ev, Isotope shift of exciton line in absorption spectrum Cu_2O, JETP Lett. (Moscow) **23**, 679–681 (1976) (in Russian)
66. F.I. Kreingol'd, K.F. Lider, V.F. Sapega, Influence of isotope substitution on the exciton spectrum in Cu_2O crystal, Fiz. Tverd. Tela (St. Petersburg) **19**, 3158–3160 (1977) (in Russian)
67. F.I. Kreingol'd, B.S. Kulinkin, Influence of isotope substitution on the forbidden gap of ZnO crystals, ibid, **28**, 3164–3166 (1986) (in Russian).
68. F.I. Kreingol'd, Dependence of band gap ZnO on zero-point energy, ibid, **20**, 3138–3140 (1978) (in Russian)
69. J.M. Zhang, T. Ruf, R. Lauck et al., Sulfur isotope effect on the excitonic spectra of CdS. Phys. Rev. **B57**, 9716–9722 (1998)
70. T.A. Meyer, M.L.W. Thewalt, R. Lauck et al., Sulfur isotope effect on the excitonic spectra of CdS. Phys. Rev. **B69**, 115214–115215 (2004)
71. G.L. Bir, G.E. Picus, *Symmetry and Deformation in Semiconductors* (Science, Moscow, 1972) (in Russian)

72. D.G. Thomas (ed.), *II–VI Semiconducting Comounds* (Benjamin, New York, 1967)
73. L.F. Lastras-Martinez, T. Ruf, M. Konuma et al., Isotopic effect on the dielectric response of Si around the E_1 gap, Phys. Rev. **B61**, 12946–12951 (2000)
74. D. Karaskaja, M.L.W. Thewalt, T. Ruf et al., Photoluminescence studies of isotopically—enriched silicon: Isotopic effects on indirect electronic band gap and phonon energies. Solid State Commun. **123**, 87–92 (2003)
75. S. Tsoi, H. Alowadhi, X. Lu et al., Electron–phonon renormalization of electronic band gaps of semiconductors: Isotopically enriched silicon. Phys. Rev. **B70**, 193201–193204 (2004)
76. A.K. Ramdas, S. Rodriguez, S. Tsoi et al., Electronic band gap of semiconductors as influenced by their isotopic composition. Solid State Commun. **133**, 709–714 (2005)
77. S. Tsoi, S. Rodriguez, A.K. Ramdas et al., Isotopic dependence of the E_0 and E_1 direct gaps in the electronic band structure of Si. Phys. Rev. **B72**, 153203–153204 (2005)
78. H. Kim, S. Rodriguez, T.R. Anthony, Electronic transitions of holes bound to boron acceptors in isotopically controlled diamond. Solid State Commun. **102**, 861–865 (1997)
79. M. Cardona, Dependence of the excitation energies of boron in diamond on isotopic mass. Solid State Commun. **121**, 7–8 (2002)
80. A.A. Klochikhin, V.G. Plekhanov, Isotope effect on the Wannier—Mott exciton levels. Sov. Phys. Solid state **22**, 342–344 (1980)
81. V.G. Plekhanov, Direct observation of the effect of isotope-induced-disorder on exciton binding energy in LiH_xD_{1-x} mixed crystals. J. Phys. Condens. Matter **19**, 086221–086229 (2007)
82. P.G. Klemens, Thermal conductivity and lattice vibrational modes, in *Solid state Physics: Advances in Research and Applications*, vol. 7, ed. by F. Seitz, D. Turnbull (Academic Press, New York, 1958)
83. M.G. Holland, Thermal Conductivity, in *Physics of III–V Compounds (Semiconductors and Semimetals)*, vol. 2, ed. by R.K. Willardson, A.C. Beer (Academic Press, New York, 1966)
84. Y.S. Toulookian, R.W. Powel, C.Y. Ho, P.G. Klemens, Thermal Conductivity Metallic Elements and Alloys. in *Thermophysical Properties of Materials*, vol. 1 (IFI Plenum Press, New York–Washington, 1970)
85. R.Z. Berman, *Thermal Conduction in Solids* (Clarendon Press, Oxford, 1976)
86. J. Callaway, Model for lattice thermal conductivity at low temperatures. Phys. Rev. **113**, 1046–1051 (1959)
87. R. Peierls, *Quantum Theory of Solids* (Clarendon Press, Oxford, 1955)
88. J.M. Ziman, *Models of Disorder* (Cambridge University Press, Cambridge, 1979)
89. I. Ya, Pomeranchuk, About thermal conductivity of dielectrics. J. Phys. (USSR) **6**, 237–246 (1942)
90. T.H. Geballe, G.W. Hull, Isotopic and other types of thermal resistance in germanium. Phys. Rev. **110**, 773–775 (1958)
91. D.G. Onn, A. Witek, Y.Z. Qiu et al., Some aspect of the thermal conductivity of isotopically enriched diamond single crystals. Phys. Rev. Lett. **68**, 2806–2809 (1992)
92. J.R. Olson, R.O. Pohl, J.W. Vandersande et al., Thermal conductivity of diamond between 170 and 1200 K and the isotopic effect, Phys. Rev. **B47**, 14850–14856 (1993)
93. L. Wei, P.K. Kuo, R.L. Thomas, Thermal conductivity of isotopically modified single crystal diamond. Phys. Rev. Lett. **79**, 3764–3767 (1993)
94. P. Debye, The Debye theory of specific heat, Ann. Phys. (Leipzig) *4*, 39, 789–803 (1912)
95. M. Cardona, R.K. Kremer, M. Sanati et al., Measurements of the heat capacity of diamond with different isotopic composition. Solid State Commun. **133**, 465–468 (2005)
96. V.G. Plekhanov, Isotope—Mixed Crystals: Fundamentals and Applications (Bentham, e-books, 2011) (ICBN: 978-1-60805-091-8)
97. M. Asen-Palmer, K. Bartkowsky, E. Gmelin et al., Thermal conductivity of germanium crystals with different isotopic composition, Phys. Rev. **B56**, 9431–9447 (1997)
98. W.C. Capinski, H.J. Maris, M. Asen-Palmer et al., Thermal conductivity of isotopically enriched Si, Appl. Phys. Lett. **71**, 2109–2111 (1997)
99. W.C. Capinski, H.J. Maris, S. Tamura, Analysis of the effect of isotope scattering on the thermal conductivity of crystalline silicon. Phys. Rev. **B59**, 10105–10110 (1999)

100. T. Ruf, R.W. Henn, M. Asen-Palmer et al., Thermal conductivity of isotopically enriched silicon, Solid State Commun. **115**, 243–247 (2000); Erratum 127, 257 (2003)
101. A.P. Zhernov, A.V. Inyushkin, Kinetic coefficients in isotopically disordered crystals. Physics-Uspekhi (Moscow) **45**, 573–599 (2002)
102. V.G. Plekhanov, Isotope engineering. Physics-Uspekhi (Moscow) **43**, 1147–1154 (2000)
103. M. Omini, A. Sparavigna, Heat transport in dielectric solids with diamond structure. Nuovo Cimento **D19**, 1537–1563 (1997)
104. A. Sparavigna, Influence of isotope scattering on the thermal conductivity of diamond, Phys. Rev. B65, 064305-1–064305-5 (2002), ibid, B67, 144305–4 (2003)
105. K.C. Hass, M.A. Tamor, T.R. Anthony, W.F. Banholzer, Lattice dynamics and Raman spectra of isotopically mixed diamond. Phys. Rev. **B45**, 7171–7182 (1992)
106. H.D. Fuchs, C.H. Grein, C. Thomsen et al., Comparison of the phonon spectra ^{70}Ge and natural Ge crystals: Effect of isotopic disorder, ibid, **B43**, 4835–4841 (1991)
107. D.T. Wang, A. Gobel, J. Zegenhagen et al., Raman scattering on α-Sn: dependence on isotopic composition, ibid, **B56**, 13167–13172 (1997)
108. S. Tamura, Isotope scattering of dispersive phonons in Ge. Phys. Rev. **B27**, 858–866 (1983)
109. S. Tamura, Isotope scattering of large-wave-vector phonons in GaAs and inSb: deformation-dipole and overlap-shell models, ibid, **B30**, 849–854 (1984)
110. F. Widulle, J. Serrano, M. Cardona, Disorder—induced phonon self-energy of semiconductors with binary isotopic composition. Phys. Rev. **B65**, 075206–075210 (2002)
111. J. Spitzer, P. Etchegoin, W.F. Banholzer et al., Isotopic disorder induced Raman scattering in diamond. Solid State Commun. **88**, 509–514 (1993)
112. R. Vogelgesand, A.K. Ramdas, T.R. Anthony, Brillouin and Raman scattering in natural and isotopically controlled diamond. Phys. Rev. **B54**, 3989–3999 (1996)
113. F. Widulle, T. Ruf, V.I. Ozhogin et al., Isotope effect in elemental semiconductors: A Raman study of silicon. Solid State Commun. **118**, 1–22 (2001)
114. N. Vast, S. Baroni, Effect of disorder on the Raman spectra of crystals: Theory and ab initio calculations for diamond and germanium. Phys. Rev. **B61**, 9387–9391 (2000)
115. N. Vast, S. Baroni, Effect of disorder on the Raman spectra of crystals: Theory and ab initio calculations for diamond and germanium. Comput. Matr. Sci. **17**, 395–399 (2000)
116. S. Rohmfeld, M. Hundhausen, L. Ley, Isotope-disorder-induced line broadening of phonons in the Raman spectra of SiC. Phys. Rev. Lett. **86**, 826–829 (2001)
117. V.G. Plekhanov, V.I. Altukhov, Light scattering in LiH crystals with LO phonons emission. J. Raman Spectrosc. **16**, 358–365 (1985)
118. V.G. Plekhanov, Comparative study of isotope and chemical effects on the exciton states in LiH crystals. Prog. Solid State Chem. **29**, 71–177 (2001)
119. V.G. Plekhanov, Isotope-induced energy-spectrum renormalization of the Wannier– Mott exciton in LiH crystals. Phys. Rev. **B54**, 3869–3877 (1996)
120. R.J. Elliott, I.P. Ipatove (eds.), *Optical Properties of Mixed Crystals* (North-Holland, Amsterdam, 1988)
121. C. Parks, A.K. Ramdas, S. Rodriguez et al., Electronic band structure of isotopically pure germanium, Phys. Rev. **B49**, 14244–14260 (1994)
122. G. Davies, J. Hartung, V. Ozhogin et al., Effects of isotope disorder on phonons in germanium determined from bound exciton luminescence. Semicond. Sci. Technol. **8**, 127–130 (1993)
123. S. Permogorov, A. Reznitsky, Effect of disorder on the optical spectra of wide-gap II–VI semiconductor solid solutions. J. Luminescence **52**, 201–223 (1992)
124. S. Permogorov, A. Klochikhin, A. Reznitsky, Disorder—induced exciton localization in 2D wide—gape semiconductor solid solutions, ibid, **100**, 243–257 (2002)
125. A.L. Efros, M.E. Raikh, Effect of composion disorder on the electronic properties in semiconducting mixed crystals, in [116]. Ch. **5**, 133–177 (1988)
126. I.M. Lifshitz, *Selected Works* (Science, Moscow, 1987) (in Russian)
127. V.A. Kanehisa, R.J. Elliott, Effect of disorder on exciton binding energy in semiconductor alloys. Phys. Rev. **B35**, 2228–2236 (1987)

128. N.F. Schwabe, R.J. Elliott, Approximation of excitonic absorption in disordered systems using a composition–component–weighted coherent–potential approximation, ibid, **B54**, 5318–5329 (1996)
129. H.A. Bethe, E. Salpiter, *Quantum Theory of One and Two Electron Atoms* (Academic Press, New York, 1957)
130. R.J. Nelson, N. Holonjak, W. Groves, Free—exciton transitions in the optical absorption spectra of $GaAs_{1-x}P_x$. Phys. Rev. **B13**, 5415–5419 (1976)
131. S.D. Mahanti, C.M. Varma, Effective electron—hole interactions in polar semiconductors, ibid, **B6**, 2209–2226 (1972)
132. S.D. Mahanti, Excitons in semiconducting alloys, ibid, **B10**, 1384–1390 (1974)
133. J. Hama, N. Kawakami, Pressure induced insulator—metal transiton in solid LiH. Phys. Lett. **A126**, 348–352 (1988)
134. V.G. Plekhanov, Experimental manifestation of the effect of disorder on exciton binding energy in mixed crystals, Phys. Rev. **B53**, 9558–9560 (1996–I)
135. V.G. Plekhanov, N.V. Plekhanov, Isotope dependence of band-gap energy. Phys. Lett. **A313**, 231–237 (2003)
136. H. Rechenberg, Historical Remarks on Zero-Point Energy and the Casimir Effect, in *The Casimir Effect 50 Years later*, ed. by M. Bordag (World Scientific, Singapore, 1999) p. 10–19
137. M. Planck, Über die begrundung des gesetz der Schwarzen strahlung. Ann. Phys. **37**, 642–656 (1912)
138. W. Nernst, F.A. Lindeman, Z. Elektrochem. Angew. Phys. Chem. **17**, 817 (1911) (cited in [136])
139. A. Einstein, O. Stern, Einige argumente fur die annahme einer molekularen agitation beim absoluten null punkt. Ann. Phys. **40**, 551 (1913)
140. H.Y. Fan, Temperature dependence of the energy gap in semiconductors. Phys. Rev. **82**, 900–905 (1951)
141. S. Zollner, M. Cardona and S. Gopalan, Isotope and temperature shifts of direct and indirect band gaps in diamond-type semiconductors, ibid, **B45**, 3376–3385 (1992)
142. G. Baym, *Lectures on Quantum Mechanics* (Benjamin, New York, 1968), p. 98
143. K.A. Milton, The Casimir effect: Recent controversis and progress. J. Phys. A: Math. Gen. **37**, R209–R277 (2004)
144. S.K. Lamoreaux, The Casimir force: Background, experiments and applications. Rep. Prog. Phys. **68**, 201–236 (2009)
145. P. Lautenschlager, M. Garriga, L. Vina et al., Temperature dependence of the dielectric function and interband critical points in silicon. Phys. Rev. **B36**, 4821–4830 (1987)
146. V.G. Plekhanov, Comparative investigation of isotopic and temperature effects involving excitons in LiH_xD_{1-x} crystals, Phys. Solid State (St. Petersburg) **35**, 1493–1499 (1993)
147. A.P. Zhernov, Isotope composition dependence of energy bands in semiconductors, Fiz. Tverd. Tela (St. Petersburg) **44**, 992–1000 (2002) (in Russian)
148. P.W. Milonni, *The Quantum Vacuum: An Introduction to Quantum Elctrodynamics* (Academic Press, New York, 1994)
149. P.W. Milonni and M.-L. Shih, Zero-point energy in early quantum theory, Am. J. Phys. **59**, 684–698 (1991)
150. T.H. Boyer, The classical vacuum (zero-point energy), Sci. Am. Mag, pp. 70–78, (Aug, 1985)
151. P. Yam, Exploiting zero-point energy, ibd, December 1997, pp. 82–85
152. H. Puthoff, Quantum fluctuations of empty space: a new Rosetta stone in physics, www.padrak.com/ine/Name.html
153. W. Nerst, Über einen versuch von quantentheorietischen Betrachtungen zuruckzukehren. Verhandl. Deut. Phys. Ges. **18**, 83–91 (1916)
154. P.A.M. Dirac, *The Principle of Quantum Mechanics* (Clarendon Press, Oxford, 1995)
155. A. Peres, *Quantum Theory: Concepts and Methods* (Kluwer Academic Publ, Dodrech, 1994)
156. B. Haisch, A. Rueda, Y. Dobyns, Insrtial mass and the quantum vacuum fields. Ann. der Phys. **10**, 393–414 (2001)

157. T.H. Boyer, Random electrodynamics: The theory of classical electrodynamics with classical electromagnetic zero-point radiation, Phys. Rev. **D11**, 790–808 (1975)
158. T.H. Boyer, Random Electrodynamics: The Theory of Classical Electrodynamics with Classical Electromagnetic Zero-Point Radiation, in *Foundations of Radiation and Quantum Electrodynamics*, ed. by A.O. Barut (Plenum Press, New York, 1980)
159. L. de la Peña and A.M. Cetto, The Quantum Dice: An Introduction to Stochastic Electrodynamics (Kluwer, Dodrecht, 1996)
160. B. Kosyakov, *Introduction to the Classical Theory of Particles and Fields* (Springer, Heidelberg, 2007)
161. E. Schrödinger, Über die kroftefreie Bewegung in dr relativoschen Quantemmechanics, Sitz. Preus. Akad. Wiss. Phys. Math. K1 **24**, 418–428 (1930); **3**, 1–10 (1931)
162. K. Huang, On the zitterbewegung of the Dirac electron. Am. J. Phys. **20**, 479–487 (1952)
163. A. Barut, N. Zanghi, Classical model on the Dirac Electron. Phys. Rev. Lett. **52**, 2003–2006 (1984)
164. H.E. Puthoff, Groung—state of hydrogen as a zero-point-fluctuation-detrmined state. Phys. Rev. **D35**, 3266–3269 (1987)
165. D.C. Cole, Yi. Zou, Quantum mechanical ground state og hydrogen obtained from classical electrodynamics, Phys. Lett. **A317**, 14–20 (2003)
166. E.W. Davis, V.L. Teofilo, B. Haisch at al., Review of experimental concepts for studying the quantum vacuum field, in *Space Technology and Applications International Forum*, SPAIF - 2006, ed. by El-Genk, 2006, pp. 1390–1401
167. V.G. Plekhanov, Manifestation and origin of the isotope effec, ArXiv: phys/0907.2024 (2009), (review)
168. H.E. Puthhoff, Source of vacuum electromagnetic zero-point energy. Phys. Rev. **A40**, 4857–4862 (1989)
169. P.W. Milonni, Semiclassical and quantum electrodynamical approaches in nonrelativistic radiation theory. Phys. Rep. **25**, 1–81 (1976)
170. M. Jammewr, *Concepts of Mass in Contemporary Physics and Philosophy*, (Harvard University Press, Cambridge, 1961)
171. E. Mach, Mechanics (Saint-Petersburg, 1909) (in Russian)
172. H.E. Puthoff, Gravity as a zero-point-fluctuation force. Phys. Rev. **A39**, 2333–2342 (1989)
173. A.D. Sakharov, Vacuum quantum fluctuation in curved space and the theory of gravitation, Dokl. Akad, Nauk SSSR. Sov. Phys. Dokl. **12**, 1040–1042 (1968)
174. M. Planck, *The Theory of Heat Radiation* (Blackinston, London, 1914)
175. B. Haisch and A. Rueda, The Zero-Point Field and Inertia, in *Causality and Locality in Modern Physics*, ed. by G. Hunter, S. Jeffers, J.-P. Vieger, (Kluwer Academic Publishers, Dodrecht, 1998) pp. 171–178
176. A. Rueda, B. Haisch, Gravity and the quantum vacuum inertia hypothesis. Ann. der Phys. **14**, 479–498 (2005)
177. B. Haisch, A. Rueda, H.E. Puthoff, Inertia as a zero-point-field Lorentz force. Phys. Rev. **A49**, 678–694 (1994)
178. T.D. Lee, *Particle Physics and Introduction to Field Theory* (Harwood Academic, London, 1988)
179. H.E. Puthoff, S.R. Little, M. Ibison, Engineering the zero-point field and polarizable vacuum for interstellar flight. IBIS **55**, 137–144 (2002)
180. C.W. Turtur, Two paradoxes of the existence of electric charge, ArXiv:phys/0710.3253 (2007)
181. R.L. Forward, Extracting electrical energy from the vacuum by cohesion foliated conductors. Phys. Rev. **B30**, 1700–1702 (1984)
182. H.B.G. Casimir, On the attraction between two perfectly conducting plates. Proc. K. Ned. Akad. Wet. **51**, 793–801 (1948)
183. P.W. Milonni, R.J. Cook, M.E. Goggin, Radiation pressure from the vacuum: Physical interpretation of the Casimir force. Phys. Rev. **A38**, 1621–1623 (1988)
184. D.C. Cole, H.E. Puthoff, Extracting energy and the heat from the vacuum. Phys. Rev. **E48**, 1562–1565 (1993)

185. A. Rueda, B. Haisch, D.C. Cole, Vacuum zero-point field pressure instabiity in astrophysical plasmas and the formation of cosmic voids. Astrophys. J. **445**, 7–16 (1995)
186. I.Tu. Sokolov, The Casimir effect is a possible source of cosmic energy. Phys. Lett. **A223**, 163–166 (1996)
187. C.E. Carlson, T. Goldman and J. Peres-Mercader, Gamma-ray burst, neutron atar quales, and the Casimir effect, Europhys. Lett. **36**, 637–642 (1996)
188. F.B. Mead, Jr., J. Nachamkin, System for converting electromagnetic radiation energy to electrical energy, US Patent No 5,590.031, issued Dec. 31, 1996
189. F. Ya. Khalili, Zero-point oscillations, zero-point fluctuations, and fluctuations of zero-point oscillations, Physics-Uspekhi (Moscow) **173**, 301–316 (2003) (in Russian)

Chapter 5
Effects Related to Isotopic Disorder in Solids

5.1 Introduction

Interest in *diffusion* is as old as metallurgy or ceramics. The first measurement of diffusion in the solid state was made by Roberts-Austen [1]. Many measurements, especially of chemical diffusion in metals, were made in the 1930s; the field was reviewed by Jost [2] and Seith [3]. Diffusion research increased after World War II; the increase was motivated by the connection among diffusion, defects and radiation damage and helped by the availability of many artificial *radiotracers*. These researchers were the first to attempt to identify the basic underlying atomistics mechanisms responsible for mass transport through solids by a quantitative investigations and theoretical analysis of the activation energies required for diffusion by exchange, *interstitial* and *vacancy* mechanisms in solids. Prior to this time, there had been little concern with treating diffusional phenomena on a microscopic basis, and most research was concerned with fairly crude observation of overall bulk transfer processes at junctions between regions with strong compositional differences. It was at this time that suggestions on how to carry out high precision, highly reproducible diffusion experiments were first put forward [4, 5]. The three major factors that determine the quality of a diffusion measurement are

(1) the method used,
(2) the care taken in the measurement and
(3) the extent to which the material is specified.

The most accurate method has, in general, been considered to be radiotracer sectioning [5], and most of this article is devoted to this method, especially to points for which special care must be taken; these are the measurement of temperature, the accuracy of sectioning and the reproducibility of counting the radioactivity. The importance of specifying the material cannot be overstated. The measured diffusion coefficient depends on the chemistry and structure of the sample on which it is measured. Impurities, non-stoichiometry of compounds, grain boundaries and dislocations can give apparent values of the diffusion coefficient that are different

V. G. Plekhanov, *Isotopes in Condensed Matter*, Springer Series in Materials Science 162,
DOI: 10.1007/978-3-642-28723-7_5,

from, and usually larger than, the true value [6, 7]. The objective of this chapter is to describe some experimental results as well as their theoretical analysis that are received in last decade. We have organized the chapter around general principles that are applicable to all materials, and then listed the particulars. The materials we consider are mainly inorganic solids, especially semiconductor and insulator materials. The effects of pressure on diffusion is omitted. Previous reviews covering mainly metals and inorganic materials have been given by Tomizuka [5], Crawford et al. [7] and last two book of Academic Press [8, 9]. Besides indicated books we should note the new books on diffusion processes [10–12].

For measurable diffusion to take place a gradient of some kind is necessary. Diffusion is a consequence of the hopping motion of atoms through a solid. The diffusion coefficient D is defined in Fick's first law [12],

$$\vec{J} == -D\vec{\nabla}C + C\vec{V}, \tag{5.1}$$

where $\vec{J}$ is the flux of atoms, C their concentration and $\vec{V}$ the velocity of the centre of mass, which moves due to the application of a force such as an electric field or a thermal gradient [13]. A number of different diffusion coefficients exist, e.g. for the diffusion of a radioactive tracer in a chemically *homogeneous solid* in the absence of external forces,

$$\vec{J}^* = -\mathrm{D}^*\vec{\nabla}\mathrm{C}^*, \tag{5.2a}$$

where the asterisk denotes the radioactive species. For diffusion in a chemical gradient,

$$\vec{J} = -D\vec{\nabla}C, \tag{5.2b}$$

where $\tilde{D}$ is the interdiffusion or chemical diffusion coefficient. Any of these equations can be combined with the equation of continuity

$$\partial C/\partial t = -\vec{\nabla} \cdot \vec{J} \tag{5.3}$$

to yield Fick's second law

$$\partial C/\partial t = \vec{\nabla} \cdot (D\nabla C), \tag{5.4a}$$

where the mass flow term has been omitted. For a tracer in a homogeneous system,

$$\partial C^*/\partial t = -\vec{\nabla}^* \cdot \vec{\nabla}^2 C^*. \tag{5.4b}$$

Equations (5.4a) and (5.4b) describe the types of diffusion experiments discussed in this chapter.

The tracer diffusion coefficient is given also in the atomistics form

$$D^* = \gamma a^2 \Gamma f, \tag{5.5}$$

where γ is a geometric factor, a the jump distance, Γ the atomic jump frequency and f the correlation factor [14]. It is thus possible, in principle, to measure D^* by measuring Γ in a resonance experiment of some kind [15].

We are concerned here with diffusion measurements where the *diffusion coefficient* is obtained via Fick's second law, i.e. from a solution of the diffusion equation [16]. Fick's second law is used rather than his first because concentrations are easier to measure than fluxes and because of D in the solid state is so small that the required steady state is seldom reached. In order to obtain a solution of the diffusion equation, the initial and boundary conditions (IC and BC) must be known. The IC corresponds to the distribution of the diffusing substance in the sample before the diffusion anneal, and the BC describes what happens to the diffusing substance at the boundaries of the sample during the diffusion anneal. If the experimental IC and BC correspond to the mathematical conditions, the mathematical solution to the diffusion equation $C(x, y, z, t)$ will describe the distribution of the diffusing substance as a function of position in the sample and of annealing time. The diffusion coefficient is finally obtained by fitting the experimentally determined $C(x, y, z, t)$ to the appropriate solution of the diffusion equation with D as a parameter.

Most laboratory experiments are arranged so that diffusion takes place in one dimension. The solution of the diffusion equation is then $C(x, t)$. One most often determines $C(x)$ at constant t, i.e. the concentration distribution along the diffusion direction after a diffusion annealing time t. It is also possible to determine $C(t)$ at a constant x (e.g. the concentration at a surface) or $\int \int C(x, t)\mathrm{dx\ dt}$ (e.g. the weight gain of a sample as a function of time). The IC, BC and solutions to the diffusion equation (for $D = \text{const.}$) for some common geometries are described below. These, and solutions for other cases, are given by Crank [14] and Carslaw and Jaeger [17].

(1) Thin Layer or Instantaneous Source Geometry (Fig. 5.1a). An infinitesimaly thin layer ($\ll (Dt)^{1/2}$) of diffusing substance is deposited on one surface of a semi-infinitive ($\gg (Dt)^{1/2}$) solid. The initial conditions is

$$C(x, 0) = M\delta(x), \tag{5.6}$$

where δ is the Dirac delta function and M the strength of the source in atoms per unit area. The boundary condition is

$$\partial C(0, t)/\partial t = 0, \tag{5.7}$$

i.e. there is no flux through the surface. The solution is

$$C(x, t)(M/\sqrt{\pi Dt})\exp(-x^2/4Dt). \tag{5.8}$$

One determines $C(x)$ for constant t.

(2) Thick Layer Geometry (Fig. 5.1b). Similar to the above, except that the layer thickness h is of the order of the diffusion distance: IC: $C(x, 0) = C_0, h \geq x \geq 0$

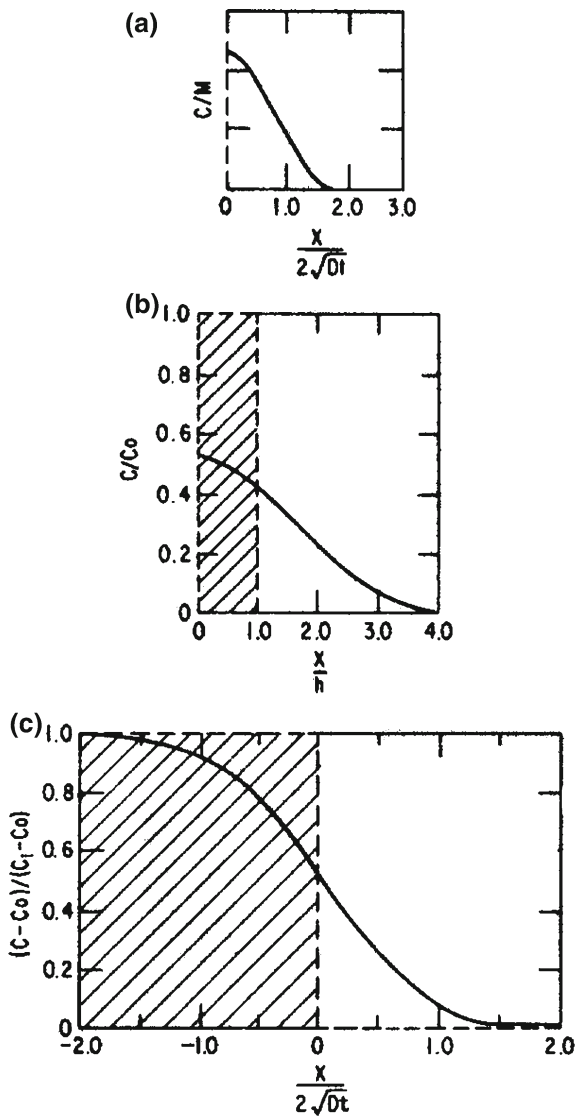

Fig. 5.1 Concentration distributions for different initial conditions. Dotted line is for $t = 0$, solid line is for a finite t. **a** Thin-layer geometry [case (1)]; **b** thick layer geometry [case (2)]; solid curve for $Dt = h^2$; **c** infinite couple [case (3)] (after Crank [14]

$$\mathrm{C(x,\,0) = 0,\, x > h.} \tag{5.7a}$$

$$\mathrm{BC : \partial C(0,\,t)/\partial x = 0} \tag{5.8a}$$

Solution:

$$C(x,t) = \frac{C_0}{2}\left[\mathrm{erf}\left(\frac{x+h}{2\sqrt{Dt}}\right) - \mathrm{erf}\left(\frac{x-h}{2\sqrt{Dt}}\right)\right], \tag{5.9}$$

where

$$\mathrm{erf}(\lambda) = \frac{2}{\sqrt{\pi}} \int_0^{\lambda} \exp(-\eta^2)\mathrm{d}\eta. \tag{5.10a}$$

Measure $C(x)$ for constant t. Note:

$$\mathrm{erfc}(\lambda) \equiv 1 - \mathrm{erf}(\lambda). \tag{5.10b}$$

item [3] Infinite Couple (Fig. 5.1c). A sample of uniform concentration C_0 is welded to a sample of uniform concentration C_1. The weld plane is situated at $x = 0$. Couple containing a volatile.

$$\begin{aligned} \text{IC: } C(x,0) &= C_1, \quad x < 0 \\ C(x,0) &= C_0, \quad x > 0. \end{aligned} \tag{5.11}$$

Solution:

$$C'(x,t) \equiv \frac{C(x,t) - C_0}{C_1 - C_0} = \left[1 - \mathrm{erf}\left(\frac{x}{2\sqrt{Dt}}\right)\right](12). \tag{5.12}$$

Measure $C(x)$ for constant t.

(4) Vapour-Solid Couple. A semi-infinite couple containing a volatile component component is placed into a dynamic vacuum at $t = 0$:

$$\text{IC: } C(x,0) = C_0, \quad x > 0 \tag{5.13a}$$

$$\text{BC: } C(0,t) = 0, \quad t > 0. \tag{5.13b}$$

Solution:

$$C(x,t) = C_0 \mathrm{erf}(\mathrm{x}/2\sqrt{Dt}). \tag{5.14a}$$

Exposing a sample initially devoid of volatile component to a vapour of the volatile component at a pressure in equilibrium with C_0 gives the analogous mathematics:

$$\text{IC: } C(x,0) = 0, \quad x > 0, \tag{5.14b}$$

$$\text{BC: } C(0,t) = C_0, \quad t > 0. \tag{5.15a}$$

Solution:

$$C(x,t) = C_0\left[1 - \mathrm{erf}(x/2\sqrt{Dt}\right] = C_0 \mathrm{erfc}(x/2\sqrt{Dt}). \tag{5.15b}$$

The same equations apply to *isotopic* exchange between solid and vapor. Measure either $C(x)$ at constant t or integral weight gain (loss) $\int_0^\infty \int_0^t C(x,t)dt\ dx$.

(5) Grain Boundary Diffusion. The mathematics in this case is more complicated [12], owing to the coupled lattice *diffusion*, but one still measures $C(x)$ at constant t.

(6) Exchange experiment [9]. This technique is used for materials for which a massive sample cannot be prepared. It involves diffusion exchange between an assembly of powder and a gas of limited volume, from which very small aliquots are drawn at different times.

In the first three sample configurations two bodies of widely different composition are brought into contact. The assumption implicit in the BC is that diffusing material passes across the resulting interface without hindrance, i.e. it is not held up by surface oxides, low solubility, chemical reactions, etc. Nonfulfilment of this condition leads to deviation of the experimental $C(x)$ from solution of the diffusion equation [18].

In the vapour-solid couple and the exchange experiment, the assumption implicit in the BC is that the surface of the solid equilibrates with the gas phase instantaneously. However, optical measurements of the change of the surface concentration at low temperature have indicated that the attainment of solid–gas equilibrium can be a slow process [12, 18].

In this connection we should add that the thin geometry has several advantages. The thin layer can be deposited without straining the sample, which is essential for single crystal samples. A thin layer also allows the use of highly specific *radioisotopes*, and thus measurements of diffusion without a chemical gradient. Diffusion under large chemical gradient can lead to deformation of the sample and generation of defects [3, 13]. For the above reasons, the thin layer geometry is most often used in experiments in which diffusion is measured in order to study the fundamentals of diffusion and defect behaviour in solids. Such experiments usually concern diffusion as a function of temperature, pressure or concentration, and small differences in D are imported, in contrast to engineering experiments in which the magnitude of the penetration of one material into another is of interest.

It should be noted that all the solutions to the diffusion equation considered above are expressed in terms of the dimensionless variable $x/(2\sqrt{Dt})$. The length $2\sqrt{Dt}\ is$ a kind of mean penetration distance, and this has to be in the same order of magnitude as the characteristic distance associated with an experiment. For sectioning experiment, the characteristic distance is the section thickness. For ion-beam depth profiling, it is the ion range, etc. [19].

In the ordinary thin-layer sectioning experiment, one wishes to measure diffusion over a drop in specific activity C of $\sim 10^3$; any effects due to diffusion along short circuiting paths are likely to show up as curvature in the penetration plot over such a range, while they may not be visible if the measurement is only over the factor of 6 in C [3]. Usually 20 sections suffice to define a penetration plot; from Eq. (8), the section thickness required to get a drop of 10^3 in C over 20 sections is

$$\theta \approx \sqrt{Dt}/3.8. \tag{5.16}$$

A preliminary estimate of D is useful in planning an experiment.
If the isotope decays significantly during the time of the experiment, more *radioisotope* has to be deposited. Under the conditions of $\theta \approx \sqrt{Dt}/3.8$, the specific activity drops by a factor of $\sim$2 per section at the 20th section. These last points on the penetration plot have the greatest weight in determining D, so the counting statistics must be maintained and the penetration plot extended as far as possible. This implies the use of an intense source of radioisotope; on the other hand, too much activity poses an unnecessary health hazard as well as increasing the dead-time correction. The *radiotracer* may rapidly reach the side surfaces of the sample by surface diffusion or evapouration, and then diffuse inward. To keep the diffusion one dimensional, one removes $\approx 6\sqrt{Dt}$ from the sides of the sample before sectioning.

5.2 Self-Diffusion Process

As it is well known, in all diffusion mechanisms the atoms under consideration have to carry out jumps between different sites [20]. If the extreme case of coherent tunneling [21] is left aside, the diffusional jumps are assisted by the thermal movement of the atoms. In the standard situation the jump rate is entirely determined by the temperature T (apart from the effects of hydrostatic pressure, which may be incorporated by formulating the theory in terms of *enthalpy* and Gibbs free energy). For the purposes of the present chapter, we may in the first approximation disregard quantum mechanical contribution to the diffusity (naturally excluding the self-diffusion in LiH), so that in cubic crystals the *diffusion coefficient* under standard conditions may be written as an Arrhenius expression

$$D_\alpha = D_{\alpha 0} \exp(-\mathrm{H}_\alpha^M / kT), \tag{5.17}$$

with the preexponential factor

$$D_{\alpha 0} = \mathrm{g}_\alpha a_0^2 \nu_{\alpha 0} \exp(\mathrm{S}_\alpha^M / k_B). \tag{5.18}$$

Here H_α^M denotes the enthalpy and S_α^M the entropy of migration, a_0 the lattice constant, $\nu_{\alpha 0}$ the attempt frequency, k_B has its usual meaning as Boltzmann's constant and g_α is a factor that takes into account the geometry of the crystal structure and the atomistics details of the different process. The subscript α refers to the defect species controlling the diffusion process, i.e. in the case of the direct interstitial mechanism it indicates the chemical nature, geometrical configuration, etc., of the interstitial involved, whereas in the case of indirect diffusion it characterises the intrinsic defects acting as diffusion vehicles. In the latter case, we should write β

instead of α if we wish to indicate that these intrinsic defects are monovacancies or monointerstitials.

The tracer *self-diffusion coefficient*, i.e. the diffusity of radioactive self-atoms under thermal-equilibrium conditions is given by [20]

$$D^T = \sum_{\beta=I,V} f_\beta D_\beta^{\mathrm{SD}} = \sum_{\beta=I,V} f_\beta D_\beta C_\beta^{\mathrm{eq}}, \tag{5.19}$$

where

$$C_\beta^{eq} = \exp(S_\beta^F/k)\exp(-\mathrm{H}_\beta^F/k_B T) \tag{5.20}$$

is the concentration of self-interstitial ($\beta = \mathrm{I}$) and monovacancy ($\beta = \mathrm{V}$) in thermal equilibrium. As it is clear, in Eq. (5.19), contributions by clusters of I or V are neglected. The f_β denote correlation factors, $D_\beta^{\mathrm{SD}} \equiv D_\beta C_\beta^{\mathrm{eq}}$ contributions to the uncorrelated self-diffusion coefficient $\sum_{\beta=I,V} D_\beta^{\mathrm{SD}}$ and S_β^F and H_β^F entropies and enthalpies of formation, respectively. Insertion of Eqs. (5.17), (5.18) and (5.20) into Eq. (5.19) yields

$$D^T = \sum_{\beta=\mathrm{I,V}} \mathrm{D}_\beta^T = \sum_{\beta=\mathrm{I,V}} f_\beta \mathrm{g}_\beta \mathrm{a}_0^2 \nu_{\beta 0} \exp(-\mathrm{G}_\beta^{\mathrm{SD}}/kT) = \sum_{\beta=\mathrm{I,V}} D_{\beta 0}^T \exp(-\mathrm{H}_\beta^{\mathrm{SD}}/kT) \tag{5.21}$$

with the preexponential factors

$$D_{\beta 0}^T = f_\beta \mathrm{g}_\beta \mathrm{a}_0^2 \nu_{\beta 0} \exp(-H_\beta^{\mathrm{SD}}/kT) \tag{5.22}$$

and the Gibbs free energy of self-diffusion

$$\mathrm{G}_\beta^{\mathrm{SD}} = \mathrm{H}_\beta^{\mathrm{SD}} - \mathrm{TS}_\beta^{\mathrm{SD}} \tag{5.23}$$

the self-diffusion enthalpy

$$\mathrm{H}_\beta^{\mathrm{SD}} = \mathrm{H}_\beta^F + \mathrm{H}_\beta^M \tag{5.24}$$

and the self-diffusion entropy

$$\mathrm{S}_\beta^{\mathrm{SD}} = \mathrm{S}_\beta^F + \mathrm{S}_\beta^M \tag{5.25}$$

The diffusion coefficient D^s of foreign substitutional atoms in *thermal equilibrium* may be derived from Eqs. (5.19) or (5.21) by inserting factor h_β under the summation signs. These factors account for the interaction between the intrinsic thermal equilibrium defects and the substitutional atoms. They depend on temperature and the atomic fraction of the substitutional atoms, unless this is small compared to unity. For more detailed and complete discussion in this field we refer the reader to reviews by Frank et al. [13, 20].

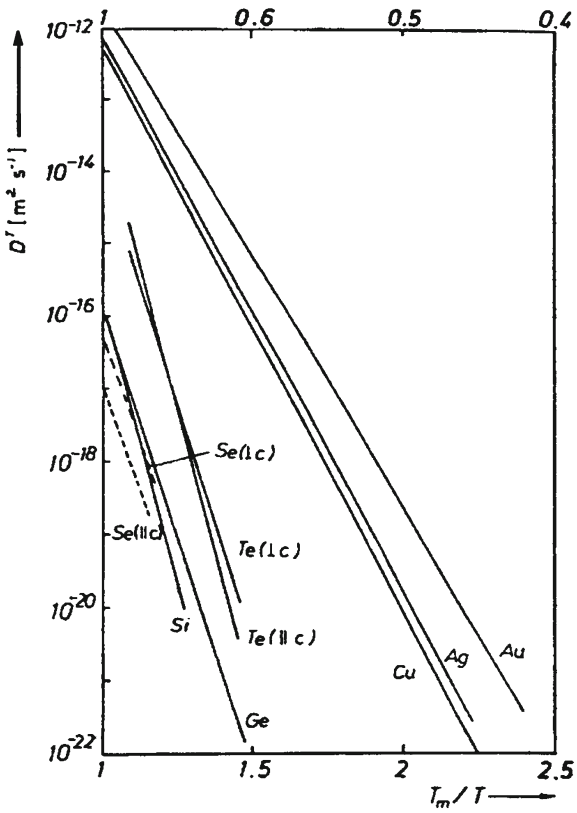

Fig. 5.2 Comparison between the self-diffusivities of the cubic semiconductors Ge and Si [20], the trigonal semiconductors Te [23, 24] and Se [25] and the typical metals Cu, Ag, Au (after [20])

Compared with *metals*, self-diffusion in *semiconductors* is a very slow process. For the elemental semiconductors this is illustrated in Fig. 5.2, in which the self-diffusivities of the cubic semiconductors Si and Ge and of the trigonal semiconductors Te and Se are compared with those of typical metals such as Cu, Ag and Au on a temperature scale normalised to the melting temperature T_m. Figure 5.2 reveals the following differences between metals and semiconductors, already emphasised by Seeger and Chik [22].

(1) Near the melting temperatures the self-diffusion in semiconductors is several orders of magnitude slower than in typical metals.
(2) At lower normalised temperatures the ratio of the self-diffusivities of metals and semiconductors becomes even larger.
Generally speaking, the origin of these differences lies in the homopolar bonding of the semiconductors (for details see [12, 16] and references therein).
As it is well known, the conventional and well-established techniques of determining the tracer self-diffusion coefficient D^T based on studying the redistribution of *radioactive* or stable tracers initially deposited on the specimen surface

of serial sectioning methods. In the case of radioactive isotopes, the redistribution may be investigated with radiation detection methods; for stable isotopes, secondary ion mass spectroscopy (SIMS) may be used (see also below).

5.2.1 SIMS Technique

The most complete description of the experimental technique for study of the *diffusion* processes in solids may be found in the excellent review by Rothman [18]. Here, we briefly discussed the peculiarity of sputtering and *SIMS* techniques.

We define microsectioning as the cutting of sections a few hundred nms or less in thickness, so that the surface on which the tracer is deposited, the "front" surface, is not necessarily flat on the scale of $\sqrt{Dt}$, and so the thickness of the individual sections are not determined separately [9, 12]. The isoconcentration contours then follow the contour of the front surface, and one must remove sections parallel to this non-flat surface, rather than parallel to a flat surface. If this condition is met and if the indulations in the front surface are gentle (radius of curvature $\rho \ll \sqrt{Dt}$), one can treat the sections as if they were flat [8].

In sputtering, material is removed by ion bombardment owing to the transfer of momentum from the bombarding ions to the atoms of the targets. A depth profile can be constructed by 1) analysing the sputtered-off material in a mass spectrometer (SIMS), 2) collecting and analysing the sputtered-off material, 3) determining the concentration of the diffusing material in the remaining surface by, e.g. Auger electron spectroscopy [26, 27], or 4) counting the residual activity of the entire sample [27]. As a rule, noble gas ions, especially Ar^+, are accelerated to a few hundred eV or more, with current densities $\leq 1\,\mathrm{mA\,cm^{-2}}$. This is called physical sputtering, in contrast to bombardment with reactive ions, which is called chemical sputtering. Typical removal rates are of the order of 10 $\mathrm{nm\,min^{-1}}$ for 1 $\mathrm{mA\,cm^{-2}}$ of 500 eV Ar^+ ions. There are two excellent reviews of the subject of sputtering [28, 29], and the reader is referred to these for an understanding of the process. All equipment for sputtering includes a vacuum chamber, pumping equipment and a controlled gas leak such as a micrometer needle valve. A high-speed pumping system is needed as gas is passed continuously and there are bursts of desorbed gases to cope with. Cold-trapped diffusion pumps, cryopumps or turbopumps have all been used. All sputtering equipment has a gaseous discharge in it. Common glow discharges are not suitable, as too high a gas pressure is required, with resulting low mean-free paths and back diffusion of the sputtered atoms. Therefore, either an ion gun or a rf power source is used. Two types of ion sources have been used in sectioning experiments, the custom-modified duoplasmatron of Maier and Schule [20], and a commercially available Kauffman-type gun [30, 31]. Almost any ion source used in ion milling should be usable The main requirement is that the source put out ion currents $\geq 1\,\mathrm{mA\,cm^{-2}}$ at $\sim$1kV over $\sim 4\,\mathrm{cm^2}$ area in a reasonably uniform beam ($\pm 10\%$ except at the very edge), and that

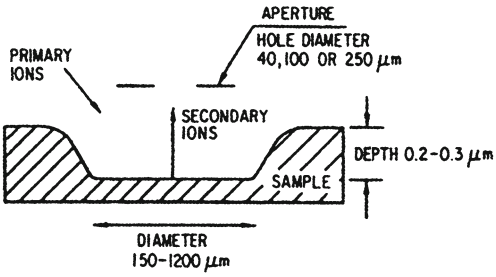

Fig. 5.3 Schematic diagram of crater caused by sputtering in a SIMS apparatus (after [20])

the current stay constant over a period of several hours. The length of a run is limited by life of the filament. In addition to the ion source, chamber, pumps and valving, one needs a collector and a sample holder. These are usually custom made. Designs have been given by Gupta and Tsui [32] and for rf systems as well as Mundy and Rothman [31] for ion gun systems. The collector is either a carousel, with six Al planchets, which allow six sections to be taken before the chamber is opened [33], or a device like a cameras back, on which poleester film is rolled; the latter allows 32 sections to be taken.

In the *SIMS* technique, the sample is bombarded by reactive ions, and the sputtered-off molecules are ionized in a plasma and fed into a mass spectrometer. The mass spectrum is scanned and the ion current for tracer and host atoms can be recorded simultaneously. The beam is swept over the sample and, in effect, digs a crater, the bottom of which is more or less flat; an aperture prevents ions originating from the edges of the crater from reaching the mass spectrometer (Fig. 5.3). The penetration plot is constructed from the plots of instaneous tracer/host atom ratio versus sputtering time and distance of sputtering time. The distance is obtained by using interferometric measurement of the total crater depth under the assumption that material is removed uniformly as a function of time. Large changes of chemical composition along the *diffusion* direction can invalidate that assumption. The limitations of the SIMS technique have been discussed by Liebl [33] and Reuter and Baglin [34], and a detailed description of its application to diffusion has been given by Macht and Naundorf [16, 35]. The major disadvantage of SIMS is its cost. The SIMS apparatus is commercially made [18] but represents a large capital investment. Not withstanding the cost of the apparatus careful controls must be applied to the measurements and artefacts [36] must be avoided.

If the entire of the sample is a section the depth of material removed is best determined by weighing on a microbalance. With care, a sample can be weighed to $\pm 3\mu$g, which corresponds to ± 150 nm for cross-sectional area of 0.1 cm^2 which is about the minimum useful area, and a density of 2 g cm^{-3}. For larger areas or densities, even better sensitivities are obtained, down to perhaps ± 10 nm [18].

5.2.2 Self-Diffusion of Li and H in LiH Crystals

Self-diffusion is the migration of constituent atoms in materials. This process is mediated by native defects in solids and thus can be used to study the dynamics and kinetics of these defects. The knowledge obtained in these studies is pivotal for the understanding of many important mass transport processes such as impurity diffusion in materials. Self-diffusion of D(H) and Li in LiH crystals is studied in papers [37–40], respectively. As was above shown the gas–solid isotope exchange method has been used for the measurement of *self-diffusion coefficients* in solids [36]. Two papers [37, 38] have reported on a thermogravimetric study of the pressure and temperature dependence of diffusion coefficient of the deuteride ion in LiH crystals. As it is well known, in this method a crystal of the compound of interest is equilibrated in a furnace with a gas usually containing an isotopic species of the diffusant. The weight change of the crystal due to the permutation process from the gas to the solid is then monitored as a function of time. By assuming that the mass uptake is due to the isotopic exchange process with deuterium gas and subsequent diffusion of the deuteride ion into the crystal and that the rate of the exchange process is diffusion controlled, the mass gain of the crystal was calculated from solution of Fick's law. The best least squares fit of the data obtained in papers [37, 38] to one–dimensional and three-dimensional models was used to find the diffusion coefficients and the activation energy for the deuteride ion.

According to [37] solution of Fick's second law [13]

$$\partial C/\partial t = \partial^2 C/\partial x^2 \tag{5.26}$$

subject to the boundary conditions

$$\begin{aligned} C(x,0) &= 0 \\ C(0,t) &= C_s, \end{aligned} \tag{5.27}$$

where C_s is the surface concentration of the diffusing species and lim C(0, t)→ 0, $x \rightarrow 0$ gives, for Q, the total amount of diffusing substance which has entered the solid at time t,

$$Q = 2A_s C_s (D/\pi)^{1/2} t^{1/2} + B, \tag{5.28}$$

where A_s is the total surface area of the crystal, D is the *diffusion coefficient* and B a constant that accounts for the initial condition that $Q \neq 0$ at $t = 0$. Q is expressed as the ratio of the number of moles of deuteride ion diffusing to total moles of LiH contained in the crystal.

Equation (5.28) may be written as

$$Q = C' t^{1/2} + B, \tag{5.29}$$

where C' is defined as

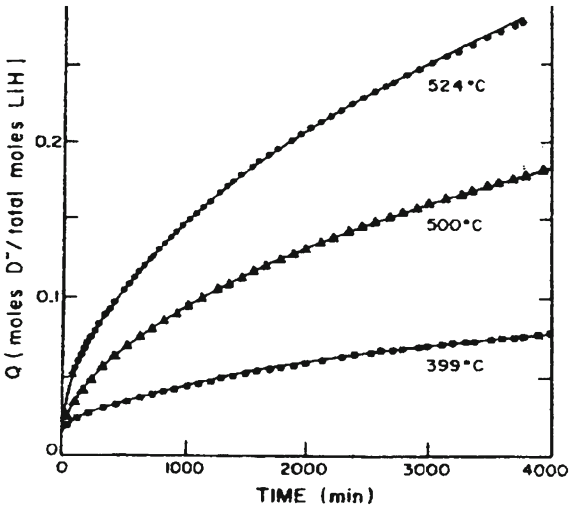

Fig. 5.4 Q as a function of time for data of samples 9, 10 and 13. The solid curves are the best least squares fit of Eq. (5.29) to the experimental data (after [38])

Table 5.1 Summary of one-dimensional semi-infinite solid data (after [38])

Sample, No.	T°C	$C' \times 10^3$, min^{-1}	C $\times 10^4$g cm^{-2}min$^{-1/2}$	E_a, kcal
8	550	4.74	3.96	22.7±2.8[a]
9	524	4.37	3.49	22±2[b]
10	500	2.80	2.52	
11	450	1.50	1.53	
12	410	1.37	0.96	
13	399	1.09	0.86	

[a] E_a as found from the best least squares fit of Eq. (28) to C with $\theta = 0.80$. The error reported is the 95% confidence level fit to the data. [b] E_a from Ref. [12]

$$C' = 2A_s C_s (D/\pi)^{1/2}. \tag{5.30}$$

With the assumption that the surface coverage C_s can be written in terms of an adsorption isotherm, θ, C' was rewritten as

$$C' = 0.8748(A_s\theta/\rho V)D^{1/2}, \tag{5.31}$$

where ρ is the density of LiH at a given temperature, V is the volume of the crystal and the constant includes the necessary factors for consistency of units. Rearrangements gives

$$C = C'(A_s/\rho V)^{-1} = 0.8748\theta D^{1/2}. \tag{5.32}$$

The values for C' were found from the fit of Eq. (5.29) to the data at each temperature (Fig. 5.4). All fits were exceptionally good (Table 5.1). Values of C calculated from C' by using the relation given in Eq. (5.26) are also given in Table 5.1.

Equation (5.32) may be written in the form

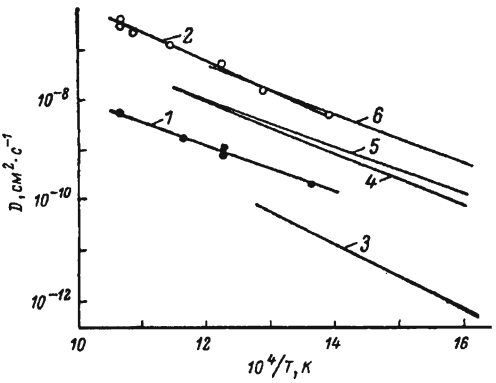

Fig. 5.5 Temperature dependence of self-diffusion coefficients Li (1, 3) and H (2, 4–6) in LiH single crystals; 1, 2 [39, 40]; 3, 6 [37]; 4, 5 [38] (after [12])

$$C = 0.8748\theta D_0^{1/2} \mathrm{e}^{-E_a/2RT} \tag{5.33}$$

by substituting for D,

$$D = \mathrm{D}_0 \mathrm{e}^{-E_a/2RT}, \tag{5.34}$$

where D_0 is a constant and E_a the activation energy.

According to Eq. (5.33), the temperature variance of C is determined by the exponential term involving temperature and the temperature dependence of the fractional surface coverage θ. If θ is known as a function of temperature, C may fit to Eq. (5.33) to give D_0 and the activation energy. Lacking knowledge of the exact variation of θ with temperature, Eq. (5.33) may be rewritten in the more convenient form

$$C/\theta = 0.8748 D_0^{1/2} \mathrm{e}^{-E_a/2RT} \tag{5.35}$$

and θ assumed to vary with temperature according to the expected behaviour outlined above. The quantity C/θ was next calculated using $\theta = T/(b + T)$ and the fit of the data to Eq. (5.29) found, giving the activation energy as 22.1±3.0 kcal. and D_0 as $4.01 \times 10^{-3} \mathrm{cm}^2\mathrm{s}^{-1}$. The activation energy thus found is in good agreement with the value obtained by Funkee and Richtering from NMR measurements, 22±2 kcal. [16].

In three-dimensional bulk *diffusion model* the solution to Fick's law [14] for a finite solid has the next relation

$$\mathrm{Q} = \theta \left\{ \begin{array}{l} 1 - \left[\sum_{u=0}^{\infty} \frac{8}{(2u+1)^2\pi^2} \exp\left(\frac{-(2u+1)^2\pi^2 Dt}{4a^2} \right) \right] \\ \times \left[\sum_{v=0}^{\infty} \frac{8}{(2u+1)^2\pi^2} \exp\left(\frac{-(2\mathrm{v}+1)^2\pi^2 Dt}{4b^2} \right) \right] \\ \times \left[\sum_{w=0}^{\infty} \frac{8}{(2w+1)^2\pi^2} \exp\left(\frac{-(2\mathrm{w}+1)^2\pi^2 Dt}{4c^2} \right) + B \right] \end{array} \right\}, \tag{5.36}$$

Table 5.2 Comparison of tracer diffusion coefficients as found from one- and three-dimensional models (after [38])

Sample No.	$T°$ C	$1-D^a \times 10^9 \mathrm{cm}^2\,\mathrm{s}^{-1}$	$3-D^b \times 10^9 \mathrm{cm}^2\mathrm{s}^{-1}$	$3-\mathrm{D}^c$
8	550	5.8	8.7	0.2±0.1
9	524	3.7	5.3	
10	500	2.3	3.4	
11	450	0.84	1.1	
12	410	0.34	0.41	
13	399	0.26	0.31	

[a] Calculated from Eq. (5.28). [b] Calculated from Eq. (30). $3-D^c$ is the data from Ref. [39, 40]

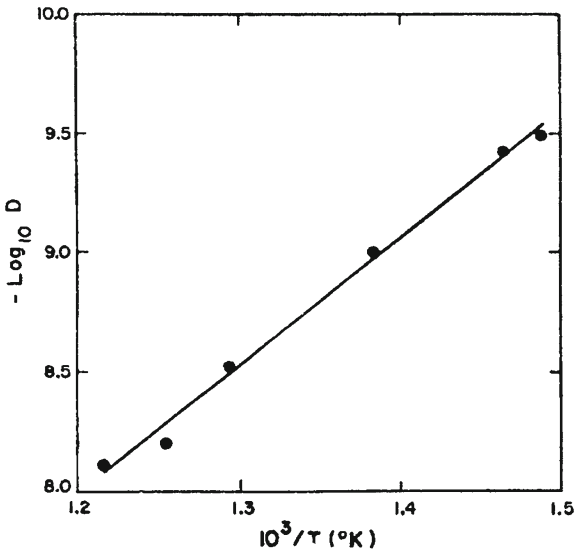

Fig. 5.6 Arrhenius plot of the diffusity of D^- in LiH in the temperature region 400−550°C for $\theta = 0.8$. The activation energy as determined from this plot is 24.3±2.6 kcal (after [38])

where the symbols are as previously defined and $2a$, $2b$ and $2c$ are the dimensions of the crystal in the x, y and z directions. The best fit of the experimental data of papers [37, 38] gives for the diffusion coefficient as a function of temperature, $D = 2.41\times10^{-2}\mathrm{e}^{-24.3\times10^3/RT}\mathrm{cm}^2\mathrm{s}^{-1}$. The diffusion coefficient for deuteride ion in lithium hydride at 465°C reported in paper [37] to have been found from three-dimensional model was $(1.9\pm0.6)\times10^{-9}\mathrm{cm}^2\mathrm{s}^{-1}$ (Fig. 5.5). The diffusion coefficient calculated from Eq. (5.36) was $1.6\times10^{-9}\mathrm{cm}^2\mathrm{s}^{-1}$. A comparison of tracer diffusion coefficients as calculated from one- and three- dimensional models is given in Table 5.2, and a plot of—log$D$ versus $10^3/T$ is given in Fig. 5.6.

The activation energies for various migrating species have been theoretically calculated by Dellin et al. [41]. They find activation energies for interstitial H^- diffusion to lie in the range 11.5 to 23 kcal. while activation energy for H^-vacancy migration is calculated to be 2.3 kcal. From these calculations interstitial H^-migration would

Table 5.3 Self-diffusion data for germanium and silicon (after [20])

Element	D_0^T (10^4 m^{2}s^{-1})	H^{SD} (eV)	Temperature range (K)	Technique
Ge	7.7	2.95	1039–1201	SG
	32	3.1	1023–1143	SG
	44	3.12	1004–1188	SM + GM
	10.8	2.99		
	24.8	3.14	822–1164	SS
	13.6	3.09	808–1177	SS
	1.2×10^{-3}	3.05	543–690	SIMS
Si	1800	4.77	1473–1673	HL
	1200	4.72	1451–1573	CS
	9000	5.13	1373–1573	ES
	1460	5.02	1320–1660	SS
	8	4.1	1173–1373	R
	154	4.65	1128–1448	SIMS,^{30} Si
	20	4.4	1103–1473	R

SG sectioning by grinding; *SAM* Steigmann's method; *GM* Gruzin's method; *SS* sectioning by sputtering; *HL* hand lapping; *CS* chemical sectioning, n activation of ^{30}Si; *ES* electrochemical sectioning; *R* (p,γ); resonance of ^{30} Si

seem possible based on the activation energy of about 24 kcal. found by Spencer et al. [38]. However, Dellin et al. [41] in agreement with Pretzel et al. [42] find that interstitial H^- is an unstable species in LiH and thus could not be the diffusing species.

To the conclusion of this part, we should indicate once more that the activation energy found by Spencer et al. [38] ~24 kcal. is in excellent agreement with the 22 kcal. determined for H^- *self-diffusion* in LiH by NMR [12]. This agreement, plus the consistencies of previous work [37] , makes D^- *vacancy* migration still the most likely species and mode of migration [39, 40].

5.2.3 Self-Diffusion in Si and Ge

In intrinsic germanium the temperature dependence of the tracer *self-diffusion coefficient* of the *radioactive isotope* ^{71}Ge has been measured by several groups [43–46] by means of different techniques (Fig. 5.7). With the exception of the latest experiments, precision grinding techniques were used to remove sections with thickness of the order of 1 μm from the diffusion zone of the annealed specimens. As a consequence, the temperature range covered by the earlier experiments is rather limited. By means of a sputtering technique for serial sectioning [46] have been able to extend the range of self-diffusion studies in Ge to diffusivities as low as 10^{-22} m^{2}s^{-1}.

The overall agreement between Ge self-diffusion data of different authors is good. In the region of overlap a small difference between the data of Vogel et al. [46] and those of the earlier workers may be seen. We tend to attribute this to problems in

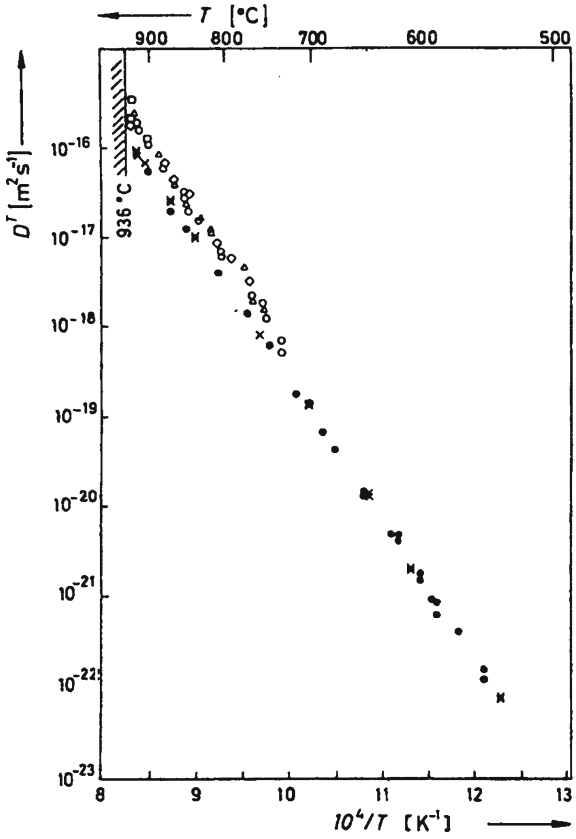

Fig. 5.7 Tracer self-diffusion coefficient of Ge as a function of temperature: (◇) [43]; (△) [44]; (□) [46]; (•) [46]; x [46] (after [20])

determining small diffusion coefficients during the earlier work. In the work of Valenta and Ramasastry [44], the condition $\delta \ll \sqrt{D^T t}$ (δ-thickness of the deposited tracer layer) was not always fulfiled. Since, nevertheless, these authors used the thin-film solution of the diffusion equation to deduce tracer diffusion coefficients, the obtained values are likely to be somewhat larger than the true D^T values. As may be seen in Fig. 5.7, the temperature dependence of the D^T data of GE is well described by an Arrhenius law (the preexponential factors D_0^T and the self-diffusion enthalpies H^{SD} obtained from measurements of different authors are compiled in Table 5.3). Seeger and Frank [47] argued that this result may be accounted for in terms of an indirect self-diffusion mechanism involving one type of intrinsic defect. Guided by further observations, they suggest that it is the vacancy mechanism [20] that controls self-diffusion in Ge. Table 5.3 shows that the preexponential factor D_0^T of Ge is considerably larger than the D_0^T values typical for metals ($10^{-6}\,\mathrm{m^2 s^{-1}} \lesssim D_0^T \lesssim 10^{-4}\,\mathrm{m^2 s^{-1}}$) [20]. Arguing that for an ordinary mechanism the product $f_{\mathrm{v}} g_{\mathrm{v}} a_0^2 \nu_{\mathrm{v}0}$ in Eq. (5.16) for $D_{\mathrm{v}0}^T (\equiv D_0^T)$ should be of the same order of magnitude for Ge and metals, Seeger and Frank [47] interpreted the large D_0^T value of Ge in terms of a large self-diffusion

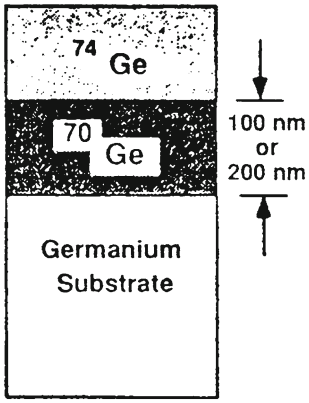

Fig. 5.8 Schematic of the isotope heterostructure used by Fuchs et al. (after [48])

entropy of the vacancy in Ge, $S_v^{SD} \approx 10\,k$. They suggested that this large S_v^{SD} value arises from a spreading out of the vacancy over several atomic volumes.

As we can see from Table 5.3 the published value of fundamental quantities such as the *diffusion coefficient* vary by several orders of magnitude for various authors [20, 47]. Such a spread in the experimental data makes it difficult to determine conclusively the underlying physical processes. Reliable diffusion data are therefore crucial to clarify the diffusion mechanisms and to accurately determine the corresponding material parameters. The conventional technique (Table 5.3) to determine the self-diffusion coefficient D^{SD} in semiconductors is to deposit s thin layer of *radioactive* tracer on the surface of the crystal (e.g. ^{71}Ge; ^{31}Si). In a subsequent annealing step the tracers diffuse into the crystal. The depth profile of the tracer atoms is then determined by serial sectioning and measurements of the corresponding radioactivity. There are several experimental difficulties arising from this method [48].

(1) Traditionally, lapping and grinding was used for the serial sectioning. This requires that the mean penetration distance $(D^{SD}t)^{1/2}$ of the tracer atoms during the time t of a diffusion anneal has to be in the μ m range. Especially in silicon, the large distance and the short half-life (2.6 h for ^{31}Si) limit this method to be applicable only to higher temperatures (larger D^{SD}). Germanium is more convenient in this respect (the half-life period of ^{71}Ge is 11.2 days), but it was not until microsectioning technique (e.g. sputtering) was invented that the measurements could be extended to lower temperatures in recent years [49–53].
(2) Surface effects such as oxidation, contamination, strain, etc. might influence the tracer diffusion substantially (e.g. through the formation of intrinsic defects). Fuchs et al. [48] recently reported results of a very accurate method to measure the *self-diffusion coefficient* of Ge which circumvents many of the experimental problems encountered in the conventional methods. These authors used germanium isotopic heterostructures (stable *isotopes*), grown by molecular-beam epitaxy (MBE). As it is well known, isotope heterostructures consist of layers

of pure (e.g. ^{70}Ge, ^{74}Ge) or deliberately mixed isotopes of a chemical element. Figure 5.8 shows the schematic of the particular samples used by Fuchs et al. [48]. At the interface only the atomic mass changes, while (to first order) all the other physical properties stay the same. In the as-grown samples, this interface is atomically flat with layer thickness fluctuations of about two atomic ML (for details see [54]). Upon annealing, the isotopes diffuse into each other (self-diffusion) with a rate which depends strongly on temperature. The concentration profiles in paper [48] were measured with *SIMS*, after pieces of the same samples have been separately annealed at different temperatures. This allows an accurate determination of the *self-diffusion enthalpy* as well as the corresponding entropy. The isotopic heterostructures are unique for the self-diffusion studies in several aspects [16].

(1) The *interdiffusion* of germanium isotopes takes place at the isotopic interface **inside** the crystal, unaffected by possible surface effects (e.g. oxidation, impurities and strain) encountered in the conventional technique.
(2) One sample annealed at one temperature provides five more or less independent measurements (Ge consists of five stable isotopes). Their initial respective concentrations vary for the different layers of the as-grown isotope heterostructure. After annealing, the concentration profile of each of the five isotopes can be analysed separately to obtain five data points for each annealing temperature. The samples were cut into several pieces. One piece was kept in paper [48] for reference (as-grown), they were separately annealed at five different temperatures (543, 586, 605, 636 and 690°C). The temperature controller permitted a variation of the temperature of 1−2°C. The recording of the concentration depth profiles of all five stable Ge isotopes was performed with SIMS. The oxygen primary beam had an impact energy of 8 keV per incident ion. The beam was rastered over a square area of about 200 μm in size and the detected secondary ions extracted from the central 30 μm diameter region of the crater. The precision of the SIMS data was estimated to be within ±5%. The depth resolution of the system was determined from profiles taken from the as-grown samples with an atomically flat interface. What theoretically should be a step function in the concentration profile appeared as a slope of about 4 nm per decade of the measured atomic fraction at the leading edge of a layer, and about 16 nm per decade at the falling edge [48, 53].

As it is well known, diffusion in the crystals occurs through jumping thermally activated between different sites in the lattice [6, 7]. In principle, there are many possibilities for such jumps (substitutional or interstitial sites, vacancies, etc. [9]. In Ge crystals, however, it is known that the only process of significance for the migration of germanium atoms is through the vacancy mechanism [53]. In this case the self-diffusion coefficient D^{SD} can be written as as Arrhenius expression [48] (Eq. (5.22))

$$D^{\mathrm{SD}} = g f a^2 \nu_0 \exp\left[\frac{-G^{\mathrm{SD}}}{k_B T}\right] = D_0 \exp\left[\frac{-H^{\mathrm{SD}}}{k_B T}\right] \tag{5.37}$$

where G^{SD} is the Gibbs free energy of self-diffusion,

$$\mathrm{G}^{\mathrm{SD}} = \mathrm{H}^{\mathrm{SD}} = \mathrm{TS}^{\mathrm{SD}}, \tag{5.38}$$

H^{SD} is the self-diffusion enthalpy, and the preexponemntial factor

$$D_0 = gfa^2\nu_0 \exp\left[\frac{S^{\mathrm{SD}}}{k_B}\right] \tag{5.39}$$

contains the self-diffusion entropy S^{SD}, the correlation factor f (f $= 1/2$ for the vacancy mechanism in the diamond lattice [6], the attempt frequency ν_0, the geometric factor g (g $= 1/8$ for vacancies in Ge and the lattice constant a; k is Boltzmann's constant (part 4.2) The enthalpy H^{SD} and the entropy S^{SD} depend on the formation (subscript F) as well as the migration (subscript M) of the vacancy:

$$H^{\mathrm{SD}} = H_F^{\mathrm{SD}} + H_M^{\mathrm{SD}} \quad \text{and} \quad S^{\mathrm{SD}} = S_F^{\mathrm{SD}} + S_M^{\mathrm{SD}} \tag{5.40}$$

The quantity which we can extract from the data of paper [48] is primarily the *self-diffusion coefficient* D^{SD} as a function of annealing temperature T. This was done in citing paper by fitting of experimental depth profiles to theory, with D^{SD} being the only fitting parameter. Equation (5.31) then allows to determine the *self-diffusion enthalpy* H^{SD}, and the self-diffusion entropy S^{SD} is deduced using Eq. (5.40). Solving Fick's diffusion equation for the specific geometry of samples used in indicated paper (Fig. 5.8), these authors obtain the atomic fraction c_i of a given germanium isotope i in terms of error functions (erf) (Eq. 5.36):

$$\begin{aligned} \mathrm{c}_i(\mathrm{x}) = &\left\{\frac{c_i^{0,\mathrm{I}} - \mathrm{c}_i^{0,\mathrm{II}}}{2}\mathrm{erf}\left[\frac{h/2 + x}{2\sqrt{D^{\mathrm{SD}}t}}\right] + \mathrm{c}_i^{0,\mathrm{I}}\right\} \\ &+ \left\{\frac{c_i^{0,\mathrm{II}} - \mathrm{c}_i^{0,\mathrm{III}}}{2}\mathrm{erf}\left[\frac{h/2 - x}{2\sqrt{D^{\mathrm{SD}}t}}\right] + \mathrm{c}_i^{0,\mathrm{III}}\right\} \end{aligned} \tag{5.41}$$

where h is the layer thickness (110 or 200 in Ge samples, see Fig. 5.8), and $\mathrm{c}_i^{0,\mathrm{I}}$, $\mathrm{c}_i^{0,\mathrm{II}}$ and $\mathrm{c}_i^{0,\mathrm{III}}$ are the initial concentrations of the isotope i in the enriched ^{74}Ge layer, in the enriched ^{70}Ge layer, and in the substrate, respectively. Figure 5.9 shows the profiles of all five isotopes of an annealed sample (586°C for 55,55h), together with a fit of the data to Eq. (5.41). For clarity only the fit to the ^{70}Ge profile is shown, but other profiles can be independently fitted as well. The excellent quality of the fit over four orders of magnitude displays the remarkable accuracy of the method used by Fuchs et al. As a reference, the corresponding concentration profiles for as-grown samples are displayed in Fig. 5.10. The annealing time was purposefully chosen such that the plateaus in the annealed samples (around 300 and 100 nm) correspond to the original concentrations in the isotopically enriched layers.

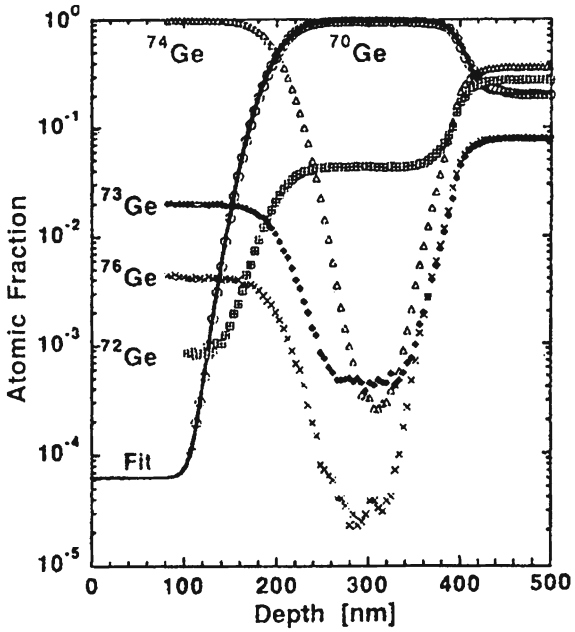

Fig. 5.9 Experimental depth profile of the atomic fraction of ^{70}Ge, ^{72}Ge, ^{73}Ge, ^{74}Ge and ^{76}Ge (symbols) of a diffusion-annealed sample (annealed at 586°C for 55.55 h). The solid line is a fit of the ^{70}Ge data of Eq. (35). For clarity, only the fit to the ^{70}Ge data is shown (after [48])

The values for the self-diffusion coefficient D^{SD} obtained at 543, 586, 605, 636 and 690°C are presented in an Arrhenius plot in Fig. 5.11. The lines in Fig. 5.11 represent the results of previous authors [9]. The variation in D^{SD} obtained from different groups is comparable with the scatter of the data within the work of each of the publications. Fitting the experimental values of D^{SD} to Eq. (5.31) Fuchs et al. obtain the self-diffusion enthalpy H^{SD} equals 3.0(5) eV. As can see from Table 5.3 this is in excellent agreement with the previously published values of 2.95–3.14 eV. The value of experimental preexponential factor D_0 is $1.2 \times 10^{-3} m^2 s^{-1}$. This compares to previously published values of $(0.78 - 4.4) \times 10^{-3} m^2 s^{-1}$. Converting D_0 into the self-diffusion entropy $S^S D$ through Eq. (5.39) they obtain $S^{SD} \approx 9\,k$ (using $\nu_0 = 8 \times 10^{12} s^{-1}$ and a $= 0.565$ nm). The self-diffusion entropy for Ge is larger than for metals (2–4) k. As an explanation, Seeger and Frank [48] invoked the idea of extended (spread-out) defects have proposed that vacancy in Ge is strongly relaxed [53].

Finally, we want to mention the effect of the *isotopic* mass on the self-diffusion coefficient [10, 11]. The many-body treatment of atomic jump processes leads to an expression for the strength of the isotope effect in terms of the correlation factor f of Eq. (5.33) and the fraction ΔK of the kinetic energy which is associated with the motion in the jump direction [10, 53].

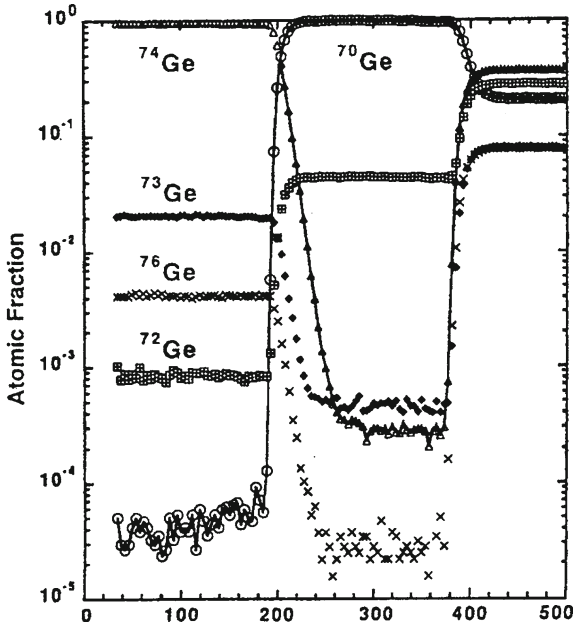

Fig. 5.10 Experimental depth profiles of the same sample as Fig. 5.9, but before annealing (after [48])

$$\frac{\left[\frac{D_{\mathrm{I}}}{D_{\mathrm{II}}}\right]-1}{\left[\frac{m_{\mathrm{II}}}{m_{\mathrm{I}}}\right]^{1/2}-1}=f\Delta K. \tag{5.42}$$

In the previous Ge self-diffusion experiments, Campbell [45] found fΔK values between 0.26 and 0.30, which translates into a ratio of $D_{SD}^{70Ge}/D_{SD}^{74Ge}$ between 1.007 and 1.008 [11, 55]. This small difference, however, is below the precision of the Fuchs et al. work. When fitting the experimental depth profilies to Eq. (5.41), they could indeed not detect any appreciable difference between the different isotopes. In addition, such small deviations would be insignificant in the Arrhenius plot (logarithmic scale of D^{SD} in Fig. 5.11) for the determination of the self-diffusion enthalpy $H^{SD}$and entropy S^{SD}.

Very recently Bracht et al. [56] have reported the diffusion of *boron*, *arsenic* and *phosphorous* in *silicone isotope* multilayer structures at temperatures between 850°C and 1100°C [52, 53]. The diffusion of all dopants and self -atoms at a given temperature is modelled with the same setting of all native point defect-related parameters. As an example, on Fig. 5.12 the concentration profiles of ^{31}Si along with the corresponding ^{30}Si profiles measured with SIMS after diffusion are shown. The diffusion of P in the isotope structure leads to an I (interstitial) supersaturation and V (vacancy) undersaturation and therewith suppresses the contribution of vacancies in P and Si diffusion compared to the diffusion of As. This increases the sensitivity of the P and Si profiles to negatively charged self-interstitial (Fig. 5.12). The demand

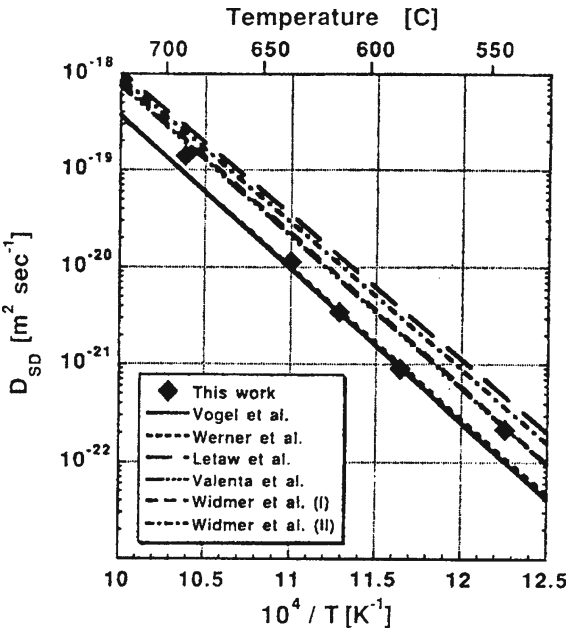

Fig. 5.11 Arrhenius plot of the self-diffusion coefficient as a function of temperature. Data of Fuchs et al. [48] agree favorably well with the most recent data [52, 53]. The older data might be less accurate [12] (after [48])

to describe the diffusion of all dopants and the corresponding Si profiles at a given temperature with the same energy levels of the native-point defects led to the conclusion that negatively charged vacancies rather than negatively charged self-interstitial dominate under n-type doping. Successful modelling of the simultaneous P and Si diffusion requires a contribution of a singly positively charged mobile P defects to P diffusion [52, 53, 57].

5.3 Isotope Dependence of Thermal Expansion Coefficient

It is well known that in real solids the forces between atoms are not truly *harmonic*. The higher the temperature, the more phonons that are excited and the more pronounced the effects of anharmonicity [59]. This leads to changes in the equilibrium separation of the atoms. The lattice therefore expands. Thermal expansion arises as a direct result of the asymmetrical dependence of potential energy on atomic separation, i.e. *anharmonicity* [59]. It is therefore not so surprising that the variation of the coefficient of *thermal expansion* with temperature parallels that of the heat capacity (details see below). When discussing the thermal behaviour of solids, it is important to remember that the energy content of the lattice resides in the phonons and not in particular atoms [60]. This may seem paradoxical, but the point is that we cannot convey thermal energy to a particular atom (we exclude the case of isolated impurity atoms). We cannot cause an atom to vibrate without exiting a collective oscillation, a

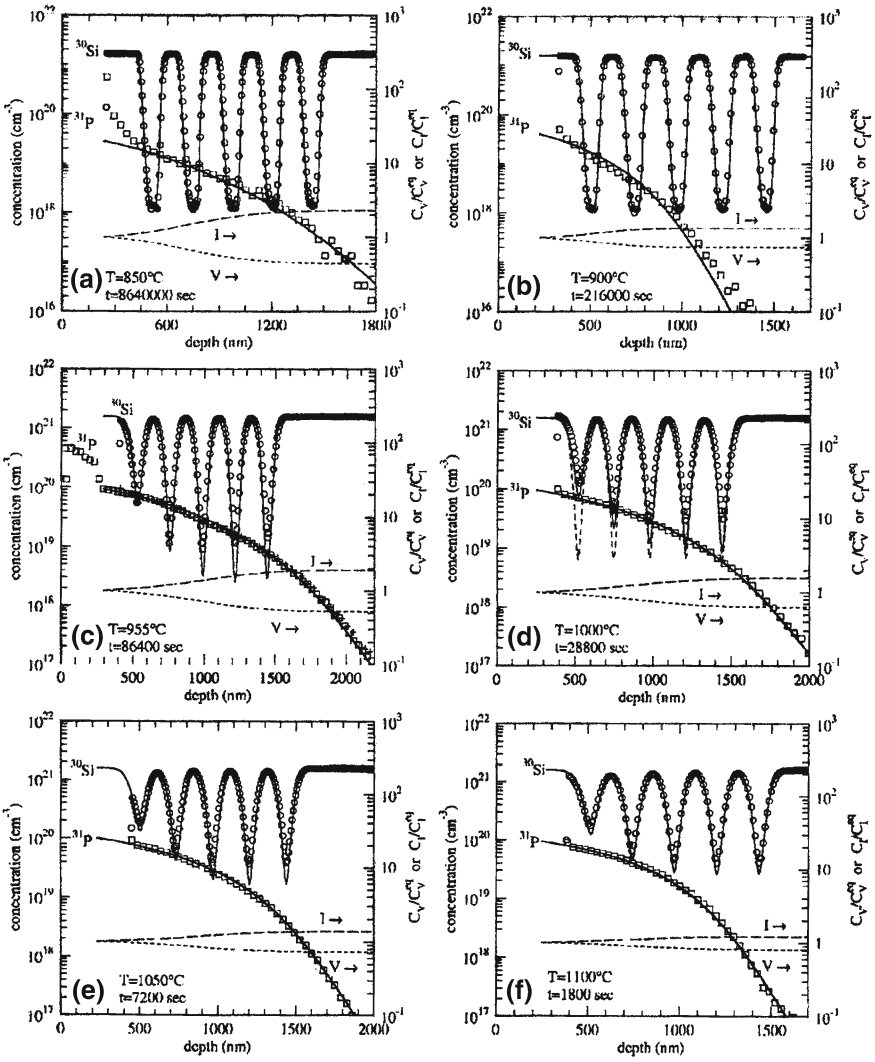

Fig. 5.12 SIMS concentration profiles of ^{31}P and ^{30}Si after annealing of the P-implanted Si isotope structure at temperatures and times indicated in the figures. The solid line in **a**–**f** represent theoretical best fit. The lower dashed lines show the corresponding super-and undersaturation of self-interstitial and vacancies, respectively. The upper dashed line in **d** is the Si profile that is expected in the case Si diffusion proceeds under intrinsic and thermal-equilibrium conditions (after [56])

phonon [61]. In a pure crystal, and within the *harmonic approximation*, two or more phonons may pass through one another without interaction. At the surface of the sample these phonons would be reflected and continue to exist in unchanged form. But in real solids we find imperfections and anharmonicity, which cause phonons

to interact, to be scattered and to decay. Phonons therefore have finite lifetime and we must think of phonon wave packets with particle-like properties. These phonons behave very much like particles in a gas: they constantly interact (collide) and in a kinetic equilibrium at a given temperature. That this is the case is particularly evident in the thermal conductivity (see below). In insulators and semiconductors (non-metals) heat is conducted solely by the phonons and one might expect thermal energy to be transported at a speed corresponding roughly to that of sound. This may be the case in nearly perfect single crystals at very low temperatures [62, 63]. However, the mutual interactions of phonons lead to mean free paths of order 100 Å, and the phonon gas therefore conducts heat in a similar manner to an ordinary gas. The energy diffuses through the gas and this is a slow process. We should recall, that Debye, long before the concept of the phonon was developed, applied the results of simple kinetic gas theory to solids with remarkable qualitative success [64].

5.3.1 Thermal Expansion Coefficient

Thermodynamical examination of the question about the thermal expansion of solid is leading to the expression [65]

$$\left(\frac{\partial V}{\partial T}\right)_P = -\left(\frac{\partial S}{\partial P}\right)_T, \tag{5.41}$$

here S is entropy and P is the pressure. To transform (5.41), we have

$$\left(\frac{\partial V}{\partial T}\right)_P = -\left(\frac{\partial S}{\partial V}\right)_T \left(\frac{\partial V}{\partial P}\right)_T, \tag{5.42}$$

or

$$\frac{\beta}{\chi_T} = \left(\frac{\partial S}{\partial V}\right)_T, \tag{5.43}$$

where $\chi_T = -\frac{1}{V}\left(\frac{\partial V}{\partial P}\right)_T$ is the *isothermal compressibility* [66].

So far the heat capacity at the constant of volume

$$C_V = \frac{1}{T}\left(\frac{\partial S}{\partial T}\right)_V \tag{5.44}$$

in such case from (5.43) it is followed

$$\beta = -\frac{C_V \chi_T}{T}\left(\frac{\partial T}{\partial V}\right)_S \tag{5.45}$$

or in different form

$$\beta = -\frac{C_V \chi_T}{T}\left(\frac{\partial \ln T}{\partial \ln V}\right)_S, \tag{5.45'}$$

where

$$\gamma = -\left(\frac{\partial \ln T}{\partial \ln V}\right)_S. \tag{5.46}$$

Here γ characterises the change of the solid temperature at the adiabatic volume's change. For the first time the relation (5.46) was obtained by Gruneisen [65]. Based on the one atom solid Grüneisen derived the fundamental law, and connected the thermal expansion coefficient with others thermodynamical meanings.

Grüneisen is based on the expression of the free energy in the Debye's [64] approximation

$$F = \mathrm{U}_0 + 3RT3\left(\frac{T}{\Theta}\right)^3 \int_0^{\theta/T} f(x)x^2 \mathrm{d}x = \mathrm{U}_0 + 3RT\left[\mathrm{f}\left(\frac{\mathrm{T}}{\theta}\right) - \frac{1}{3}D\left(\frac{\mathrm{T}}{\theta}\right)\right], \tag{5.47}$$

where

$$f(x) = \ln\left[1 - \exp(-x)\right] \tag{5.48}$$

and

$$D(x) = \frac{3}{x^3}\int_0^x \frac{\xi^3}{e^{\xi}-1}. \tag{5.49}$$

Here U_0 is the energy of *zero-point vibrations* which is the function of the volume only. Taking into account expression (5.50)

$$P = -\left(\frac{\partial F}{\partial V}\right)_T \tag{5.50}$$

then from (47) we get

$$P = -\left(\frac{\partial U_0}{\partial V}\right)_T - \frac{1}{\theta}\left(\frac{\partial \theta}{\partial V}\right)_T 3RTD\left(\frac{\theta}{T}\right). \tag{5.51}$$

Using the expression for the inner energy in the Debye approximation $\mathrm{E} = 3RTD(\frac{\theta}{T})$, we obtain

$$P + \left(\frac{\partial U_0}{\partial V}\right)V = -\frac{\partial \ln\theta}{\partial \ln V}\mathrm{E} = \gamma \mathrm{E}, \tag{5.52}$$

where the value of

$$\gamma = -\frac{\partial \ln\theta}{\partial \ln V} \tag{5.53}$$

is known as Grüneisen's parameter, characterised the change of the Debye's temperature with the change of the volume. Differentiating expression (5.51) on T at $V = \text{const}$. we will have

$$\left(\frac{\partial P}{\partial T}\right)_V V = \gamma C_V. \tag{5.54}$$

From Eq. (5.54) and using the thermodynamical relations we have

$$\left(\frac{\partial P}{\partial T}\right)_V = -\frac{\left(\frac{\partial V}{\partial T}\right)_P}{\left(\frac{\partial V}{\partial P}\right)_T} \tag{5.55}$$

and in the final form, we obtain

$$\frac{1}{V}\left(\frac{\partial V}{\partial T}\right)_P = \gamma \frac{C_V}{V}\left[-\frac{1}{V}\left(\frac{\partial V}{\partial P}\right)_T\right]$$
$$\text{or} \quad \beta = \gamma \frac{C_V}{V}\chi_T. \tag{5.56}$$

The expression (5.56) is named the relation of Grüneisen and links the thermal expansion coefficient (β) with Grüneisen's parameter (γ) and other thermodynamical meanings (here V is a molecular volume).

The temperature dependence of the thermal expansion coefficient may be established from relation (5.56). Since γ (its meaning vibrates in the range $1 \div 3$) in the Grüneisen approximation from the temperature is not dependent and χ_T and V are the weak temperature functions, so temperature pace of the thermal expansion coefficient will determine the temperature's pace of the *specific heat*. It means that at $T = 0\,\text{K}\beta$ aspires to zero also. At high temperature β aspires to constant value.

According Landau and Lifshitz [65] the thermodynamical potential at low temperature is expressed as:

$$\Phi = \Phi_0(P) - \frac{\pi^2 T^4 V_0(P)}{30(\hbar\bar{\nu})^3}, \tag{5.57}$$

where Φ_0 (P) is not dependent on the temperature part of the thermodynamical potential, $\bar{\text{v}} = \bar{\text{v}}(P)$ is the velocity of the sound. Expressing through volume the thermodynamical potential

$$V = \frac{\partial \Phi}{\partial P} = V_0(P) - \frac{\pi^2 T^4}{30\hbar^3}\frac{\partial}{\partial P}\left(\frac{V_0}{\bar{\text{v}}^3}\right) \tag{5.58}$$

we will obtain the following expression for the *thermal expansion coefficient*:

$$\beta = -\frac{2\pi^2 \text{T}^3}{15\hbar^3 \text{V}_0}\frac{\text{d}}{\text{d}p}\left(\frac{V_0}{\bar{\text{v}}^3}\right). \tag{5.59}$$

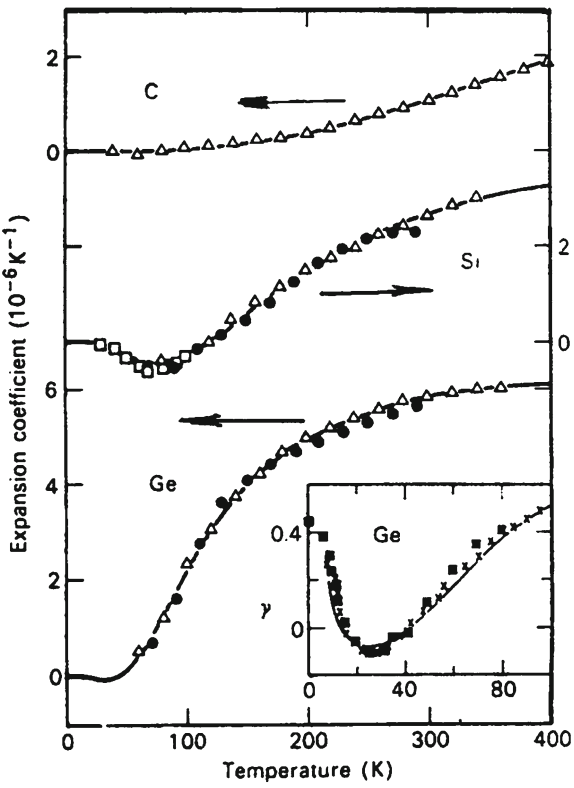

Fig. 5.13 Comparison the experimental results with calculation one for C, Si and Ge. (1) theory [71]; (2)–(4) experimental results according to (2) [67]; (3) [68]; and (4) [69] (after [70])

From this relation it is evident that at the low temperatures the coefficient of the thermal expansion is proportional to the cube of absolute temperature.

At the high temperatures the thermodynamical potential has next form

$$\Phi = \Phi_0 (P) - C_V T \ln T + C_V T \ln \hbar \bar{\nu} (P) , \tag{5.60}$$

and analogous for preceding one for β, we have

$$\beta = \frac{C_V}{V_0 \bar{\nu}} \frac{d\bar{\nu}}{\mathrm{d}P} \tag{5.61}$$

From the last relation it can be seen that the sign of β will be determined by the sign of $\frac{d\bar{\nu}}{\mathrm{d}P}$.

As an example in the Fig. 5.13 it displays the temperature dependence of β for the well known semiconductors C, Ge and Si.

From this picture it can be seen that there is no bad agreement between the theory and experiment, although as a rule that is not observed [80]. The experimental data on the temperature dependence of the thermal expansion coefficient in the wide

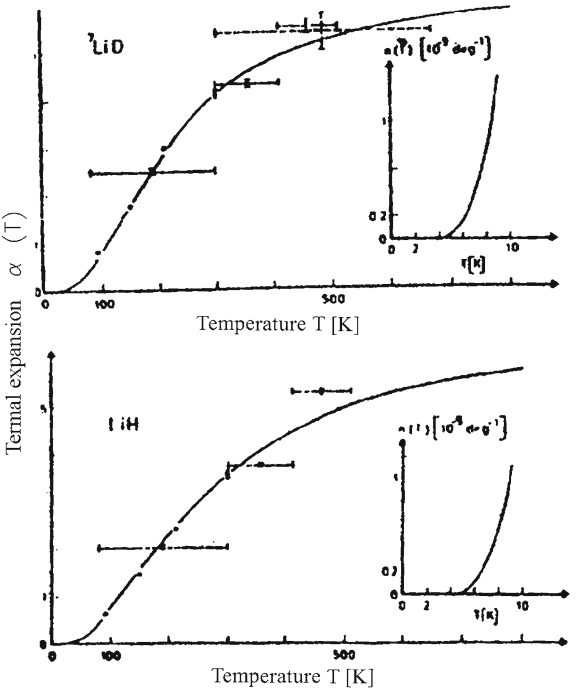

Fig. 5.14 Linear thermal expansion of LiH(^{7}LiD) (after [75])

temperature range are shown that in low temperature range the β is decreased more quickly at the decreasing temperature than this is following from the Grüneisen low and in the high temperature range is continuing slow growth [73, 74]. As an example of above mentioned, α linear coefficient is essentially linear with T at higher temperature. More precisely and in more temperature range thermal expansion of LiH was investigated by Jex [75]. His results are displayed in Fig. 5.14, where we can see that the experimental results agree very well with calculated ones.

The mean Grüneisen constant of ^{7}LiD and ^{7}LiH is depicted in Fig. 5.15. It can be seen that in the wide temperature range the value of γ is almost constant, that is one more to indicate on the weak dependence γ from temperature, but $\gamma_{\mathrm{LiH}} > \gamma_{\mathrm{LiD}}$ in the temperature range $100 \leq T \leq 300$ K [76].

The pressure and temperature derivatives of the *elastic moduli* of single crystal LiH have been determined at room temperature by Gerlich and Smith [77]. Figure 5.16 presents the Gerlich and Smith's results of the variation the natural velocity with pressure, for sound waves propagating in the [100] direction. The dots are the experimental data points, while the straight lines are a linear least square fit to them.

From the slopes of the lines, $(\rho_0 v^2)^l_{P=0}$ may be evaluated, where v is the natural velocity, P the pressure, ρ_0 zero pressure density and ^{l} designates differentiation with respect to pressure. The values of $(\rho_0 v^2)^l_{P=0}$ thus determined are shown in Table 5.4.

Since the specimen with [110] parallel faces much longer than the one with [100] faces, and as the echo pattern for the former was much superior to the one with the

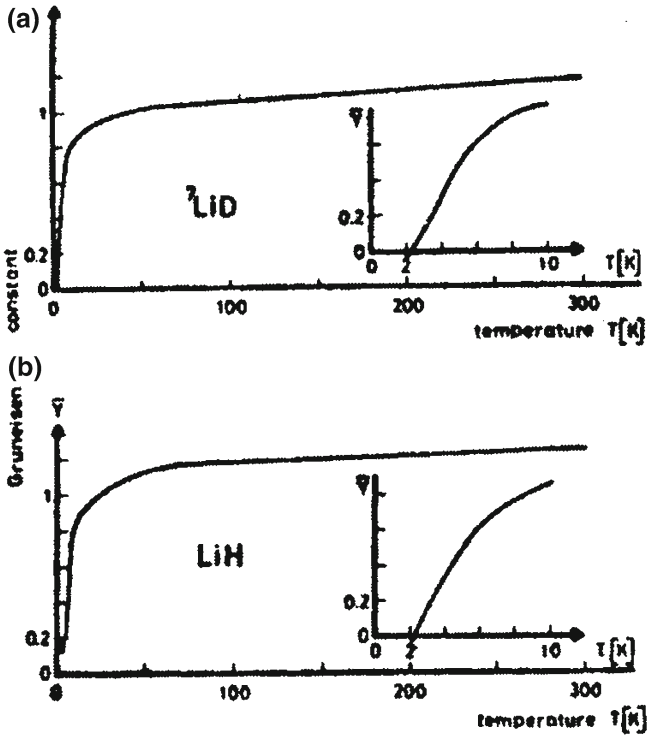

Fig. 5.15 Mean Grüneisen constant of **a** ^{7}LiD and **b** ^{7}LiH (after [75])

Table 5.4 Values of $(\rho_0 W^2)_P = 0'$ for the three propagation modes in the ⟨110⟩ direction (after [77])

Mode	$C'_1 1$	C'	C_{44}
$(\rho_0 W^2)_P = 0'$	6.21±0.07	3.65±0.04	1.57±0.07

Table 5.5 Pressure derivatives of the second-order elastic moduli (after Gerlich and Smith [77])

$\frac{\partial C'_{11}}{\partial P}$	$\frac{\partial C'}{\partial P}$	$\frac{\partial C_{44}}{\partial P}$	$\frac{\partial C_{11}}{\partial P}$	$\frac{\partial C_{12}}{\partial P}$	$\frac{\partial B^s}{\partial P}$
7.17±0.07	3.94±0.04	2.06±0.07	9.05±0.18	1.17±0.18	3.80±0.15

[100] faces, the latter being quite poor, only the [110] propagation data were used for evaluating the pressure and temperature derivatives of the elastic moduli. The results of the pressure derivatives of C'_{11}, C' and C_{44} corrected for the misalignment in the propagation direction (Fontanella and Schuele [78]), together with their associated errors, are shown in Table 5.5.

It is interesting to note that pressure derivative of the bulk modulus, $\partial B^S/\partial P$, is relatively small, some magnitude as in AHC [79]. Hence under high compressive

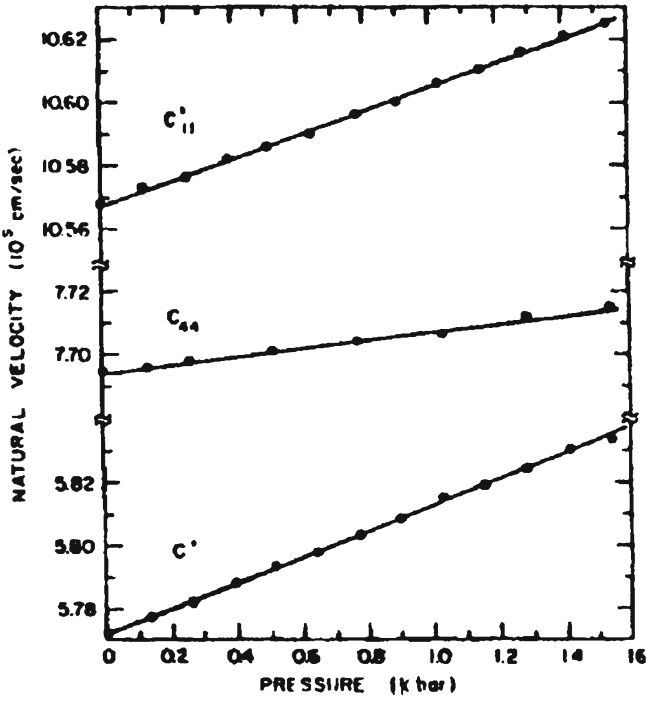

Fig. 5.16 Natural velocity as a function of the pressure for the ⟨110⟩ propagation direction (after [77])

Table 5.6 Athermaly extrapolated 0 K values of the elastic moduli. (Units $10^1$1dyn./cm^2) (after Gerlich and Smith [77])

C'_{11}	C'	C_{44}	C_{11}	C_{12}
9.630	3.338	5.093	7.875	1.199

stress, LiH will not stiffer up too much, making it more susceptible to fusion. Table 5.1 of Ref. 79 presents the values of the temperature derivatives of the above elastic moduli, as well as results of Haussuhl and Skorczyk [81] and Table 5.6 presents the thermal 0 K values of the elastic moduli. From the pressure derivatives of the elastic moduli, and the room and low temperature values of the latter, the mode Grüneisen parameters in any crystalline direction, as well as the low and high temperature limiting values of the Grüneisen constant γ_L and γ_H may be evaluated.

The mode Grüneisen parameters for some crystalline directions of high symmetry are shown in Fig. 5.17. Here 1 denotes the longitudinal mode, 2 and 3 the fast and slow shear modes respectively. The values of all three mode Gr üneisen parameters vary strongly with crystalline direction, due to the fact that the reciprocal of the *elastic stiffness* and the pressure derivatives of the latter vary in opposite sense. The

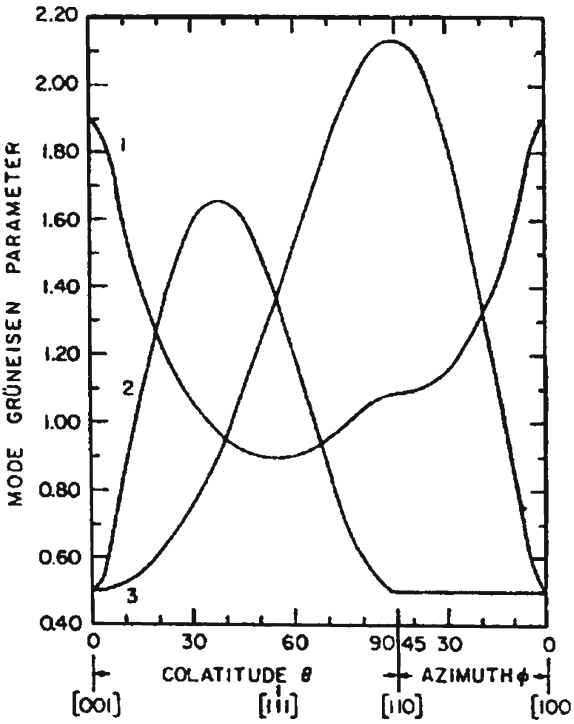

Fig. 5.17 Mode Grüneisen parameters for some crystalline directions of high symmetry (after Gerlich and Smith [77])

Table 5.7 Elastic and thermal Gruneisen constants (after Gerlich and Smith [77])

	γ_L	γ_H
Elastic data	1.21	1.12
Thermal data		1.28 (300 K)

values of γ_L and γ_H, together with the values of the room temperature Grüneisen constant, obtained from thermal expansion data, are shown in Table 5.7. As can be seen, γ_L and γ_H are quite close in magnitude, and agree well with thermal data.

5.3.2 Isotope Influence on the Linear Thermal Expansion Coefficient

Ubbelohde [82] pointed out in 1936 that the substitution of one *isotope* for another, in a solid chemical compound, will lead to differences in the rotational and *vibrational frequencies* of the *molecules*, without producing any significant change in the structure of the potential energy of the solid. These substitutions cause changes in the lattice constant, a, and in the coefficient of thermal expansion, α, of the solid. The influence of isotopic composition on the thermodynamic properties of substances

Table 5.8 α, s $\times 10^6$ for isotopic LiH (after Anderson et al. [83])

Isotopic composition	−190−25°C	25−140°C	140−240°C
^{6}LiH	21.0 ± 0.3	34.4 ± 0.8	50.0 ± 1.0
^{7}LiH	19.8 ± 0.4	37.4 ±0.4	53.3 ± 0.6
^{6}LiD	24.0 ± 1.0	38.4 ± 1.8	54.3 ± 1.0
^{7}LiD	24.8 ± 0.4	42.9 ± 1.0	55.0 ±1.4
^{7}LiT	26.4 ± -0.5		

is usually considered to be manifestation of the quantum nature of matter. At high temperatures in the classical limit any mass effect on thermodynamic quantities disappears and hence any quantum isotopic effect vanishes [65]. The dependence of the thermal expansion coefficient α from the temperature T in many cases is dictated by the temperature behaviour of the specific heat (see below). It is explained that usually the integral coefficient of Grüneisen γ is weak dependence from T. There have been several investigations of the isotope effect on the lithium hydride [75, 83]), KCN [84] and Ge [78, 80, 85, 87]. Table 5.8 lists the measured coefficient of thermal expansion of LiH and its isotope analogue over the temperature ranges −190°−240°C [83]. Here, contrary to the effect found with lattice constants (for more details see below) the heavier isotopes have the larger coefficient of thermal expansion. Table 5.9 lists the ratios of the α's for these same temperature intervals. Several points should be emphasised about Tables 5.8 and 5.9. There is a definite discrepancy in α for ^{6}LiH compared to α for ^{7}LiH in the −190°−25°C range. There is no reasonable explanation for the higher value of ^{6}LiH over ^{7}LiH [88]. It would be expected that the difference would be small due to the closeness of the *reduced masses* (μ) of ^{6}LiH and ^{7}LiH; however, the reversal appears to be anomalous. Table 5.9 shows that for any given combination the ratio $\alpha_{\text{light}}/\alpha_{\text{heavy}}$ approaches 1 as the temperature is increased. Again, all ratios should be exactly one if no isotope effect were present. The greater the relative mass differences between isotopes under study, the lower the ratio $\alpha_{\text{light}}/\alpha_{\text{heavy}}$.

This is especially noticeable in comparing the data for ^{6}Li and ^{7}Li it is seen the ratios are all close to one, indicating very little effect. Theoretical estimation of the ratio $\alpha_{\text{LiH}}/\alpha_{\text{LiD}}$ at 298 K is 0.80 and experimentally, the value $\alpha_{\text{LiH}}/\alpha_{\text{LiD}}$ for the −190−25°C was 0.81. This value approaches 1.0 at the higher temperatures. The Debye theory predicts a larger heat capacity for the heavier element ($C_{\text{heavy}} > C_{\text{light}}$) than the Grüneisen relation $\alpha = \gamma C_V/3\chi_T V$; it is expected that $\alpha_{\text{heavy}} > \alpha_{\text{light}}$. This difference in physical properties resulting from isotopic substitution becomes much less pronounced as the temperature is increased, and should eventually become negligible [89]. These results are shown in the Fig. 5.18. For comparison, in the Fig. 5.18 the results of measurements of the linear thermal expansion coefficients for two samples Ge: $^{\text{nat}}$Ge and ^{70}Ge (99.99%) [86, 87] are shown. It can be seen from this figure that the difference $\Delta\alpha$ for two samples Ge one order less than $\Delta\alpha$ in case of LiH and LiD. In conclusion of this part we should mention once more the results of measurements of $\Delta\alpha$ for KCN of different isotopic composition. The precise

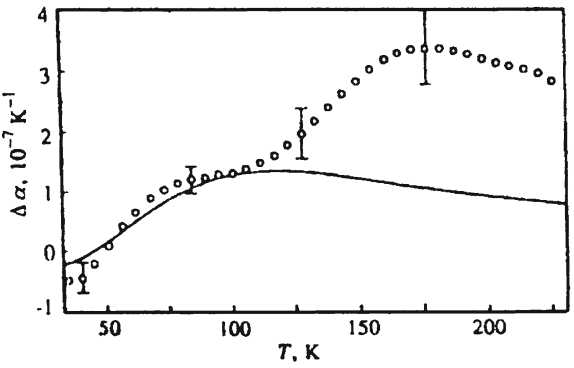

Fig. 5.18 The temperature dependence of the factor $\Delta\alpha = \alpha_c\,(\mathrm{M_{c1}}) - \alpha_c\,(\mathrm{M_{c2}})$, where $\mathrm{M_{c1}} = 72.59\,(^{\mathrm{nat}}\mathrm{Ge})$ and $\mathrm{M_{c2}} = 70\,(^{70}\mathrm{Ge})$. The full line is the theory, and dots are experiments (after [74])

measurements are shown to have no evidence of influence of isotopic composition on the thermal expansion coefficient or the compression isotherms [84].

5.4 Heat Capacity and Debye Temperature

5.4.1 The Lattice Theory of Heat Capacity

Specific heat data are probably the oldest source of information about phonons in crystal lattices and were, in fact, one of the sources of the original paradoxes that led to the development of modern quantum theory. The nonconstancy of the specific heats of crystals as a function of temperature was not explicable by classical theory [59]. The term specific heat is customarily used as a synonym for heat capacity per gram. In most theoretical calculations the heat capacity per gram molecule is the natural quantity to calculate, since this then refers to the properties of a fixed number of particles.

The heat capacity of a solid is measured as $c_p = \left(\frac{\Delta Q}{\Delta T}\right)_p$ where ΔQ is the heat input, ΔT the change in temperature and p is the pressure, which is constant. The The heat capacity which is obtained from most theoretical calculations is C_v, that pertaining to constant volume, which is equal to $\left(\frac{\partial E}{\partial T}\right)_\mathrm{v}$, where E is the internal energy and V the volume. The assumption is made here that the internal energy is a function of two parameters only, in this case T and V, though the concept of heat capacity can be generalised to include other parameters. A relation linking C_p and C_v can be obtained from general thermodynamical considerations [90, 91]

$$C_p - C_v = \beta^2 V T/\kappa. \tag{5.62}$$

The main features of thermal motion in a solid can be explained based on the temperature dependence of the *heat capacity*. The heat capacity per mole of substance is defined as the energy that should be supplied to a mole of the substance in order to increase its temperature by 1 K. Therefore, as pointed above, the heat capacity at constant volume equals

$$C_v = (\partial E/\partial T)_v, \tag{5.63}$$

i.e. as the energy of a system changes by ∂E, its temperature changes by ∂T. From the point of view of classical statistics, for each degree of freedom of the system, there is an energy equal to $k_{\mathrm{B}}T/2$. According to the law of uniform distribution of the energy over degrees of freedom, the average energy of such a system is equal to the production of the number of degrees of freedom by $k_BT/2$. As is known [59], this result, which is valid for ideal gases, can also be applied to systems of interacting particles when the interaction forces are harmonic, i.e. obey Hooke's law. In this case, we will consider the model crystalline lattice consisting of N atoms, which execute small vibrations near equilibrium positions in sites. Each atom vibrates independently of its neighbors in three mutually perpendicular directions, i.e. it has three independent vibrational degrees of freedom. In the *harmonic approximation*, such an atom can be represented by a set of three linear harmonic oscillators. As the oscillator vibrates, its kinetic energy periodically transforms to the potential energy and vice versa. Because the kinetic energy (which is exactly equal to the potential energy) equals $k_BT/2$, the average total energy of the oscillator, which is equal to a sum of the kinetic and potential energies, is k_BT. Therefore, the total energy of a crystal consisting of N atoms is

$$\mathrm{E} = 3Nk_BT. \tag{5.64}$$

Thus, the molar heat, which is defined as the energy required to increase the temperature by 1 K, is equal to

$$C_v = 3Nk_B = 3R, \tag{5.65}$$

where R is the molar gas constant [$R = 8.314\mathrm{J/(mol.K)}$]. Expression (5.65) is the well-known Dulong and Petit's law. Note that this law is valid for many *insulators* and *metals* at sufficiently high temperatures. However, at sufficiently low temperatures, none of the substances obey this law. According to the experimental data, the heat capacity C_{v} at low temperatures is proportional to T^3. This dependence cannot be explained within the framework of the classical model, and one must use the concepts of quantum statistics to explain it. The dependence of C_{v} is explained in the Einstein's model using two assumptions: a solid is represented by a set of identical harmonic oscillators, which oscillate independent of each other with the same frequency in three mutually perpendicular directions, their energy being quantized according to Planck [90, 91]. Thus, the problem is reduced to the calculation of the average vibrational energy of an atom along one of the three mutually perpendicular directions. The total thermal energy of the system is obtained by multiplying the result by $3N$. According to the definition of the average value,

$$\langle E\rangle = \frac{\sum_{n=o}^{\infty} \mathrm{n}\hbar\omega \mathrm{e}^{-\mathrm{n}\hbar\omega/(k_B T)}}{\sum_{n=o}^{\infty} \mathrm{e}^{-\mathrm{n}\hbar\omega/(k_B T)}}, \tag{5.66}$$

where $\mathrm{e}^{-\mathrm{n}\hbar\omega/(k_B T)}$ is the Boltzmann factor, which determines the state of the system with energy $\hbar\omega$; and the number of oscillators that oscillate with energy is proportional to $\mathrm{e}^{-\mathrm{n}\hbar\omega/(k_B T)}$. By introducing a new variable $x = -\hbar\omega/(k_B \mathrm{T})$, after transformation (5.66), we obtain

$$\langle E\rangle = \hbar\omega \frac{\mathrm{d}}{\mathrm{d}x} \ln\left(1 + \mathrm{e}^{x} + \mathrm{e}^{2x} + \cdots\right) = \frac{\hbar\omega}{\mathrm{e}^{x} - 1}. \tag{5.67}$$

By returning to the previous variable, we obtain

$$\langle E\rangle = \frac{\hbar\omega}{e^{\hbar\omega/(k_B T)} - 1}. \tag{5.68}$$

Thus, the total energy related to vibrations of N atoms in the lattice is

$$E = 3N \frac{\hbar\omega}{e^{\hbar\omega/(k_B T)} - 1}. \tag{5.69}$$

For $kT \gg 1$, i.e. at high temperatures, by expanding the exponential into a series $e^{\hbar\omega/(k_B T)} - 1 = 1 + \frac{\hbar\omega}{k_B T} + \cdots - 1 \cong \frac{\hbar\omega}{k_B T}$, we obtain

$$E = 3Nk_B \mathrm{T} \quad \text{and} \quad C_v = 3Nk_B, \tag{5.70}$$

i.e. Dulong and Petit's law. However, the result obtained in the low-temperature limit, when $\hbar\omega \gg k_B \mathrm{T}$ and $e^{\hbar\omega/(k_B T)} \gg 1$, is new. In this case, we have $E = 3N\hbar\omega e^{-\hbar\omega/(k_B T)}$ and $C_v \cong Nk_B(\frac{\hbar\omega}{k_B T})^2 e^{-\hbar\omega/(k_B T)}$. Therefore, C_v exponentially decreases with decreasing temperature. The *heat capacity* calculated in the Einstein model decreases with decreasing temperature faster than in reality (the $-T^3$ law). As it is well known, the discrepancy between experimental data and the Einstein theory results from the assumption that each individual atom executes *harmonic oscillations* with a frequency of ω independent of the rest of the atoms. Having retained the main idea of Einstein, Debye introduced an additional assumption that harmonic oscillators oscillate with different frequencies and their energy is quantized according to Planck. The total elastic energy at a temperature of T is equal to the integral over ω from the energy of the oscillator with a frequency of ω multiplied by the number of oscillators (phonon modes) per unit frequency interval:

$$\mathrm{E} = \frac{9Nk_B T}{\left(\frac{\theta}{T}\right)^3} \int_0^{\omega_D} \frac{x^3 \mathrm{d}x}{\mathrm{e}^{x} - 1}. \tag{5.71}$$

where $x = \hbar\omega/(k_B T)$, and $\theta = \hbar\omega_{\mathrm{D}}/k_B$. Expression (5.71) is called the interpolation Debye formula, and

$$D(\theta/T) = \frac{3}{(\theta/T)^3}\int_0^{\omega_D} \frac{x^3 \mathrm{d}x}{e^x - 1} \tag{5.72}$$

is the Debye function. Expression (5.71) is interesting, because the energy and, hence, the heat capacity [see Eq. (5.67)] is expressed at any temperature via a single parameter θ, which is called the characteristic temperature of a solid or the *Debye temperature*. Its physical meaning, as is known, is that $k_B T = \hbar\omega_{\mathrm{D}}$ represents a maximum quantum of vibrational energy of a lattice [72, 92]. This quantity is the only parameter that takes into account the type of a substance, and its value varies from 100 to 2000 K for different substances [62]. The high value of the Debye temperature is well explained by high rigidity of the interatomic bonds. The Debye function D(θ/T) cannot be calculated explicitly; however, the analytic expressions for the energy and heat capacity can be obtained in the limiting cases of low and high temperatures.

(a) High temperatures, i.e. $k_B T \gg \hbar\omega$ or $x < I$ in (5.71). In this case, the denominator in the integrand can be expanded into a series to obtain $e^x - I \approx I + x - I = x$. Then, expression (5.71) will take the form

$$E = \langle E_a \rangle = 9Nk_B\theta\left(\frac{T}{\theta}\right)^4 \int_0^{\omega_D} x^2 \mathrm{d}x = 3RT. \tag{5.73}$$

Therefore, the heat capacity $C_v = 3R$, i.e. it is independent of temperature and changes according to Dulong and Petit's law.

(b) Low temperatures, i.e. $\hbar\omega \gg k_B T$ or $x \gg 1$. In this case, the upper integration limit in (5.73) can be set ∞. Then, the result of integration is independent of temperature, and the exact value of the integral is

$$\int_0^{\infty} \frac{x^3 \mathrm{d}x}{\mathrm{e}^x - 1} = \frac{\pi^4}{15} \quad \text{and} \quad E = \frac{3\pi^4 Nk_B\theta}{5}\left(\frac{T}{\theta}\right)^4. \tag{5.74}$$

The latter expression is exact at low temperatures, and it adequately describes the temperature dependence of energy. In this case, the heat capacity $C_v = \gamma T^3$. This dependence well agrees with experimental data within the narrow temperature range (near 0 K). Microscopic calculation based on the phonon formalism also gives (5.71) [60, 61]. Therefore, one can conclude that the concept of phonons permits the use of mathematical ideas and procedures applicable to common real particles [93].

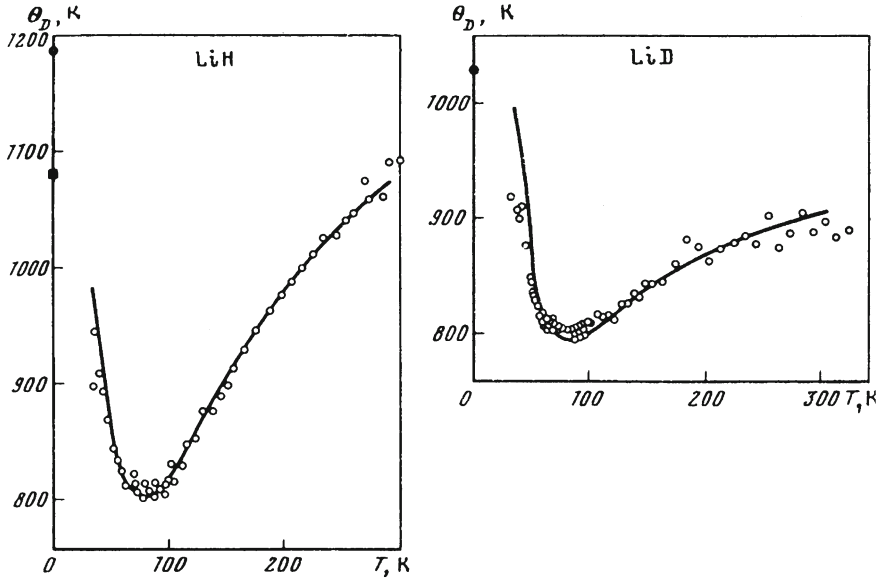

Fig. 5.19 The temperature dependence of the Debye temperature θ_D for ^{7}LiH (**a**) and ^{7}LiD (**b**) (after [97])

5.4.2 Different Method of θ_D Determination

The definition of a θ_D value is that it is equal to $\hbar\omega/k_B$, where ω is either a characteristic frequency or some average frequency [92]. A great deal of confusion has been caused by the assumption that θ_D values derived from different physical properties of a solid should be equal. Such an assumption may have been justified in the early stages of *specific heat* theory, but it has long outlived its usefulness. It would seem advisable to restrict the term θ_D to the representation of specific heat data only, since θ_D is not a constant, it is worthwhile on occasion to indicate the temperature or temperature range. In all other cases θ_D values should be labelled in such a way that their origin is made evident. The simplest case is that of θ_D (*elastic*—[80]), i.e. the θ_D value derived from the elastic constants of a solid. This is equal to θ_D if both are measured at sufficiently low temperatures. Otherwise they are not in general equal, though it may be possible to derive a relation between them at other temperatures for a theoretical lattice model.

5.5 Effect of the Isotopic Composition of a Crystal Lattice on the Specific Heat

The early low-temperature specific heat was measured by Gūnther from room temperature down to 74 K [94]. First detailed measurements of the specific heat of lithium hydride in a wide temperature range from 3.7 to 295 were performed by

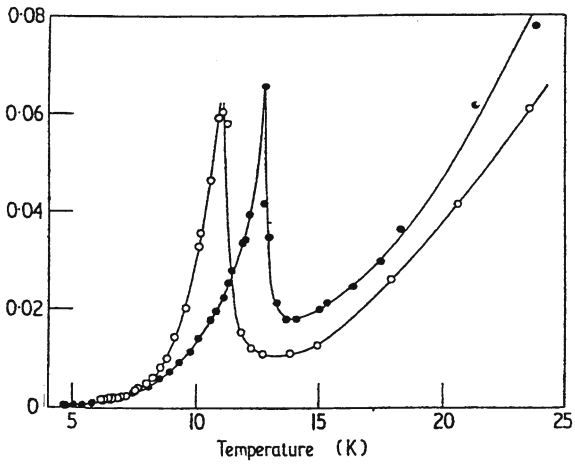

Fig. 5.20 The specific heat C_P of ^{7}LiH (○) and ^{7}LiD (●) at low temperature (after [97])

Kostryukov in 1961 [95]. In this paper, the unusual behaviour of specific heat was observed between 10 and 20 K. As is shown above, at low temperatures, the heat capacity at a constant volume is $C_v \sim \gamma T^3$. Kostryukov observed strong deviations from the T^3 law, which were dependent on the sample prehistory, and explained them by the presence of free molecular hydrogen in lithium hydride. However, by using a special experimental procedure, Kostryukov managed to obtain more reproducible results that only slightly deviated from the T^3 dependence. Based on these results cited author estimated the *Debye temperature* of lithium hydride to be $\theta_D = 860K$ (Table 5.2 in review of Plekhanov [96]). Later, Yates et al. [97] carefully studied the low-temperature ($5 < T < 320$ K) specific heat of lithium hydride. In this paper, the effect of the isotopic substitution (H → D) on the specific heat was studied for the first time (Fig. 5.19). Yattes et al. high-purity and high-stoichiometric samples were investigated (the total content of impurities $<2 \times 10^{-5}$). The C_p(T) dependence measured by Yates et al. at T > 30 was used for calculating the Debye temperature from the relation $C_v = \text{const.}\ (T/\theta_D)^3$. The value of θ determined in this way, as was shown above, depends on the temperature. It is known that this dependence is explained by the deviation of the postulated Debye spectrum from a real phonon spectrum. The values of θ_D found from the extrapolation of $\theta_D(T)$ to $T = 0$ (Fig. 5.19) are equal to $\theta_D(\text{LiH}) = 1190 \pm 80$ and $\theta_D(\text{LiD}) = 1030 \pm 50$ K. One can see that the value of the Debye temperature for LiH obtained by Yates et al. is higher than that obtained by Kostryukov. In addition, data on the Debye temperature show that this temperature decreases with increasing isotope mass in accordance with the theory. Comparison of Debye temperatures calculated from elastic constants($\theta_D = 1083 - 1135$ K at 300 K) [77, 98] and calorimetric data ($\theta_D = 1190 \pm 80$ K at 0 K) [97] shows that they are in agreement, especially for LiH crystals. Note the strong temperature dependence of the Debye temperature of LiD crystals, which has not yet been adequately explained. It is likely that the Debye temperature of diamond also strongly depends

on temperature [66, 93]. Figure 5.20 displays interesting features in the results below 25 K.Associating the term anomaly with a situation in which the heat capacity rises with diminishing temperatures, the results for ^{7}LiH and ^{7}LiD will each be seen to contain anomalies, having peaks at temperatures of 11.1±0.2 K and 12.8 ± 0.2 K, respectively. The results of Fig. 5.20 can be little doubt that the peaks observed in the *specific heats* of the two compounds at low temperatures do not arise from spurious origins, and that they are truly characteristic of the compounds. When they occur in dielectric crystals, anomalies of this type are most commonly caused by movements of atoms, and in this case it seems likely that such a rearrangement takes place in the region of 11.1K in the case of ^{7}LiH and in the region of 12.8K in the case of ^{7}LiD. Accordingly cited authors [97] observed λ-type anomaly of the heat capacity and concluded that this anomaly in the temperature dependence of $C_p(T)$ is related to some phase transition. Indeed, Schumacher in the early 1960s had already predicted [99] that lithium hydride should undergo a *phase transition* in the pressure range between 3 and 4 kbar. Later Berggren [100], by using a simple qualitative model, found that the binding energy in LiH with the structure of CsCl type is higher than with the NaCl structure. Based on these results, the authors [97] assumed that anomalies observed in LiH are related to the polymorphic transition from NaCl structure to CsCl structure. However, attempts to find this transitions, which were made in several papers [101–104] by using an external pressure of up to 330 kbar [105], failed. Note here that the CsCl $\longrightarrow$ NaCl phase transition was also not found in a recent paper [105], where the effect of the external pressure on CsH was investigated. Note also that numerous experimental studies on *reflection spectra* in *exciton* region and *Raman spectra* [66, 93] in these crystals did not reveal noticeable anomalies in the above temperature range [72].

In recent years, analogous investigations were performed on semiconducting crystals [106, 107]. Figure 5.21 displays the molar heat capacity of the three investigated Ge isotope samples, again in a plot of $C_p(T)/T^3$ against T (Fig. 5.21, lower panel), as well as in the representation of the corresponding calculated Debye temperature θ_D as a function of temperature T (upper panel). Molar heat capacity and Debye temperature show the characteristic low temperature behaviour known from Ge and other solids [107]. Most typical is the strong minimum of $\theta_D(T)$ around 20K, as a typical for diamond structure, due to the serious departure from the Debye approximation. Anharmonic effects become important only for $T > \theta_D(0)/3$, where $\theta_D(T)$ saturates and starts to decrease with increasing T [107]. Calculations for the difference $\Delta C_{\text{isotope}}$ between the values of molar heat capacity of the isotopes show that $\Delta C_{\text{isotope}}$ increases with temperature since $C_p(T)$ increases most strongly for the material with the greatest molar mass (compare, please with LiH data). $\Delta C_{\text{isotope}}$ reaches a maximum around $\theta_D(0)/4$ ($\approx$90 K for Ge) and at the limit of high temperatures, it approaches zero [80, 108].

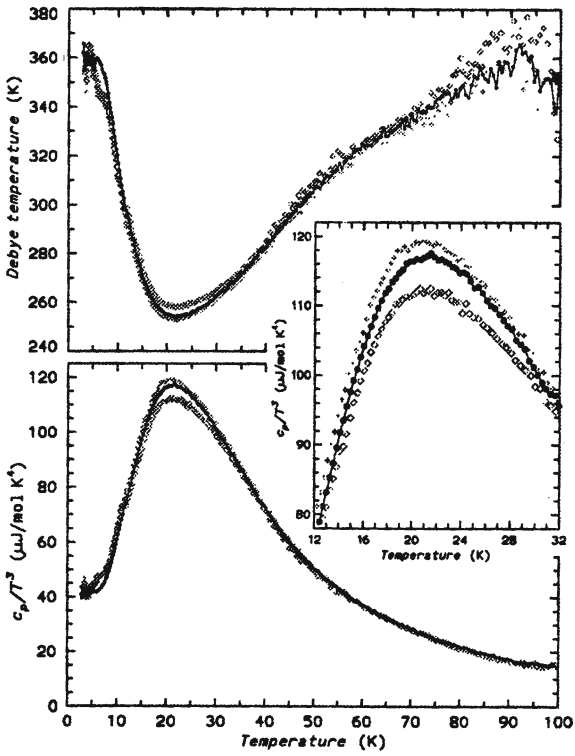

Fig. 5.21 Molar heat capacity $C_P(T)$ of the three measured crystal samples: $^{70/76}$Ge (+), ^{nat}Ge (circles connected by a thin line) and ^{70}Ge ($\diamond$): plot of C_P/T^3 against T (lower panel), and (upper panel corresponding Debye temperature θ_D as a function of temperature T. The insert shows a magnification of the plot in the lower panel (after [106])

5.6 Dependence of the Lattice Constant on Isotopic Composition and Temperature

5.6.1 Background

The *lattice parameter* at any given temperature is determined by three different contributions. First and most obvious is the size of the atomic radii and the nature of the chemical bonding between them, which are most important in determining interatomic spacings and crystal structure. Second is the effect of temperature on the distance between atoms which normally produces a *volume expansion* with increasing temperature. Finally, there is the effect of the *zero-point displacement*, which is a purely quantum effect no classical analogue. This last contribution results from the fact that the lowest energy state of the system, the *zero-point energy*, generally corresponds in an anharmonic potential to an atomic displacement somewhat larger than that associated with the potential minimum. Since the zero-point displacement is usually a small contribution to the lattice parameter at 0 K, its contribution if often ignored, particularly since its magnitude is difficult to determine experimentally. An important exception (see below), however is the crystals which are *isotopic* variants

of lithium hydride. Since they are chemically identical, the contribution to the lattice parameters due to the atomic radii and chemical bonding may be taken as constant in all of them. Consequently, the differences in the lattice parameters at various temperatures may be attributed solely to differences in the thermal expansion and the zero-point displacement. As it happens, these differences are relatively large in these crystals mostly because of the large relative differences in the atomic masses in the three isotopic forms of hydrogen, and the relatively large changes which these produce in the anion–cation reduced masses [76]. The first paper devoted to the calculation of a change in the molecular volume upon *isotopic substitution* was the paper of London [109], which has now become classic. He started with an expression for the free energy using the Einstein free energy function to reach the expression

$$\frac{M}{V}\frac{\mathrm{d}V}{\mathrm{d}M} = \frac{\gamma\beta}{V}\left[U - E_0 - \mathrm{T}C_v\right]\left[\frac{\mathrm{d}\ln\nu}{\mathrm{d}\ln M}\right], \tag{5.75}$$

where, V is molecular volume, M is the atomic mass, γ is Gruneisen constant $\gamma = \frac{\alpha V}{\beta C_v}$, α is the *volume expansion coefficient*, β is compressibility, $\mathrm{C_v}$ is the molar specific heat, $\mathrm{E_0}$ is the potential energy, ν is the phonon frequency and U is the total energy.

For *monoatomic* solids

$$\mathrm{d}\ln\nu/\mathrm{d}\ln M = -1/2 \tag{5.76}$$

and $d\mathrm{V}/d\mathrm{M}$ can be expressed through a Debye function with characteristic temperature θ_D. At high temperatures, one can express Debye function by a power series in $(\theta_D/T)^2$. Then Eq. (5.75) becomes

$$\frac{M}{V}\frac{\mathrm{d}V}{\mathrm{d}M} = -\frac{1}{20}\alpha T\,(\theta_D/T)\left[1 + \frac{11}{420}\,(\theta_D/T)^2 + \cdots\cdots\right] \tag{5.77}$$

and at absolute zero

$$\frac{M}{V}\frac{\mathrm{d}V}{\mathrm{d}M} = -\frac{9}{16}\frac{\gamma\beta}{V}R\theta_D. \tag{5.78}$$

Here R is the gas constant.

For *diatomic* cubic crystal with atomic masses M and m, we have [92]

$$\nu^2 \sim \left(\frac{1}{M} + \frac{1}{m}\right) \tag{5.79}$$

Therefore

$$\frac{\mathrm{d}\ln\nu}{\mathrm{d}\ln M} = -\frac{1}{2}\frac{1}{\left(1 + \frac{M}{m}\right)} \tag{5.80}$$

which leads to

$$\frac{M}{V}\frac{\mathrm{d}V}{\mathrm{d}M} = -\frac{1}{20}\alpha T\,(\theta_D/T)^2\,\frac{1}{1+\frac{M}{m}}. \tag{5.81}$$

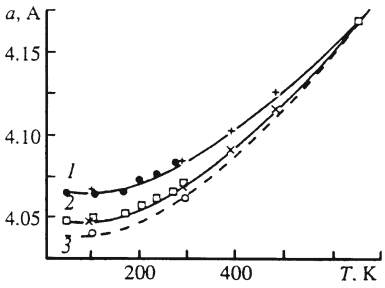

Fig. 5.22 Temperature dependence of the lattice constant of *1* LiH; *2* LiD; and *3* LiT crystals. Experimental data are taken from Smith and Leider [113] and Anderson and co-workers [83]. The solid line is theoretically calculated (after Plekhanov [96])

As pointed out by London, in order to obtain more accurate results one should have a detailed knowledge of the frequency spectrum since ν is not dependent on M in a simple fashion. The values predicted by London's analysis are in reasonable agreement with the experimental findings [109].

5.6.2 Lithium Hydride

Various investigators [83, 88, 96, 110] experimentally and theoretically examined the effect of *isotope substitution* on the lattice parameter of the LiH crystals [111, 112]. These investigations demonstrate that the *isotope effect* on the lattice parameter and coefficient of thermal expansion shows a definite trend in which the lighter isotopes produce larger lattice parameters and smaller coefficients of thermal expansion than the heavier isotopes. The effects are more pronounced when lighter element is substituted and at low temperatures. Closely related to the molar volume is the thermal expansion [89]. Table 5.11 gives values of lattice constants and thermal expansion coefficients for isotopic LiH [82, 83, 88, 96, 113]. The data indicate that the isotope effect, e.g. lighter isotopes having larger lattice constants, is reduced at higher temperatures. Heavier isotopes have larger thermal expansion coefficients. Similar findings were reported also by other workers [96, 111, 114, 115]. These findings are expected since Debye theory predicts a larger heat capacity (see, also above) for heavier isotopes, and then from the Gruneisen relation (Eq. (5.56)),

$$\alpha = \gamma C_v / 3\beta V, \tag{5.82}$$

one can obtain $\alpha_{\text{heavy}} > \alpha_{\text{light}}$.

After classical London's paper [109], later in of Anderson et al. [83], a simple empirical expression that related changes in the *reduced mass* μ of the unit cell and in the lattice constant a upon isotopic substitution was suggested:

$$a = A\mu + B, \tag{5.83}$$

Table 5.9 Ratio of α,s for isotopic LiH (after Anderson et al. [83])

Ratio	$-190-25$°C	$25-140$°C	$140-240$°C
$\frac{\alpha_H}{\alpha_D}$ for ^{6}Li	0.879	0.896	0.921
$\frac{\alpha_{rmH}}{\alpha_D}$ for ^{7}Li	0.805	0.872	0.969
$\frac{\alpha(^6\text{Li})}{\alpha(^7\text{Li})}$ for H	1.060	0.920	0.982
$\frac{\alpha_H}{\alpha_T}$ for ^{7}Li	0.750		
$\frac{\alpha_D}{\alpha_T}$ for ^{7}Li	0.932		

where A and B are constants, which are, however, dependent on temperature. This relation can be readily obtained taking into account a linear temperature dependence of the lattice constant, which is typical for high temperatures. The nonlinear temperature dependence of the lattice constant of LiH and LiD crystals [83, 113] observed in experiments (Fig. 5.22) can be described by the second-degree polynomial

$$\frac{\Delta a}{a} = \frac{\sqrt{\mu_{\text{LiD}}} - \sqrt{\mu_{\text{LiH}}}}{\sqrt{\mu_{\text{LiH}}\mu_{\text{LiD}}}} \left[A + B(T - T_0) + C(T - T_0)^2\right], \qquad (5.83')$$

where $\Delta a = a_{\text{LiH}} - a_{\text{LiD}}$, $\text{I}/\mu_{\text{LiH}} = 1/M_{\text{H}} + 1/M_{\text{Li}}T = 25$°C, and $\theta = 1080$ K is the Debye temperature of a LiH crystal. The values of constants A , B and C determined by the method of least squares, are presented in Table 5.11. For comparison, the values of these constants, calculated in a similar way for *diamond*, *silicon*, and *germanium* [116], are also given. The value of temperature T = 810 K, at which the lattice constant is the same for LiH and LiD crystals, was found from theoretical calculations. The *lattice constant* is equal to 4.165 Å. This means that the temperature dependence $a(T)$ in LiD crystals (a heavy isotope), which have a smaller Debye temperature, is stronger than in LiH crystals. This general conclusion is valid for a broad class of compounds, from an ionic LiH crystal to a covalent germanium crystal. It follows from theoretical calculations (Fig. 5.22) that for $T > 810$, the lattice constant of LiD crystals is larger than that of LiH crystals. This agrees qualitatively with the results of microscopic calculations of the temperature dependence of a change in the unit cell upon isotopic substitution, according to which $\text{a}_{\text{LiH}} = \text{a}_{\text{LiD}}$ at -900–950 K [111]. The change in the lattice constant upon isotopic substitution is mainly determined by the anharmonicity of vibrations, which results in the dependence of the distance between atoms on the vibration amplitude, i.e. on the mean vibrational energy. It is well known that the vibrational energy depends not only on temperature, but also on the isotopic composition as well. Therefore, to take into account the thermal expansion of a crystal lattice, one should consider the effect of anharmonic terms in the expression for potential energy of pair interaction between atoms at temperature T [93].

Table 5.10 Lattice constants and thermal coefficients for isotopic LiH (after Anderson et al. [83])

Material Lattice constants,	−190°C	25°C	140°C	240°C
^{6}LiH	4.066	4.0851	4.1013	4.1218
^{7}LiH	4.0657	4.0829	4.1005	4.1224
^{6}LiD	4.0499	4.0708	4.0888	4.1110
^{7}LiD	4.0477	4.0693	4.0893	4.1119
^{7}LiT	4.0403	4.0633	–	–
Material Thermal expansion coefficient $\alpha \times 10^6$				
	−190−25°C	25−140°C	140−240°C	
^{6}LiH	21±0.3	34.3±0.8	50±1.0	
^{7}LiH	19.8±0.4	37.4±0.4	53.3±0.6	
^{6}LiD	24.0±1.0	38.4±1.8	54.3±1.0	
^{7}LiD	24.8±0.4	42.9±1.0	55.0±1.4	
^{7}LiT	26.4±0.5	–	–	

Table 5.11 Values of coefficients of polynomial (5.83′) describing the temperature dependence of the lattice constant upon isotopic substitution of a mass (after Plekhanov [96])

Substance	A $\times 10^3$	B $\times$ 10^6	C $\times$ 10^9
LiH	55.4	−55.54	−102.8
C	−5.48	3.55	8.21
Si	−1.60	3.94	−6.90
Ge	−0.72	2.27	−6.40

5.6.3 Germanium and Silicon

Among semiconducting crystals the Ge crystal was the first for which the dependence of the lattice constant on an isotope effect was investigated both theoretically and experimentally [116–118]. In the very first paper [117] this dependence was experimentally studied in a highly perfect crystal of natural isotopic composition (average $M = 72.59$) and the second crystal was isotopically enriched, containing 95.8% of ^{74}Ge (average $M = 73.93$). Using the following equation (analogous Eq. 5.84) for the relative changes in the lattice constant a with isotopic mass at low temperature ($e^{-\frac{\hbar\omega}{k_B T}} \ll 1$)

$$\frac{\Delta a}{a} = -\frac{C}{a^3}\frac{\Delta M}{M}\left(\gamma_0 \hbar\omega_0 + \frac{3}{4}\gamma_a k_B \theta_D\right), \tag{5.84}$$

where $\gamma_0 = 1.12$ and $\gamma_a = 0.40$ are the Gruneisen parameters for optical and acoustical phonon modes in Ge, $\theta_D = 374\,K$ is the Debye temperature and $\hbar\omega_0 = 37.3$ meV. Buschert et al. evaluated the Eq. (5.84) for a 95.8 % enriched ^{74}Ge crystal in comparison with a natural crystal. Equation (5.84) predicts 12×10^{-6} and 6×10^{-6} reduction in a for $T = 0$ and $T = 300\,K$, respectively. Buschert et al. [117] experimentally found reductions of 14.9 and 6.3 ppm at 77 K and $T = 300\,K$,

respectively. The agreement between calculated and measured values is very good considering the uncertainties of the Gruneisen parameter values used in the theory. After this paper [117] two theoretical papers were published [116, 118] where were studied the isotope effect and its temperature dependence. In the paper of Pavone and Baroni [116] the dependence of the lattice constant of C, Si and Ge upon their isotopic purity using the first-principles calculations, performed by treating nuclear vibrations by density-functional perturbation theory. The main results of this paper was depicted in Fig. 5.23. The values of the constant A, B and C (Eq. (5.81)) as fitted to theoretical data for the three materials studied in the paper of Pavone and Baroni [116] as well as for LiH [96] are reported in Table 5.11. Noya et al. [118] studied the dependence of the lattice parameter upon the isotope mass for five isotopically pure Ge crystals by quantum path-integral Monte Carlo simulations. The interatomic interactions in the solid were described by an empirical of the Stillinger-Weber type. At 50 K the isotopic effect leads to an increase of 2.3×10^{-4} Å in the lattice parameter of ^{70}Ge with respect ^{76} Ge. Comparison of the simulation results with available experimental date for ^{74}Ge [117] shows that the employed model provides a realistic description of this anharmonic effect. It was shown by Noya et al. that the calculated fractional change of the lattice parameter of ^{74}Ge with respect to a crystal whose atoms have the average mass of natural Ge amounts to $\frac{\Delta a}{a} = -9.2 \times 10^{-6}$ at $T = 0\,\mathrm{K}$, that is almost in agreement with results of Buschert et al. [114]. More detailed investigations of the crystal lattice constants of Ge was performed by Ma and Tse [120]. The temperature dependence of the equilibrium lattice constants for five isotopically pure Ge crystals and naturally occurring Ge were calculated from ab initio electronic theory within quasiharmonic approximation (Figs. 5.24, 5.25). At very low temperature (close to 0 K) the inclusion of zero-point motion is shown to account quantitatively for observed differences in the lattice constants between the isotopes (Fig. 5.25). The discrepancy between the theoretical and experimental thermal expansion on ^{73}Ge isotope alone is unlikely to provide a satisfactory explanation of this discrepancy. The cited authors thought that perhaps the nuclear spin (for ^{73}Ge $-$ $I = 9/2$) may have a subtle effect on the phonon property of this crystal affecting the thermal expansion [120].

5.6.4 Diamond

The *isotopic dependence* of the *lattice constant of diamond* has also attracted interest in connection with the above thermal properties (see above part of thermal conductivity). Banholzer et al. [121] reported the lattice constant of natural and ^{13}C diamond by X-ray diffraction using the powder samples and single crystals. Holloway and coworkers [114, 115] examined the influence of the isotope ratio on the lattice constant of mixed crystals of $^{13}C_x^{12}C_{1-x}$ by single-crystal X-ray diffractometry. According their results, the lattice constant, as in case of LiH [122], decreased linearly with ^{13}C content according to the expression

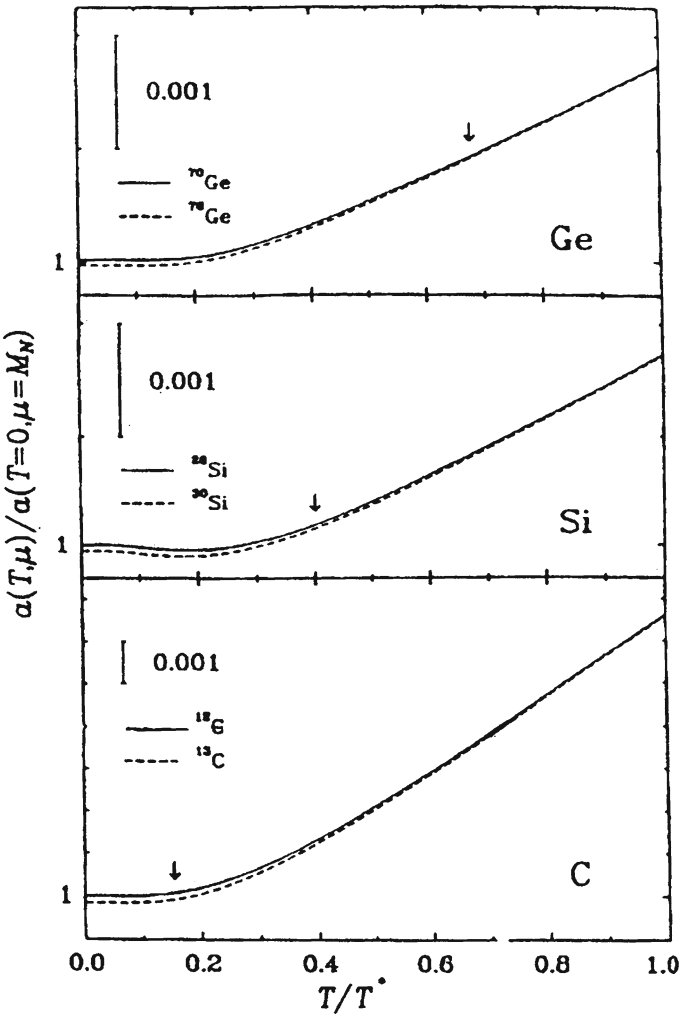

Fig. 5.23 Dependence of the equilibrium lattice constant of C, Si and Ge upon temperature for different isotopic masses. The temperature is given in units of T^* $\left[T^*\,(\mathrm{C}) = 1941\,\mathrm{K},\ T^*\,(\mathrm{Si}) = 744\,\mathrm{K},\ T^*\,(\mathrm{Ge}) = 440\right]$. The arrows indicate the room temperature (25°C). The lattice constants are in units of the zero-temperature lattice constants at the natural isotopic compositions ($a_{\mathrm{C}} = 6.71$; $a_{\mathrm{Si}} = 10.23$; and $a_{\mathrm{Ge}} = 10.61$ a.u.). Note the different units in three panels, which are indicated by the vertical bars (after Pavone et al. [116])

$$\mathrm{a(x)} = 3.56714 - 5.4 \times 10^{-4}\mathrm{x}. \tag{5.85}$$

The fractional difference Δa/a between both end compositions is -1.5×10^{-4}. The *lattice constants* of the five samples of the mixed-diamond with different *isotopic compositions* were studied in the paper of Yamanaka et al. [123]. In this paper it

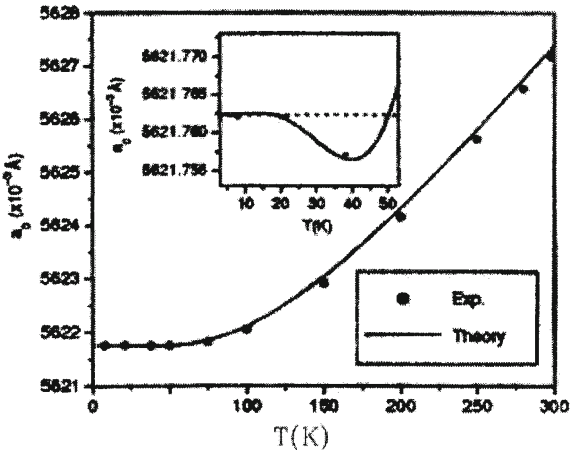

Fig. 5.24 Temperature dependence of the calculated lattice parameter for ^{70}Ge. The inset shows details at low temperature below 53 K. The solid line is the calculated results in [119] (after [120])

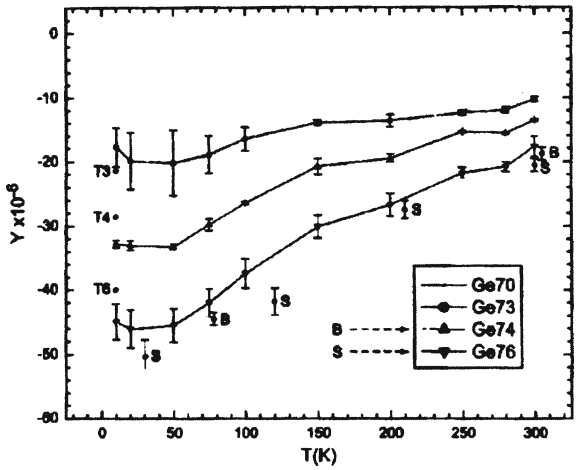

Fig. 5.25 Plots of $Y = [a(M) - a(70)]/a(70)$ with temperature (after [120])

was shown that the standard deviations of the lattice constant were in the range of $5 \div 9 \times 10^{-5}$ Å. The lattice constant is varied (Fig. 5.26) with the isotope ratio and it can be expressed in quadratic form as

$$a(x) = 3.56712 - 9.0 \times 10^{-4}x + 3.7 \times 10^{-4}x^2, \tag{5.86}$$

where $x = \left[\frac{^{13}C}{^{12}C+^{13}C}\right]$.

This expression is in contrast to linear relation reported by Holloway and coworkers [114, 115]. A linear relation between the lattice constant and *isotope ratio* would be somewhat puzzling, because compressibility and Gruneisen parameter are not the same for different isotopes [96].

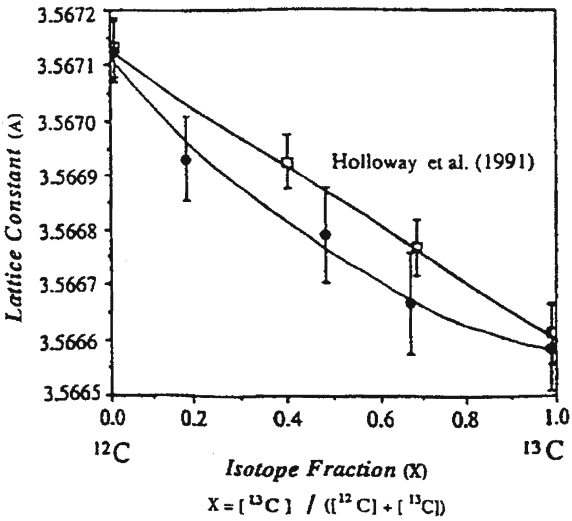

Fig. 5.26 Isotope dependence of the lattice constant of diamond. The curved line shows the quadratic (Eq. (5.86)), which fits to solid circles obtained by Yamanaka et al. The straight line fits to open squares those obtained by Holloway et al. [114, 115] (after Yamanaka et al. [119])

In conclusion of this section we should stress the premier role of the anharmonic effect in the dependence of a on the isotopic effect. Really, as was pointed out by Vogelgesang and coworkers [124] the concentration-dependent lattice parameter incorporating zero-point motion in combination with anharmonicity, deduced from Eq. 2.43 of Ref. [80]

$$a(x) = a_{12} - \frac{\hbar g_1}{\left(6k_1^3 M_{12}\right)^{\frac{1}{2}}}\left[1 - \left(\frac{M_{12}}{M_x}\right)^{1/2}\right] \tag{5.87}$$

with $M_x = (1-x)\,M_{12} + xM_{13}$. A comparison of Eq. (5.87) with the date of Holloway et al. for a(x) and $k_1 = 3B_s a = 4.76 \times 10^5$ dyn/cm for natural diamond yields $g_1 = (4.5 \pm 0.4) \times 10^{14}$ erg/cm^3. Yamanaka's et al. results analyzed in the same manner yields $g_1 = (4.7 \pm 0.4) \times 10^{14}$ erg/cm^3, i.e. very close to the Holloway's date.

5.6.5 Compound Semiconductors: GaAs, ZnSe

These compounds were studied in the papers of Garro et al. [125] and Debernardi and Cardona [126]. In *binary semiconductors*, the calculations of the dependence of volume (or *lattice parameter*) on isotopic masses is more complicated. It is not possible to write the relative variation of the crystal volume as a simple function of the relative variation of the mass. Phonon frequency depends differently on the two masses, and this dependence has to be known, together with the corresponding

Gruneisen parameter for all phonon modes, in order to calculate the dependence of the lattice constant on the isotopic masses. For ZnSe Garro et al. have employed an 11-parameter rigid-ion model (RIM, [66, 127]) at two different unit-cell volumes to obtain the Gruneisen parameters. Due to the absence of a similar dynamical model for GaAs (note, that the only stable As isotope is ^{75}As), an estimation of the variation of its lattice parameter with Ga and As masses has been performed by interpolating ZnSe and Ge results. In order to connect the change in volume with phonon parameters Garro and co-workers used the Helmholtz free energy F, which is related for a system of independent oscillators (phonons) through a partition function [116]. In terms of the energy of individual oscillators, F can be written as

$$F = \sum_{\nu,\vec{q}} \left\{ \frac{1}{2}\hbar\omega_\nu\left(\vec{q}\right) + kT\ln\left[1 - \exp\left(-\hbar\omega_\nu\left(\vec{q}\right)/kT\right)\right]\right\}. \tag{5.88}$$

The volume of a sample is related to the bulk modulus through $\left(\frac{\Delta V}{V}\right)_T = -\frac{\Delta p}{\mathrm{B_s}}$, while p can be written as $p = \left(\frac{\Delta F}{\Delta V}\right)_T$. Using these expressions, we can write

$$V = V_0 + \frac{1}{B_s}\sum_{\nu,\vec{q}} \hbar\omega_\nu\left(\vec{q}\right)\gamma_\nu\left(\vec{q}\right)\left[n_B\left(\omega_\nu\left(\vec{q}\right)\right) + \frac{1}{2}\right], \tag{5.89}$$

where it has introduced the mode Gruneisen parameters $\gamma_\nu\left(\vec{q}\right)$ defined as $\gamma_\nu\left(\vec{q}\right) = -\frac{\partial \ln\omega_\nu}{\partial \ln V}$ and $n_B\left(\omega_\nu\left(\vec{q}\right)\right)$ is the Bose–Einstein factor. In the last equation, V_0 represents the crystal in the limit of infinitive masses. In terms of the lattice constant of the conventional unit cell ($\mathrm{a_0}$ in the limit of infinitive masses) for zinc-blend-type materials last equation can be written as

$$\frac{a\left(M_1,M_2\right) - \mathrm{a_0}}{a_0} = \frac{4\hbar}{3B_s a_0^3}\sum_{\nu,\vec{q}}\left[\omega_\nu\left(\vec{q}\right)\gamma_\nu\left(\vec{q}\right)\left[n_B\left(\omega_\nu\left(\vec{q}\right)\right) + \frac{1}{2}\right], \tag{5.90}$$

where $a(M_1, M_2)$ is the lattice constant for a finite mass of atoms 1 and 2 in the primitive cell at a given temperature. Here we are interested in the change of the lattice parameter when one of the atomic masses changes $\left(\frac{\partial \ln \mathrm{a}}{\partial \mathrm{M_k}}\right)$ and in the low temperature limit in which $\mathrm{n}_B \approx 0$. If we change the mass of atom $k (k = 1; 2)$ from M_k to $M_\mathrm{k} + \Delta M_\mathrm{k}$, the relative change in the lattice parameter is

$$\begin{aligned}\frac{a\left(M_k + \Delta M_k\right) - a(M_k)}{a\left(M_k\right)} &\simeq \frac{\left[a\left(M_k + \Delta M_k\right) - a_0\right] - \left[a\left(M_k\right) - a_0\right]}{a_0} \\ &\simeq \frac{2\hbar}{3B_s a_0^3}\sum_{\nu,\vec{q}}\Delta_k\left[\omega_\nu\left(\vec{q}\right)\gamma_\nu\left(\vec{q}\right)\right].\end{aligned} \tag{5.91}$$

$\Delta_k \left[\omega_\nu \left(\overrightarrow{q}\right) \gamma_\nu \left(\overrightarrow{q}\right)\right]$ is the mean difference of the quantity in brackets evaluated at two different isotopic masses. As was shown by Garro et al. this term is usually negative for an increase in either of the masses. Thus it can be understood as an 'isotopic concentration' of the lattice parameter.

The calculation of Eq. (5.91) requires an integration over the whole Brillouin zone. For this reason, it is convenient to define the 'lattice spectral function'.

$$\Phi\left(M_1, M_2; \Omega\right) = \frac{2\hbar}{3B_s a_0^3} \sum_{\nu, \overrightarrow{q}} \Omega\gamma_\nu \left(\overrightarrow{q}\right) \delta\left[\Omega - \omega_\nu \left(\overrightarrow{q}\right)\right] \tag{5.92}$$

which represents the spectral dependence of the changes in lattice parameter induced by a mass configuration M_1 and M_2. In terms of Eq. (5.92), Eq. (5.91) becomes

$$\frac{\Delta_k a}{a} = \int_0^{\Omega_{\max}} \mathrm{d}\Omega \Delta_k \Phi\left(M_1, M_2; \Omega\right). \tag{5.93}$$

Garro et al. calculated the spectral functions to two different *isotopic masses* of Zn. These authors compared the results of ZnSe with those of Ge obtained by Pavone and Baroni [116], it was noted that the effect of changing both masses in the unit cell is nearly the same for both materials. However, for Ge the two atoms contribute equally, while for ZnSe the contributions of the *anion* and the *cation* are rather asymmetric. The dependence of the GaAs lattice parameter on the Ga and As masses has been obtained by linear interpolation of the values found for Ge and ZnSe because of the less extensive knowledge of Gruneisen parameters for GaAs than for ZnSe. Debernardi and Cardona [126] have described an efficient way to compute the derivatives of the *lattice constant* with respect to the mass in polar semiconductors. It is necessary to point out at the absence of the *isotopic effect* for the lattice constant in KCN crystals [84].

References

1. W.C. Roberts-Austen, Bakerian Lecture: On the diffusion of metals, Philos Trans. Royal. Soc. (London) A **187**, 383–415, (1896)
2. W. Jost, *Diffusion in Solids, Liquids, Gas* (Academic Press, New York, 1952)
3. W. Seith, *Diffusion in Metallen* (Springer, Berlin, 1954)
4. L. Slifkin, D. Lazarus, C.T. Tomisuka, Self-diffusion in pure polycrystalline silver. J. Appl. Phys. **23**, 1032–1034 (1952)
5. C.T. Tomizuka, in *Diffusion Methods of Experimental Physics*, ed. by K. Lark-Horrowitz, V.A. Johnson, vol. 6, Part A (Academic Press, New York, 1959), pp. 364–413
6. N.F. Mott, R.F. Gurney, *Electronic Processes in Ionic Crystals* (Clarendon Press, Oxford, 1948)
7. J.H. Crawford Jr., L.M. Slifkin (eds.), *Point Defects in Solids*, vol. 1–2 (Plenum Press, London, 1975)

8. A.S. Nowick, J.J. Burton (eds.), *Diffusion in Solids: Recent Developments* (Academic Press, New York, 1975)
9. G.E. Murch, A.S. Nowick (eds.), *Diffusion in Crystalline Solids* (Academic Press, New York, 1984)
10. H. Mehrer, in *Diffusion in Solids, Fundamentals Methods, Materials, Diffusion-Controlled Processes*, vol. 155 (Springer, Berlin, 2007)
11. P. Heitjans, J. Kärger (eds.), *Diffusion in Condensed Matter Methods Materials, Models* (Springer, Berlin, 2008)
12. V.G. Plekhanov, Applications of isotope effect in solids. J. Mater. Sci. **38**, 3341–3429 (2003)
13. J.R. Manning, *Diffusion of Atoms in Crystals* (Princeton, New Jersey, 1968)
14. J. Crank, *The Mathematics of Diffusion* (Oxford University Press, New York, 1975)
15. D. Wolf, *Spin Temperature and Nuclear-Spin Relaxation in Matter: Basic Principles and Applications* (Oxford University Press, New York, 1979)
16. V.G. Plekhanov, *Applications of Isotopic Effects in Solids* (Springer-Verlag, Berlin, 2004)
17. H.S. Carslaw, C. Jaeger, *Conduction Heat in Solids* (Oxford University Press, New York, 1959)
18. S.J. Rothman, *The measurement of tracer diffusion coefficients in solids*, in [9], chap. 1, p. 1–61
19. N.L. Pterson, W.K. Chen, Cation self-diffusion and the isotope effect in $Mn_{\delta}O$, in [8], Chap. 2, pp. 115–157. J. Phys. Chem. Solids **43**, 29–38 (1982)
20. W. Frank, U. Gösele, H. Mehrer et al., *Diffusion in silicon and germanium*, in [9], Chap. 2, pp. 63–141
21. D.E. Aboltyn, Ya.E. Karis, V.G. Plekhanov, Experimental manifestation of the role of phonons in the formation and motion of point defects in alkali halide crystals. Sov. Phys. Solid State **22**, 510–511 (1980)
22. A. Seager, K.P. Chik, Diffusion mechanisms and point defects in silicon and germanium. Phys. Stat. Solidi **29**, 455–542 (1068)
23. R.N. Ghashtagor, diffusion in tellurium. I. Anisotropy and impurity effects. Phys. Rev. **155**, 598–602 (1967)
24. M. Werner, H. Mehrer, H. Siethoft, Self-diffusion and antimony diffusion in tellurium, J. Phys. C: Solid State Phys. **16**, 6185–6197 (1983)
25. P. Bratter, H. Gobrecht, Self-diffusion in selenium. Phys. Status Solidi **37**, 869–878 (1970)
26. D.M. Holloway, Applications of depth profiling by Auger sputter techniques. J. Vac. Sci. Technol. **12**, 392–399 (1975)
27. J.W. Mayer, J.M. Poate, in *Thin Film Interdiffusion and Reactions*, ed. by N.B. Urli, J.B. Corbett (Springer, Berlin, 1981)
28. R. Behrisch, *Introduction and overview in Sputtering by Particle Bombardment, II*, ed. by R. Behrisch (Springer, Berlin, 1981), Chap. 1, pp. 1–10
29. B. Chapman, *Glow Dicharge Processes* (Wiley, New York, 1980)
30. R.D. Reader, H.R. Kauffman, Optimization of an electron-bombardmention source for ion machining. J. Vac. Sci. Technol. **12**, 1344–1347 (1975)
31. J.N. Mundy, S.J. Rothman, An apparatus for microsectioning diffusion samples by sputtering, Ibid, A **1**, 74–78 (1983)
32. D. Gupta, R.R.C. Tsui, A universal microsectioning technique for diffusion. Appl. hys. Lett. **17**, 294–297 (1970)
33. H. Liebl, Secondary-ion mass spectrometry and its use in depth profiling. J. Vac. Sci. Technol. **12**, 385–399 (1975)
34. W. Reuter, J.E.E. Baglin, Secondary-ion mass spectrometry and Rutherford backscattering spectroscopy for the analysis of thin films, Ibid, **18**, 282–288 (1981)
35. M.-P. Macht, V. Naundorf, Direct measurement of small diffusion coefficients with secondary mass spectroscopy, J. Appl. Phys. **53**, 7551–7558 (1982)
36. G.J. Slusser, J.S. Slattery, Secondary-ion mass spectrometry analysis of semiconductor layers. J. Vac. Sci. Technol. **18**, 301–304 (1981)

37. D.S. Catlett, J.N. Spencer, G.J. Vogt, Hydrogen transport in lithium hydride as a function of pressure. J. Chem. Phys. **58**, 3432–3438 (1973)
38. J.N. Spencer, D.S. Catlett, G.J. Vogt, Hydrogen transport in lithium hydrides a function of temperature, Ibid, **59**, 1314–1318 (1973)
39. V.B. Ptashnik, TYu. Dunaeva, Self-diffusion of lithium and hydrogen ions in lithium hydride single crystals. Fiz. Tverd. Tela **19**, 1643–1647 (1977)
40. Yu.M. Baikov, V.B. Ptashnik, T.Yu. Dunaeva, Influence of isotope composition of hydrogen on the electric conductivity of solid lithium hydride, Fiz. Tverd. Tela. **20**, 1244–1246 (1978) (in Russian)
41. T.A. Dellin, G.J. Dienes, C.R. Rischer et al., Low-temperature volume expansion of LiH-LiT. Phys. Rev. B **1**, 1745–1753 (1970)
42. F.E. Pretzel, D.T. Vier, E.G. Szklarz et al., Los Alamos Sci. Lab. Rep. LA 2463 (1961) cited in [40]
43. H. Letaw Jr, W.M. Portnoy, L. Slifkin, Self-diffusion in germanium. Phys. Rev. **102**, 636–639 (1956)
44. M.W. Valenta, C. Ramasastry, Effect of heavy doping on the self-diffusion of germanium, Ibid, **106**, 73–75 (1957)
45. D.R. Campbell, Isotope effect for self-diffusion in Ge, Ibid, B **12**, 2318–2324 (1975)
46. G. Vogel, H. Hettich, H. Mehrer, Self-diffusion in intrinsic germanium and effects of doping on self-diffusion in germanium. J. Phys. C: Solid State Phys. **16**, 6197–6208 (1983)
47. A. Seeger, W. Frank, On the theory of the diffusion of gold into dislocated silicon wavers. Appl. Phys. A **27**, 171–176 (1982)
48. H.D. Fuchs, W. Walukiewicz, W. Dondl et al., Germanium $^{70}Ge/^{74}$ Ge isotope heterostructures: an approach to self-diffusion studies. Phys. Rev. **B51**, 16817–16821 (1995)
49. Beke D.L. (ed.), *Diffusion in Semiconductors and Non-Metallic Solids*, Landolt-Börnstein, New Series, Group III, vol. 33A, (Springer, Berlin, 1998)
50. M. Schulz (ed.), *Impurities and Defects in Group IV Elements, IV–IV and III–V Compounds*, Landolt-Börnstein, New Series, Group III, vol. 41A2, Part α, (Springer, Berlin, 2002)
51. M. Schulz (ed.), *Impurities and Defects in Group IV Elements, IV–IV and III–V Compounds*, Landolt-Börnstein, New Series, Group III, vol. 41A2, Part β, (Springer, Berlin, 2003)
52. H. Bracht, N.A. Stolwijk, *Solubility in Silicon and Germanium*, Landolt-Börnstein, New Series, Group III, vol. 41A2, Part α, (Springer, Berlin, 2002)
53. N.A. Stolwijk, H. Bracht, *Diffusion in Silicon, Germanium and Their Alloys, Landolt-Börnstein, New Series, Group III*, vol. 33A (Springer, Berlin, 1998)
54. J. Spitzer, T. Ruf, W. Dondl et al., Raman scattering by optical phonons in isotopic $^{70}(Ge)^{74}_n(Ge)_n$ superlattice. Phys. Rev. Lett. **72**, 1565–1568 (1994)
55. H.D. Fuchs, K.M. Itoh, E.E. Haller, Isotopically controlled germanium: A new medium for the study of carrier scattering by neutral impurities. Philos. Mag. B **70**, 661–670 (1994)
56. H. Bracht, H.H. Silvester, Self- and foreign-atom diffusion in semiconductor isotope heterostructures. II Experimental results for silicon, Phys. Rev. B **75**, 035211/1–21, (2007)
57. H. Bracht, Self- and foreign-atom diffusion in semiconductor isotope heterostructures. I. Continuum theoretical calculations, Ibid, B **75**, 035210/1–16, (2007)
58. G. Leibfried, W. Ludwig, in *Theory of Anharmonic Effects in Crystals Solid State Physics*, ed. by F. Seitz, D. Turnbull (Academic Press, New York, 1961) p. 275–445
59. N.W. Aschcroft, N. David Mermin, *Solid State Physics* (Harcourt Brace College Publishers, New York, 1975)
60. G.P. Srivastawa, *The Physics of Phonons* (Hilger, Bristol, 1990)
61. I.E. Tamm, Eine Bemerkung zur Diracschen Theorie der Lichtenstroung und Dispersion. Zs. Phys. **62**, 705–708 (1930)
62. M. Blackman, in *The specific heat of solids Handbuch der Physik*, ed. by S. Flüge, Vol 7, Pt. 1 (Springer-Verlag, Berlin, 1955) p. 325–367
63. P. Klemens, in *Thermal Conductivity and Lattice Vibrational Modes Solid State Physics*, ed. by F. Seitz, D. Turnbull, Vol. 7 (Academic Press, New York, 1959) p. 1–98
64. P. Debye, The Debye theory of specific heat, Ann. Phys. (Leipzig) **39**(4) 789–803 (1912)

65. L.D. Landau, E.M. Lifshitz, *Statistical Physics* (Pergamon Press, New York, 1968)
66. V.G. Plekhanov, Isotope effect on the lattice dynamics of crystals. Mater. Sci. & Eng. R **35**, 139–237 (2001)
67. D.F. Gibbons, Thermal expansion of some crystals with the diamond structure. Phys. Rev. **112**, 136–140 (1958)
68. D.N. Batchelor, R.O. Simons, Lattice constants and thermal expansivities of silicon and calcium ftuoride between 6 and 322K. J. Chem. Phys. **41**, 2324–2330 (1964)
69. A.S. Okhotin, A.S. Pushkarski, V.V. Gorbachev, *Thermophysical Properties of Semiconductors (Moscow* (Atom Publ House, London, 1972). (in Russian)
70. S.I. Novikova, *Thermal Expansion of Solids* (Science, Moscow, 1974) (in Russian)
71. G. Dolling, R.A. Cowley, The thermodynamic and optical properties of germanium, silicon, diamond and gallium arsenide. Proc. Phys. Soc. **88**, 463–494 (1966)
72. V.G. Plekhanov, Elementary excitations in isotope-mixed crystals. Phys. Reports **410**, 1–235 (2005)
73. T.H. Baron, J.G. Collins, G.K. White, Thermal expansion of solids at low temperatures. Adv. Phys. **29**, 609–730 (1980)
74. V.I. Ozhogin, A.V. Inyushkin, A.N. Taldenkov, et al., Isotope effect for thermal expansion coefficient of germanium, JETP (Moscow) **115**, 243–248 (1999) (in Russian)
75. H. Jex, Thermal expansion and mode Gruneisen parameters of LiH and LiD. J. Phys. Chem. Solids **35**, 1221–1223 (1974)
76. B.W. James, H. Kherandish, The low temperature variation of the elastic constants of LiH and LiD. J. Phys. C: Solid State Phys. **15**, 6321–6339 (1982)
77. D. Gerlich, C.S. Smith, The pressure and temperature derivatives of the elastic module of lithium hydride. J. Phys. Chem Solids **35**, 1587–1592 (1974)
78. J.J. Fontanella, D.E. Schuele, Low temperature Gruneisen parameter of RbI from elasticity data, Ibid **31**, 647–654 (1970)
79. J.R. Hardy, A.M. Karo, *The Lattice Dynamics and Statics of Alkali Halide Crystals* (Plenum Press, New York, 1979)
80. V.G. Plekhanov, *Isotope-Mixed Crystals: Fundamentals and Applications* (Bentham, e-books, 2011). ISBN 978-1-60805-091-8
81. S. Haussuhl, I. Skorczyk, Elastische und thermoelastische Eigenschaften von LiH und LiD einkristallen. Zs. Krist. **130**, 340–345 (1969)
82. A.R. Ubellohde, *The Molten State of Substances* (Metallurgy, Moscow, 1982) (in Russian)
83. G.L. Anderson, G. Nasise, K. Phillipson et al., Isotopic effects on the thermal expansion of lithium hydride. J. Phys. Chem. Solids **31**, 613–618 (1970)
84. R.B. Von Dreele, J.G. Morgan, S.M. Stishov, Thermal expansion and equation of state of KCN of different isotopic composition, JETP (Moscow) **114**, 2182–2186 (1998) (in Russian)
85. A.P. Zhernov, Thermal expansion of germanium crystal lattice with different isotope composition, Fiz. Tverd. Tela (St. Petersburg) **40**, 1829–1831 (1998)
86. A. P. Zhirnov, Statistical displacement about isotope impurities and remain resistance, JETP (Moscow) **114**, 2153–2165 (1998) (in Russian)
87. I.G. Kuleev, I.I. Kuleev, Influence normal processes of phonon–phonon scattering on maximum values of thermal conductivity isotope pure Si crystal, JETP (Moscow) **122**, 558–569 (2002) (in Russian)
88. V.I. Tyutyunnik, Effect of isotope substitution on thermal expansion of LiH crystal. Phys. Status Solidi (b) **172**, 539–543 (1992)
89. V.S. Kogan, Isotope effect in structuring properties. Sov. Phys. Uspekhi **5**, 579–618 (1963)
90. M. Planck, Zur Theorie der Wämestrahlung. Ann Phys. **336**, 758–768 (1910)
91. Ch. Kittel, *Thermal Physics* (Wiley, New York, 1969)
92. M. Born, K. Huang, *Dynamical Theory of Crystal Lattice* (Oxford University Press, Oxford, 1988)
93. V.G. Plekhanov, Isotope effect in lattice dynamics, Physics-Uspekhi (Moscow) **46**, 689–717 (2003); Lattice dynamics of isotope-mixed crystals, ArXiv:cond-mat/1007.5125
94. P. Günter, Ann. Phys. **63**, 476 (1920) cited in [97]

95. V.N. Kostryukov, The capacity of LiH between 3.7 and 295K, Zh. Fiz. Khim. (Moscow) **35**, 1759–1762 (1961) (in Russian)
96. V.G. Plekhanov, Lattice dynamics of isotopically mixed crystals, Opt. Spectr. (St. Petersburg) **82**, 95–124 (1997)
97. G. Yates, G.H. Wostenholm, J.K. Bingham, The specific heat of ^{7}LiHand^{7}LiD at low temperature. J. Phys. C: Solid state Phys. **7**, 1769–1778 (1974)
98. M.W. Guinan, C.F. Cline, Room temperature elastic constants of ^{7}LiHand^{7}LiD. J. Nonmetals **1**, 11–15 (1972)
99. D.P. Schumacher, Polymorphies transition of LiH. Phys. Rev. **126**, 1679–1684 (1962)
100. K.-F. Berggren, A pseudopotential approach to crystalline lithium hydride, J. Phys. C: Solid State Phys. **2**, 802–815 (1969)
101. F.F. Voronov, V.A. Goncharov, Compressions of lithium hydride, Fiz. Tverd. Tela (St. Petersburg) **8**, 1643–1645 (1966) (in Russian)
102. D.R. Stephens, E.M. Lilley, Compressions of isotopes lithium hydride. J. Appl. Phys. **39**, 177–180 (1968)
103. Q. Johnson, A.C. Mitchel, Search for the NaCl and CsCl transition in LiH by flash X-ray diffraction. Acta Cryst. **A31**, S241–S245 (1975)
104. Y. Kondo, K.J. Asaumi, Effect of pressure on the direct gap of LiH. J. Phys. Soc. Japan **57**, 367–371 (1988)
105. K. Chandehari, A. Ruoff, Band gap and index refraction of CsH to 25 GPa. Solid State Commun. **95**, 385–388 (1995)
106. W. Schnelle, E. Gmelin, Heat capacity of germanium crystals with different isotopic composition. J. Phys: Condens. Matter **13**, 6087–6094 (2001)
107. M. Sanati, S.K. Estreicher, Specific heat and entropy of GaN, Ibid **16**, L327–L331 (2004)
108. U. Piestergen, in *Heat capacity and Debye temperature Semiconductors and Semimetals*, ed. by R.K. Willardson, A.C. Beer, Vol. 2 (Academic Press, New York, 1966) p. 49–62
109. G. London, The difference in molecular volume of isotopes. Z. Phys. Chem. Neue Folge **16**, 3021–3029 (1958)
110. A.R. Ruffa, Thermal expansion and zero-point displacement in isotopic lithium hydride. Phys. Rev. B **27**, 1321–1325 (1983)
111. E.E. Shpil'rain, K.A. Yakimovich, T.N. Mel'mikova, *Thermal Properties of Lithium Hydride, Deuteride and Tritide and Their Solutions* (Energoatomizdat, Moscow, 1983) (in Russian)
112. A.A. Berezin, A.M. Ibragim, Effects of the diversity of stable isotopes on properties of materials. Mater. Chem. Phys. **19**, 420–437 (1988)
113. D.K. Smith, H.R. Leider, Low-temperature thermal expansion of LiH. J. Appl. Crystal. **1**, 246–249 (1968)
114. H. Holloway, K.C. Hass, M.A. Tamor et al., Isotopic dependence of lattice constants of diamond. Phys. Rev. **B44**, 7123–7126 (1991)
115. H. Holloway, K.C. Hass, M.A. Tamor et al., Isotopic dependence of lattice constants of diamond. Phys. Rev. B **45**, 6353E (1992)
116. P. Pavone, S. Baroni, Dependence of the crystal lattice constant on isotopic composition. Solid State Commun. **90**, 295–297 (1994)
117. R.C. Bushert, A.E. Merlin, S. Pace et al., Effect of isotope concentration on the lattice parameter of germanium perfect crystals. Phys. Rev. B **38**, 5219–5221 (1988)
118. J.C. Noya, C.P. Hrrero, R. Ramirez, Isotope dependence of the lattice parameter of germanium from path-integral Monte Carlo simulations. Phys. Rev. B **56**, 237–243 (1997)
119. C.P. Herrero, Dependence of the silicon lattice constant on isotopic mass. Phys. Status Solidi (b) **220**, 857–867 (2000)
120. Y. Ma, J.S. Tse, Ab initio detrmination of crystal lattice constant and thermal expansion for germanium isotopes. Solid State Commun. **143**, 161–165 (2007)
121. W. Banholzer, T. Anthony, Diamond properties as a function of isotopic composition. Thin Solid Films **212**, 1–10 (1992)
122. W.B. Zimmerman, Lattice constant dependence on isotopic composition in the ^{7}Li(H, D) system. Phys. Rev. **B5**, 4704–4707 (1972)

123. T. Yamanaka, S. Morimoto, H. Kanda, Influence of the isotope ratio on the lattice constant of diamond, Ibid **B49**, 9341–9343 (1994)
124. R. Vogelgesang, A.K. Ramdas, S. Rodriguez et al., Brillouin and Raman in natural and isotopically controlled diamond. Phys. Rev. B **54**, 3989–3999 (1996)
125. N. Garo, A. Cantarero, T. Ruf et al., Dependence of the lattice parameters and energy gap of zinc-blende-type semiconductors on isotopic mass. Phys. Rev. B **54**, 4732–7440 (1996)
126. A. Debernardi, M. Cardona, Isotopic effect on the lattice constant in compound semiconductors by perturbation theory: An ab initio calculation. Phys. Rev. B **54**, 11305–11310 (1996)
127. H. Bilz, W. Kress, *Phonon Dispersion Relations in Insulators* (Springer, Berlin, 1979)

Chapter 6
Traditional Application of Stable and Radioactive Isotopes

6.1 Background

This chapter reviews the applications of *isotopetronics* in different modern technologies and science. It is briefly describes the application of stable isotopes. This chapter describes the new reactor technology-*neutron transmutation doping (NTD)*, capture of thermal neutrons by isotope nuclei followed by *nuclear* decay produces new elements, resulting in a number of possibilities for *isotope* selective doping of solids. The importance of this technology for studies of *semiconductor* doping as well as *metal-insulator transitions* and neutral impurity scattering process is underlined. The introduction of particle irradiation into processing of semiconductor materials and devices creates a new need for additional understanding of atomic-displacement-produced defects in semiconductors. It is shown that measurement of decay rates of induced *radioactivity* and the system of clearance and certification such as to allow the solids to be internationally transported as "Exemt Material", as defined in *IAEA Regulations*, are dealt with. There is a short description of the theory and practice of semiconductor lasers. The discovery of the linear luminescence of *free excitons* observed over a wide temperature range has placed *lithium hydride*, as well as crystals of *diamond* in line as prospective sources of coherent radiation in the UV spectral range. For LiH, isotope tuning of the exciton emission has also been shown. It was shown that use of the neutron transmutation doping of materials allows new kinds of technology for producing optical fibres. This chapter contains a brief description of many traditional (e.g. human health, geochronology, etc.) and new applications (memory and quantum information) in technology and science. The main customers of isotopes are *pharmaceutical* and *biomedical* industries. They use them for diagnostic purposes, such as markers of products whose final bodily destination is known. For instance ^{13}C, with a nuclear magnetic moment can be applied to studies with NMR scanners. ^{18}F is effectively used in *Positron Emission Tomography (PET)*.

The material of this chapter stresses the perspective of new directions of nanotechnology—isotoptronics.

V. G. Plekhanov, *Isotopes in Condensed Matter*, Springer Series in Materials Science 162, 207
DOI: 10.1007/978-3-642-28723-7_6, © Springer-Verlag Berlin Heidelberg 2013

6.2 The NTD Process: A New Reactor Technology

The neutron transmutation doping (NTD) process involves the cooperation of semiconductor materials specialists, device producers, radiation damage and defect specialists and reactor personnel. Of all possible interactions among these groups, those with the reactor community have traditionally been the weakest. Reactor personnel have, therefore, had the greatest learning curves to overcome. It is to the credit of both the reactor community and the semiconductor industry that these difficulties have been overcome so readily in the few years since 1975 when NTD silicon first appeared on the market. The transmutation doping process simply involves irradiation of an undoped semiconductor with a thermal neutron flux. The major advantages of the NTD process are illustrated schematically in Fig. 6.1. The homogeneity in NTD-Si is a result of a homogeneous distribution of silicon isotopes in the target material and the long range of *neutrons* in *silicon*. Doping accuracy is a result of careful neutron flux integration. The material improvements offered by the NTD process form the basis for semiconductor device improvement (for details see [1]).

As is well known, research reactor facilities provide the best source of thermal neutrons for this purpose at present (see e.g. [2–5]). These reactors are ideally suited for such projects because they have usually been constructed with sample irradiation as one of the prime design requirements. Although these reactor facilities provide a source of thermal ($E \sim 0.025\,eV$) neutrons, this thermal flux is always accompanied by a fast neutron component which is not useful in providing doping transmutations, but does produce *radiation damage* (displacements of atoms from their normal lattice sites) which must be repaired by annealing, the process of heating the irradiated material to temperatures sufficiently high that the irradiation produced defects become mobile and can removed.

To understand the process further, we must be concerned with the interactions of neutrons, both thermal and fast, with the target material to be doped. Because neutrons are neutral particles, their range of penetration in most materials is usually very long. They interact only very weakly with atomic electrons through their magnetic movements. Being neutral, *neutrons* see no *Coulombic* barrier at the target nuclei and, therefore even very slow neutrons may reach into the nucleus without difficulty. In fact, the slower the neutron velocity, the greater is the time of interaction between the neutron and the target nucleus. We, therefore, expect the probability of neutron capture by the target nuclei to be enhanced at low neutron energies.

This interaction is described in terms of a capture *cross-section*, σ_c, where the number of captures per unit volume, N, is given by

$$N = N_T \sigma_c \Phi, \tag{6.1}$$

where N_T is the number of target nuclei per unit volume, σ_c the capture cross-section and $\Phi = \phi t$ is the influence (flux times time) given in n/cm^2. Figure 6.2 shows the capture cross-section as a function of neutron energy for silicon as averaged over all three stable silicon isotopes [6]. Similar behaviour is found individually for each

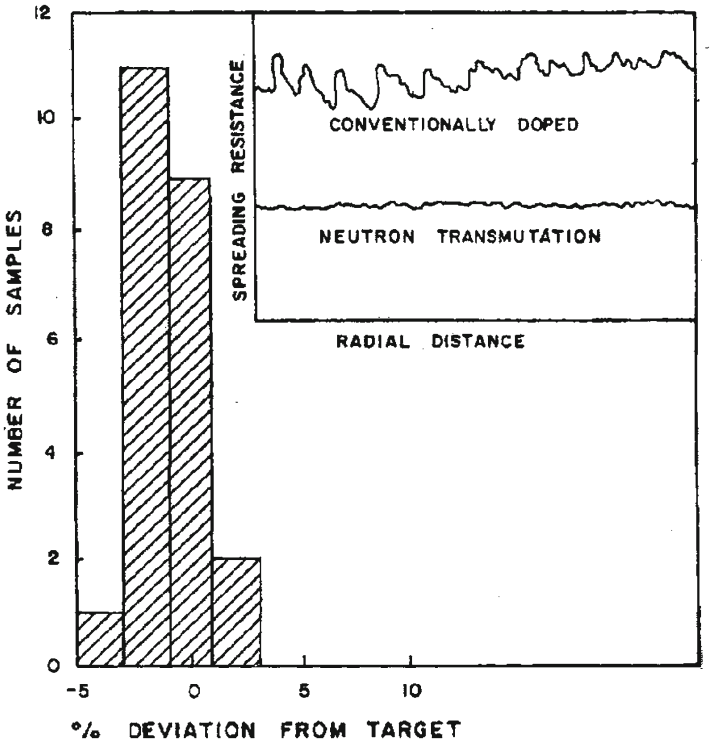

Fig. 6.1 Advantages of NTD process. Histogram of irradiation target accuracy obtained for commercial sample lot at NURR. Insert is a schematic representation of spreading resistance traces across a wafer diameter for conventionally doped and NTD Si (after [6])

silicon isotope. It can be seen in Fig. 6.2 that for low energies:

$$\sigma_c \sim E^{-1/2} \sim 1/V. \tag{6.2}$$

For a given nuclear radius, (1/V) is proportional to the interaction time. Therefore, the cross-section represents a probability of interaction between the nucleus and neutron.

After neutron capture, the target *nucleus* differs from the initial nucleus by the addition of the nucleon and is a new isotope in an excited state which must relax by the emission of energy in some form. This emission is usually in the form of electromagnetic radiation (photons) of high energy usually called gammas (see e.g. [9] and references therein). The time for decay of this excess energy by gamma emission can be very short (prompt gammas) or can take an appreciable time in which case a half-life a factor of two, can be measured. The gamma emission spectrum is characteristic of the nuclear energy levels of the transmuted target nuclei and can be used as a powerful trace substance technique called neutron activation analysis (NAA),

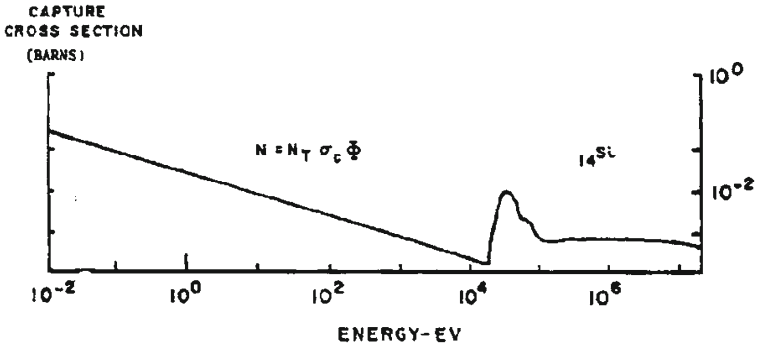

Fig. 6.2 Neutron capture cross-section as a function of neutron energy for natural silicon (after [6])

to detect quantitavely impurity levels as low as 10^9 atoms/cm^3 [10]. A typical trace substance NAA gamma spectrum is shown in Fig. 6.3. Each emission line is characteristic of a particular nuclear transition of a particular isotope. The absorption of a neutron and the emission of gammas is represented by the notation:

$$A_{X(n,\gamma)}A + 1_X, \tag{6.3}$$

where (n, γ) represents (*absorption, emission*), A is the initial number of nucleons in the target element X before neutron absorption while A + 1 is the number after absorption. It is possible for the product isotope $A + 1_X$ to be naturally occurring and stable. In many cases, however, the product isotope is unstable. Unstable isotopes further decay by various modes involving the emission of electrons (β-decay), protons, α-particles, K-shell electron capture or internal conversion until a stable isotopic state is reached (for details see, e.g. [12]). These decays produce radioactivity and can be characterised by their half-lives $T_{1/2}$. In the case of silicon, three stable target isotopes are transformed by (n, γ) reactions [7, 8] as follows:

$$\begin{aligned}
&(92.3\%)^{28}\mathrm{Si(n,\gamma)}^{29}\mathrm{Si}, \sigma_c = 0.08\,\mathrm{b};\\
&(4.7\%)^{29}\mathrm{Si(n,\gamma)}^{30}\mathrm{Si}, \sigma_c = 0.28\,\mathrm{b};\\
&(3.1\%)^{30}\mathrm{Si(n,\gamma)}^{31}\mathrm{Si} \rightarrow^{31} \mathrm{P} + \beta^-, \sigma_c = 0.11\,\mathrm{b};\ (T_{1/2} = 2.62\,\mathrm{h}).
\end{aligned} \tag{6.4}$$

The relarive abundance of each stable silicon isotope is shown in parenthesis (see also [9]). The cross-sections are expressed in barns (1 barn = 10^{-24}cm^2). The first two reactions produce no dopants and only redistribute the relative abundances slightly. The third reaction produces ^{31}P, the desired donor dopant [13, 14], at a rate of about 3.355 ppb per $10^{18}n_{th}$cm^{-2} [4]. This production is calculated using Eq. (6.3), the ^{30}Si ($N_T \cong 5 \times 10^{22}$ Si·cm$^{-3} \times 0.031$).

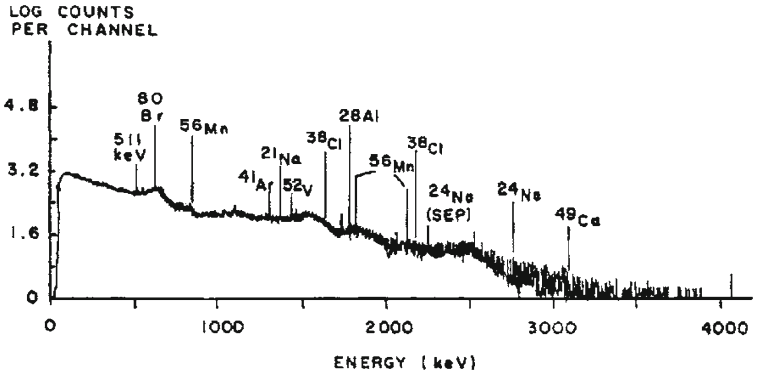

Fig. 6.3 Typical neutron activation analysis (NAA) gamma-ray spectrum to search for trace substances deposited on an air filter after 1 min. irradiation at MURR (after [10])

In addition to the desired *phosphorus* production reaction and its relatively short half-life for β^- decay, the reaction

$$^{31}\mathrm{P(n,\,\gamma)}^{32}\mathrm{P} \rightarrow {}^{32}\mathrm{S} + \beta^-, \sigma_c = 0.19\,\mathrm{b}\ (\mathrm{T}_{1/2} = 14.3\,\mathrm{d}) \tag{6.5}$$

occurs as a secondary undesirable effect. The decay of ^{32}P is the primary source of radioactivity in NTD float fine Si. Of course, any undesirable trace impurities in the silicon starting material can lead to abnormally long half-life activities which may require that material be held out of production until exempt limits are reached. These factors have stimulated on the subject of radiation protection. Once the dopant phosphorus has been added silicon ingot by transmutation of the ^{30}Si isotope, the problems remain to make this radiation damaged and highly disordered material useful from an electronic device point of view. Several radiation damage mechanisms contribute to the displacement of the silicon atoms from their normal lattice position (details see below). These are:

1. Fast neutron knock-on displacements;
2. Fission gamma induced damage;
3. Gamma recoil damage;
4. Beta recoil damage;
5. Charged particle knock-on from (n,p); (n,α) etc reactions (for details see [9])

Estimates can be made of the rate at which Si atom displacements are produced by these various mechanisms, once a detailed neutron energy spectrum of the irradiation is known, and these rates compared to the rate at which phosphorus is produced.

The number of displaced atoms per unit volume per second, N_D, is estimated from the equation

$$\mathrm{dN}_D/\mathrm{dt} = \mathrm{N}_T \sigma \phi \nu, \tag{6.6}$$

where N_T is the number of target atoms per unit volume, ϕ is the flux of damaging particles and ν is the number of displacements per incident damaging particle. The *cross-section* for gamma induced displacements in silicon is small while the cross-sections for (n,p); (n,α), etc., are of the order of millibarns and have thresholds in the MeV range. The fast neutron knock-on displacements can be calculated from the *elastic neutron scattering* cross-section once the reactor neutron energy spectrum is known. Estimates of fission spectra and graphite moderated fission spectra can be found in the literature [15].

Even if the fast neutron damage could be completely eliminated, the recoil damage mechanisms, which are caused by thermal neutron capture, still would produce massive numbers of displacements compared to the number of phosphorus atoms produced. In the case of gamma recoil, a gamma of energy $\hbar\omega$ carries a momentum $\hbar\omega$/c which must equal the Si isotope recoil momentum MV. The recoil energy

$$\mathrm{E}_R = \frac{1}{2}\mathrm{MV}^2 = \frac{1}{2}\frac{(\hbar\omega)^2}{MC^2} \tag{6.7}$$

is, therefore, departed to the silicon atom of mass M for each gamma emitted. An average overall possible silicon isotope gamma emission and cross-sections yields an average recoil energy of 780 eV [16] which is significantly higher than the Si displacement energy. A similar effect is encountered for ^{31}Si β^- decay. The β^- carries a momentum

$$\mathrm{p} = \frac{1}{c}\sqrt{\mathrm{E}_\beta^2 - \left(m_0c^2\right)^2} \equiv \mathrm{MV}. \tag{6.8}$$

Therefore,

$$\mathrm{E}_R = \frac{1}{2}\mathrm{MV}^2 = \frac{1}{2}\left[\mathrm{E}_\beta^2 - \left(m_0c^2\right)^2\right] \Big/ \left(Mc^2\right). \tag{6.9}$$

For a β^- emitted with an energy of 1.5 MeV, E_R = 33.2 eV or roughly twice the displacement threshold.

From the above considerations, a very crude estimate of the number of displacements per phosphorus atom produced can be made. The results of the estimation are shown in Table 6.1. While the absolute numbers of displacements should not be taken literally, the relative magnitudes of the amounts of damage produced by these various mechanisms are probably orders of magnitude correct. An inspection of Table 6.1 indicates that the gamma recoil mechanism is significant relative to the quantity of phosphorous produced even in highly moderated reactors. We are led to the inescapable conclusion that transmutation doping will always produce significant amounts of radiation damage which must be repaired in some way. These defects introduce defect levels into the band gap which cause free carrier removal and a reduction in carrier mobility and minority carrier lifetime (see, e.g. [16]).

The defects produced by neutron irradiation are removed by *thermal annealing* as discussed previously. It is at this point in the process where disagreement as to the

Table 6.1 Number of displaced silicon atoms per phosphorus produced for various damage mechanisms shown for an in-core fission spectrum and a graphite moderated spectrum (after [6])

Damage particle/ Position	In core	In pool
Fast neutron	4.06×10^6	1.38×10^4
Fission gamma	3.64×10^3	36.4
Gamma recoil	1.29×10^3	1.29×10^3
Beta recoil	2.76	2.76
Total DISP/(P)	4.06×10^6	1.51×10^4

best procedure is likely to be the greatest. The spectrum of possible defect structures and their energetics is impressively large and incompletely understood. Therefore, annealing procedures according to Meese [6] will be based on art rather than on exact science. They will also tend to become proprietary for this reason.

This is unfortunate since it is precisely in this area that fundamental knowledge is needed to produce the best possible product. Although carrier concentration and mobility recovery are easily obtainable by various annealing procedures, minority carrier lifetime recovery is very elusive at present.

So, *neutron transmutation* offers both advantages and disadvantages over conventionally doped silicon (for details see [9]).

Advantages

1. Precision target doping (=1% or better).
2. Better axial and radial uniformity.
3. No microresistivity structure.

Disadvantages

1. Irradiation costs.
2. Reduction in minority carrier lifetime.
3. Radioactive safeguards considerations.

The steady growth of the *NTD-silicon* (and others NTD-semiconductors) market suggests (see also below) that the advantages are outweighing the disadvantages. We should add that the reactor facilities in details have been reviewed in [7, 8].

6.3 Experimental Results

6.3.1 Ge

As was noted above, neutron transmutation (NT) is especially intriguing for semiconductors for several reasons. First, the NT process can create new elements removed by just one atomic number. Considering for the moment the elemental group-IV semiconductors Ge and Si, this means that the donors As and P will be created,

respectively, following neutron capture and β-decay of *isotopes* of these semiconductor elements. The new elements are, of course, the prototypical donors. Neutron capture leads to NTD. Second, the number of new atoms ${}^{A+1}_{Z+1}\mathrm{N}$ created is simply (see also above)

$$ {}^{A+1}_{Z}\mathrm{N} = \mathrm{n}\sigma_n {}^{A}_{Z}\mathrm{N}, \tag{6.10} $$

where n being the total neutron fluency (cm^{-2}), σ_n the *cross-section* for thermal neutron capture (cm^2), and ${}^{A}_{Z}\mathrm{N}$ the atom concentration of the specific isotope in the given isotope mixture (cm^{-3}) (either natural or man made). Considering that the values of σ_n lie in the $10^{-23} \div 10^{-24}\mathrm{cm}^{-2}$ range (see above), it recognises that very large neutron fluences are required to transmute a significant number of atoms of one element into another. Whereas this may pose problems to fulfil the medieval alchemist's dream, it is perfectly suited for the person who wants to dope semiconductors. With the thermal neutron fluences available in modern nuclear reactor (see also [7, 8]) one can dope Ge up to the *metal-insulator (MI)* transition ($2\text{–}3 \times 10^{17}\ \mathrm{cm}^{-3}$) while Si can be doped with phosphorus to several times $10^{15}\ \mathrm{cm}^{-3}$ [17]. As will be shown below this is due to the small atom concentration of ${}^{30}_{14}\mathrm{Si}$ and the modest value of the thermal capture cross-section. Third, there are elements that have light isotopes which upon neutron capture transmute to a lower Z element either by electron capture or by positron decay. In this case acceptors are created. A classical case is the transmutation of ${}^{70}_{32}\mathrm{Ge}$ into ${}^{71}_{31}\mathrm{Ga}$.

The main advantage of the *NTD* method, as we know at present, is the precision doping which is connected with the linear dependence of concentration of doping impurities on the doze of neutron irradiation. Such dependence is numerous observed in the different experiments (see, e.g [18–22]). As an example, in Fig. 6.4 there is shown the dependence of the concentrations doped phosphorus on the doze of irradiation the Si crystal in nuclear reactor. This dependence was measured with the help of Hall effect. However, at the large doze of neutron irradiation there is observed the nonlinear dependence. In Fig. 6.5 is shown the results of paper [24] where it was observed the deviation from linear law at the large doze of neutron irradiation of the sample of ${}^{74}\mathrm{Ge}$ which was annealed after irradiation at $\mathrm{T} = 460°\mathrm{C}$ during different time (see also caption of Fig. 6.5). A more amazing effect was observed at the second irradiation of the samples of ${}^{74}\mathrm{Ge}$ previously strong doped with As by NTD method. Instead, expectable increase of the concentration free charges (electrons) n there is observed with the decreased n. This decrease was directly proportional to the neutron irradiation doze of ${}^{74}\mathrm{Ge}$ crystals. Both effects are details analysed in papers [21, 24].

The transmutation of the stable germanium isotopes via capture of thermal neutrons is well understood. Table 6.2 contains all the information relevant to NTD of germanium. Haller et al. [18] quoted the values of the thermal neutron capture *cross-section* σ_n of three sources [25–27]. The information of Table 6.2 permits the computation of the acceptor and donor concentrations for a known neutron exposure. Not only are these concentrations important but the ratio of the sum of all minority dopants (donors) and the sum of all majority dopants (acceptors), i.e. the compensation K, is crucial for the low temperature conduction. For the case of germanium, one obtains K from the following equation (see also [18])

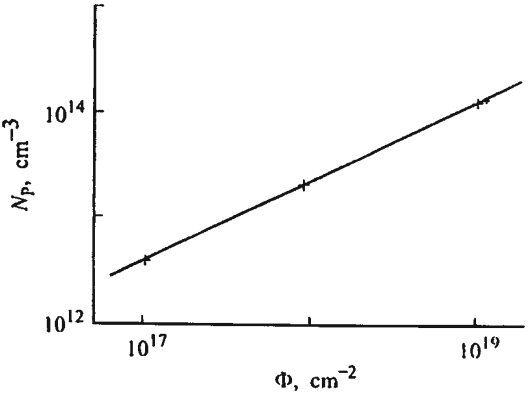

Fig. 6.4 The dependence of the phosphorus atoms concentration on the neutron irradiation doze of Si crystals and followed annealing at 800°C during 1 h. The dependence was measured by Hall effect (after [23])

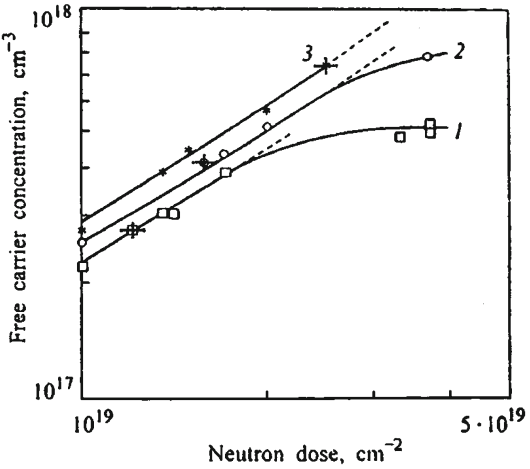

Fig. 6.5 The dependence of the concentration of free electrons in ^{74}Ge NTD on the irradiation of the thermal neutron doze and followed annealing at 460°C during 24 (1), 50 (2) and 100 (3) h. (after [24])

Table 6.2 Characteristics of the transmutation process of germanium (after [18])

Isotope	Abundance (%)	NCCS (barn)	NCDR	Dopant Type
$^{70}_{32}$Ge	20.5	3.4; 3.2; 3.25	$^{70}_{32}$Ge(n, γ) $\rightarrow^{71}_{32}$ Ge $\rightarrow^{71}_{31}$ Ga	p
$^{72}_{32}$Ge	27.4	0.98; 1.0; 1.0	$^{72}_{32}$Ge(n, γ) $\rightarrow^{73}_{32}$ Ge	
$^{73}_{32}$Ge	7.8	14.0; 14.0; 15.0	$^{73}_{32}$Ge(n, γ) $\rightarrow^{74}_{32}$ Ge	
$^{74}_{32}$Ge	36.5	0.62; 0.5; 0.52	$^{74}_{32}$Ge(n, γ) $\rightarrow^{75}_{32}$ Ge $\rightarrow^{75}_{33}$As	n
$^{76}_{32}$Ge	7.8	0.36; 0.2; 0.16	$^{76}_{32}$Ge(n, γ) $\rightarrow^{77}_{32}$ Ge $\rightarrow^{77}_{33}$As $\rightarrow^{75}_{34}$Se	n

NCCS = Neutron Capture Cros-Sections; NCDR = Neutron Capture and Decay Reactions

$$K = \left(\sum \text{donors}\cdot\text{cm}^{-3}\right)/\left(\sum \text{acceptors}\cdot\text{cm}^{3}\right) = (N_{As} + N_{Se})/N_{Ga}. \quad (6.11)$$

The substitutional *selenium* impurities are double donors providing two electrons for compensation. Therefore, they are counted twice in the sum of donors. Using

the different values for σ_n, one finds K ranging from 0.322–0.405 for crystals with negligible initial donor and acceptor concentrations. It would be of great help for both the basic understanding of the hopping conduction [28] as well as for application of neutron-transmutation-doped germanium as, for example , bolometer material [18], if these cross-sections could be accurately evaluated in one or more well-characterised nuclear reactors (see above).

In order to obtain the above K values and thus take full advantage of NTD, Haller et al. chose the purest available Ge crystals as a starting material. Germanium is, in this respect, ideally suited for NTD because it can be purified at present time down to concentrations of $\lesssim 10^{11}\mathrm{cm}^{-3}$ (see e.g. [29]). Such low concentrations are negligible when compared with the dopant concentrations after NTD in the low $10^{16}\mathrm{cm}^{-3}$ range. According to [18] the concentrations of electrically inactive impurities such as *hydrogen, carbon, oxygen* and *silicon* can be as high as $10^{14}\mathrm{cm}^{-3}$. Of all the isotopes of these impurities only $^{30}_{14}\mathrm{Si}$ transmutes to an electrically active impurity, phosphorus, a shallow donor. With only one silicon atom in every 4.4×10^8 germanium atoms and only 3% os all silicon atoms being $^{30}_{14}\mathrm{Si}$ which has a neutron capture cross-section much smaller than the germanium isotope cross-sections, Haller et al estimate that less than one phosphorus donor is produced for every 10^{11} gallium majority acceptors during the NTD process. These authors concluded that ultra-pure germanium crystals are virtually perfect starting material. For the NTD study, they have chosen an ultra-pure germanium single crystal which they have grown at the crystal growth facility described early (see also [18, 29] and references therein).

The measured resistivities (ρ) in [18] are presented in Fig. 6.6. The results of these measurements yield the mobility μ:

$$\begin{aligned} \rho &= (\mathrm{p}\mu e)^{-1}, \text{ and} \\ \mathrm{R}_H &= (\mathrm{p}e)^{-1} \text{and} \\ \mu &= \mathrm{R}_H/\rho, \end{aligned} \tag{6.12}$$

where p is free hole concentration, e is charge of the electron and R_H is the magnitude from Hall measurement.

The mobility values are only useful down to the temperature where hopping conduction sets in. The mobility values agree well with published values for melt-doped material in the temperature range above the hopping regime. This indicates that the concentration of residual radiation damage or other free-carrier scattering centres must be very small. Figure 6.6 shows the log (resistivity) versus 1000/T dependence for six NTD germanium samples. The number next to each curve corresponds to the acceptor (gallium) concentration in each sample. For comparison Haller et al. have also measured gallium-doped germanium samples which have extremely small values of K. These so-called uncompensated samples were cut from crystals which were doped in the melt and were grown in the ultra-pure germanium crystal-growing equipment, and not NTD doped. The compensating donor concentration in these crystals is estimated to be less than 10^{11}–$10^{12}\mathrm{cm}^{-3}$. The resulting K is of the order of 10^{-4}–10^{-5}. The resistivity-temperature dependence of these NTD samples

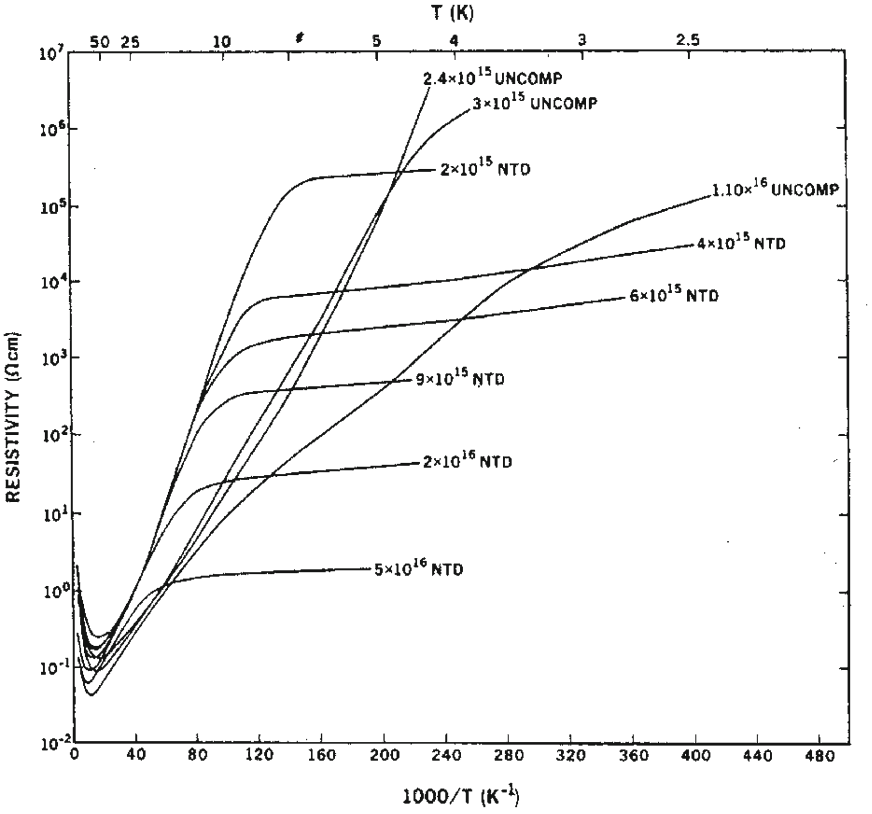

Fig. 6.6 Resistivity as a function of 1000/T for NTD and uncompensated germanium samples. Each curve is labelled by the gallium concentration obtained by either NTD or melt doping (after [18])

is characterised by three regimes. At high temperatures (room temperature down to about 50 K), the resistivity decreases because the carrier mobility increases. Below about 50 K carrier freeze out begins and reduces the free hole concentration rapidly. The slope of the freeze out in highly compensated material as proportional to the acceptor binding energy $E_A - E_V \simeq 11$ meV. At still lower temperatures, the appearance of hopping conduction causes the resistivity to increase only very slowly. All six *NTD* germanium samples show these three resistivity regimes very clearly. The low-compensated samples show different $\log(\rho)$ versus 1/T dependences. A third conduction mechanism has been proposed for such material [30]. It is based on the idea that carriers can "hop" from neutral to a neighbouring neutral acceptor thereby forming a positively charged acceptor. The NTD process in high-purity germanium leads to a fixed compensation which in turn results in a certain slope of the $\log(\rho)$ versus 1/T dependence for a given neutron exposure.

6.3.2 Metal-Insulator Transition

In the next part of this paragraph we briefly discuss the *metal-insulator transition (MIT)* [28, 31–33] in transmuted Ge. In the literature there is an intensive debate whether MIT is a phase transition of first or second order and what are the experimental conditions to obtain it at finite temperatures and in a real (disordered) system (see, e.g. [19, 20, 22, 34]. If the MIT is as second order *phase transition* a further challenge is the solution of the so-called puzzle of the critical index, μ for the scaling behaviour of the metallic conductivity near the MIT, i.e. just above the critical impurity concentration N_c and as small compensation, K. According to the scaling theory of the MIT for doped semiconductors [32, 33], the conductivity at zero temperature $\sigma(0) = \sigma(T \rightarrow 0)$, when plotted as a function of impurity concentration N, is equal to zero on the insulating side of the MIT and remains finite on the metallic side, obeying a power law in the vicinity of the transition,

$$\sigma(0) \propto \left[\left(N/N_c\right) - 1\right]^{\mu}, \tag{6.13}$$

where N_c is the critical impurity concentration of the given system and μ is the critical currently, conductivity exponent. The value of μ, determined experimentally, is compared with theoretical predictions. $\mu \approx 0.5$ has been obtained with nominally uncompensated *semiconductors* (Si : P [35], Si :As [36–38], Ge : As [39], Si : B [40]) while $\mu \approx 1$ has been found with compensated semiconductors (Ge : Sb [41], Si : P,B [42], Ge : Ga, As [43]) and amorphous alloys [43–46]. Exceptions are uncompensated Ge : Sb with $\mu \approx 1$ [7, 8] and Ga_xAr_{1-x} amorphous alloys with $\mu \approx 0.5$ [47, 48]. As was shown in [19] the value $\mu \approx 0.5$ obtained with simple systems like uncompensated semiconductors turns out to be inconsistent with theoretical prediction [31–33, 46]. In his original theory Mott considered only the electron–electron ($e^- - e^-$) interaction (*Mott transition*) and predicted a discontinuous transition of $\sigma(0)$ at N_c [49]. Although there is much evidence for the importance of $e^- - e^-$-interactions, no experimental observation of such an abrupt transition has been reported. Anderson's ideas of MIT is based solely on the disordered potential arising from randomly distributed dopants (*Anderson transition*) [50]. This led to the development of the well known "scaling theory" which predicted $\mu \approx 1$ for 3D systems (see also [32, 33] and references therein). More recently, higher order calculations of the scaling theory (exclusively with disorder and no interactions) predict $\mu \approx 1.3$ [51, 52], and more importantly, this value is shown to be independent of time reversal invariance [53] and of strength of spin-orbit interactions [54] (see also [20]). It is therefore clear that the effect of disorder alone cannot explain the experimental results of $\mu \approx 0.5$ or 1. Chayes et al. combined the theories of Mott and Anderson and successfully set the lowest limit $\mu > 2/3$ [55]. This result permits $\mu \approx 1$ obtained with compensated semiconductors and amorphous alloys. However, there still is no theory which convincingly explains $\mu \approx 0.5$ found for uncompensated semiconductors.

Even with today's advanced semiconductor technology, melt-doping of bulk semiconductors always leads to inhomogeneous dopant distributions due to impurity segregation and striation during crystal growth [34]. In [19, 34] these difficulties have been overcome by applying the NTD technique to a chemically pure, isotopically enriched ^{70}Ge [19] and ^{74}Ge [34] crystals. The ^{70}Ge crystal of isotopic composition $\left[^{70}\mathrm{Ge}\right]$ = 96.2 at. % and $\left[^{72}\mathrm{Ge}\right]$ = 3.8 at. % was grown in [19] using the Czochralski method developed for ultra-pure Ge [29]. The as-grown crystal was free of dislocations, p-type with an electrically active net-impurity concentration less than $5\times10^{11}\,\mathrm{cm}^{-3}$. In [34] was used isotopically engineered germanium which was grown from pure ^{74}Ge, enriched up to 94%, or by addition of a controlled portion of Ge with natural isotopic content to the ^{74}Ge material. In this way, both the doping as well as the compensation are very homogeneous due to the NTD and the compensation by controlled mixtures of ^{74}Ge and ^{70}Ge which transmute to ^{75}As donors and ^{71}Ga acceptors. Four series of n-type NTD-Ge with different K were grown [29]. The values of K are proportional to the product of the isotopic abundance and the thermal neutron cross-section of all isotopes producing impurities (see above): $\mathrm{K} = \mathrm{N}_{Ga}/(\mathrm{N}_{As} + \mathrm{N}_{Se})$, whereas the impurity concentration is additionally proportional to the irradiation doze. A very small fraction of ^{72}Ge becomes ^{73}Ge which is stable, i.e. no other acceptors or donors are introduced. Use NTD since it is known [1, 56] to produce the most homogeneous, perfectly random dopant distribution down to the atomic level. Figure 6.7 shows the temperature dependence of the resistivities (ρ) of 14 insulating samples in the range $\mathrm{N} = 0.16 - 0.99\mathrm{N}_c$ for NTD^{70}Ge : Ga crystals. The analogueous picture for NTD^{74}Ge : Ga is shown in Fig. 6.8. All curves become linear only when $\ln\rho$ is plotted against $\mathrm{T}^{-1/2}$ in good agreement with theory of variable range hopping conduction for strongly interacting electrons [28]:

$$\rho = \rho_0 \exp\left(\mathrm{T}_0/\mathrm{T}\right)^{1/2}, \tag{6.14}$$

where ρ_0 is a prefactor and T_0 is given by

$$\mathrm{T}_0 \approx 2.8\mathrm{e}^2/\mathrm{k}(\mathrm{N})\xi(\mathrm{N}), \tag{6.15}$$

where k(N) and ξ(N) are the dielectric constant and localisation length depending on N, respectively. Moreover, $\mathrm{k}(\mathrm{N}) \propto [\mathrm{N}_c/\,(\mathrm{N}_c - \mathrm{N})]^s$ and $\xi(\mathrm{N}) \propto [\mathrm{N}_c/\,(\mathrm{N}_c - \mathrm{N})]^\zeta$ as N approaches N_c from the insulating side so that T_0 becomes [28]

$$\mathrm{T}_0 = \mathrm{A}\,[(\mathrm{N}_c - \mathrm{N})\,\mathrm{N}_c]^\alpha\,. \tag{6.16}$$

Here, $\alpha = \mathrm{s} + \zeta$ is to be determined experimentally [19].

Figure 6.9 shows the dependence of T_0 as function of $\mathrm{N}_d = \mathrm{n}/\,(1 - \mathrm{K})$ for different K of ^{74}Ge : Ga [34]. These authors used the intersection point of these dependencies with the x-axis as a tool for the detrmination of N_c(K) very early. The left half of Fig. 6.10 shows the experimentally determined T_0 versus [Ga] (filled diamonds) together with the result of a three-parameter-fitting using A, N_c and α as variables in Eq. (6.16) (solid curve) [19]. These authors deduced [Ga] using the following

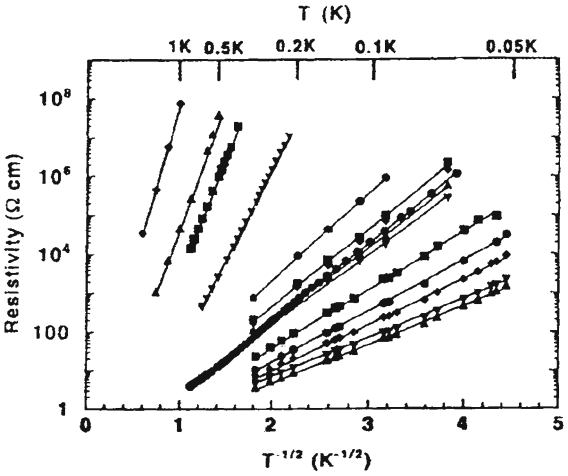

Fig. 6.7 The logarithm of the resistivity plotted as a function of $T^{-1/2}$ for 14 insulating NTD ^{70}Ge:Ga samples. Gallium concentration from top to bottom in units 10^{16} cm^{-3} are 3.o2; 8.00; 9.36; 14.50; 17.17; 17.52; 17.61; 17.68; 17.70; 17.79; 17.96; 18.05; 18.23 and 18.40 (after [19])

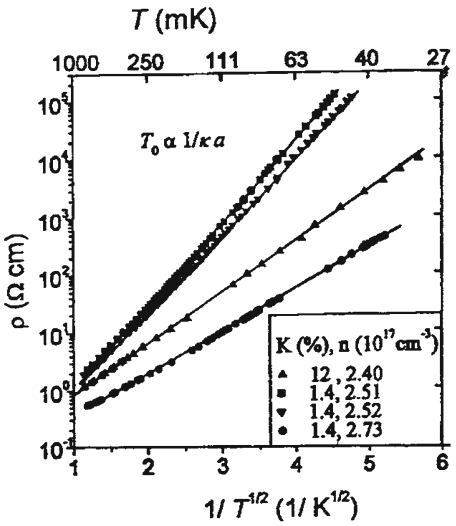

Fig. 6.8 Typical temperature dependences of the resistivity as a function of $T^{-1/2}$ for four samples NTD ^{70}Ge:Ga crystals (after [34])

equation $\left[^{71}\mathrm{Ga}\right](\mathrm{cm}^{-3}) = 0.1155 \times \mathrm{n}(\mathrm{cm}^{-2})$ as a sample, since it was known the precise neutron fluency used in each irradiation. The best fit of T_0 with Eq. (6.16) was obtained with the values $\alpha = 1.03 \pm 0.038$ and $N_c = (1.855 \pm 0.012) \times 10^{17}\mathrm{cm}^{-3}$. A much larger value of $\alpha \approx 2$ has been reported for Ge : As using only three samples with the highest N being far from the transition $0.56N_c$) [58]. In [19], it has been obtained $\alpha = 1$ with 14 homogeneously doped samples of [Ga] $= 0.16 - 0.99N_c$, all demonstrating the lh$\rho \propto T^{-1/2}$ dependence, i.e. this data set should be considered to be the first reliable determination of the hoping conductivity exponent α for a particular *semiconductor* system.

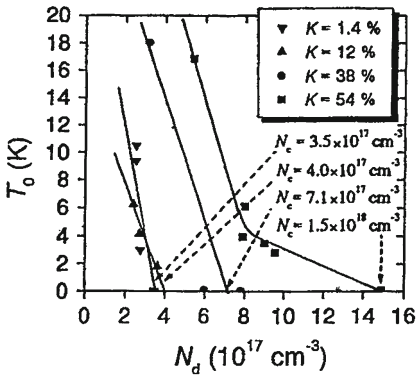

Fig. 6.9 Determination of N_c from the extrapolation $T_0 \to 0$ in the range $T_0 > T$ (after [34])

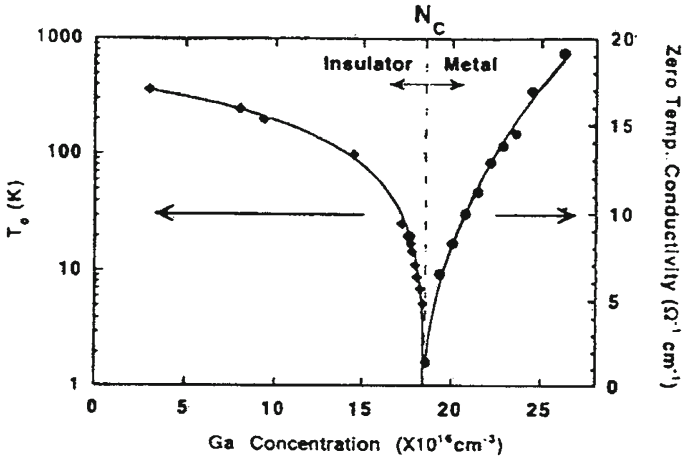

Fig. 6.10 The left side shows (^{70}Ge) as a function of Ga concentration (*diamond*). The solid curve is the best fit obtained with Eq. (6.16) (with $\alpha \approx 1$). The right side shows the zero temperature conductivity σ (*circle*) obtained from the extrapolation in Fig. 6.11 for the metallic samples as a function of Ga concentration (*bullet*). The solid curve is the best fit obtained with Eq. (6.16) (after [19])

Figure 6.11 shows the conductivity σ according to the results of [19] in ten metallic samples plotted against $T^{1/2}$. Extrapolation of each curve to T = 0K, i.e. the determination of the zero temperature conductivity $\sigma(0)$, yields a very small error since the dependence of σ on T for all samples is very weak. The right half of Fig. 6.10 shows $\sigma(0)$ as a function of [Ga] (filled circles) together with a fit obtained by the scaling expression Eq. (6.13) (solid curve). The values of the parameters determined in [19] from this fit are $\mu = 0.502 \pm 0.025$ and $N_c = (1.856 \pm 0.003) \times 10^{17}\text{cm}^{-3}$. This value presents $\mu \approx 0.5$ for uncompensated Ge : Ga semiconductors with high confidence, since the two values of N_c obtained from the scaling of T_0 [Eq. (6.16)] and $\sigma(0)$ [Eq. (6.13)] agree perfectly (for details see also [22, 34]).

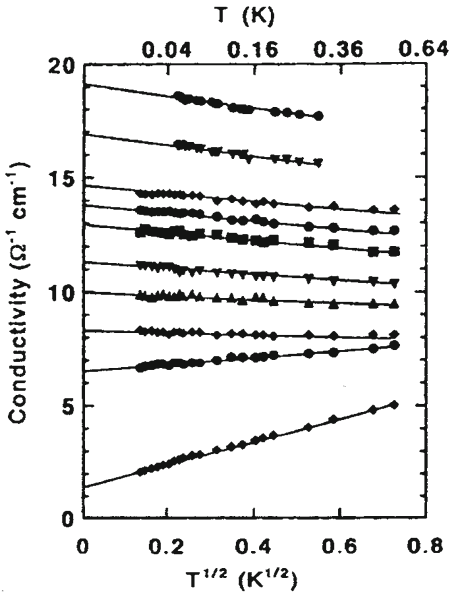

Fig. 6.11 Conductivity plotted as a function of $T^{1/2}$ for 10 metallic NTD ^{70}Ge:Ga samples. Sold lines indicate extrapolation to T = 0 K. Gallium concentration from top to bottom in units of 10^{16}cm^{-3} are 18.61; 19.33; 20.04; 20.76; 21.47; 22.19; 22.90; 23.62; 24.50 and 26.25 (after [19])

6.3.3 Neutral-Impurities Scattering

The low-temperature mobility of free carriers in semiconductors is mainly determined by ionised- and *neutral-impurity scattering*. The *ionised-impurity scattering* mechanism has been extensively studied (see e.g. [58] and references therein), and various aspects of this process are now quite well understood. Scattering by neutral impurities (see also [59]) is much less than by ionised centres, i.e. its contribution is significant only in crystals with low compensation and at very low temperatures where most of the free carriers are frozen on the impurity sites. The availability of highly enriched isotopes of Ge which can be purified to residual dopant levels $<10^{12}$cm^{-3} has provided the first opportunity to measure neutral impurity scattering over a wide temperature range. Three Ge *isotopes* transmute into shallow acceptors (Ga), shallow donors (As) and double donors (Se) (see also above):

$$
\begin{aligned}
&{}^{70}_{32}\mathrm{Ge} + \mathrm{n} \rightarrow {}^{71}_{32}\mathrm{Ge}_{EC(t_{1/2}=11.2days)} \rightarrow {}^{71}_{32}\mathrm{Ga} + \nu_e,\\
&{}^{74}_{32}\mathrm{Ge} + \mathrm{n} \rightarrow {}^{75}_{32}\mathrm{Ge}_{\beta^-(t_{1/2}=82.2min)} \rightarrow {}^{75}_{32}\mathrm{As} + \beta^- + \bar{\nu}_e,\\
&{}^{76}_{32}\mathrm{Ge} + \mathrm{n} \rightarrow {}^{77}_{32}\mathrm{Ge}_{\beta^-(t_{1/2}=11.3\ h)} \rightarrow \beta^- + \bar{\nu}_e + {}^{77}_{32}\mathrm{As}_{\beta^-(t_{1/2}=38.8h)} \rightarrow {}^{77}_{32}\mathrm{Se} + \beta^- + \bar{\nu}_e
\end{aligned}
\tag{6.17}
$$

The isotopes ^{72}Ge and ^{73}Ge are transmuted into the stable ^{73} Ge and ^{74}Ge respectively. Controlling the ratio of ^{70}Ge and ^{74} Ge in bulk Ge crystals allows fine-tuning of the majority—as well as the minority carrier concentration. Currently, this is the

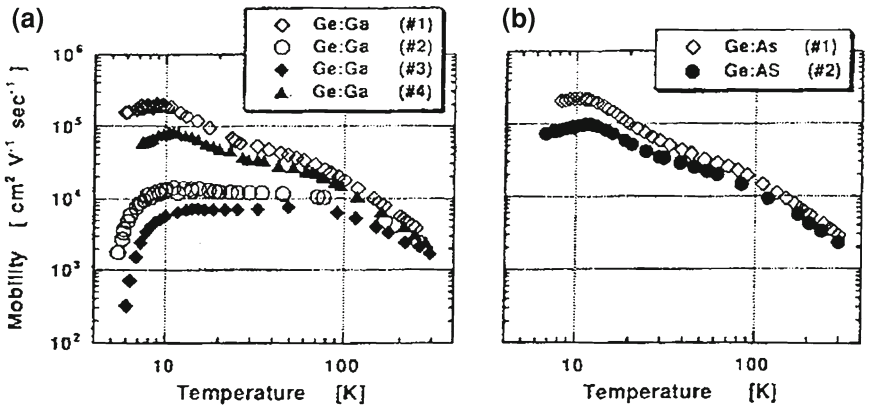

Fig. 6.12 Temperature dependence of the carrier mobility of (**a**) p-type and (**b**) n-type NTD Ge crystals (after [60, 61])

best method to vary the free-carrier concentration independently from compensation ratio. As opposed to other doping methods, *NTD* yields a very homogeneous, perfectly random distribution of the dopants down to the atomic levels [59]. Thus, isotopically controlled crystals offer a unique possibility to study systematically the scattering mechanism of the charge carriers in semiconductors. Extensive Hall-effect and resistivity measurements from room temperature down to 4.2 K yielded very accurate free-carrier concentrations and mobilities as a function of temperature and doping level were done in [60–63]. Itoh et al. have performed temperature-dependent Hall measurements on four different p-type and two-different n-type Ge crystals. The n-type crystals were obtained through NTD of isotopically enriched ^{74}Ge, and the p-type crystals correspondingly from NTD of isotopically enriched ^{70}Ge. The neutron cross-section for the neutron capture of the isotope for these irradiations were determined to be $\sigma_c(^{70}\,\mathrm{Ge}) = 2.5(5)\times10^{-24}\mathrm{cm}^2$ and $\sigma_c(^{74}\mathrm{Ge}) = 0.6(1)\times10^{-24}\mathrm{cm}^2$ by Itoh et al. [64]. To remove structural defects due to the unintentional irradiation with fast neutrons, all samples had to be thermally annealed at 650°C for 10 s in a rapid thermal annealer. Hall mobility obtained from the conductivity and free-carrier concentration data (listed in the Table 6.3) are displayed in Fig. 6.12. A magnetic field of 3 kG was used, that is, for the temperature range of interest for the neutral impurity scattering the high-field limit $\mu B \gg 1$ is satisfied and the Hall mobility can be equated with the drift mobility.

Fuchs et al. [60, 61] analysed the mobility data of Fig. 6.12 in terms of scattering of the carriers from phonons (μ_1), ionised impurities (μ_i) and neutral impurities (μ_n) assuming next rule

$$\frac{1}{\mu} = \frac{1}{\mu_1} + \frac{1}{\mu_i} + \frac{1}{\mu_n}. \tag{6.18}$$

Table 6.3 Carrier concentration of the Ge crystals used in the work of Fuchs et al. [60, 61]

p - type		$N_A - N_D$	N_D	$K = N_D/N_A$
	Ge:Ga #1	3.1×10^{14}	3×10^{12}	9×10^{-3}
	Ge:Ga #2	7.7×10^{15}	9×10^{13}	1.2×10^{-2}
	Ge:Ga #3	1.7×10^{16}	2×10^{14}	1.2×10^{-2}
	Ge:Ga #4	1.0×10^{15}	1.2×10^{13}	1.2×10^{-2}
n - type		$N_D - N_A$	N_A	$K = N_A/N_D$
	Ge:As #1	3.5×10^{14}	8.5×10^{12}	2.4×10^{-2}
	Ge:As #2	1.2×10^{15}	1.2×10^{13}	1.0×10^{-2}

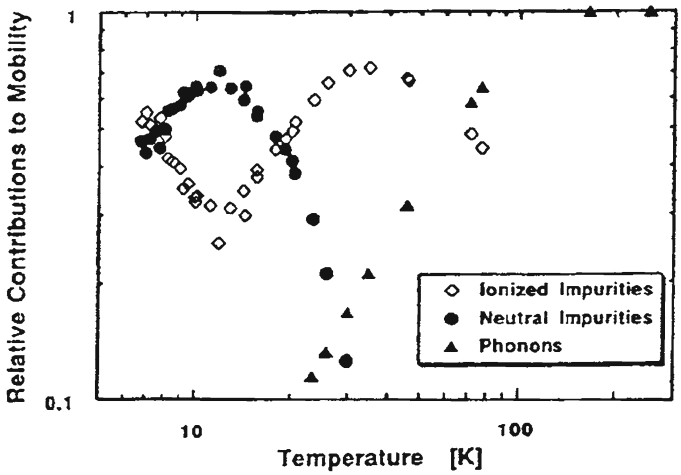

Fig. 6.13 Temperature dependence of the relative contributions to the mobility. Note that the mobility is dominated by neutral impurity scattering below 20 K (^{70}Ge:Ga #2 crystal) (after [60, 61])

To extract the *neutral impurity scattering* contribution, they subtracted $1/\mu_1 + 1/\mu_i$ from the measured $1/\mu$. The relative contributions of phonon scattering ($1/\mu_1$), *ionised impurity scattering* ($1/\mu_i$) and the resulting neutral impurity scattering ($1/\mu$ - $1/\mu_1$ - $1/\mu_i$) are plotted in Fig. 6.13 (data Ge : Ga #2). For $T > 80$ K, phonon scattering is the dominant scattering mechanism. Comparing Figs. 6.12 and 6.13, it becomes clear that the "dip" in the carrier mobility around 50 K is caused by scattering from ionised impurities, which dominate the scattering of the carriers between 20 and 80 K. The flattering and saturation of the mobilities below 20 K originate from neutral impurity scattering, which can only be observed in crystals with very high crystalline quality and low compensation like isotopically enriched NTD Ge crystals used in [63].

The experimental data, obtained in [63] allow these authors quantitative comparison with theory. According to Erginsoy [65], the inverse relaxation time τ^{-1}, the scattering rate, for *neutral-impurity scattering* equals:

$$\tau^{-1} = \frac{20kN_N\hbar^3}{m*^2\,\mathrm{e}^2}, \tag{6.19}$$

where k is dielectric constant, e is the electron charge, $N_N is$ the neutral-impurity concentration and m* is the electron effective mass. Equation (6.19) can be considered only as a first-order approximation because the prefactor 20 is an empirically determined constant and only the lowest s partial wave is taken into account in the phase-shift calculation (see also [66–68]). McGill and Baron [69] have used for $\tau^{-1}_{neutral}$ the following equation:

$$\tau^{-1}_{neutral} = \frac{4\pi \mathrm{N}_N\hbar\mathrm{e}}{2km*\mathrm{E}_B}\sum_{\mathrm{l}=0}^{\infty}\frac{(\mathrm{l}+1)}{4\mathrm{w}^{1/2}}\left[3\sin^2\left(\delta_l^- - \delta_{l+1}^-\right)+\sin^2\left(\delta_l^+ - \delta_{l+1}^+\right)\right], \tag{6.20}$$

where E_B is the binding energy of the scattering centres, $\mathrm{w} \equiv \mathrm{E}/\mathrm{E}_B$ and E is the incident electron energy, and δ_l^+ and δ_l^- are the lth partial shift for the singlet and triplet states respectively. In [69] is graphically shown the accurate $\tau^{-1}_{neutral}$ as a function of w for neutral-impurity scattering in semiconductors. This result has been considered as an appropriate model for neutral-impurity scattering in semiconductors and has been discussed in detail in many standard textbooks (see, e,.g. [70]).

Meyer and Bartoli reevaluated this task and obtained an analytical expression that is essentially the same as the graphical solution of authors of [69] but covering a wider incident-electron energy range (see also [71]):

$$\tau^{-1}_{neutral} = \frac{A(\mathrm{w})\mathrm{kN}_N\hbar^3}{m*^2_H\mathrm{e}^2}, \tag{6.21}$$

with

$$\mathrm{A(w)}=\frac{35.2}{\mathrm{w}^{1/2}}\frac{\left(1+\mathrm{e}^{-50\mathrm{w}}\right)\left(1+80.6\mathrm{W}+23.7\mathrm{w}^2\right)}{\left(1+41.3\mathrm{w}+133\mathrm{w}^2\right)}\left[\frac{1}{\mathrm{w}}\ln\left(1+\mathrm{w}\right)-\frac{\left(1+0.5\mathrm{w}-1.7\mathrm{w}^2\right)}{(1+\mathrm{w})^3}\right] \tag{6.22}$$

Here, m^*_H is the hydrogenic effective mass given by

$$m^*_H = \frac{\mathrm{E}_B k^2 \mathrm{m}_0}{\mathrm{E}_H}. \tag{6.23}$$

In the last equation m_0 is the electron rest mass and $\mathrm{E}_H = 13.6\mathrm{eV}$ is the binding energy of hydrogen. In total-mobility calculation Itoh et al. [63] employ a standard relaxation-time approximation. This approach is valid because they are limiting to low temperatures (T<25K) where the inelastic optical-phonon deformation-potential scattering is negligible. Three scattering mechanisms are considered: neutral-impurity, ionised-impurity and acoustic-phonon deformation-potential scat-

tering. The neutral-impurity scattering contribution was calculated using both Eqs. (6.19) and (6.21) so it can compare the models of Erginsoy and Meyer and Bartoli with the experimental results of [63]. The concentration of neutral-impurity centres as a function of temperature $N_N(T)$ in each sample is given by the next relation

$$N_N(T) = N_{MJ} - N_{MN} - n(T). \tag{6.24}$$

Here, N_{MJ}, N_{MN} and n(T) are the majority–impurity, minority–impurity and free-carrier concentrations, respectively. For the *ionised-impurity scattering*, Itoh et al. employ the Brooks-Herring expression [71, 72]:

$$\tau_{ion}^{-1} = \frac{\pi N_I e^4 (k_B T)^{-3/2} x^{-3/2}}{(2m*_{con})^{1/2} k^{1/2}} \left[\ln\left[1+\frac{4x}{a}\right] - \frac{4x/a}{1+4x/a} \right], \tag{6.25}$$

where

$$a = \frac{2\pi\hbar^2 e^2 n}{m* k k_B^2 T^2}, \tag{6.26}$$

and $x = E/k_B T$ (E is the incident electron energy), m^*_{con} is the average conductivity effective mass, and N_I is the ionised-impurity concentration. The temperature-dependent N_I in each sample is given by

$$N_I(T) = n(T) + 2N_{MN}. \tag{6.27}$$

For the acoustic-phonon deformation-potential scattering [73]:

$$\tau_{ac}^{-1} = B_{ac} (m*_{con} T)^{3/2} x^{1/2}, \tag{6.28}$$

where the constant B_{ac} has well-established values for n- and p-type Ge as shown in Table 6.4. Having found τ^{-1} of all three scattering mechanisms, Itoh et al. calculated an average $\langle\tau\rangle$ using the Maxwell-Boltzman integration:

$$\langle\tau\rangle = \frac{4}{3\sqrt{\pi}} \int_0^\infty \frac{x^{3/2}\exp(-x)}{\tau_{ac}^{-1}+\tau_{ion}^{-1}+\tau_{neutral}^{-1}} dx. \tag{6.29}$$

Finally, the total mobility μ_{tot} was given by

$$\mu_{tot} = e \langle\tau\rangle / m^*_{con} \tag{6.30}$$

All parameters required for the mobility calculations are well known in Ge (see Table 6.4). The only unknown material parameters at this point are sample-dependent N_{MJ}, N_{MN} and n(T) in Eqs. (6.24) and (6.27). All three parameters as shown below, can be determined precisely for each sample by performing variable-temperature Hall-effect measurements. Consequently, all mobility calculations are performed

Table 6.4 Parameters used in the total-mobility calculations (after [63])

	Ga:As (n-type)	Ge:HGa (p-type)
k	16	16
m^*_{con}	$0.12m_0$	$0.28m_0$
[a] B_{ac}	$1.08 \times 10^{10}\ g^{3/2}K^{-3/2}$	$9.50\times10^{8}g^{3/2}K^{-3/2}$
B_B (theoretical)	12.5 meB [b]	11.2 meV [c]

[a] The values of B are determined experimentally using ultrapure n-and p-type Ge of $N_{MJ} \sim N_{MN} \sim 3 \times 10^{11}cm^{-3}$

[b] M. Altarelli, W.Y. Hsu and R.A. Sabatini, J. Phys. C 10, L605 (1977)

[c] A. Baldareshi and N.O. Lipari, in Proc. 13th Inern. Conf. Phys. Semicond. (F.G. Fumi, ed, North-Holland, Amsterdam, 1976) p.595

without any adjusable or scaling parameters. The experimental curves are fitted with the following standard semiconductor statistics [74], which describes the temperature dependence of the free-carrier concentration in semiconductors doped by shallow majority impurities N_{MJ} and compensated by minority impurities N_{MN}:

$$n(T)=\frac{2\,(N_{MJ}-N_{MN})}{\left\{[+1\,(N_{MN}/gN_B)\exp(E_{MJ}/k_BT)]+\sqrt{[+1\,(N_{MN}gN_B)\exp(E_{MJ}/k_BT)]^2+(4/gN_B)\,(N_{MJ}-N_{MN})\exp(E_{MJ}k_BT)}\right\}}, \tag{6.31}$$

where $g = \frac{1}{2}$ ($g = 4$) is the spin degeneracy for a donor (acceptor), N_B is the effective conduction- (valence-) band density of states, and E_{MJ} are the experimentally determined ionization energies: 14 and 11.07 meV for As and Ga, respectively (Table 6.4).

Figure 6.13 shows the relative strength of the scattering from the ionised and the neutral impurities. There is only a relatively small temperature region in which the scattering from the neutral impurities dominates. This range extends to higher temperatures as the free-carrier concentration is increased. The calculated "transition temperatures" above which the ionised impurities are the main scattering centres (see also [75]) compare very well with the experimental results of Itoh et al. [63] (see also Fig. 6.14).

We now turn our attention to the low-temperature regime where mobilities are dominated by *neutral-impurity scattering*. Figure 6.14 shows a direct comparison of the experimental results with theoretical total-mobility curves calculated. For each sample two theoretical total-mobility curves are calculated: one using Erginsoy's model (Eq. 6.19) and the other using Meyer and Bartoli model (Eq. 6.21). A strikingly good agreement was obtained between the experimental and theoretical mobilities calculated with the model of Meyer and Bartoli for all samples (see Fig. 6.14).

In order to demonstrate the importance of the homogeneous dopant distribution, Itoh et al. have performed the same study on samples cut from Ge ; Ga crystals grown by the conventional Czochralski method, where Ga impurities were introduced to Ge melt during the crystal growth. These authors observed deviations of the measured mobility from the theoretical calculations, which are most likely due to inhomogeneous Ga impurity distributions in melt-doped Ge. Only the use of NTD

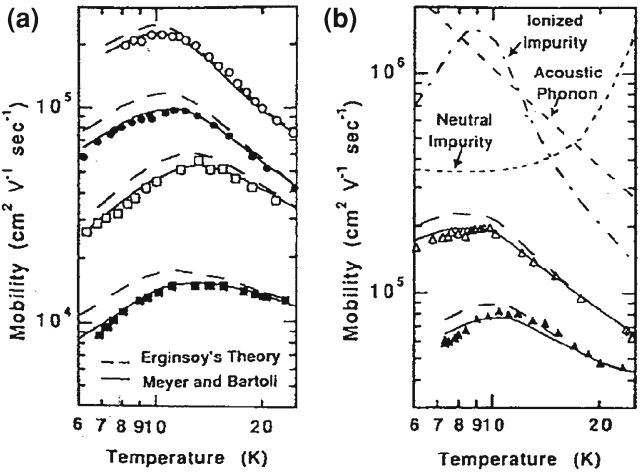

Fig. 6.14 Data points represent experimentally measured carrier mobility in (**a**) four ^{74}Ge:As and (**b**) two ^{70}Ge:Ga samples. For a direct comparison theoretically calculated mobility using Erginsoy's model (*broken line*) and the model of Meyer and Bartoli (*solid line*) is shown for each sample. The contributions of the different scattering mechanisms to the total mobility of the ^{70}Ge:Ga-1 sample are shown in the upper half of (**b**) (after [63])

semiconductors with randomly distributed dopants allows for an accurate test of the neutral impurity-scattering models.

6.3.4 Si

It is well known that doping of *silicon* single crystals by incorporation of impurities from the melt during solidification in most cases leads to an inhomogeneous distribution of impurities in the solids [3, 14, 48]. This is due to the fact that nearly all impurities in silicon have thermal equilibrium distribution coefficients much less than unity and that the solidification or crystal grows at each position of the interface is characterised by a different state of thermal inequilibrium leading to distribution coefficients that in space and time continuously change and result in a nonuniform impurity distribution [76, 77]. In actual crystal production the nonuniformity is further enhanced by lack of control of exactly constant melt volume and feed of the doping impurity. The most widely used doping elements in silicon are boron and phosphorus. *Boron* has a distribution coefficient between 0.9 and 1 which makes a doping uniformity of $\pm 10\%$ easily obtainable (see, e.g. [48]). The thermal equilibrium distribution coefficient for phosphorus of approximately 0.3 leads in general to the above-mentioned large doping variations both on a macroscale (centre to periphery) and on a microscale (striations). No other n-type doping element has a larger distribution coefficient. Fast diffusing p-type dopants (Ga, Al) are available, electron

mobility is greater than hole mobility, and contact alloying technology is reasonable, because n-type silicon is generally used for solid-state power devices [7, 8, 76]. With avalanche breakdown voltages being determined from areas with lower resistivities, use of a conventionally doped material results in hotspot formation prior to breakdown and very high forward voltage drop leading to excessive heat dissipation because of a safe punch through design [13, 14, 48].

Phosphorus doping by means of *NTD* was suggested by Lark-Horovitz [78] and others (see, e.g. [7, 8]) for homogeneity purposes and has been applied for high-power thyristor manufacturing in [13, 14, 48, 79]. Hill et al. [79] demonstrated how such a *homogeneous* phosphorus doping may result in a "theoretical design" possibility for high-power components (see below).

The process used for fractional transmutation of silicon into phosphorus and thereby performing n-type doping

$$^{30}_{14}\mathrm{Si(n,\gamma)} =^{31}_{14} \mathrm{Si}^{\beta^-}_{2.62h} \rightarrow^{31}_{15} \mathrm{P} \tag{6.32}$$

was first pointed out by Lark-Horovitz in 1951 [78]. Apart from special applications [80] and research, the above process was, however, not utilised to any extent until the early 1970s, at which time manufacturers of high-power thyristors and rectifiers for high-voltage direct current transmission lines, in particular, initiated usage of the transmutation doping process [79, 81, 82]. The reasons for not using the *neutron* doping method throughout the 1960s may be found in the lack of a processing technology which could benefit from a more uniform doping, insufficient availability of high resistivity starting material and the lack of nuclear reactors with irradiation capacities in excess of that needed for testing fuel and materials for nuclear power stations.

Let us, for the following discussion, assume that completely uniform neutron doping may be accomplished. The homogeneity of the doped silicon is in this case determined by the background doping, i.e. the distribution of impurities in the starting material, where the net impurity concentration may be of either donor or acceptor type. Let us further, for simplicity, consider starting material of one conductivity type and assume complete n-type conduction after irradiation and annealing. With C_S being the net impurity concentration of the starting material and C_D the resulting donor concentration after irradiation we have, for both n- and p-type material,

$$C_D^{\max} - C_D^{\min} = C_S^{\max} - C_S^{\min}. \tag{6.33}$$

In such case we may define

1. the homogeneity factors for the starting material (α_S) and for the neutron doped material (α_D), respectively

$$\alpha_S = \frac{C_S^{\min}}{C_S^{\max}} \tag{6.34}$$

and

Table 6.5 Values for homogeneity factor α_D as function of homogeneity factor α_s of starting material and doping factor f_D as defined in text (after [81])

α_S/f_D	.1	.2	.3	.4	.5	.6	.7	.8	.9
1	.1	.2	.3	.4	.5	.6	.7	.8	.9
2	.55	.6	.65	.7	.75	.8	.85	.9	.95
5	.82	.84	.86	.88	.9	.92	.94	.96	.98
7	.87	.89	.90	.91	.93	.94	.96	.97	.99
10	.91	.92	.93	.94	.95	.96	.97	.98	.99
20	.955	.96	.965	.97	.975	.98	.985	.99	.995
50	.98	.98	.99	.99	.99	.99	.99	.996	.998
100	.991	.992	.993	.994	.995	.996	.997	.998	.999

$$\alpha_D = \frac{C_D^{\min}}{C_D^{\max}} \tag{6.35}$$

and

2. the doping factor

$$f_D = \frac{C_D^{\max}}{C_S^{\max}}. \tag{6.36}$$

From this is easily derived

$$1 - \alpha_D = \frac{1-\alpha_S}{f_D}. \tag{6.37}$$

Table 6.5 summarises values of α_D as a function of α_S and f_D. It is seen that in order to obtain neutron-doped silicon with, for instance, a homogeneity factor greater than 0.9, it is necessary to use a doping factor of at least 7 when starting from "undoped" n-type material in which the homogeneity factor is typically not greater than 0.3 when taking the microcavitations (striations) into account. Examples of such neutron-doped silicon are shown in Figs. 6.15 and 6.16. It should be noted that in terms of resistivity, which is often used for impurity characterisation, a doping factor f_D means use of starting material with minimum resistivity a factor f_D or $2.8f_D$ greater than the resistivity after neutron doping for n- and p-type starting material, respectively. The difference is due to the electron mobility being 2.8 times greater than the hole mobility. In conclusion it should be generally noted that in order to make neutron-doped silicon with significantly more uniform resistivity than conventionally doped material, a doping factor $f_D = 5$ or more should be applied.

Following Janus and Malmros [81] let us consider further the theoretical case where a cylindrical silicon crystal is surrounded by a material with the same *neutron absorption* and scattering efficiency as the silicon itself (see Fig. 6.17). Let us furthermore assume a thermal neutron flux gradient along an x axis perpendicular to the crystal axis with the neutrons coming from an external source. In this case the *neutron flux* will have the form

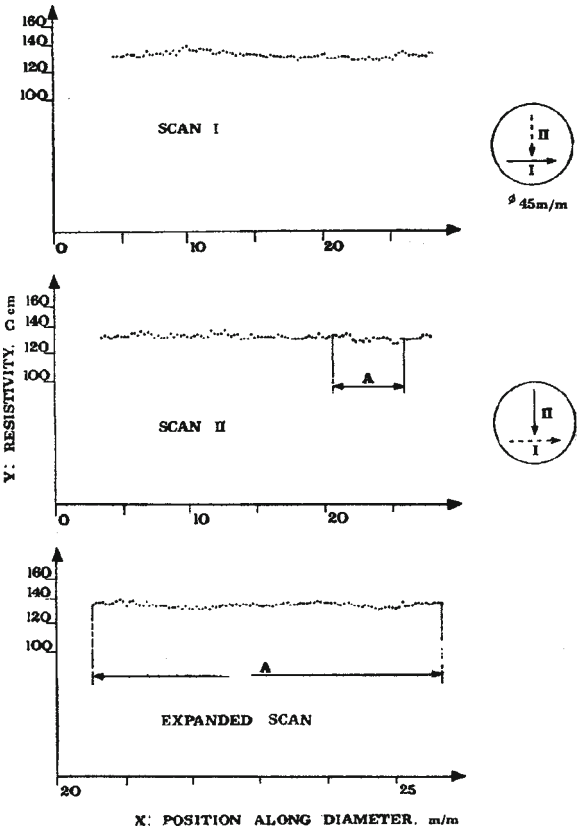

Fig. 6.15 Spreading resistance measurements of a thermal neutron irradiation doped silicon slice. Step-length on scan 1 and 2 is 250 μm and on scan 3 step-length is 50 μm. Starting material has been selected greater than 1500 Ωcm n-type (after [81])

$$\Phi = \Phi_0 \cdot \exp\left(-\frac{x}{b}\right), \tag{6.38}$$

where b, the decay length, may be obtained from the formula

$$b = (3 \cdot \sigma_{Si} \cdot \sigma_{Si,t} \cdot C_{Si}^2)^{-0.5}. \tag{6.39}$$

$\sigma_{Si} = 0.16 \cdot 10^{-24} cm^2$ is the mean of the absorption *cross-sections* for the three silicon isotopes, ^{28} Si, ^{29}Si and ^{30}Si weighted with their abundances. $\sigma_{Si,t} = 2.3 \cdot 10^{-24} cm^2$ is the total cross-section (absorption + scattering) and $C_{Si} = 4.96 \cdot 10^{22} cm^{-3}$ is the total number of silicon atoms in $1 cm^3$. Hence b may be calculated as:

$$b_{silicon} = 19\,cm. \tag{6.40}$$

In order to improve the doping homogeneity in the cylindrical crystal this will be slowly rotated around its axis. The time average of this flux at the distance r from

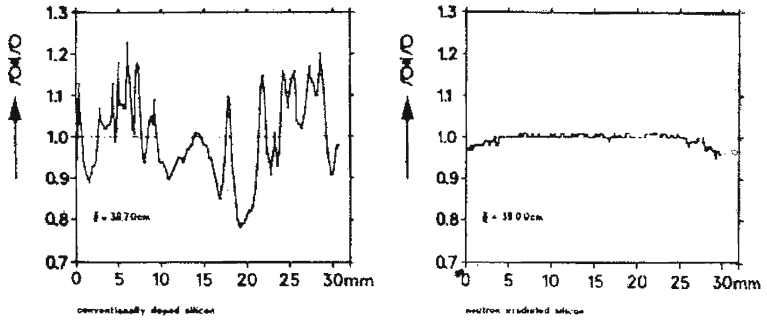

Fig. 6.16 Typical lateral microscopic resistivity distributions in conventionally doped silicon and in silicon doped by neutron irradiation (after [48])

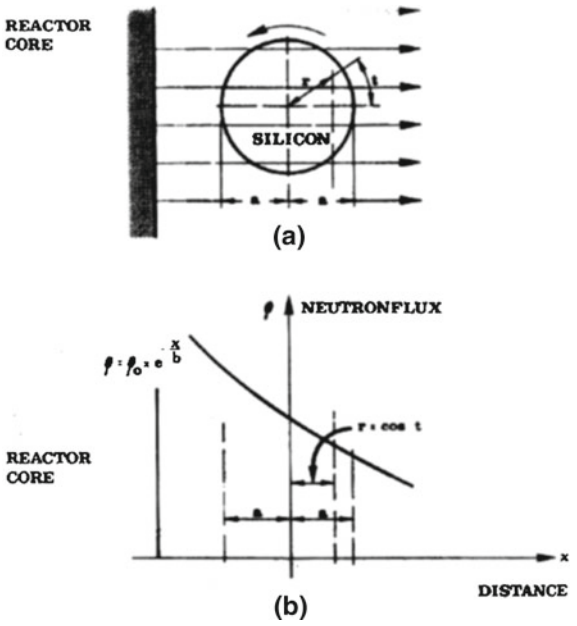

Fig. 6.17 Irradiation configuration. **a** *Top view* of the facility with the cylindrical crystal situated outside the core rotating around its cylindrical axis. *Arrows* indicate overall direction of neutrons. The flux does not vary along the cylindrical axis. **b** The neutron flux is a function of the distance from the reactor core (after [81])

this axis is

$$\bar{\Phi} = \frac{1}{\pi}\int_0^{\pi} \Phi_0 \exp\left[-\frac{r}{b}\cos t\right] dt = \Phi_0\left[1+\frac{1}{4}\left(\frac{r}{b}\right)^2 \ldots\right]. \tag{6.41}$$

The ratio between the neutron dose at the periphery and at the axis of the crystal cylinder will then be

$$\frac{\bar{\Phi}(a)}{\bar{\Phi}(0)} \simeq 1 + \frac{1}{4}\left(\frac{a}{b}\right)^2, \tag{6.42}$$

where a is the crystal radius (Fig. 6.17).

For intrinsic starting material the irradiation doped silicon will thus have a homogeneity factor of

$$\alpha_D \simeq 1 - \frac{1}{4}\left(\frac{a}{b}\right)^2 \simeq 0.956 \tag{6.43}$$

for an 80-mm-diameter crystal, i.e. the absorption limiting factor for the obtainable radial variations.

In the above analysis we have neglected the effects of fast neutron moderation in the silicon. By comparison, however, of irradiations performed in reactors with fast neutron fluxes from 10^{-4} to 1 times the thermal flux and with different flux gradients, the authors of [81] have observed no influence on the resistivity homogeneity due to fast neutron moderation in the silicon.

In irradiated silicon crystals for *semiconductor* device applications only two isotopes ^{31}Si and ^{32}P are of importance in connection with *radioactivity* of *neutron* doped material. For thermal neutron doses less than 10^{19} neutron/cm^2, no other elements have been detected emitting radiation. Futhermore, ^{31}Si, having a half-life of 2.62 h, decays to an undetectable level in 3–5 days. For this reason, it will be discussed the radioactivety only of the ^{32}P isotope. Figure 6.18 pictures the ^{32}P activity as a function of final resistivity for a variety of thermal neutron flux levels typical for the nuclear test reactors in use. As was shown in [81] absolute flux determination to 1% accuracy has proven obtainable for instance by means of calorimetric boron carbide monitors.

$$^{31}_{15}\mathrm{P}(\mathrm{n},\gamma)^{32}_{15}\mathrm{P}^{\beta^-}_{14.3d} \rightarrow ^{32}_{16}S \tag{6.44}$$

as a secondary one with ^{31}P concentration at each instant in time being dependent on the neutron dose received and the time allowed for the $^{31}_{14}\mathrm{Si}^{\beta^-}_{2.62h} \rightarrow ^{32}_{15}\mathrm{P}$ decay.

From Fig. 6.18 it may be observed that neutron doping below 5 Ω· cm can be performed only when accepting cool down periods corresponding to the ^{32} P *halflife* of 14.3 days. The exempt limit for inactivity of $2 \times 10^{-3}\,\mu$Ci/g shown in the figure is representative for most European countries, as well as being the value recommended by the *International Atomic Energy Agency (IAEA)*, Vienna, Austria [83]. It should be added that careful cleaning of the silicon prior to insertion in a nuclear reactor is vital to avoid radioactive surface contamination. For the safety of the personnel and the end product users, a double check upon shipping from the reactor sites and upon reception in the silicon plant, respectively, is carried out to secure that only inactive material (below the exempt limit) is being further processed after the neutron doping. In general, this implies shipment from the reactor not earlier than 4 days after irradiation.

The use of *NTD* is of particular interest to thyristor manufacturers where n-type starting material is required for the basic p-n-p structure [75, 77]. Some advantages for high power device design and performance include:

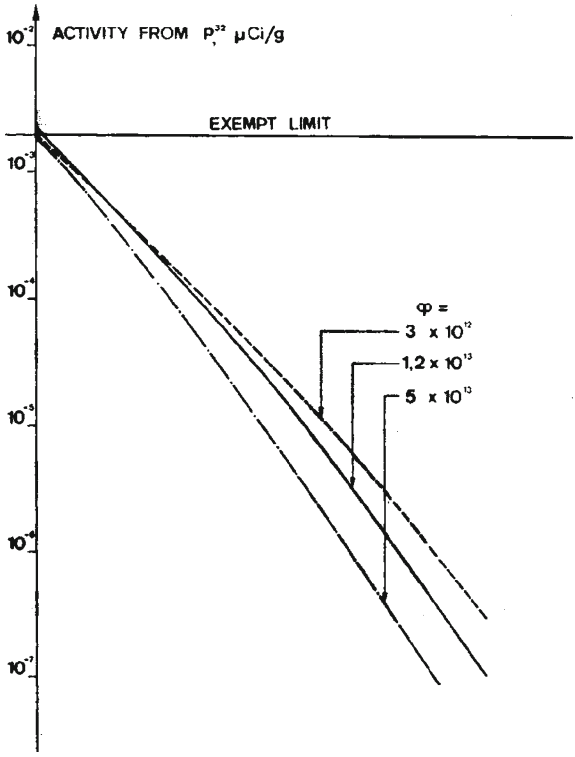

Fig. 6.18 The radioactivity of the ^{32} P isotope in silicon after 4 days of cool down subsequent to irradiation. It may be observed that the activity as function of the resistivity obtained depends on the neutron flux used (after [81])

1. more precise control of avalanche breakdown voltage,
2. more uniform avalanche breakdown, i.e. greater capacity to withstand overvoltages,
3. more uniform current flow in forward direction, i.e. greater surge current capacity, and
4. narrower neutral zone and therefore narrower base and lower forward voltage drop V_f.

The summary of some points concerning the preparation of NTD silicon for special applications on an R and D scale is described in [77, 79]. The production of large quantities of NTD silicon for power devices is described in [26]. More recently (see, e.g [84]) the NTD technique has also been proposed for the effectual doping of P in a-Si:H films. The results of [84] show that NTD technique is an excellent method for doping of P in a-Si:H.

Despite intensive study over many years and considerable progress, no clear understanding has emerged as one of the fundamental issues regarding the *MIT* in doped semiconductors and amorphous *metal-semiconductor* mixtures: whether and under what circumstances the Hall coefficient diverges as the transitions are approached

(see above for Ge). As is well known in the localised regime the spatial behaviour of the wave functions is usually described by an exponential decay length reflecting the spatial extent of the wave function (see e.g. [85–87]). Dai et al. recently showed that the Hall coefficient of Si:P diverges at the transitions, as it does in Si:B [88] and Ge:Sb [89]. The difference in the behaviour of MIT according to these authors may be connected with a different degree of compensation. It is also possible that the MIT is different in a persistent photoconductor, where the disorder is particularly strong and the concentration of shallow donors is varied and controlled through illumination (for details see also [86, 87]).

6.3.5 Other Compounds

The NTD method was used with success in a study of compound semiconductors: GaAs [90–93] and GaP [94, 95]. NTD of GaAs is based on the following thermal neutron capture nuclear reactions (see also [90]):

$$^{69}\mathrm{Ga(n,\gamma)}^{70}\mathrm{Ga}^{\beta^-}_{21.1\mathrm{min}} \rightarrow ^{70}\mathrm{Ge}, \tag{6.45}$$

$$^{71}\mathrm{Ga(n,\gamma)}^{72}\mathrm{Ga}^{\beta^-}_{14.1h} \rightarrow ^{72}\mathrm{Ge}, \tag{6.46}$$

$$^{75}\mathrm{As(n,\gamma)}^{76}\mathrm{As}^{\beta^-}_{26.3\mathrm{h}} \rightarrow ^{76}\mathrm{Se}. \tag{6.47}$$

The relative abundances of the isotopes involved in the reactions and the *cross-sections* for these reactions are such that the ratio of Se and Ge concentrations produced is

$$\mathrm{N}_{Se}/\mathrm{N}_{Ge} = 1.46. \tag{6.48}$$

Selenium is a typically shallow substitutional donor in GaAs with an electronic energy level a few meV from the conduction bans edge [96]. Germanium in GaAs is an amphoteric impurity which acts as a shallow donor (also a few meV from the conduction band) is situated on a Ga site and as an acceptor level at $\mathrm{E}_V + 0.04\,\mathrm{eV}$ if situated on an As site [56]. Since, if electronically active, all of the Se atoms and some portion of the Ge atoms are expected to act as donors, NTD of GaAs is expected to dope GaAs more n-type. The addition of donors moves the Fermi level (E_F) away from the valence band (E_V) to the conduction band (E_C). If a sufficiently high concentration of donors is added, $\mathrm{E_F}$ will move to the upper half of the band gap and the GaAs will be converted to n-type. Analysis of Hall effect data as a function of temperature provides a means of measuring the donor content in irradiated GaAs samples. Young et al. were thus able to compare electrically active added donor content to the NTD-produced impurity concentrations determined from nuclear measurements.

Table 6.6 Room temperature results for Hall effect samples of GaAs annealed 830°C/20 min (after [90])

Sample No	NTD Dose/cm^3	n(−) or P (+) in cm^{-3}	μ, cm^{2}V^{-1}s$_{-1}$
1,2	3.8×10^{15}	$+ 2.3 \times 10^{16}$	360
3	8.5×10^{15}	$+ 2.4 \times 10^{16}$	341
4	1.7×10^{16}	$+ 1.9 \times 10^{16}$	337
10	2.7×10^{16}	$+ 8.6 \times 10^{15}$	242
12	7×10^{16}	$- 1.6 \times 10^{16}$	1251
20	1.5×10^{17}	$- 7.7 \times 10^{16}$	3960
15	2.8×10^{17}	$- 2.3 \times 10^{17}$	3631
16, 18	6.3×10^{17}	$- 4.9 \times 10^{17}$	3110

The Hall effect analysis also allows them to determine concentrations and energy levels (E) of impurities or defects in the p-type GaAs samples if the Fermi level in the material moves near E at some temperature over the range of measurements. This technique thus provides a means of identifying and measuring undercompensated acceptor content in the samples. The low temperature *photoluminescence* technique used in [90] measured donor-to-acceptor or conduction-band-acceptor luminescence. It provides an accurate determination of the position of acceptor electronic levels in the GaAs, permitting positive identification of impurities or defects with known luminescence lines. Identifications of lines due to specific impurities or defects can be made using luminescence techniques regardless of the position of the Fermi level in material. Little detailed information concerning an acceptor level can be obtained from Hall effect if that acceptor is overcompensated. However, the presence of specific acceptors can be detected by luminescence techniques even in n-type samples. On the other hand, luminescence data do not provide the quantitative information obtainable from Hall effect measurements.

The results of room temperature measurement of the electrical properties of eight annealed NTD GaAs samples are summarised in Table 6.6. The total NTD dose (N_{Se} + N_{Ge}), the carrier concentration and carrier type (negative values of concentration indicate n-type), along with carrier mobility at room temperature are indicated in Table 22 of [90]. Note that following an NTD dose sufficient to produce 7×10^{16} atoms/cm^3 is initially present in the samples. Therefore, 7×10^{16} donors/cm^3 would indeed be expected to just overcompensate the p-type material. The results presented in Table 6.6 show that the p-type samples become progressively less p-type and the n-type samples progressively more n-type with increasing NTD dose. Because the donor levels in GaAs are very shallow, they remain fully ionised in the temperature range of Young et al experiments, so that the measured electron concentration is practically temperature independent (see Fig. 6.4 in Ref.[90]). This measured n for each sample is approximately equal to total donor minus total acceptor concentration.

Figure 6.19 shows the measured in [90] added electrically active donor concentration in eight *NTD* samples as a function of N_{Se} and of (N_{Se} + N_{Ge}) added by transmutation as determined from nuclear activity measurements. The uncertainty in

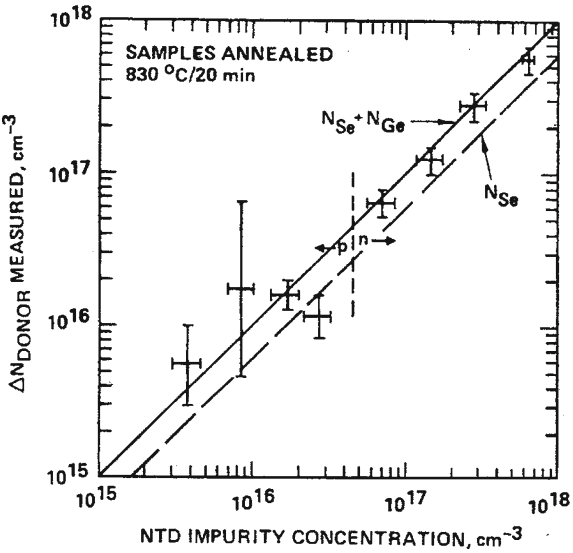

Fig. 6.19 Measured added donors vs NTD produced impurity content (after [90])

determining added donor content in the p-type samples is large because of the complexity of analysing material with multiple independent acceptor levels in closely compensated cases. The added donors can be much more accurately determined in the more highly doped n-type samples. The results shown in Fig. 6.19 imply that all of the *selenium* and a substantial fraction of the Ge atoms introduced by transmutation act as donors following the 830°C/20 min anneal. As will be shown below from photoluminescence measurements a fraction of Ge atoms produced by transmutation are on acceptor rather than donor sites in GaAs samples.

Figure 6.20 shows relative luminescence spectra for the four n-type samples respectively. The spectral positions indicated by arrows for carbon acceptor, the Ge acceptor, and 0.07 eV acceptor correspond to donor (or band) to acceptor luminescence lines. The most important conclusion to be drawn from a comparison of the spectra for the control and eight NTD samples is that Ge acceptors not present in the "starting material" control sample are introduced by the NTD process. The increase in intensity of the Ge acceptor line with increasing dose relative to both the carbon and 0.07 eV acceptor lines indicates that Ge acceptor content increases with increasing transmutation doping. Therefore, some of the Ge atoms produced by NTD in these samples are acting as acceptors rather than donors. *Photoluminescence* measurement studies of the control and eight annealed NTD samples at longer wavelengths indicate another new line present only in NTD samples at about 9450 Å. The intensity of this line increases with increasing NTD dose.

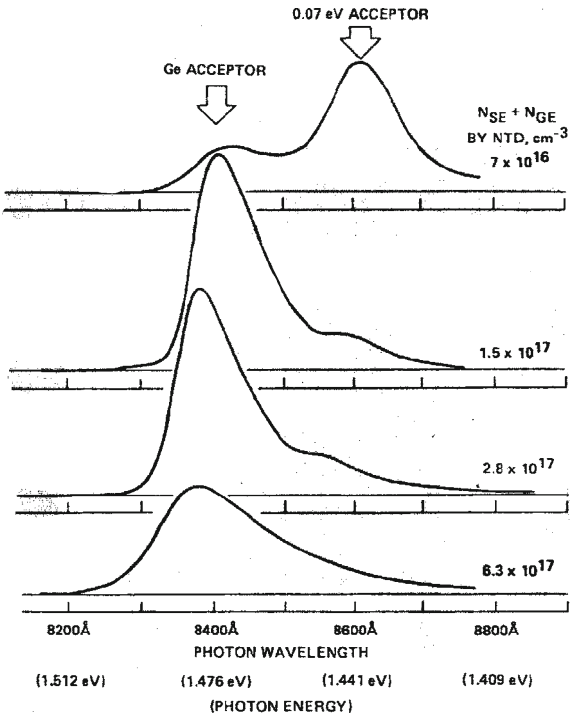

Fig. 6.20 Relative photoluminescence spectra for four n-type NTD samples. The four spectra are not normalized with respect to each other (after [90])

6.4 Optical Fibre

6.4.1 Optical Communication

Optical communication using *fibres* is a major new technology which will profoundly impact telephone systems, computer interconnections and instrumentation (internet). Fibre links provide several major advantages over conventional electronic communications systems. These include immunity to electromagnetic interference, thinner and lighter cables, lower transmission losses (especially for very data rates) and potential kilometer-long-link capabilities extending to the gigahertz region.

An optical waveguide is a *dielectric* structure that transports energy at wavelengths in the infrared or visible ranges [97, 98] of the electromagnetic spectrum. In practice, *waveguides* used for optical communications are highly flexible fibres composed of nearly transparent dielectric materials. The *cross-section* of these fibres is small—comparable to the thickness of a human hair—and generally is divisible into three layers as shown in Fig. 66. The central region is the *core*, which is surrounded by the*cladding*, which in turn is surrounded by a protective *jacket*. Within the core, the refractive-index profile n can be uniform or graded, while the cladding index is typically uniform [99, 100]. The two situations correspond to the *step-index* and

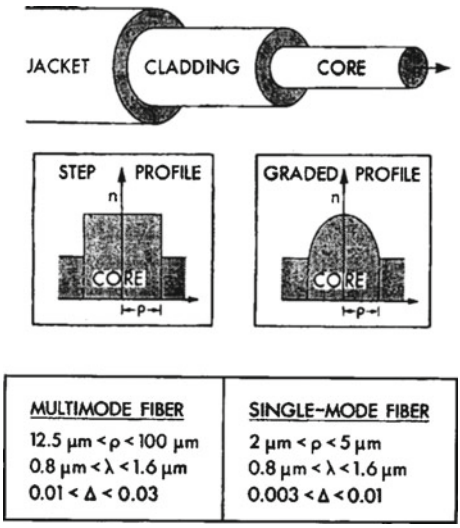

Fig. 6.21 Nomenclature, profiles and ranges of dimensions for typical optical fibres, where ρ is the core radius, λ is the free-space wavelength of light and $\Delta = \left(1 - n_{cl}^2/n_{co}^2\right)/2$ (after [99])

graded-index profiles shown in the insets in Fig. 6.21. It is necessary that the core index be greater than the cladding index [101], at least in some region of the cross-section, if guidance is to take place. For the majority of applications, most of the light energy propagates in the core and only a small fraction travels in the cladding. The jacket is almost optically isolated from the core, so for this reason we usually ignore its effect and assume an unbounded cladding for simplicity in the analysis.

As usual optical waveguides can be conveniently divided into two subclasses called *multimode waveguides* (with comparatively large cores) and *single-mode waveguides* (with comparatively small cores). The demarcation between the two is below. Multimode waveguides obey the condition (see e.g. [102]) $(2\pi\rho/\lambda)\left(n_{co}^2 - n_{cl}^2\right)^{1/2} \gg 1$, where ρ is a linear dimension in the core, e.g. the radius of the fibre core, λ is the wavelength of light in free space, n_{co} is the maximum refractive index in the core and n_{cl} is the uniform refractive index in the cladding.

As will be shown below, electromagnetic propagation along optical waveguides is described exactly by Maxwell's equations. However, it is well known that classical geometric optics provides an approximate description of light propagation in regions where the refractive index varies only slightly over a distance comparable to the wavelength of light. This is typical of multimode optical waveguides used for communication. Thus, the most direct and conceptually simple way to describe light propagation in multimode waveguides is by tracing rays along the core (see also [103–105]). By using classical geometric optics, we should ignore all wave effects. In multimode waveguides, wave effects are usually negligible [99], but there are exceptional situations when such effects accumulate exponentially with the distance light travels. Naturally in this cases, wave effects must be retained, since they can have a significant influence on long waveguides. In each such situation, we modify the classical geometric optics description by taking into account the local plane

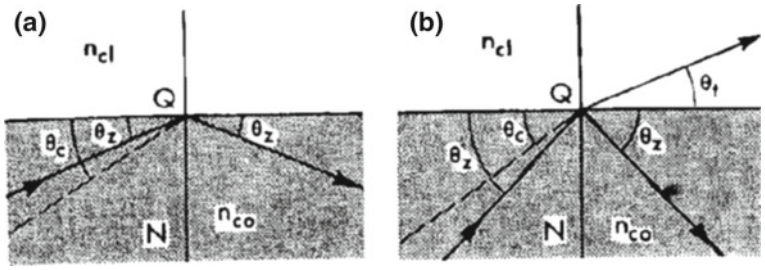

Fig. 6.22 Reflection at a planar interface between unbounded regions of refractive indices n_{co} and $n_{cl} < n_{co}$ showing (**a**) total internal reflection and (**b**) partial reflection and refraction (after [7, 8])

wave nature of light. The phenomenan of greatest practical interest in fibres used for long distance communications is the spread of pulses as they propagate along the fibre. For idealised multimode fibres, pulse spreading is easily described by classical geometric optics. But since propagation in multimode guides is so complex simple models and physical understanding are generally of much greater assistance than a precise, exact analysis [105].

6.4.2 Nuclear Technology in fibre Preparation

The *reflection* and *transmission* of a plane wave, or ray, which is incident on a planar interface between two semi-infinite, uniform media is determined by Snell's laws (see, e.g. [101, 106]). In Fig. 6.21, the refractive indices of the medium of incidence and the second medium are n_{co} (core) and n_{cl} (cladding) $< n_{co}$, respectively, and the critical angle $\alpha_c = \sin^{-1}(n_{cl} n_{co})$. Further, we denote the angles of incidence, reflection and transmission, or refraction, relative to the normal QN (see Fig. 6.22) by α_i, α_r, and α_t, respectively. The incident, reflection and transmitted, or refracted, rays and the normal QN are coplanar. If $\alpha_i > \alpha_c$, the incident ray in Fig. 6.22a undergoes total internal reflection and $\alpha_r = \alpha_i$, but if $\alpha_i < \alpha_c$ there is partial transmission, or refraction, as shown in Fig. 6.22b and the angles satisfy

$$\alpha_i = \alpha_r \tag{6.49}$$

and

$$n_{co} \sin\alpha_i = n_{cl} sin\alpha_t \tag{6.50}$$

Usually for the planar waveguides it is convenient to express these laws in terms of the complementary angles of incidence, reflection and transmission, i.e. $\theta_z = \pi/2 - \alpha_i = \pi/2 - \alpha_r$ and $\theta_t = \pi/2 - \alpha_t$ and the complementary critical angle $\theta_c = \pi/2 - \alpha_c$.

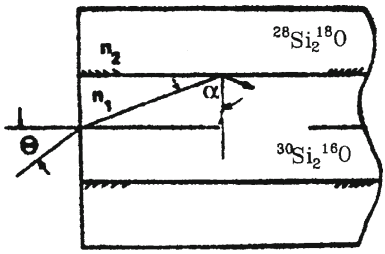

Fig. 6.23 Isotopic fibre in which the core and cladding are both pure SiO_2, but with a different isotopic composition (after [127])

One of the possible major applications of *isotopic engineering* are considered in isotopic *fibre-optics* and *isotopic optoelectronics* at large (see also [106]). It is known that for typical solids the lattice constant variations of isotopically different samples are usually within the limits

$$\frac{\Delta d}{d} \sim 10^{-3} \div 10^{-4} \tag{6.51}$$

Let us define an *isotopic fibre* as a structure in which core and cladding have the same chemical content but different isotopic composition (see Fig. 6.23) The boundary between different isotopic regions form an isotopic interface. The difference in the refractive index on both sides of the isotopic interface could lead to the possibility of total internal reflection of light and, consequently, could provide an alternative route to the confinement of light. For a quantitative estimate let us consider a boundary between SiO_2 (the main component of silica) where body sides are identical chemically and structurally but have a different isotopic content—e.g. $^{28}Si^{16}O_2$ and $^{30}Si^{18}O_2$, respectively (Fig. 6.23). In the first approximation the refractive index n is proportional to the number of light scatterers in the unit volume. From the Clausius-Mosotti relation (see, e.g. [107]) for the refractive index one can deduce the following proportion (at $\Delta n << \mathrm{n}$)

$$\frac{\Delta n}{n} \simeq 3\mathrm{c}\frac{\Delta d}{d}, \tag{6.52}$$

where c is a dimensionless adjustment factor of the order of unity. Substituting Eq. (6.51) into Eq. (6.52) we can obtain

$$\frac{\Delta n}{n} \sim 3\times 10^{-3} \div 10^{-4} \tag{6.53}$$

Using the Snell law of light *refraction* we obtain the following expression for the ray bending angle θ when light travels through the refractive boundary (see, also Fig. 6.22)

$$\theta \simeq \alpha_0 - \arcsin\left(\frac{n_1}{n_2}\sin\alpha_0\right), \tag{6.54}$$

where α_0 is the angle between the falling ray and the direction normal to the interface. For a sliding ray ($\alpha_0 \simeq 90°$), which is the control case for light confinement in fibres, the combining of Eqs. (6.53) and (6.54) leads to an estimate

$$\theta \sim 1.5 \div 4.5° \tag{6.55}$$

Thus, the *isotopic fibres* in which core and cladding are made of different isotopes the half-angle of the acceptance-cone could be up to several degrees [108]. The resulting lattice mismatch and strains at the isotopic boundaries are correspondingly one part per few thousand [106] and, therefore, could be tolerated. Further advancement of this " isotopic option" could open the way for an essentially monolitic optical chip with built-in isotopic channels inside the fully integrated and chemically uniform structure.

Besides that we should pay attention to the fact that composition (different isotopes) fluctuation are subject to the restoring force of the total free energy of the glass system which will also seek to minimise itself. Using isotope pure materials for core and cladding we should receive significant less Rayleigh scattering (for details see [108]).

6.5 Radioactive Isotopes

Radioactive isotopes (RI) are radioactive atoms of common elements like *carbon, cobalt, or sodium*, etc. Usually RI are located in atomic "ash" that is left behind after uranium atoms are split in a "nuclear pile". Some RI are produced from exposure of common elements to powerful radiation inside a *nuclear* reactor during fission. Fission occurs when an atom's nucleus splits into two or more smaller nuclei, producing a large amount of energy. RI release radiation in the form of alpha, beta and gamma rays. The strength of the r*adiation* is relative to the rate where*radioactive* material decays. Because of this, different radioisotopes can be used for different purposes, depending on their strength.

Some radioactive elements, such as radium–224, radium–226, radon 222, polonium–210, tritium (^{3}H), carbon–14, etc. are found in nature, but most radioactive materials are produced commercially in nuclear reactors or cyclotrons (see, e.g. [**?**])—also called particle accelerators. With nuclear reactors and cyclotrons, it is possible to make useful amounts of radioactive material safely and at low cost. Usually only one type of radionuclide can be produced at a time in a cyclotron, while a reactor can produce many different radionuclides simultaneously. As for unstable isotopes, there are over 1,000 some of which exist in nature, but most of which have been created synthetically in laboratories in nuclear reactors or cyclotrons. Although accelerators do create small quantities of lingering radioactivity, they do not pose the staggering high-level waste and proliferation problems associated with nuclear reactors, nor do they have any potential for catastrophic accidents of any kind, nor are they capable of producing weapons materials in militarily significant amounts.

It should be recognised that RI have been used in *nuclear medicine*, industry and scientific research (solids).

6.5.1 Human Health

Nuclear Medicine is a branch of medicine that uses radiation to provide information about the functioning of a person's specific organs or to treat disease. In most cases, the information is used by physicians to make a quick, accurate diagnosis of the patient's illness. The thyroid, bones, heart, liver and many other organs can be easily imaged, and disorders in their function revealed. In some cases radiation can be used to treat diseased organs, or tumours (see, e.g. [109]–[114]). Five Nobel Laureates have been intimately involved with the use of radioactive tracers in medicine.

In the developed countries (26% of world population) the frequency of diagnostic nuclear medicine is 1.9% per year, and the frequency of therapy with radioisotopes is about one-tenth of this. In Europe there are some 10 million nuclear medicine procedure per year. The use of radiopharmaceuticals in diagnosis is growing at over 10% per year. Nuclear medicine was developed in the 1950s by physicians with an endocrine emphasis, initially using iodine–131 to diagnose and then treat thyroid disease. In recent years specialists have also come from radiology, as dual CT/PET (see below) procedures have become established.

As is well known, diagnostic techniques in nuclear medicine use radioactive tracers which emit gamma rays from within the body. These tracers are generally short-lived isotopes linked to chemical compounds which permit specific physiological processes to be scrytinised. They can be given by injection, inhalation or orally. The first type where single photons are detected by a gamma camera which can view organs from many different angles. The camera builds up an image from the points from which radiation is emitted; this image is enhanced by a computer and viewed by a physician on a monitor for indications of abnormal conditions [115, 116].

A more recent development is *Positron Emission Tomography* (*PET* [109, 112, 117–120]) which is a more precise and sophisticated technique using *isotopes* produced in a cyclotron. A positron-emitting radionuclide is introduced, usually by injection, and accumulates in the target tissue. As it decays it emits a positron, which promptly combines with a nearby electron resulting in the simultaneous emission of two identifiable gamma rays in opposite directions. These are detected by a PET camera and give very precise indication of their origin. PET has the most important clinical role in oncology, with fluorine–18 as the tracer, since it has proven to be the most accurate non-invasive method of detecting and evaluating most cancers. It is also used in cardiac and brain imaging [112]. This particular image shows brain activity of a patient with Alzheimer's disease in Fig. 6.24.

New procedures combine PET with computed X-ray tomography (*CT*) scans to give coregistration of the two images (*PETCT*), enabling 30% better diagnosis than with traditional gamma camera alone. It is a powerful and significant tool which provides unique information about a wide variety of diseases from dementia to

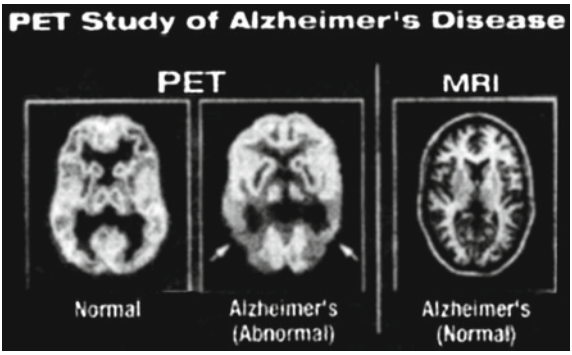

Fig. 6.24 Present picture (PET) shows brain activity of a patient with Alzheimer's disease (after [118–120])

cardiovascular disease and cancer (oncology). Positioning of the radiation source within the body makes the fundamental difference between nuclear medicine and other imaging techniques such as X-rays. Gamma imaging by either method described provides a view of the position and concentration of the radioisotope within the body. Organ malfunction can be indicated if the isotope is either partially taken up in the organ (cold spot), or taken up in excess (hot spot). If a series of images is taken over a period of time, an unusual pattern or rate of isotope movement could indicate malfunction in the organ. A distinct advantage of nuclear imaging over X-ray techniques is that both bone and soft tissue can be imaged very successfully. This has led to its common use in developed countries where the probability of anyone having such a test is about one in two and is rising.

Besides diagnosis, the *RI* is very effectively used in radiotherapy. Rapidly dividing cells are particularly sensitive to damage by radiation. For this reason, some cancerous growths can be controlled or eliminated by irradiating the area containing the growth. External irradiation can be carried out using a gamma beam from a radioactive cobalt–60 source, though in developed countries the much more versatile linear accelerators are now being utilised as a high-energy X-ray source (gamma and X-rays are much the same).

Internal radiotherapy is by administering or planting a small radiation source, usually a gamma or beta emitter, in the target area. Iodine–131 is commonly used to treat thyroid cancer, probably the most successful kind of cancer treatment. It is also used to treat nonmalignant thyroid disorders. Iridium–192 implants are used especially in the head and breast. They are produced in wire form and are introduced through a catheter to the target area. After administering the correct dose, the implant wire is removed to shielded storage. This brachitherapy (short-range) procedure gives less overall *radiation* to the body, is more localised to the target tumour and is cost effective.

Treating leukaemia may involve a bone marrow transplant, in which case the defective bone marrow will first be killed off with a massive (and otherwise lethal) dose of radiation before being replaced with healthy bone marrow from a donor. Many therapeutic procedures are palliative, usually to relieve pain. For instance,

a strontium–89 and increasingly samarium–153 are used for the relief of cancer-induced bone pain. Rhenium–186 is a newer product for this (see, also [116, 121]).

For some medical conditions, it is useful to destroy or weaken malfunctioning cells using radiation. The radioisotope that generates the radiation can be localised in the required organ in the same way it is used for diagnosis—through a radioactive element following its usual biological path, or through the element being attached to a suitable biological compound. in most cases, it is beta radiation that causes the destruction of the damaged cells. This is *radiotherapy*. Short-range radiotherapy is known as brachytherapy, and this is becoming the main means of treatment.

Although radiotherapy is less common than diagnostic use of radioactive material in medicine, it is nevertheless widespread, important and growing. An ideal theraeutic radioisotope is a strong beta emitter with just enough gamma to enable imaging, e.g. lutetium–177. This is prepared from ytterbium–176 which is irradiated to become Yb–177 which decays rapidly to Lu–177. Yttrium–90 is used for treatment of cancer, particularly non-Hodgkin's lymphoma, and its more widespread use is envisaged, including for arthritis treatment.

Iodine–131 and phosphorus–32 are also used for therapy. Iodine–131 is used to treat the thyroid for cancers and other abnormal conditions such as hyperthyroidism (over-active thyroid). In a disease called Polycythemia vera, an excess of red blood cells is produced in the bone marrow. Phosphorus–32 is used to control this excess. A new and still experimental procedure uses boron–10 which concentrates in the tumour. The patient is then irradiated with neutrons which are strongly absorbed by the boron, to produce high-energy alpha particles which kill the cancer. Some examples of RI very effectively used in everyday life are presented in Table 19 of Ref. [122].

6.5.2 Geochronology

The main data of the *geochronology* from which all conclusions are based are elemental isotopic abundance of the radionuclides which are largely deduced from meteorites. Meteorites are the prime source of information concerning the earliest stage of the solar system since they have undergone virtually no physical or chemical change since their time of formation approximately 4.6×10^9 years ago. The most primitive meteorites are believed to be carbonaceous chondrites which are largely heterogeneous agglomerations of particles which have undergone little heating since their formation. Other sources of elemental abundance determinations include the Earth, Moon, cosmic rays, Sun, and other stellar surfaces. A key result is the high degree of isotopic homogeneity among the aforementioned sources which support the nebular hypothesis for the formation of the solar system. The essence of the nebular hypothesis is that the Sun, planets, comets, asteroids and meteorites formed from a common gaseous nebula which was well mixed. The formation of our solar system from a gaseous nebula is not precisely understood and the most extensive work in this area can be seen in [123]. However, the recent determination of small

variations in *isotopic* abundance indicates that some elements of different *nucleosynthetic* histories were not completely mixed. The understanding of these variations is already constraining the detailed steps of solar system formation by imposing mixing timescales (see, e.g. [124–126]).

Although it is no surprise that determination of the age of the Earth (geochronology) is based on physical phenomena it is less expected that this is also the case for the chronology of a substantial part of the archaeological record. Of course on Roman sites the layer- by-layer finds, particularly of coins with inscriptions, often permit dating by reference to the enduring writings of contemporary authors, for example Julius Caesar, and in any case such writings establish the basic chronology of the period. To some extent the same is true further back in time, notably by relating to the king-lists giving the reign durations of the Egyptian pharaohs; these lists extend back to the First Dynasty and the earliest pyramid at about 5,000 years ago—though even this age is not science-independent since, because of missing sections of the lists, it is reliant on an astronomical calculation of the date of a recorded stellar event (see, also [127]). Beyond 5,000 years ago all was conjecture until the so-called "*radiocarbon revolution*" in the early 1950s [128] ; from then on the 'deeper the older' was replaced by ages based on the laboratory-measured half-life (5,568–5,730 years) of ^{14}C. Today, the main dating tool for the last 50,000 years or so is based on the radiocarbon method [129–134] (see, also [135]). The main *radioactive* methods for the periods before the time span of radiocarbon are potassium–argon, uranium-series dating, and fission-track dating. Thermoluminescence (TL) [135–138] overlaps with radiocarbon in the time period for which it is useful, but also has potential for dating earlier epochs—as do optical dating [136] and electron spin resonance (*EPR*)—all trapped electron dating methods that rely indirectly on radioactive decay.

The journal *Radiocarbon* publishes the most up-dated curves which in principle permit the conversion of radiocarbon dates into calibrated dates. The calibration curve (see Fig. 6.25) produced by Stuiver et al. [129, 130] combines the available data from tree—rings, uranium–thorium dated corals, and varve-counted marine sediment, to give a curve from 24,000 to 0 Cal BP. Calibration programs and curves can be obtained directly from the Radiocarbon website at www.radiocarbon.org. Several programs are now available which use a statistical methodology, termed Bayesian, to generate probability distributions of age estimations for single ^{14}C. The crucial point is that in any publication it should be indicated whether or not the radiocarbon determination has been calibrated, and if it has been, by which particular system or curve. Radiocarbon dating by the accelerator mass spectrometry (AMS) technique is opening up new possibilities. Precious objects and works of art can now be dated because minute samples are all that is required. In 1988 AMS dating resolved the long-standing controversy over the age of the Turin Shroud (Fig. 6.26), a piece of cloth with the image of a man's body on it that many genuinely believed to be the actual imprint of the body of Christ. Laboratories at Tuscon, Oxford and Zurich all placed it in the fourteenth century AD (present time), not from the time of Christ at all, although this remains a matter of controversy. Radiocarbon looks set to maintain its position as the main dating tool back to 50,000 years ago for organic materials.

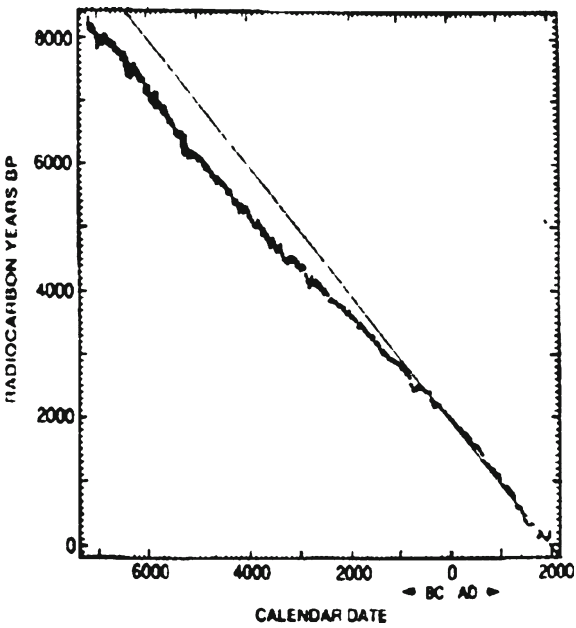

Fig. 6.25 Calibrated radiocarbon timescale based on Irish oak. The straight line indicates the ideal radiocarbon/calendar age timescale (after [129])

For inorganic materials, however, TL and other, new, techniques are very useful (see below).

The preceding techniques are *nuclear* in the strict sense of the world: the essence of the dating clock is the build-up of a dauther product, as with potassium—argon and uranium—series, or the gradual disappearance of a radioactive isotope, as with radiocarbon. Unlike the preceding techniques luminescence dating is remarkable in utilising a phenomena of which variants can be seen with the naked eye. There are two variants of luminescence dating: *TL* and optically stimulated luminescence (*OSL*), the latter also being referred to as optical dating [136]. For both variants, the latent dating information is carried in the form of trapped electrons; these are electrons which have been ionised by nuclear radiation and which have diffused into the vicinity of a defect in the lattice that is attractive to electrons, for example, such as a negative-ion vacancy, and have become trapped there (see Fig. 6.27). The nuclear radiation is from radioelements in the sample and in its surroundings; there is also a small contribution from cosmic rays. The more prolonged the exposure to ionising radiation the greater the number of trapped electrons, which hence increases with years that have elapsed since the last event at which the traps were emptied. This setting of the clock to zero is the event dated and it can be due to the agency of heat, as with pottery, or of light, as with geological sediment. A measure of the number of trapped electrons is obtained by stimulation—by heat in the case of TL and by light on the case of OSL. In either case stimulation causes the eviction of electrons from their traps whereupon they diffuse around the crystal until some form of recombination centre is found, such as a defect activated by being charged with

Fig. 6.26 Part of the Turin Shroud, bearing the image of a man's head. Radiocarbon AMS dating has given a calibrated age range for the cloth of a 1,260-1,390 years of present time (see, however, text)

a hole. The time spent in diffusion is very short and recombination can be regarded as instantaneous. In the case of a luminescence centre there is emission of light, the colour being characteristic of the type of centre. Figure 6.27 gives an indication of the overall mechanism; it is an over-simplified representation of reality but forms a useful basis for discussion (for details see also [133, 134]). It is presumed that there is no shortage of activated luminescence centres and also that the radiation flux is not sufficient to cause any significant increase in the number of centres over the age span of the sample. An alternative to the picture given is to consider the process to be dominated by trapped holes; however, although this may represent reality in some cases it is irrelevant to the discussion of most phenomenan and it is convenient to use a description based on trapped electrons (see, also [135]). A similar description is relevant to dating by EPR except that there is then no eviction.

The basis of the evaluation of age is summarised in Fig. 6.28. The 'natural' signal resulting from the natural irradiation during burial, is compared with signals, from the sample, resulting from known doses of nuclear radiation; these are controlled by a calibrated radioisotope source. This procedure allows evaluation of the paledose, the laboratory dose of nuclear radiation needed to induce 'artificial' luminescence equal to the natural signal. According to [135] the evaluation of age is given by

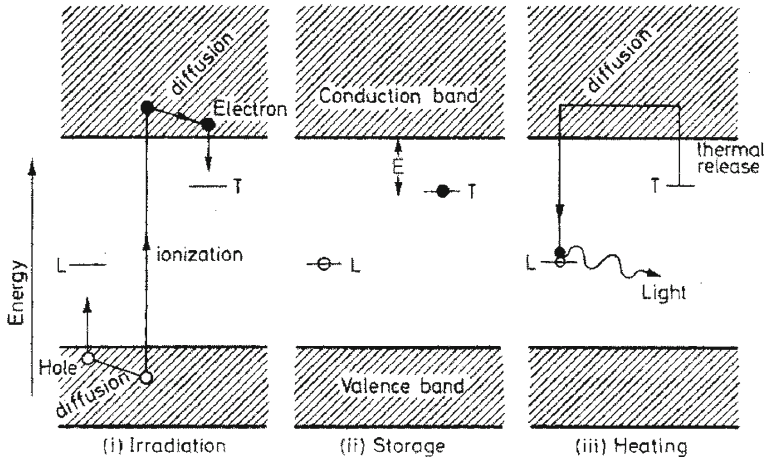

Fig. 6.27 Energy-level representation of the thermoluminescence. *i*-ionisation due to exposure of the crystal to the flux of nuclear radiation, with trapping of electrons and holes at defects, T and L, respectively. *ii*-Storage during antiquity; the lifetime of the electrons in the traps needs to be much longer than the age span of the sample in order that leakage be negligible. The lifetime is determined by the depth E of the trap below the conduction band, and for dating purposes we are interested in those deep enough ($\sim$1.5 eV) for the lifetime to be the order of a million years or more. *iii*-To observe thermoluminescence the sample is heated and there is a certain temperature at which the thermal vibration of the crystal lattice causes eviction Some of these evicted electrons reach luminescence centres, and if so, light is emitted in the process of recombining at those centres. Alternatively, the electron may recombine at a non-luminescence centre (a "killer" centre) or be captured by a deeper trap (after [135])

$$\mathrm{T} = \frac{\text{Paleodose}}{\text{Dose} - \text{rate}}. \tag{6.56}$$

The dose-rate represents the rate at which energy is absorbed from the flux of nuclear radiation; it is evaluated by assessment of the radioactivity of the sample and its surrounding burial material, this is carried out both in the laboratory and in the field.

At present, together with flint and calcite, the minerals of dominant interest archaeologically are quartz and feldspar, whether from pottery (to which mineral grains are added as temper), from sediment, or from volcanic products (see also [134, 135]). The age range covered by the various types of sample and technique is remarkable—from a few tens of years to around half a million. The limitation with quartz and flint is usually due to the onset of saturation—when all traps have become occupied; with feldspar it is more likely to be due to inadequate electron retention in the traps Fig. 6.28.

Figure 6.29 shows an example of a *TL glow-curve*. A crucial feature of TL measurement is suppression of so-called 'spurious' TL. This is not induced by radiation and is a surface phenomenan which is not well understood-prior inter-grain friction plays a part but there are other influences as well. Fortunately, it can be avoided if the TL oven is flushed with high purity nitrogen or argon, after removal of air;

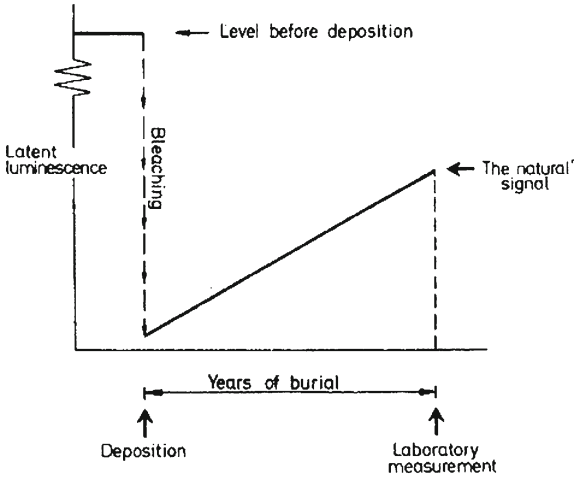

Fig. 6.28 The event dating, whether in thermoluminescence dating or in optical dating, is the setting to zero, or near zero, of the latent luminescence acquired at some time in the past. With sediment this zeroing occurs through exposure to daylight ("bleaching") during erosion, transport and deposition, whereas with fired materials, it is through heating. Subsequently, the latent signal builds up again through exposure to the weak natural flux of nuclear radiation. For OSL the dating signal is obtained by exposure of the grains from the sample to a beam of light; for TL it is obtained by heating (after [138])

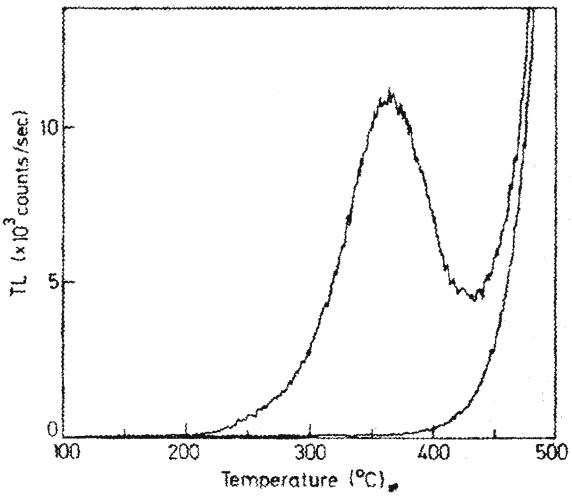

Fig. 6.29 Natural glow-curve for burned flint from the lower Paleolitrhic site at Belvedere, Holland (after [135])

elimination is also enhanced by red-rejection colour filters. The glow-curve from a sample in which there is only one trap type consists of a broad peak but in practice several trap types are usually present in a sample and the glow-curve consists of a number of overlapping peaks [139]. For archaeological or geological dating the

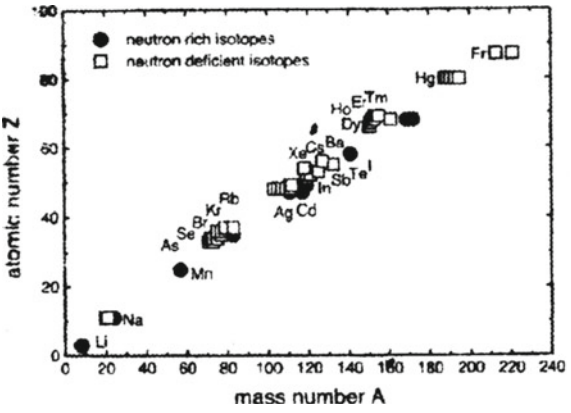

Fig. 6.30 Radioactive isotopes used for solid-state physics experiments (after [142, 143])

glow-curve region of interest is upwards of 300°C; below this temperature the TL is from traps that are so shallow that they will have suffered serious loss of electrons during the centuries of burial.

6.5.3 Solid-State Physics

The first application of radioactive*isotopes* in solid-state physics research dates back to almost a century, when radioactive lead atoms were used to study *self-diffusion* in lead [140]. The '*radiotracer diffusion*' technique was born. Nowadays, it is a common method for investigating atomic diffusion processes in solids (see, also above). Up to now approximately 100 different radioactive isotopes have been used (see, Fig. 6.30) in *nuclear* solid-state physics [141], ranging from ^{8} Li up to ^{213}Fr. They are produced by nuclear reactions in reactors or at accelerators and the doping of the host lattice is performed either by nuclear reactions inside the material, by recoil implantation or by diffusion or implantation after nuclear production and chemical separation. The radioactive nuclei are used as probes of their structural or electronic environment either in metals [144], insulators [145], semiconductors or superconductors [146] and also on surfaces and interfaces [147–150]. However, a major part of the activity is focused on the investigation of defects and impurities in semiconductors such as Si, Ge, III–V or II–VI compounds (see also [151]).

The characteristic lifetimes of *radioactive isotopes* can be used to label and identify defect levels in semiconductors which can be detected by photoluminescence [92] and *Raman-scattering* spectroscopy [152]. Magerle et al. [92] show *photoluminescence* spectra of GaAs doped with ^{111}In that decays to ^{111} Cd. ^{111}In is isoelectronic to Ga and hence occupies Ga lattice sites in GaAs. It decays to ^{111}Cd with a lifetime $\tau_{111_{In}} = 98$ h by electron capture [152]. Since the recoil energy of the Cd *nucleus* due to the emission of the neutrino is much smaller than the typical displacement energy in GaAs [7, 8], ^{111}Cd atoms on Ga sites (Cd_{Ga}) are created by the decay of ^{111} In on

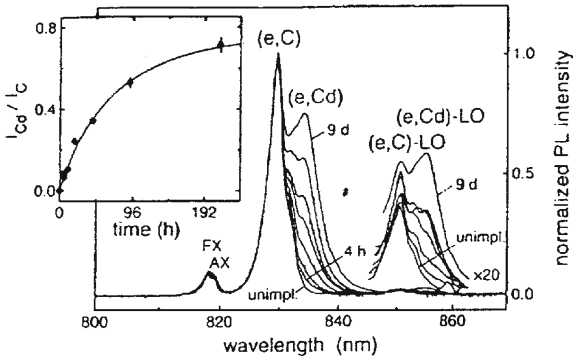

Fig. 6.31 Photoluminescence spectra of undoped and ^{111}In doped GaAs successively taken 4h; 7h; 12h; 22h; 2d; 4d and 9d after doping. all spectra are normalized to the intensity of the (e, C) peak. In the inset, the height I_{Cd}/I_C of the (e,C) peak in these spectra is shown a function of time after doping with ^{111}In. The solid line is a theoretical fit (see text) (after [92])

Ga sites ($^{111}In_{Ga}$) and act there as shallow acceptors. This chemical transmutation was monitored by photoluminescence spectroscopy. Figure 6.31 shows successively taken photolumunescence spectra from the ^{111}In doped sample. A spectrum from the undoped part is also shown. The photoluminescence spectrum of the undoped part of the sample shows the features well known for undoped *MBE-grown* GaAs [7, 8]. The peaks FX and AX around 819 nm are due to the recombination of free and bound excitons. The peak (e,C) at 830 nm and its LO phonon replica (e,C)-LO at 850 nm are due to recombination of electrons from the conduction band into C acceptor states. The recombination of electrons from donor states into C acceptor states appears as a small shoulder on the right-hand sides of either of these two peaks. C is a residual impurity in GaAs present in MBE-grown material with a typical concentration between 10^{14} and 10^{15}cm^{-3} [106]. Magerle et al. determined the height I_{Cd}/I_C of the (e, Cd) peak normalised to I_C as the function of time after doping. These was done by substracting the normalised spectrum of the undoped part from the normalised spectra of the ^{111}In doped part. The height I_{Cd}/I_C of the (e,Cd) peak remaining in these difference spectra is displayed in the inset of Fig. 6.31. The Indicated authors fitted these data by

$$\frac{I_{Cd}}{I_C}(t) = \frac{I_{Cd}}{I_C}(t=\infty)\left(1 - e^{-\frac{t}{\tau}}\right) \tag{6.57}$$

and obtained a time constant $\tau = 52(17)$ h, which is not the *nuclear lifetime* $\tau_{111_{In}} = 98$ h of ^{111}In. Evidently I_{Cd}/I_C is not proportional to N_{Cd}. The *photoluminescence* intensity I_{Cd} is proportianal to the recombination rate of excess carriers per unit area through Cd acceptors states $\Delta n_L B_{Cd} N_{Cd}$, where B_{Cd} is a recombination coefficient. The excess sheet carrier concentration in the implanted layer Δn_L can be expressed in terms of the total carrier lifetime in the implanted layer τ_L and the generation rate of excess carriers per unit area in the implanted layer $f_L G$ by using the first of the two equilibrium conditions

$$f_L G = \frac{\Delta n_L}{\tau_L} \text{ and } f_B G = \frac{\Delta n_B}{\tau_B} \tag{6.58}$$

The second one describes the balance between the generation rate $f_B G$ and the recombination rate of excess carriers $\frac{\Delta n_B}{\tau_B}$ in the bulk. The total generation rate G is proportional to the incident photon flux and $f_L + f_B = 1$. expression for τ_L, the cited authors assumed two additional recombination processes in the implanted layer: the radiative recombination via Cd acceptors and nonradiative recombination due to residual implantation damage, and write the recombination rate in the small single approximation (see, e.g, [106]) as

$$\frac{\Delta n_L}{\tau_L} = \frac{\Delta n_L}{\tau_B} + \Delta n_L B_{Cd} N_{Cd} + \Delta n_L B_{nr} f_{nr} N_{Cd} \tag{6.59}$$

Here, $\Delta n_L B_{nr} f_{nr} N_{Cd}$ is the nonradiative recombination rate per unit area due to residual implantation damage, $f_{nr} N_{Cd}$ is the concentration of these nonradiative recombination centres, and B_{nr} is the corresponding recombination coefficient. Hence Δn_L and Δn_B can be expressed as a function of N_{Cd} and the recombination rates through all the different recombination channels and thereby the relative photoluminescence peak intensities can be deduced. I_C is proportional to the sum of the (e,C) recombination rates per unit area in the implanted layer and the bulk and within this model *it* can obtain

$$I_C \propto \frac{\Delta n_L + \Delta n_B}{\tau_C} = G \frac{\tau_B}{\tau_C} \left(\frac{f_L}{1 + \Phi_{Cd}/f_B b} + f_B \right) \tag{6.60}$$

Here, Φ_{Cd} is the dose between 10^9 and $10^{13} cm^2$. Thereby, $\tau_C = 1/B_C N_C$ is an effective lifetime describing the recombination probability through C acceptor states and b is a constant defined below. With the help of Eqs. (6.58) and (6.60) can be obtained (assuming that the detection efficiencies of both peaks are equal) the following relation between I_{Cd}/I_C and Φ_{Cd}:

$$\frac{I_{Cd}}{I_C} = \frac{\Delta n_L B_{Cd} N_{Cd}}{(\Delta n_L + \Delta n_B)/\tau_C} = \frac{a}{1 + b/\Phi_{Cd}}, \tag{6.61}$$

with

$$a = \frac{f_L}{f_B} \frac{B_{Cd}}{(B_{nr} f_{nr} + B_{Cd})} \frac{\tau_C}{\tau_B} \text{ and } b = \frac{d}{f_B (B_{nr} f_{nr} + B_{Cd}) \tau_B} \tag{6.62}$$

This model describes quantitatively the dependence of (e, Cd) intensity of N_{Cd} and the cited authors use it to describe the increase of I_{Cd}/I_C with time in the ^{111}In-doped sample. In [151] the authers model the change of the carrier lifetime τ_L with time t in the ^{111}In doped sample as

$$\frac{1}{\tau_L} = \frac{1}{\tau_B} + B_{Cd} N_{In} \left(1 - e^{-\frac{t}{\tau}}\right) B_{nr} f_{nr} \tag{6.63}$$

where $N_{In} = \Phi_{In}/d$ is the initial ^{111}In concentration, $\tau = \tau_{111_{In}} = 98.0$ h is the nuclear lifetime of ^{111}In, and B_{Cd}, B_{nr} and f_{nr} are the same constants as above. Thereby, we assume following Magerle et al. that the same kinds of nonradiative recombination centres are produced by In doping as by Cd doping and that the Cd concentrations are identical to the ^{111}In concentration profile. Taking into account all the above we can write that

$$\frac{I_{Cd}}{I_C} = \frac{a}{1 + b/\Phi_{In}\left(1 - e^{-\frac{t}{\tau}}\right) + c/\left(e^{-\frac{t}{\tau}} - 1\right)}, \tag{6.64}$$

where a and b are the same constants as above and $c = B_{nr}f_{nr}/(B_{nr}f_{nr} + B_{Cd})$. This c term accounts for the fact that the ^{111}In doped sample the concentration of nonradiative centres is not changing with Cd concentration. Magerle et al. fitted Eq. (6.64) to the data shown in the inset of Fig. 6.31, keeping $\tau = 98.0$h, $a = 1.25$ and $b = 3.0 \times 10^{11}\text{cm}^{-2}$, and obtained $\Phi_{In} = 4.49 \times 10^{11}\text{cm}^{-2}$ and c = 0.5 (2). This fit is shown as a solid line and agrees perfectly with the experimental data. In the conclusion of this part it should be noted that this identification technique is applicable to a large variety of defect levels since for most elements suitable radioactive isotope exist (for details see [107]).

Coupling between the LO phonon mode and the longitudinal plasma mode in NTD semi-insulating GaAs was studied in [152] using Raman-scattering spectroscopy and a Fourier-transform infrared spectrometer. Raman spectra are shown in Fig. 6.32 for unirradiated, as-irradiated and annealed samples. The remarkable feature is the low intensity and asymmetric linewidth of the LO-phonon spectrum observed in annealed samples, which are annealed above 600°C. The behaviour is not understood by considering the only LO phonon. We should pay attention to the electrical activation of NTD impurities, which begin to activate electrically around 600°C. In the long-wavelength limit, the valence electrons, the polar lattice vibrations and the conduction electrons make additive contributions to the total dielectric response function [7, 8]:

$$\varepsilon_T(0, \omega) = \varepsilon_\infty + (\varepsilon_0 - \varepsilon_\infty) / \left[\left(1 - \omega^2/\omega_t^2\right) - \omega_p^2 \varepsilon_\infty/\omega^2\right] \tag{6.65}$$

The high-frequency value (L_+) of the mixed *LO-phonon-plasmon* modes is calculated from the roots of the dielectric constant of Eq. (6.65). The frequencies of the L_+mode and of the longitudinal plasma mode $\omega_p = \left(4\pi ne^2/\varepsilon_\infty m*\right)^{1/2}$ for various annealing temperatures are listed in Table 6.7. Here, n is the electron concentration, m* the effective mass in the conduction band ($= 0.07m_0$) and ε_∞ ($= 11.3$) the optical dielectric constant. The mixed LO-phonon-plasma mode appears around 300 cm^{-1} for electron concentration of $(0.8\text{-}2)\text{x}10^{17}\text{cm}^{-3}$. The phonon strength [153] for the high-frequency mode (L_+) of the interacting plasmon-LO-phonon mode is about 0.95 for an electron concentration of $1\text{x}10^{17}\text{cm}^{-3}$, while that for the low-frequency mode (L_) is below 0.1. Therefore, the asymmetric linewidth of the Raman spectrum observed in the annealed NTD GaAs arises from both the LO-phonon and L_+ modes, but the L_ mode is not observed because of a very weak phonon strength. As a result,

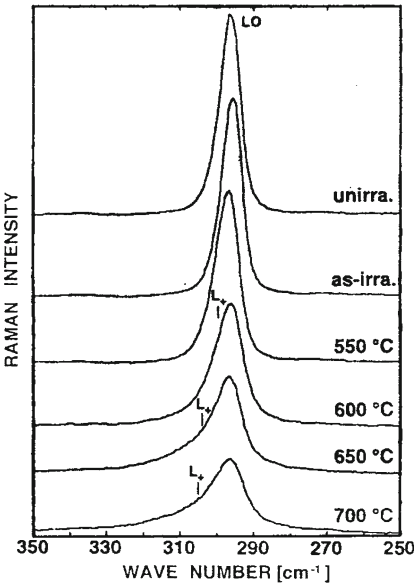

Fig. 6.32 Raman spectra at room temperature taken for the various annealing temperatures of (100) oriented NTD GaAs irradiated withneutron dozes. The coupling L_+ mode is observed at annealing temperature above 600°C (after [151])

Table 6.7 Electron concentrations and the coupling modes of NTD GaAs (after [151])

Sample	EC (cm^{-3})	LO-phonon frequency (cm^{-1})	L_+mode(cm^{-1})	PF (cm^{-1})
unirradiated	$1 \sim 2 \times 10^7$	296.6		
as - irradiated	a	295.6		
500°C annealed	a	297.8		
600°C annealed	8.2×10^{16}	296.0	299	96.4
650°C annealed	2.2×10^{17}	296.6	304	158
700°c annealed	2.5×10^{17}	296.2	305	168

the LO-phonon intensity decreases with increasing coupling, and L_+ mode appears beside the LO-phonon peak.

The *absorption spectra* in the various annealing temperatures for NTD GaAs are shown in Fig. 6.33. In unirradiated samples, an absorption around 2350 cm^{-1} is assigned as the antisymmetric stretching vibration of CO_2 arising from CO_2 in an ambient atmosphere.The absorption peaks observed around 500 cm^{-1} are also assigned as a two-phonon overtone scattering [153] of transverse optical phonons (TO); these were observed at 493 cm^{-1} [2TO (X)] , 508cm^{-1} [2TO (L)], and 524 cm^{-1} [2TO (Γ)], respectively. In as-irradiated samples, a continuous absorption extending to the higher energy was observed. Although this origin cannot be attributed to interstitial anion clusters as discussed in neutron irradiated GaP [155, 156]. In samples annealed above 600°C, the remarkable absorption was observed at wave numbers below 1450 cm^{-1}. The absorption increases with increasing annealing temperature (see Fig. 6.33). This behaviour arises from the fre-electron absorption

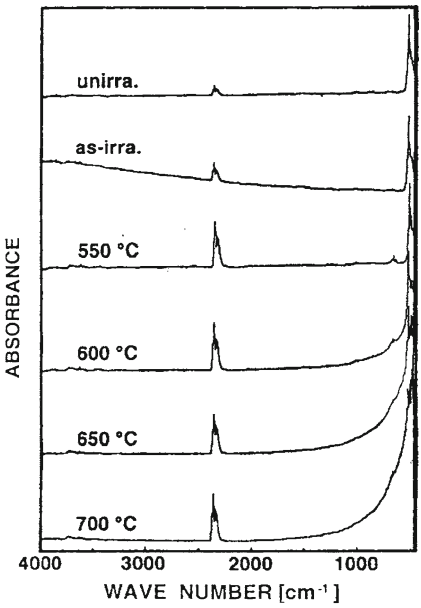

Fig. 6.33 Infrared-absorption spectra at room temperature taken for the various annealing temperatures of the NTD GaAs used for the Raman scattering experiments (after [153])

due to the activation of NTD impurities, which occur at annealing temperatures above 600°C. The free-electron absorption observed is consistent with a collective motion as a plasmon mode described in Raman-scattering studies.

Kuriyama et al. [95] studied by a photoluminescence method the transmuted impurities Ge ans S in NTD semi-insulating Gap. In NTD GaP, Ge and S impurities are transmuted from Ga and P atoms by (n,γ) reactions, respectively. Ge in GaP is an amphoteric impurity for which both the donor and acceptor states appear to be deep. The ratio between transmuted impurities Ge and S is about 16 : 1. Unfortunately, after the transmutation reactions, the transmuted atoms are usually not in their original positions but displaced into interstitial positions due to the recoil produced by the γ and β particles in the nuclear reactions. In addition, the defects induced by the fast neutron irradiation disturb the electrical activation of transmuted impurities. However, Frenkel type defects [155] in NTD GaP were annealed out between 200 and 300°C, while P antisite (P_{Ga}) defects of $\sim 10^{18} cm^{-3}$ annihilated at annealing temperatures between 600 and 650°C. Therefore, transmuted impurities, Ge and S, would be substituted on Ga and/or P lattice sites by annealing at around 650°C.

Figure 6.34 shows the photoluminescence (PL) spectra of unirradiated and NTD GaP. The PL spectrum (peak 1) of unirradiated samples shows signature of the DA pair recombination involving S donor and carbon acceptor [155]. Two (peaks 2 and 3) of the replicas occur at energies consistent with electronic transitions accompanied by zone-centre optical phonons with energies 50.1 meV (LO_Γ) and 100.2($2LO_\Gamma$). Sulphur, silicon and carbon in GaP are the most common residual impurities [155]. In *NTD-GaP* the main transition energy was observed as 1.65 eV. Since Ge in GaP

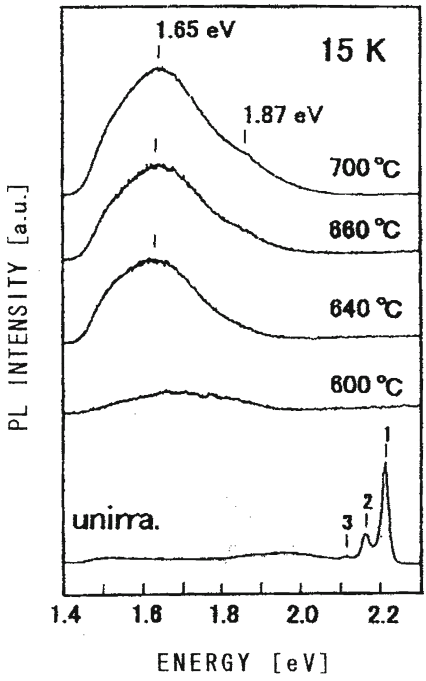

Fig. 6.34 Photoluminescence (PL) spectra taken at 15 K for unirradiated and NTD-GaP. PL peaks 1, 2 and 3 in unirradiated GaP represent $S_p - C_p$ DA pair recombination, its LO-phonon replica, and 2LO-phonon replica, respectively. 1.65 and 1.87 eV emissions in NTD-GaP are attributed to $Ge_{Ga} - Ge_P$ complex and $S_p - C_p$ DA pair recombination, respectively (after [95])

is the amphoteric impurity with deep acceptor and donor levels, strong phonon co-operation will also occur, but optical transition rates will be significant only for associates. A Similar situation has been proposed for Si in GaP [155], forming a nearest-neighbor $Si_{Ga} - Si_P$ complex. Therefore, the broad emission would be expected to arise from a nearest-neighbor $Ge_{Ga} - Ge_P$ coupled strongly to the lattice. To confirm the presence of the $Ge_{Ga} - Ge_P$ compose, the temperature dependence of the half-width, W, of the broad emission was measured. If the localised electron transitions from the excited state to the ground state of this complex centre produce the characteristics luminescence, the dependence would be appear to follow the configuration-coordinate (CC) [106] model equation:

$$W = A\,[\coth\,(h\nu/2kT)]^{1/2}\,, \tag{6.66}$$

where A is a constant whose value is equal to W as the temperature approaches 0 K and $h\nu$ is the energy of the vibrational mode of the excited state. In Fig. 6.35, Eq. (6.66) has been fitted to the experimental value for NTD-GaP. For the estimation of W, the spectrum of the 1.65 eV band was substracted from that of the 1.87 eV band.. The value of $h\nu$ used was 0.025 eV. The good fit to this equation that was found for the $Ge_{Ga} - Ge_P$ centre in NTD-GaP shows the validity of applying the CC model. The Results of [95] indicate that NTD method is a useful one for introducing Ge donor, resulting from a fact that Ge atoms are transmuted from Ga lattice sites

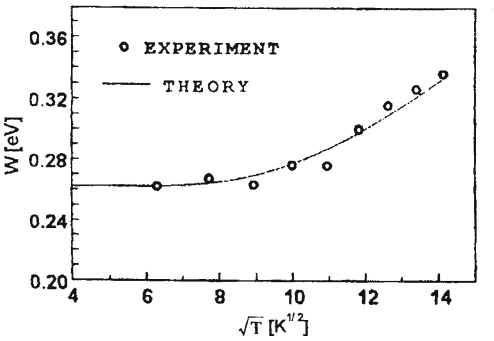

Fig. 6.35 Variation of the half-width W with the square root of the temperature T for the 1.65 eV in NTD-GaP. solid line is a theoretical fitr with hν 0.025 eV (after [95])

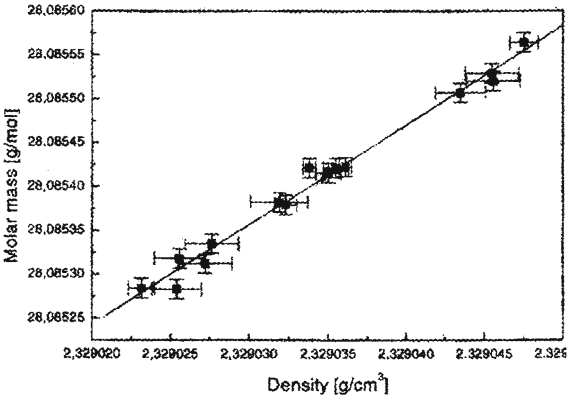

Fig. 6.36 Molar mass versus density of Si single crystal samples. The result for the molar volume derived from the linear data is m_{Si}/ρ = 12.0588207 (54) cm^3mol^{-1} (after [161])

in GaP. The obtained results are consistent with the presence of the $Ge_{Ga} - Ge_P$ complex as described earlier.

To conclude this part we briefly describe the present definition of the kilogram with mass of a certain number of silicon atoms [165, 166]. To determine a new value of the Avogadro constant with a relative combined standard uncertainty of 2×10^{-8}, the mass determinaed of a 1 kg ^{28}Si sphere is crucial and should be determination to an unprecedented level of accuracy. By this year (2009), the laboratories involved in the International Avogadro Project (the list of the participants in this Project, see e. g. in [160]), should be able to determine the mass of a 1 kg silicon sphere under vacuum with combined standard uncertainty of 4 μg.

The value derived from the slope of the function $M_{Si} = f(\rho)$ as shown in Fig. 6.36 leads to what can be considered our best knowledge for the molar volume in single-crystal silicon [159], M_{Si}/ρ = 12.0588207(54) cm^3mol^{-1}. The combination of this value with the 1998 the *Committee on Data for Science and Technology (CODATA)* recommended value of the Si lattice parameter [166] leads to an Avogadro constant N_A 6.0221330(27) $\times 10^{23}$ mol^{-1}, a candidate for consideration in future adjustments

of the values of the constants by CODATA put forward by the CCM Working Group on the Avogadro constant. This value disagrees by more than 1 part in 10^6 with the CODATA 1998 recommended value for N_A based on Planck's constant as determined mainly by watt balance experiments (for details see, also [159–166]).

6.6 Low-Dimensional Devices

6.6.1 Introduction

Nanoscience is not physics, chemistry, engineering or biology—it is all of them. The high level of circuit integration in today's silicon technology could not have been achieved with III–V semiconductors. However, from the point of view of operating speed, III–V devices show many advantages (see below), mainly due to the high carrier mobility, μ, and lower *effective mass* of electrons in III–V compounds [167, 168]. As is well known, carrier mobility in GaAs is about one order of magnitude higher than that of *silicon* [169]. In fact, the electron velocity in a semiconductor under the effect of an applied external fiel is probably the most representative parameter for the design of high-speed advanced electronic circuits. Figure 6.37 shows the maximum operation frequency (in GHz) of different modulation-doped field effect transistors (*MODFETs*) as a function of gate length (in microns) [169]. Due to their particular characteristics, these transistors are also called high electron mobility transistors (*HENTs*) [170]. For comparison purpose, Fig. 6.37 also includes typical parameters of silicon metal-oxide-semiconductor field effect transistors (*MOSFETs*) as well as GaAs MESFETs. In this picture frequency values are given at room temperature (300 K) although these frequencies are much higher for operation temperature close to 0 K, as a consequence of the increase in mobility at low temperature (see, e.g. [171]). At present, MODFET devices with gate lengths about 100 nm and maximum operation frequencies at room temperature of several hundreds of GHz are available.

Another very interesting quantum effect to take into account for the development of advanced transistors is the so-called resonant tunnelling effect [170]. Resonant tunnelling diodes (*RTD*), based on that effect, basically consist of a quantum well surrounded by two potential barriers thin enough to allow electron tunnelling. Due to the extremely low electron transit time through these semiconductors structures, electronic devices based on RTDs can operate at extremely high frequencies, in the range of 1 THz. By the addition of an RTD to a bipolar transistor or to a FET, it is possible to built resonant tunnelling transistor (*RTT*). In these transistors, the resonant tunnel structure injects very hot electrons (i.e. electrons of very high kinetic energy) into the transistor active region. The reduction of the characteristic device size to the nanometric range leads to a notable reduction in the number of electrons contained in the electric signals transferred through electronic devices. This tendency has led to the development of the so-called single-electron transistor (*SET*). As will be seen

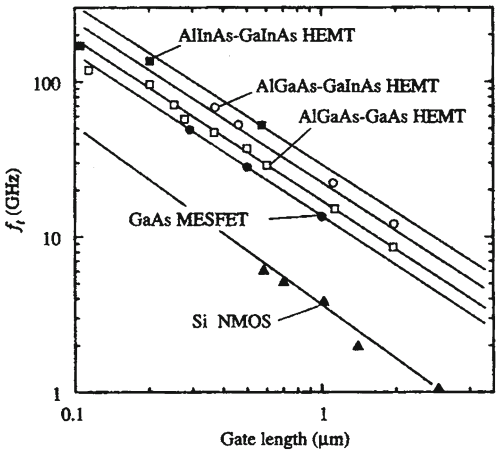

Fig. 6.37 Maximium operation frequencies reached by MODFET, MESFET and MOSFETs as function of gate length (after [183, 184])

below, the performance of SETs is based on the *Coulomb* blockade effect, which is manifested in *zero-dimensional semiconductor* structures-QDs (see, Chap. 5).

6.6.2 Resonant Tunnelling Diodes

As shown above, electrons in heterojunctions and QWs can respond with very high mobility to applied electric fields parallel to the interfaces (see, also [82]). In this paragraph, the response to an electrical field perpendicular to the potential barriers at the interfaces will be considered. Under certain circumstances, electrons can tunnel through these potential barriers, constituting the so-called perpendicular transport (see, also [172]). Tunnelling currents through heterostructures can show zones of negative differential resistance (*NDR*) (see, Fig. 6.37), which arise when the current level decreases for increasing voltage (see [173]). The operation of NDR QW electronic devices is based on the so-called resonant tunnel effect (RTE), which takes place when the current travels through a structure formed by two thin barriers with a QW between them. The I–V characteristics of RTE devices are depicted in Fig. 6.38. This figure also shows the representation of the conduction band of a double heterojunction with a QW between the junctions. The thickness of the QW is supposed to be small enough (5–10 nm) as to have only one allowed energy level E_1 (resonant level). The well region is made from lightly doped GaAs surrounded by higher gap AlGaAs (see, e.g. [174, 175]). The outer layers are made from heavily doped n-type GaAs (n^+ GaAs) to facilitate the electrical contacts. The Fermi level of the n^+ GaAs is represented within the conduction band, since it can be considered a degenerated semiconductor [176].

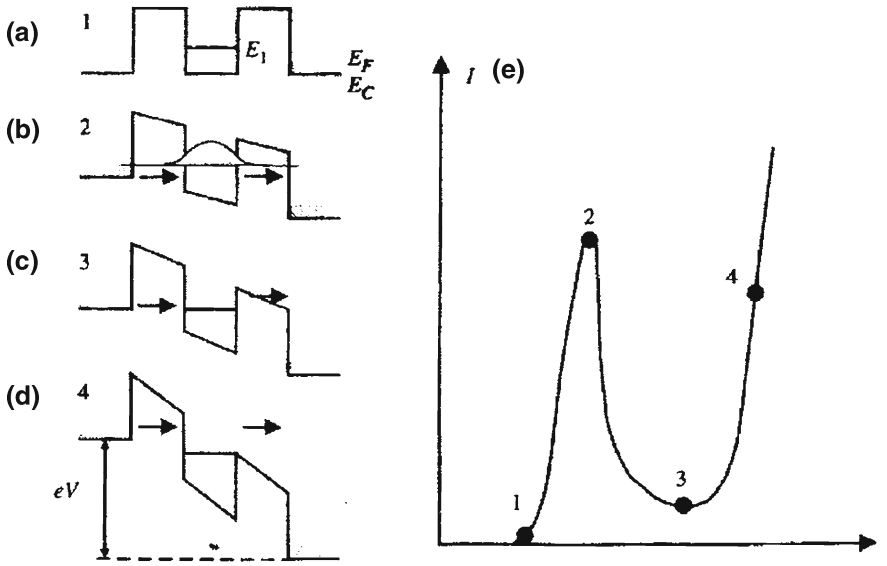

Fig. 6.38 Schematic representation of the conduction band of a resonant tunnel diode: **a** with no valtage; (**b**–**d**) for increasing applied voltage; **c** -current-voltage characteristic

Let us suppose that an external voltage, V, is applied, starting from 0V. It can be expected that some electrons tunnel from the n^+ GaAs conduction band through the potential barrier, thus resulting in increasing current for increasing voltage (region 1-2 in the I–V curve of the Fig. 6.38c). When the voltage increases, the electron energy in n^+ GaAs increases until the value $2E_1/e$ is reached, for which the energy of the electrons located in the neighbourhood of the Fermi level coincides with that of level E_1 of the electrons in the well (see, Fig. 6.38b). In this case, resonance occurs and the coefficient of quantum transmission through the barriers rises very sharply. In effect, when the resonant condition is reached, the electron wave corresponding to the electrons in the well is coherently (see, e.g. Fig. 10.18 in [178]) reflected between two barriers. In this case, the electron wave incident from the left excites the resonant level of the electron in the well, thus increasing the transmission coefficient (and thus the current through the potential barrier (region 2 in Fig. 6.38c). If the voltage further increased (region 2–3), the resonant energy level of the well is located below the cathode lead Fermi level and the current decreases, thus leading to the so-called negative differential resistance (NDR) region (region 2–3 of the Fig. 6.37). Finally, for even higher applied voltage, Fig. 6.38d, the current again rises due to the thermo ionic emission over the barrier (region 4). RTD used in microwave applications are based on this effect. A figure of merit used for RTD is the peak-to-valley current ratio of their I-V characteristic, given by the ratio between the maximum current (point 2) and the minimum current in the valley (point 3). Although the normal values of the figure of merit are about five for AlGaAs-GaAs structures at room temperature, values up to 10 can be reached in devices fabricated from strained InAs layers, surrounded

by AlAs barriers and operating at liquid nitrogen temperature [174]. If RTD are simulated by a negative resistance in parallel with a diode capacitance C and a series resistance R_S, as is the case with normal diodes, it is relatively easy to demonstrate that the maximum operation frequency increases as C decreases. The resonant tunnel diode is fabricated from relatively low-doped semiconductors, which results in wide depletion regions between the barriers and the collector region, and accordingly, small equivalent capacity. For this reason, RTDs can operate at frequencies up to several THz, much higher than those corresponding earlier tunnel diodes which just reach about 100 GHz, with response time under 10^{-13} s. Small values of the NDR , i.e. an abrupt fall after the maximum on the I-V curve result in high cut-off frequencies of operation. In fact, RTDs are the only purely electronic devices that can operate up to frequencies close to 1 THz, the highest of any electron transit time device (see, also [177]).

6.6.3 Field Effect Transistors

The previously analysed diodes are simplest electronic devices, for which the current is controlled by the diode bias and vice versa. A useful function can be performed mainly due to nonlinearity of current-voltage dependences. In contrast, in three-terminal devices known as transistors, there exist the possibility of controlling the current through two electrodes by varying the voltage or the current through third electrode. Below, we briefly describe the *field effect transistors (FETs)* on the base of the nanowires. Nanowire FETs can be configurated by depositing the nanomaterial onto an insulating substrate surface, and making source and drain on the ends nanowire. Figure 6.39 illustrates this approach. There , we show a schematic diagram of a Si-nanowire FET with the *nanowire* , the metal source and drain electrodes on the surface of the SiO_2/Si substrate (see, also [178]). This approach may serve as the basis for hybrid electronic systems consisting of nanoscale building blocks integrated with more complex planar silicon circuitry [171]. We should note that an extremely small FET may be built on the basis of carbon nanotubes [179]. In conclusion of this part we have noted that the nanowire devices discussed here have great potential for applications in nano and optoelectronics.

6.6.4 Single-Electron-Transistor

The so-called single electronics [175, 180–184] which appeared in the late 1980s, is at present a tremendously expanded research field covering future digital and analogue circuits, metrological standards, sensors, and quantum information processing and transfer [184]. The basic device, called a *single electron device (SED)*, literally enables the control of electrons on the level of an elementary charge (see, also [177, 178]). There are rich varieties SEDs (see, e.g. [196, 198–201]), but the operation principle of all SEDs is basically the same. SEDs rely on a phenomenan that occurs

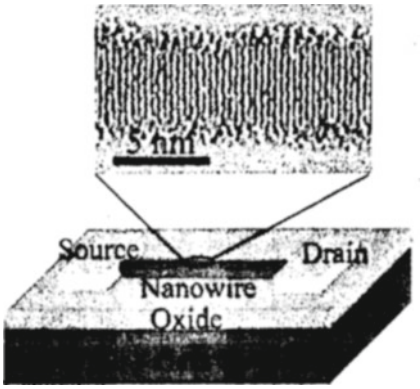

Fig. 6.39 A schematic diagram of a Si-FET with nanowire, the metal source, and drain electrodes on the surface of a SiO_2/Si substrate (after [178])

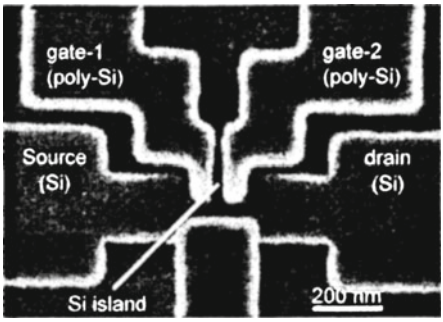

Fig. 6.40 A scanning electron microscope image of a single electron transistor (after [186])

when electrons are to enter a tiny conducting material (Fig. 6.40). When the tiny conducting material, or metallic "island", is extremely small, the electrostatic potential of the island significantly increases even when only one electron enters it. For example, for a nanometer scale island having a capacitance C of, say, 1 aF (10^{-18} F), the increase in the voltage, which is e/C with e = 1.6 $\cdot 10^{-19}$ C, reaches 160 mV. This is much larger than the thermale noise voltage at room temperature, 25.9 mV. Coulomb repulsion prevents additional electrons from entering the island unless the island potential is intentional lowered by an external bias. If the island potential is lowered gradually, the other electrons can enter the island one by one with negligibly small power dissipation (for details see [182–186] and references therein).

The single-electron transistor works as follows. The electron transfer is determined by two factors: the *Coulomb* charging of the dot and the quantised energy levels in the dot (see above). If the drain is biased with respect to the source, an electric current occurs in the regime of single-electron transfer. By applying the voltage to the gate and changing the QD parameters, one can change the conditions of electron tunnelling and affect the source-drain current. Examples of modulation of the conductance in single-electron transistors by the gate voltage are presented in Fig. 6.41. The devices have almost the same geometry. Their dimensions are large

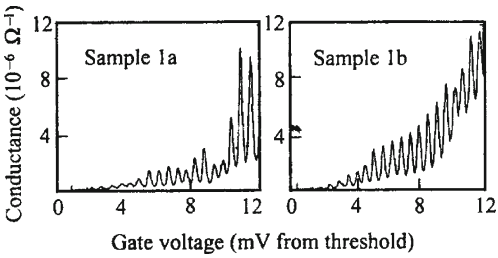

Fig. 6.41 Conductance as a function of V_g for two samples with the same geometry (after [183, 184])

enough to have a number of quantised levels. In Fig. 6.41 each peak in the conductance corresponds to transfer of one electron, when an energy level enters into resonance with the electron states in the contacts. Though the conductance versus gate-voltage dependences are different, i.e. not reproducible, the peak spacing is the same for both devices. It is determined by the change in the gate voltage required to change the charging energy of the QDs by one electron. Figure 6.41 shows clearly that the electric current is modulated significantly by the gate voltage. Thus, for transistors with single-electron transport, strong control of very small electric current may be possible.

6.7 Solid-State Lasers

6.7.1 Background

As is well known, the word *laser* is an acronym for "light amplification by the stimulated emission of radiation", a phrase which covers most, though not all, of the key physical processes inside a laser. Unfortunately, that concise definition may not be very enlightening to the nonspecialist who wants to use a laser but has less concern about the internal physics than the external characteristics. A general knowledge of laser physics is as helpful to the laser user as a general understanding of *semiconductor* physics is to the circuit designer. From a practical standpoint, a laser can be considered as a source of a narrow beam of monochromatic, coherent light in the visible, infrared or UV parts of spectrum. The power in a continuous beam can range from a fraction of a milliwatt to around 20 kW in commercial lasers, and up to more than a megawatt in special military lasers. Pulsed lasers can deliver much higher peak powers during a pulse, although the average power levels (including intervals while the laser is off and on) are comparable to those of continuous lasers.

The range of laser devices is broad. The laser medium, or material emitting the laser beam, can be a gas, liquid, crystalline solid or *semiconductor* crystal and can range in size from a grain of salt to filling the inside of a moderate-sized building. Not every laser produces a narrow beam of monochromatic, coherent light. A typical laser beam has a divergence angle of around a milliradian, meaning that it will spread

to one meter in diameter after traveling a kilometre. This figure can vary widely depending on the type of laser and the optics used with it, but in any case it serves to concentrate the output power onto a small area. Semiconductor diode lasers, for example, produce beams that spread out over an angle of 20–40° hardly a pencil-thin beam. Liquid dye lasers emit at a range of wavelengths broad or narrow depending on the optics used with them. Other types emit at a number of spectral lines, producing light that is neither truly monochromatic nor coherent. Practically speaking, lasers contain three key elements. One is the laser medium itself, which generates the laser light. A second is the power supply, which delivers energy to the laser medium in the form needed to excite it to emit light. The third is the optical cavity or resonator, which concentrates the light to stimulate the emission of laser radiation. All three elements can take various forms, and although they are not always immediately evident in all types of lasers, their functions are essential. Like most other light sources, lasers are inefficient in converting input energy into light; efficiencies can range from under 0.01 to around 20% [187–189].

Semiconductor lasers, like other lasers, have population inversions which lead to stimulated emission of photons. Semiconductor laser is different from other lasers primarily because the energy levels in semiconductors must be treated as continuous distributions of levels rather than as discrete levels [195]. We shall assume that the densities of states in the conduction and valence bands of the semiconductor are known functions of energy, and that the occupations of these levels are characterised by quasi-Fermi levels [73]. Then the probability that the state of energy E in the conduction band is occupied by an electron is

$$f_c\,(E) = 1/\{1 + exp\,[(E - F_c)\,/kT]\}, \tag{6.67}$$

where f_c is the quasi-Fermi level for the conduction band, k is Boltzmann's constant, and T is absolute temperature. A corresponding expression applies in the valence band, with quasi-Fermi level f_v. For a system in thermal equilibrium, the quasi-Fermi levels are equal to each and become the Fermi level E_F. In an excited system we have $F_c > f_v$, and we can use the separation of the quasi-Fermi levels as a measure of the excitation. The use of quasi-Fermi levels greatly simplifies the treatment of systems with many energy levels, or with continuous distributions of levels, because one quantity represents the occupation probability of many levels. The concept of quasi-Fermi level in an excited system is valid provided the scattering rate of carriers within a band is rapid compared to the recombination rate between bands, i.e. if the carriers within the conduction band and within the valence band rapidly establish a quasi-equilibrium among themselves although the conduction band and the valence band are not in equilibrium with each other For semiconductors with substantial numbers of free carriers, carrier–carrier scattering will lead to the establishment of quasi-equilibrium (see e.g. [191, 192]).

The original semiconductor lasers were p-n junctions prepared by diffusion of acceptor impurities into n-type GaAs, and this is still one of the most common structures. Semiconductors with **k**-conserving transitions at the energy gap are strongly favoured for lasing, but some impurity levels can lead to stimulated emission in

indirect-gap semiconductors, e.g. [194]. All the p-n junction lasers are excited by passing current through the p-n junction, and the excitation rate is characterised by the current density. When a forward current flows, electrons are injected into the p-type material and holes are injected into the n-type material, the latter to a much smaller extent partly because of the lower hole mobility. In heterojunctions, potential barriers play a major role in the injection of carriers [193]. The excess of electron and hole concentrations over their equilibrium values creates a local population inversion and leads to stimulated emission of photons at sufficiently high excitation levels. The layer near the p-n junction where this occurs is called the active region or active layer of the device. Figure 91. of Ref. [7] shows that the effective thickness of the active layer in graded junction lasers increases as the current density increases. This leads to smaller quasi-Fermi level separations and to less efficient use of the excitation for lasing. Heterostructure lasers (see also [193]) contain built-in potential barriers for the electrons which tend to confine them to regions of fixed width. Thus the excitation can be used most effectively.

A second class of excitation methods involves excitation with photons [197] or with an electron beam [196]. For optical excitation, the active layer thickness will be of the order of $1/\alpha$, where α is the absorption coefficient of the incident photons. For electron beam excitation, the active layer thickness will be of the order of the penetration depth of the electrons, which is a function of their energy (see, e.g. [198, 199]). In both cases, diffusion of carriers will add a distance of the order of the diffusion length to the thickness given. If sufficiently thin samples are used, the excitation state may be relatively uniform through the sample, provided surface recombination is unimportant. The excitation rate for the externally excited structure can be converted into an equivalent current density. For photons, the absorbed photon flux is multiplied by the electronic charge provided that each absorbed photon gives rise to an electron-hole pair. It should be added that values of about $3E_g$ are necessary to create one e-h pair [197]. This means that the main part of the incident pump energy is transferred to heat. This is one of the disadvantages of e-beam pumping.

With increasing excitation intensity, frequently laser action is observed in the *excitonic luminescence*. However, the direct recombination of an exciton can never give rise to laser action, because the coupled exciton–photon system corresponds in the resonant approximation to two linearly coupled harmonic oscillators. The equations of motion of this system do not contain the nonlinearity which is necessary to describe laser action. The participation of a third field is required in order to introduce the possibility of laser action [200, 201], i.e. the laser action in exciton systems has to be a parametric process in which a pump field, a signal field and an idler field participate.

Below, we describe a scheme for lasing action involving excitons in a pure crystal [202, 203].

As shown above optical transitions in pure III–V compounds which can be used for laser action are band–band transitions. In II–VI compounds (as well as LiH [106] and etc.), the recombination process of electrons and holes via exciton states is more favourable than the band-band transition [204–206]. During the last four decades laser action has been obtained in II–VI compounds by electron beam bombardment

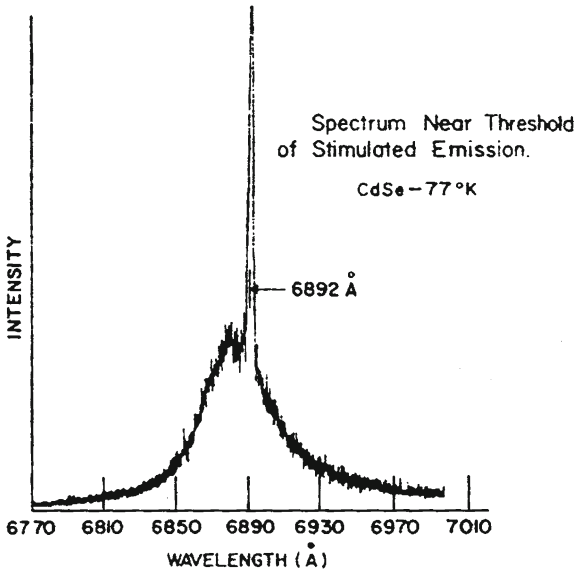

Fig. 6.42 The onset of stimulated emission in CdSe at 77 K (after [209])

[207–211], by optical excitation [205, 212–214]. The laser transitions involve the A_1-nLO phonons, where n = 1; 2. Gain measurements [210, 211, 213] and simultaneous measurements of the emission intensities of the A_1 line (direct A-exciton recombination [205]) and the A_1-LO line also confirm the statement that in CdS the A_1-LO (A_1-2LO) line starts to lase for sufficiently high pump rates (see also Fig. 6.42) (for details see [209]). In [200, 201] Haug calculated the temperature dependence of the maximum gain frequency at threshold. The result is simple in the low-temperature limit (see, also [7])

$$\Delta_{\max} \rightarrow \frac{3}{2}\mathrm{kT} \tag{6.68}$$

and also in the high-temperature limit

$$\Delta_{\max} \rightarrow (3\kappa \mathrm{kT/B})^{2/5} \exp(-2\hbar\nu/5kT, \tag{6.69}$$

where $2\kappa = 1.25{\cdot}10^{12}\mathrm{s}^{-1}$, corresponding to losses of $100\,\mathrm{cm}^{-1}$, $B = 1.55{\cdot}10^{35}$ $\mathrm{erg}^{-3/2}\mathrm{s}^{-1}$ for CdS crystals. These limiting results have also been given by Mashkevich et al. [214]. The typical experimental gain I_{thr} (T) dependence, obtained in [213] is presented in Fig. 6.43. There are shown some spectra of stimulated emission at different temperatures. The authors of [213] indicated some contradiction of their experimental results with theoretical description.

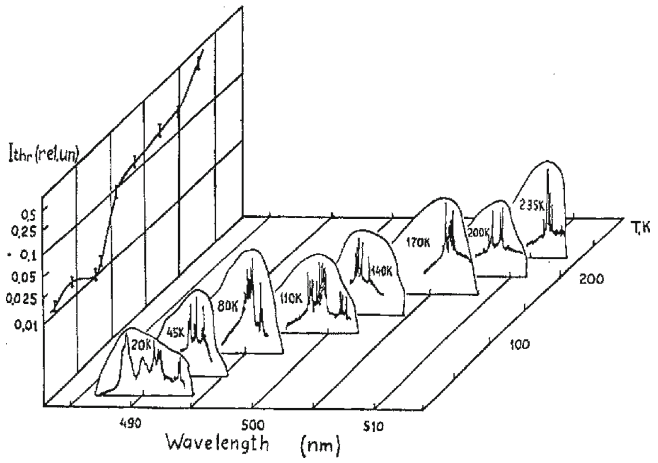

Fig. 6.43 The dependence $I_{thr}(T)$ and some examples of (above-threshold) lasing spectra (in the range of A_1-1LO; A_1-2LO phonons) at different temperature (after [214])

6.7.2 Isotope-Mixed Bulk Lasers

As was shown in [7, 8, 215, 216] another application of *isotope pure* and *isotope mixed crystals* that will be discussed here is related to the possibility of using an isotopically mixed medium (e.g. LiH_xD_{1-x} or ${}^{12}C_x^{13}C_{1-x}$) as an oscillator of coherent radiation in the ultraviolet spectral range [216, 217]. To achieve this, the use of indirect electron transitions involving, say, LO phonons was planned [200, 201, 217]. As was shown above using indirect electron transitions involving phonons to degenerate coherent radiation in semiconductors was originally proposed by Basov et al. (see [207, 208] and reference therein). Kulevsky and Prokhorov [212] were the first to observe stimulated radiation using emission lines of LO phonon repetitions in CdS crystals on two-photon excitation (see also [219]). The detection of LO phonon replicas of free-exciton luminescence in wide-gap insulators attracted considerable attention to these crystals (see e.g. [219]). At the same time it allowed one to pose a question about the possibility of obtaining stimulated emission in UV (VUV) region (4–6 eV) of the spectrum, where no solid-state sources for coherent radiation exist yet. In the first place this related to the emitters working on the transitions of the intrinsic electronic excitation (exciton). The last one provides the high energetical yield of the coherent emission per unit volume of the substance.

In this part we will discuss the investigation results of the influence of the excitation light density on the resonant secondary emission spectra of the *free-exciton* in the wide-gap insulator $LiH_xD_{1-x}(LiH_{1-x}F_x)$ crystals. The cubic LiH crystals are typical wide-gap ionic insulator with $E_g = 4.992$ eV [220] with relatively weak *exciton-phonon interaction* however: $E_B/\hbar\omega_{LO} = 0.29$ where E_B and $\hbar\omega_{LO}$ are exciton binding energy and longitudinal optical phonon's energy , respectively.

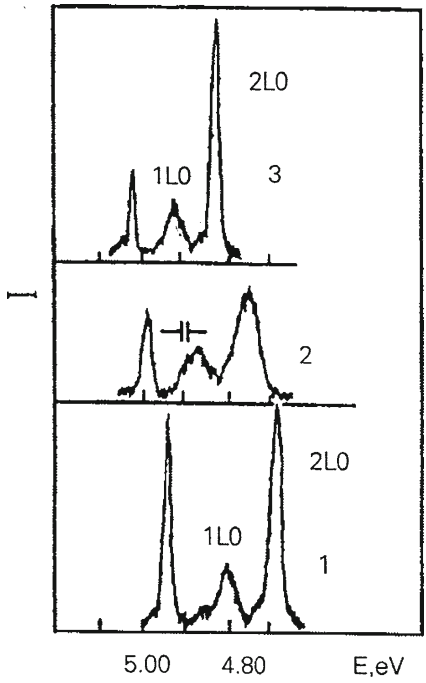

Fig. 6.44 Photoluminescence spectra of free excitons at 4.2K: 1–LiH; 2–LiH_xD_{1-x} and 3-LiD crystals (after [220])

Besides, it might be pointed out that the analogueous relation for CdS, diamond and NaI is 0.73; 0.45 and 12.7, respectively (Plekhanov [221]). Figure 6.44 depicts, as an example, the exciton luminescence spectrum of pure (LiH and LiD) and mixed (LiH_xD_{1-x}) crystals at a low temperature. analogueous results for $^{12}C_x^{13}C_{1-x}$ mixed diamond crystals are shown in Fig. 98 of Ref [7]. A common feature of all three spectra depicted in Fig. 6.44 is a phononless emission line of free excitons and its 1LO and 2LO phonon replicas. An increase in the density of the exciting light causes a burst of the radiation energy in the long-wave wing of the emission of the 1LO and 2LO repetitions at a rate is higher for the 1LO repetion line [215, 216]. Further investigations have shown [221] that with the increase of the excitation light intensity at the beginning a certain narrowing can be observed, followed by widening of the line of 2LO phonon replica with a simultaneous appearance of a characteristics, probably mode structure. A proximity of the exciton parameters of LiH and CdS (ZnO) crystals allowed to carry out the interpretation of the density effects in LiH on the analoguey with these semiconducting compounds. Coming from this in the paper [221] it was shown that for the observed experimental picture on LiH crystals to suppose the exciton–phonon mechanism of light generation [203] is enough for the excitons density about $10^{15}cm^{-3}$. This is reasonable value, if the high quality of the resonator mirror-the crystal cleavage "in situ" and relatively large exciton radius (r = 40 Å [220]) is taken into account. To this light mechanism generation must be also promoting a large value of the LO phonon energy ($\hbar\omega_{LO} = 140$ meV). Owing

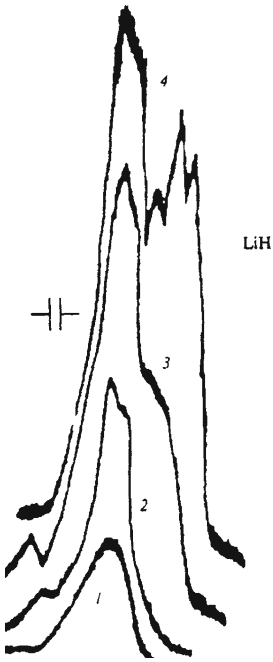

Fig. 6.45 The dependence of the shape of 2LO replica line on the excitation intensity (I_0) light: 1 − $0.05I_0$; 2 − $0.09I_0$; 3 − $0.35I_0$; 4 − I_0 (after [221])

to this the radiative transition is being realised in the spectral region with a small value of the absorption coefficient, and thus with a small loss in resonator (for details see also [220]) Fig. 6.45.

6.7.3 Light-Emitting Diodes and Lasers of Low-Dimensional Structures

So far we have studied electronic nanoscale devices, i.e. a class of devices that exploits electrical properties of *nanostructures* and operates with electric input and output signals. Another class is composed of optoelectronic devices, which are based on both electrical and optical properties of materials and work with optical and electric signals. In this paragraph we will analyse two very important classes of optoelectronic devices: *light-emitting diodes* and*lasers*. As will be shown below, the energy of the electric current flowing through these diodes is transformed into light energy. These *optoelectronic* devices have a huge number of applications and deserve consideration in detail (see, also [222–225]).

Although stimulated emission [106] from the injection laser diode is very important, practically, subthreshold operation of the diode—when only spontaneous light is emitted—is in many cases advantageous and has a number of applications. Diodes

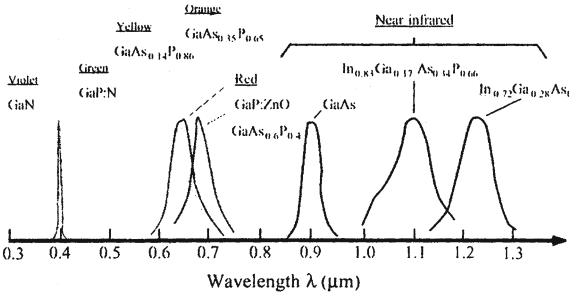

Fig. 6.46 The spectra of light-emitting semiconductor diodes with different band gaps (after [169])

operating with spontaneous light emission are called light-emitting diodes [224]. The important characteristic of the light-emitting diode is the spectral distribution of emission The spectrum of emission is determined, primarily, by the electron/hole distributions. Thus, the ambient temperature T, defines both spectral maximum and the spectral width of emission. The peak value of the spectral distribution can be estimated as [174, 177].

$$\hbar\omega = \mathrm{E}_g + \frac{\mathrm{k_B T}}{2} \tag{6.70}$$

The full width at half maximum of the distribution is $\Delta\omega \approx 2\mathrm{k_B T}/\hbar$ and is independent of ω. In terms of the wavelength, λ, we obtain

$$\Delta\lambda = [\lambda_m^2/(2\pi c)\,\Delta\omega]$$

or

$$\Delta\lambda = 1.45\lambda^2 k_B T, \tag{6.71}$$

where λ_m corresponds to the maximum of the spectral distribution, $\Delta\lambda$ and λ_m are expressed in micrometers, and $\mathrm{k_B T}$ is expressed in eV. Figure 6.46 shows the spectral density as a function of the wavelength for light-emitting diodes based on various materials. For these different materials, the spectral linewidth increase in proportion to λ^2, in accordance with Eq. (6.71). From Fig. 6.46, one can see that light-emitting diodes cover a wide spectral region from the infrared-about 8 μm for InGaAsP alloys-to the near ultraviolet- 0.4 μm for GaN. Light-emitting diodes are, indeed very universal light sources [225].

Semiconductor lasers incorporating low-dimensional heterostructures., QWs and QDs, are attracting considerable interest in their potential for improved performance over QW lasers (see, e.g. [224, 225]). This prediction is based, in the single-particle picture, on the sharper density of states resulting from the confinement of the charge carriers in two or three directions. Among other advantages, the ideal QD and QWr lasers would exhibit higher and narrower gain spectrum, low threshold currents, better stability with temperature, lower diffusion of carriers to the device surfaces, and a narrower emission line than double heterostructure or QW lasers (see, also [227]). The

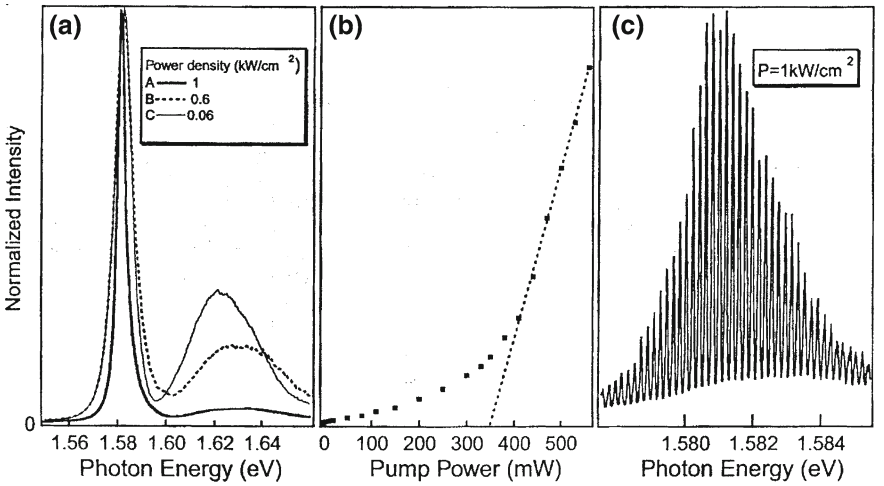

Fig. 6.47 **a** Photoluminescence spectra at 10 K of the QWr laser sample above, below and near the lasing threshold in TE-polarisation. **b** Dependence on input excitation power of the PL output power;arrows indicate the excitation powers used for the optical spectra depicted in (**a**). **c** High resolution emission spectrum above the lasing threshold showing the Fabri–Perrot modes of the optical cavity (after [228])

observation of lasing from excitons in optically excited V-groove GaAs/AlGaAs QWr laser structures was described in detail in [229]. The observable emission is attributed to the recombinations of excitons associated with the lowest energy electron- and hole-subbbands of the QWr. Moreover, these authors show that the emission energy remains nearly constant within the inhomogeneously broadened *photoluminescence* line of the QWrs for both continuous wave (cw) and pulsed optical excitation over a wide range of power densities. These results corroborate the important role played by electron-hole Coulomb correlations [229, 230] in the optical emission from quasi - 1D QWrs in the density regime of the Mott transition.

Optical emissions of the *QWr laser* structure are displayed in Fig. 6.47 for different values of the optical power density below, at and above the threshold for lasing in the QWr. Upon increasing the pump power, these authors observe a nearly constant energy of the peak at 1.581 eV that corresponds to the optical transition $e_1 - h_1$ associated with the ground electron-hole-subband of the QWrs. A significant spectral narrowing is also found as the power density is increased and crosses the lasing threshold. This evidences the existence of amplified spontaneous emission within this inhomogeneously broadened PL line in this density regime. The observable emission intensity varies linearly at low excitation power over three orders of magnitude (from 0.1 to 100 mW) [229]). Above the lasing threshold (at 350 mW) the intensity variation is again linear (see, Fig. 6.47b), indicating that the modal gain is saturated. In Fig. 6.47c, a high-resolution emission spectrum obtained above threshold features well-resolved Fabry-Perot modes that correspond to different longitudinal optical modes within the inhomogeneous line of the QWr-PL. Detailed investigations of PL

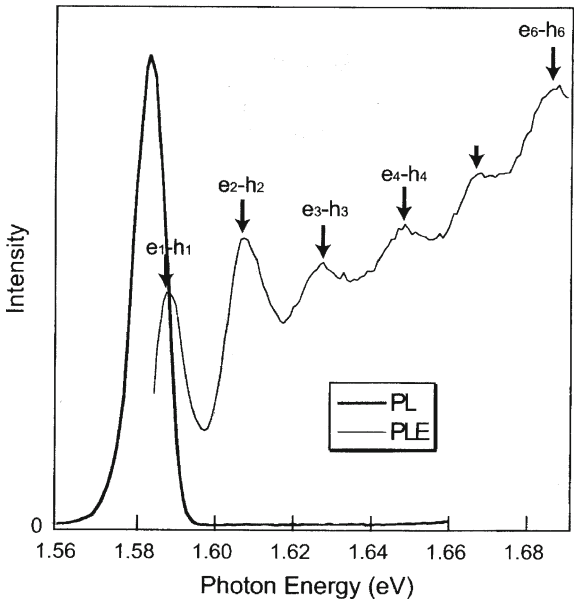

Fig. 6.48 Linearly polarised PLE spectrum and the corresponding PL spectrum of an etched QWr laser sample at 10 K. The polarization of the excitation is parallel tothe wire axis. The different optical transition $e_n - h_n$ are marked by arrows (after [228])

and PLE spectra (see, Fig. 6.48) of the QWr allowed the indicated authors to conclude that the lasing emission originates from the recombination of excitons as is the case for the QWr-peak of the cw-PL spectrum (for details see [229]).

In *QDs*, as indicated above, carriers are confined in the three directions in a very small region of space, producing quantum effects in the electronic properties. As we can see from Fig. 6.3 of Chap. 4, the electronic joint density of states for QD shows sharp peaks corresponding to transitions between discrete energy levels of electrons and holes. Outside these levels the DOS vanishes. In many ways, the electronic structure of a QD resembles that of a single atom [227]. Lasers based on QDs could have properties similar to those of conventional ion gas lasers, with the advantage that the electronic structure of a QD can be engineered by changing the base material, size and shape. Next, we assume that the QDs are small enough so that the separation between the first two electron energy levels for both electrons and holes is much larger than the thermal energy kT. Then for an undoped system, injected electrons and holes will occupy only the lowest level. Therefore, all injected electrons will contribute to the lasing transitions from the E_{1e} to the E_{1hh} levels, reducing the threshold current with respect to other systems with lower confinement. The evolution of the threshold current density obtained along the years for various laser structures is shown in Fig. 6.49. The lowest threshold currents have already been reached for QD lasers [232]. As long as the thermal energy is lower than the separation between the fist and second levels, the emission band in an ideal QD laser is very sharp and does not depend on temperature (see, also [159]). Therefore, QD lasers should have a better stability with temperature without the need for cooling.

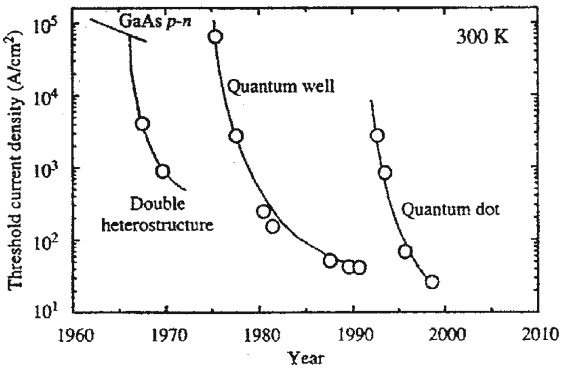

Fig. 6.49 Evolution of threshold current density for lasers based on different confinement structures (after [233])

We should add that QD lasers have the narrowest spectrum and the highest gain (for details see, also [174, 177, 225]).

6.7.4 Quantum Well Photodetectors

In principle, *QWs* can be used for the detection of light in any spectral region. As we all know the optical properties to interband transitions in QWs are quite different from those correspnding to bulk materials, since one has to consider both the 2D optical density of states (see, Chap. 4) and the fact that excitonic absorption is much stronger in 2D systems. With respect to intraband transitions, in contrast to the 3D situation, 2D systems can show transitions without the necessity of involving phonons. Intraband transitions can be among electrons (or holes) in confined states in wells, or between confined states and the continuum (see, Fig. 6.50). These transitions can be tailored for detection of light (*IR photodetectors* [170, 171]. Thus, it is in the IR region between 2 and 20 microns,that QW photodetectors are preferably used for example in applications of night and thermal imaging (see, also [97, 98]). The problem with photodiodes based on band-to band transitions across the band-gap E_g in p-n *homojunctions* is that they require materials with very low values of E_g, which makes it necessary to work at cryogenec temperatures. For instance, in the case of III–V compounds this leaves us with In $As_{1-x}SB_x$ with x $\approx$ 0.5. Some A_2B_6 compounds like HgCdTe can also be used in the IR, but these materials are quite soft, difficult to process, and have large dark currents. The perspective of QW potodetectors are isotope-mixed germanium as well as other isotope-mixed materials. In QWs, wavelength tunability is easily implemented since the energies of the levels in a QW can be adjusted by the fabrication parameters, in particular its width. Figure 6.50 shows the absorption transitions suitable for IR detection for a single QW under the action of an applied electric field, although practical devices are

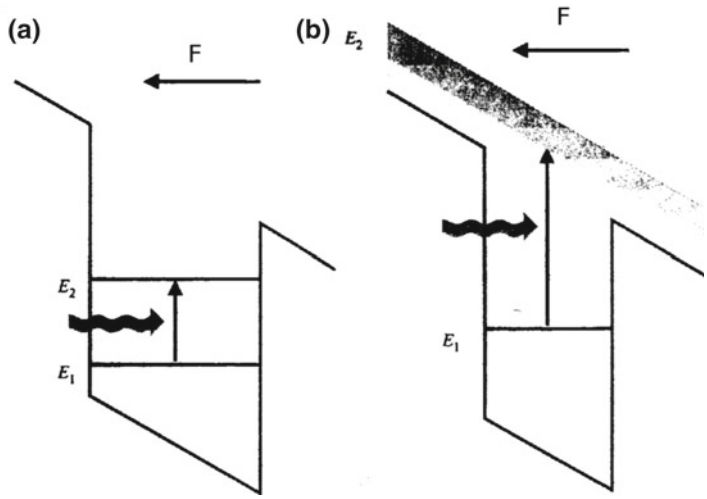

Fig. 6.50 Optical absorption transition for IR detection in a QW: **a** intersubband transitions; **b** transion from a bound state to the continuum narrow band outside the potential wells. F is the applied electric field

made with *MQWs*. In Figure 6.50a there are two energy levels in each well, the second level being located close to the top of the barriers. The separation between levels should be in the range 0.1–0.2 eV, which for III–V compounds implies a width of the wells about 10 nm [170]. Sometimes, it is more effective to make use of absorption transitions between a single level in the well and the first continuum narrow band outside it (Fig. 6.50b). In the case of the system AlGaAs-GaAs -AlGaAs, this energy is about 0.12 eV, and therefore, the spectral response is around 10μm [171]. The advantage of using this scheme is that the photodetector dark current is smaller than for the previous case in which the carriers had to leave the wells by tunnelling (for details, see [174]).

References

1. J.M. Meese, (ed.), *Neutron Transmutation Doping in Semiconductors* (Plenum Press, New York, 1979)
2. M.A. Krivoglaz, *Theory of Scattering X-rays and Thermal Neutrons by Real Crystals* (Science, Moscow, 1967) (in Russian)
3. G. Dolling, in *Dynamical Properties of Solids*, ed. by G.K. Horton, A.A. Maradudin (North-Holand, Amsterdam, 1974)
4. B. Dorner, *Inelastic Neutron Scattering in Lattice Dynamics, Springer Tracts in Modern Physics*, vol. 93. (Berlin, Springer, 1982)
5. V.G. Plekhanov, Isotope effect in lattice dynamics. Physics Uspekhi **46**, 689–715 (2003)
6. J.M. Meese, in *Neutron Transmutation Doping in Semiconductors*, ed. by J.M. Meese (New York-London, Plenum Press, 1979), pp. 1–10

7. V.G. Plekhanov, Applications of isotope effecr in solids. J. Mater. Sci. **38**, 3341–3429 (2003)
8. D.E. Cullen, P.J. Hlavac, *ENDF/B Cross Sections* (Brookhaven National Laboratory, New York, 1972)
9. L.S. Smirnov (ed.), *Semiconductors Doped by Nuclear Reactions*, (Science, Novosibirsk, 1981) (in Russian)
10. D. De Soete, *Neutron Activation Analysis* (Wiley, New York, 1971)
11. K.N. Mukhin, *Introduction in Nuclear Physics* (Atomizdat, Moscow, 1965) (in Russian)
12. M. Tanenbaum, A.D. Mils, Preparation of uniform resistivity n-type silicon by nuclear transmutation. J. Electrochem. Soc. **108**, 171–174 (1961)
13. M.S. Snöller, IEEE Trans. Electron. Devices ED-21 313 (1974)
14. W. Haas, M.S. Snöller, Phosphorus doping of silicon by means of neutron irradiation. J. Electron. Mater. **5**, 57–68 (1976)
15. D.S. Billington, J.H. Crawford, Jr., *Radiation Damage in Solids*, Chap. 2 (Princeton University Press, Princeton, 1961)
16. V.S. Vavilov, *Influence of Radiation on the Semiconductors*, (Science, Moscow, 1963) (in Russian)
17. E.E. Haller, Isotopically engineered seniconductore. J. Appl. Phys. **77**, 2857–2878 (1995)
18. E.E. Haller, N.P. Palaio, M. Rodder, W.L. Hansen, E. Kreysa, *NTD Germanium: A Novel Material for Low Temperature Bolometers*, in ed. by R.L. Larrabee, Neutron Transmutation Doping of Semiconductor Materials, (Plenum Press, New York, 1984), pp. 21–36
19. K.M. Itoh, E.E. Haller, J.W. Beeman, W.L. Hansen, Hopping conduction and metal-insulator transition in isotopically enriched neutron-transmutation-doped ^{70}Ge:Ga. Phys. Rev. Lett. **77**, 4058–4061 (1996)
20. I. Schlimak, M. Kaveh, R. Ussyshkin et al., Determination of the critical conductivity exponent for the metal - insulator transition at nonzero temperatures: universality of the transition. Phys. Rev. Lett. **77**, 1103–1106 (1996)
21. I. Schlimak, Neutron transmutation doped semiconductors: science and applications. Fiz. Tverd. Tela. **41**, 794–798 (1999) (in Russian)
22. R. Rentzsch, A.N. Ionov, Ch. Reich, V. Ginodman, I. Schlimak, Influence of the disorder germanium changed by compensation on the critical indices of the metal-insulator transition. Fiz. Tverd. Tela. (St. Petersburg) **41**, 837–840 (1999)
23. A.N. Ionov, M.N. Matveev, D.V. Shmik, Determination of the caefficients of neutron transmutation doped germanium. J. Techn. Phys. (St.Petersburg) **59**, 169–170 (1989) (in Russian)
24. I. Schlimak, A.N. Ionov, R. Rentzsch, J.M. Lazebnik, On the doping of isotopically controlled germanium by nuclear transmutation with a high concentration of shallow donor impurities. Semicond. Sci. Technol. **11**, 1826–1830 (1996)
25. H.C. Schweinler, Some consequences of thermal neutron capture in silicon and germanium. J. Appl. Phys. **30**, 1125–1126 (1959)
26. J. Guldberg (ed.), *Neutron-Transmutation-Doped Silicon* (Plenum Press, New York, 1981)
27. C.M. Lederer, J.M. Hollander, I. Perlman (eds.), *Table of Isotopes*, 6th edn. (Wiley, New York, 1967)
28. B.I. Shklovskii, A.L. Efros, *Electronic Properties of Doped Semiconductors: Solid State Series*, vol. 45 (Springer, Berlin, 1984)
29. E.E. Haller, W.L. Hansen, F.S. Goulding, Physics of ultra-pure germanium. Adv. Phys. **30**, 93–138 (1981)
30. H. Fritzsche, *The Metal Non-Metal transition in Disordered Systems*, ed. by L.R. Friedman, D.P. Tunstall, Scotish Universities Summer School in Physics, (St. Andrews, Scotland, 1978)
31. N.F. Mott, *Metal-Insulator Transition*, 2nd edn. (Taylor and Francis, London, 1990)
32. N.F. Mott, Electrons in disordered structures. Adv. Phys. **50**, 865–945 (2001)
33. P.A. Lee, T.V. Ramakrishnan, Disordered electronic systems. Rev. Mod. Phys. **57**, 287–336 (1985)
34. R. Rentzsch, A.N. Ionov, Ch. Reich, A. Müller, The scaling bahaviour of the metal-insulator transition of isotopically engineered neutron-transmutation-doped germanium. Phys. Stat. Solidi (b) **205**, 269 (1998)

35. T.F. Rosenbaum, K. Andres, G.A. Thomas, F.N. Bhatt, Sharp metal-insulator transition in a random solid. Phys. Rev. Lett. **45**, 1723–1726 (1980)
36. P.F. Newman, D.F. Holcomb, Phys. Rev. **B28**, 638 (1983)
37. Metal-insulator transition in a double-donor system, Si:P, As. Phys. Rev. Lett. **51**, 2144–2147 (1983)
38. W.N. Shafarman, D.W. Koon, T.G. Castner, dc conductivity of arsenic-doped silicon near metal-insulator transition. Phys. Rev. B **40**, 1216–1231 (1989)
39. A.N. Ionov, M.J. Lea, R. Rentzsch, Metal-insulator transition in neutron transmutation doped n-type germanium. JETP Lett. (Mosc.) **54**, 470–473 (1991)
40. P. Dai, Y. Zhang, M.P. Sarachik, Critical conductivity exponent for Si:B. Phys. Rev. Lett. **66**, 1914–1917 (1991)
41. G.A. Thomas, Y. Ootuka, S. Katsumoto, S. Kobayashi, W. Sasaki, Evidence for localization effects in compensated semiconductors. Phys. Rev. B **25**, 4288–4290 (1982)
42. M.J. Hirsch, U. Thomanschefsky, D.F. Holcomb, Critical behavior of the zero-temperature conductivity in compensated silico, Si:(P, B). Phys. Rev. B **37**, 8257–8261 (1988)
43. A.G. Zabrodskii, K.N. Zinov'eva, Sov. Phys. JETP **59**, 425 (1984)
44. M. Rohde, H. Micklitz, Indication of universal behavior of Hall conductivity near metal-insulator transition in disordered systems. Phys. Rev. B **36**, 7572–7575 (1987)
45. G. Hertel, D.J. Bishop, E.G. Spencer, R.C. Dynes, Tunneling and transport measurements at the metal-insulator transition of amorphous Nb:Si. Phys. Rev. Lett. **50**, 743–746 (1983)
46. W.L. McMillan, J. Mochel, Electron tunneling experiments on amorphous $Ge_{1-x}Au_x$. Phys. Rev. Lett. **46**, 556–557 (1981)
47. Th Zint, M. Rohde, H. Micklitz, Metal-insulator transition in amorphous Ga–Ar mixtures: critical exponents of electrical transport parameters and behavior of superconductivity. Phys. Rev. B **41**, 4831–4833 (1990)
48. E.W. Hass, M.S. Schnöller, Phosphorous doping of silicon by means of neutron irradiation. IEEE Trans. Electron Dev. ED **23**, 803–805 (1976)
49. N.F. Mott, The basis of the electron theory of metals, with special reference to the transition metals. Proc. Phys. Soc. (Lond.) A 62, 416–425 (1949)
50. P.W. Anderson, Absence of diffusion in certain random. Phys. Rev. **109**, 1492–1505 (1958)
51. A. MacKinnon, B. Kramer, One-parameter scaling of localization length and conductance in disordered systems. Phys. Rev. Lett. **47**, 1546–1549 (1981)
52. M. Henneke, B. Kramer, T. Ohtsuki, Localization length and conductance in disordered systems. Europhys. Lett. **27**, 389–392 (1994)
53. E. Hafstetter, M. Schreiber, Does broken time reversal symmetry modify the critical behavior at the metal-insulator transition in 3-dimensional disordered systems? Phys. Rev. Lett. **73**, 3137–3140 (1994)
54. T. Kawarabayashi, T. Ohtsuki, K. Slevin, Y. Ono, Anderson transition in three-dimensional disordered systems with symplectic symmetry. Phys. Rev. Lett. **77**, 3593–3596 (1996)
55. J. Chang, M.M. Dacorogna, M.L. Cohen, Superconductivity in high-pressure metallic phases of Si. Phys. Rev. Lett. **54**, 2375–2378 (1985)
56. R.D. Larrabee (ed.), *Neutron Transmutation Doping of Semiconductor Materials* (Plenum Press, New York, 1984)
57. A.N. Ionov, I.S. Shlimak, M.N. Matveev, An experimental determination of the critical exponents at the metal-insulator transition. Solid State Commun. **47**, 763–766 (1983)
58. D. Chattopadhyay, H.J. Queisser, Electron scattering by ionized impurities in semiconductors. Rev. Mod. Phys. **53**, 745–768 (1981)
59. V.G. Plekhanov, Isotope engineering, Phys. Uspekhi (Mosc.) **170**, 1147–1152 (2000) (in Russian)
60. K. Itoh, W.L. Hansen, E.E. Haller, J.W. Farmer, V.I. Ozhogin, in *Proceedings of the 5th International Conference on Shallow Levels in Semiconductors*, Kobe, Japan, 1992
61. H.D. Fuchs, K.M. Itoh, E.E. Haller, Isotopically controlled germanium: a new medium for the study of carrier scattering by neutral impurities. Philos. Mag. B **70**, 661–670 (1994)

62. W. von Ammon, Neutron transmutation doped silicon-technologica and economic aspects. Nucl. Instrum. Methods B **63**, 95–100 (1992)
63. K.M. Itoh, W. Walukiewicz, H.D. Fuchs, J.W. Beeman, E.E. Haller, V.I. Ozhogin, Neutral-impurity scattering in isotopically engineered Ge. Phys. Rev. B **50**, 16995–17000 (1994)
64. K. Itoh, W.L. Hansen, V.I. Ozhogin et al., High-purity isotopically enriched ^{70}Ge and ^{74}Ge single crystals: isotope separation, purification and growth. J. Mater. Res. **8**, 1341–1347 (1993)
65. C. Erginsoy, Neutral impurity scattering in semiconductors. Phys. Rev. **79**, 1013–1014 (1950)
66. A.I. Ansel'm, Influence resonant scattering of the charges on the impurity centres on the electrical properties of semiconductors, Zh. Eksp. Teor. Fiz. (Mosc.), **24**, 83–89 (1953) (in Russian)
67. N. Sclar, Neutral impurity scattering in semiconductors. Phys. Rev. **104**, 1559–1561 (1956)
68. N. Sclar, Ionized impurity scattering in nondegenerate semiconductors, **104**, 1548–1558 (1956)
69. T.C. McGill, R. Baron, Neutral impurity scattering in semiconductors. Phys. Rev. B **11**, 5208–5210 (1975)
70. B.K. Ridley, *Quantum Process in Semiconductors*, 3^{rd} *ed* (Clarendon Press, Oxford, 1993)
71. R.D. Dingle, Scattering of electrons and holes by charged donors and acceptors in semiconductors, Philos. Mag. 46831–46840 (1955)
72. H. Brooks, Theory of the electrical properties of germanium and silicon. Adv. Electron. Electron Phys. **7**, 85–182 (1955)
73. W. Shockley, *Electrons and Holes in Semiconductors* (Van Nostrand Reinhold, Princeton, 1950)
74. J. Blakemore, *Semiconductor Statistics*, 2nd edn. (Dover, New York, 1985)
75. V.G. Dzhakeli, Z.S., Kachlishvili, To the theory of acattering on neutral impurity atoms. Sov. Phys. Semicond. **18**, 1482–1484 (1984)
76. B.J. Baliga, Neutron transmutation doped silicon for power semiconductor devices, in *Neutron Transmutation Doping of Semiconductor Materials*, ed. by R.D. Larrabeeed, (Plenum Press, New York, 1984), pp. 167–180
77. J.W. Farmer, J.C. Nugent, Transient current spectroscopy of neutron irradiated silicon, in *Neutron Transmutation Doping of Semiconductor Materials*, ed. by R.D. Larrabee, (Plenum Press, New York, 1984) pp. 225–240
78. K. Lark-Horowitz, Bombardment semiconductors by nuclons, in *Proceedings Conference on semiconductor materials*, ed. by H.K. Henish (Butterworth, London, 1951) pp. 47–79
79. M.J. Hill, P.M. van Iseghem, W. Zimmerman, Prepararion and application of neutron transmutation doped silicon for power device research, IEEE Trans. Electron Device ED **23**, 809–813 (1976)
80. J. Messier, Y. le Corroler, J.M. Flores, Thick junctions made with nuclear compensated silicon. IEEE Trans. Nucl. Sci. NS - **11**, 276–279 (1964)
81. H.M. James, O. Malmros, Application of thermal neutron irradiation for large scale production of homogeneous phosphorous doping of floatzone silicon. IEEE Trans. Electron Devices ED **23**, 797–802 (1976)
82. P.V. van Iseghem, p-i-n epitaxial structures forhigh power devices. IEEE Trans. Electron Devices ED **23**, 823–825 (1976)
83. International Atomic Energy Agency Regulations for the Safe Transport of Radioactive Materials, Rev. Ed., 1973, p. 8
84. H. Hamanaka, K. Kuriyama, M. Yahagi et al., Doping of phosphorus in hydrogenated amorphous silicon by a neutron transmutation doping technique. Appl. Phys. Lett. **45**, 786–788 (1984)
85. D.W. Koon, T.G. Castner, Does the Hall coefficient exhibit critical behavior approaching the metal-insulator transition? Phys. Rev. Lett. **60**, 1755–1758 (1988)
86. P. Dai, Y. Zhang, M.P. Sarachik, Critical behavior of the Hall coefficient of Si:P at the metal-insulator transition. Phys. Rev. B **49**, 14039–14042 (1994)
87. H. Grussbach, M. Schreiber, Determination of the mobility edge in the Anderson model of localization in three dimensions by multifractal analysis. Phys. Rev. B **51**, 663–666 (1995)

88. P. Dai, Y. Zhang, M.P. Sarachik, Critical behavior of the Hall coefficient of Si:B. Phys. Rev. Lett. **70**, 1968–1971 (1993)
89. S.B. Field, T.F. Rosenbaum, Critical behavior of the Hall conductivity at the metal-insulator transition. Phys. Rev. Lett. **55**, 522–524 (1985)
90. M.H. Young, A.T. Hunter, R. Baron, O.I. Marsch, Neutron transmutation doping of p-type Czochralski–Grown galliuym arsenide, in *Neutron Transmutation Doping of Semiconductor Materials*, ed. by R.D. Larrabee (Plenum Press, New York, 1984), pp. 1–20
91. R. Rentzsch, K.J. Friedland, A.N. Ionov, Negative magnetoresistance of neutron transmutation-doped gallium arsenide at vriable-range hopping. Phys. Stat. Solidi (b) **146**, 199–206 (1988)
92. R. Magerle, A. Burchard, M. Deicher, T. Kerle, Radioactive isotopes in photoluminescence experiments: identification of defect levels. Phys. Rev. Lett. **75**, 1594–1597 (1995)
93. K. Kuriyama, K. Sakai, LO-phonon and plasmon coupling in neutron-transmutation-doped GaAs. Phys. Rev. B **53**, 987–989 (1996)
94. K. Kuriyama, Y. Miyamoto, T. Koyama, O. Ogawa, Ion channeling study of the lattice disorder in neutron irradiated GaP. J. Appl. Phys. **86**, 2352–2354 (1999)
95. K. Kuriyama, K. Ohbora, M. Okada, Photoluminescence from transmuted impurities in neutron-transmutation-doped semi-insulating GaP. Solid State Commun. **113**, 415–418 (2000)
96. S.M. Sze, *Physics of Semiconductor Devices* (Wiley, New York, 1969)
97. H. Kressel (ed.), *Semiconductor Devices for Optical Communications: Topics in Applied Physice*, vol. 39 (Springer, Berlin, 1982)
98. P.C. Becker, M.R.X. de Barras, in *Materials for Optoelectronics*, ed. by M. Quilec (Kluver Academic Publishers, Boston, 1996)
99. A.W. Snyder, J.D. Love, *Optical Waveguide Theory* (Chapman and Hall Medical, London, 1996)
100. D. Marcuse, *Light Transmission Optics* (Van Nostrand, New York, 1972)
101. W.B. Allan, *Fibre Optics Theory and Practice* (Plenum Press, New York, 1973)
102. N.S. Kapany, *Fiber Optics* (Academic Press, New York, 1967)
103. J.A. Arnaud, *Beam and Fibre Optics* (Academic Press, New York, 1976)
104. D. Marcuse, *Theory of Dielectric Optical Waveguides* (Academic Press, New York, 1974)
105. J.E. Midwinter, *Optical Fibers for Transmission* (Wiley, New York, 1979)
106. V.G. Plekhanov, *Applications of the Isotopic Effect in Solids* (Springer, Berlin, 2004)
107. R.W. Pohl, *Itroduction into Optics* (Science, Moscow, 1947) (in Russian)
108. L.M. Zhuravleva, V.G. Plekhanov, Method of Fiber's Manufacture. Patent of Russian Federation N 2302381, 10 July 2007
109. J. Ruth, The uses of radiotracers in the life sciences. Rep. Prog. Phys. **72**, 01670–23 (2009)
110. L.L. Gol'din, M.F. Lomakov, O.V. Savchenko et al., Application of high energy charged particles in medicine, Uspekhi Phys. (Mosc.) **110**, 77–99 (1973) (in Russian)
111. U. Amaldi, G. Kraft, Radiotherapy with beams of carbon ions. Rep. Prog. Phys. **68**, 1861–1882 (2005)
112. M.M. Ter-Pogossian, in *Positron Emission Tomography*, ed. by I. Reivich, A. Alovi (Alan R. Press, New York, 1985)
113. S.I. Adelstein, F.Y. Manning, *Isotopes for Medicine and Life Science* (National Academy Press, Washington, 1995)
114. J. Harbert, A.F.G. de Roche, *Textbook of Nuclear Medicine: Basic Science*, vol. 1 (Lea and Fetiger, Filadelphia, 1984)
115. http://www.nupece.org/iai2001/report/B43.pdf
116. http://www.cbvp.com/nmrc/mia.html
117. S. - C. Huang, Principles of tracer kinetic modeling in positron emission tomography and autoradiography, in *Positron Emission Tomography and Autoradiography: Principles and Applications for the brain and Heart*, ed. by M.E. Phelps, M.C. Mazotta, M.R. Schelbert, (Raven, New York, 1986
118. S.R. Berman, Positron emission tomography of heart in, cardiac nuclear medicine, 3rd edn. in *Health Professons Division*, ed. by M.C. Gerson (McGraw-Hill, New York, 1997)

119. P.E. Valk, D.L. Bailey, D.W. Townsend, *Positron Emission Tomography: Basic Science and Clinical Practice* (Springer, New York, 2004)
120. H. Bender, H. Palmelo, P.E. Valk, *Atlas of Clinical PET in Oncology: PET versus CT and MRI* (Springer, New York, 2000)
121. http://www.vbvp.com/nmrc/nucmed.html
122. V.G. Plekhanov, Manifestation and Origin of the Isotope Effect, ArXiv, phys/0907.2024 (2009), p. 195
123. T. Gehrels (ed.), *Protostars and Planets* (University of Arizona Press, Tuscon, 1978)
124. G. Wallerstein, I. Jhen Jr, P. Parker, et al., Synthesos of the elements in stars: forty years of progress. Rev. Mod. Phys. **69**, 995–1084 (1997)
125. S. Esposito, Primordial Nucleosynthesis: Accurate Prediction for Light Element Abundances, ArXiv:astro-ph/ 9904411
126. W.H. King, *Isotope Shift in Atomic Spectra* (Plenum, New York, 1984)
127. V.G. Plekhanov, *Isotope-Mixed Crystals: Fundamentals and Applications* (Bentham, e-books, 2011). ISBN 978-1-60805-091-8
128. W.F. Libby, *Radiocarbon Dating* (University of Chicago Press, Chicago, 1952)
129. M. Stuiver, C.W. Pearson, High-precision bidecadel calibration of the radiocarbon timescale, Ad 1950–500 BC and 2500–6000 BC. Radiocarbon **35**, 1–23 (1993)
130. M. Stuiver, P.J. Reimer, Extended (super14)C data base and revisited CALIB 3.0 (super 14)C age calibration program, ibid, 35 (N 1) pp. 215–230 (1993)
131. R.E. Taylor, *Radiocarbon Dating: An Archaeological Perspective* (Academic Press, New York, 1987)
132. R.E. Taylor, M.J. Aitken (eds.), *Chronometric Dating in Archaeology* (Plenum Press, New York, 1997)
133. E.M.D. Symabalisty, D.N. Schramm, Nucleocosmochronology. Rep. Progr. Phys. **44**, 293–328 (1981)
134. M. Wolfsberg, W.A. van Hook, P. Paneth et al., *Isotope Effects: In the Chemical, Geological and Bio Sciences* (Springer, Berlin, 2009)
135. M.J. Aitken, *Thermoluminescence* (Academic, London, 1985)
136. M.J. Aitken, *Introduction in Optical Dating* (Oxford University Press, Oxford, 1985)
137. M.J. Aitken, C.B. Stinger, P.A. Mellars (eds.), *The Origin of Modern Humans and the Impact of Chronometric Dating* (Princeton University Press, Princeton, 1993)
138. M.J. Aitken, Archaelogical dating using physical phenomena. Rep. Progr. Phys. **62**, 1333–1376 (1999)
139. S.W.S. McKeever, *Thermoluminescence of Solids* (Cambridge University Press, Cambridge, 1985)
140. J. Groh, G.V. Hevesey, Ann. Phys. **65**, 318 (1920), cited in [135]
141. G. Schatz, A. Weidinger, J.A. Gardner, *Nuclear Condensed Matter* (Wiley, New York, 1996)
142. D. Forkel-Wirth, Exploring solid state physics properties with radioactive isotopes. Rep. Prog. Phys. **62**, 527–597 (1999)
143. D. Forkel-Wirth, M. Deicher, Radioactive isotopes in solid state physics, Nucl. Phys. A **693**, 327–341 (2001)
144. M. Lindros, H. Hass, H. Pattyn et al., Unusually large substitutional fraction for Fr implanted in Fe observed by emission channeling. Nucl. Instrum. Methods **B64**, 256–260 (1992)
145. M. Restle, H. Quintel, C. Ronning, Lattice sites of ion implanted Li in diamond. Appl. Phys. Lett. **66**, 2733–2775 (1995)
146. V.S. Amarel, Microscopic studies of radioactive Mg implanted in $YBa_2Cu_3O_6 + x$ superconductor. J. Magn. Magn. Mater. **177-81**, 511–512 (1998)
147. J. Lohmuller, H. Hass, G. Schatz, PAC investigation of $^{77} \longrightarrow ^{77}$Se on silicon, Hyperfine Interact. **97/98**, 203–207 (1996)
148. H. Granzer, H. Hass, G. Schatz, Magnetic hyperfine fields at Se adatoms on Ni surfaces. Phys. Rev. Lett. **77**, 4261–4264 (1996)
149. H.H. Bertschat, H. Hass, R. Kowallik, New approach for range measurements of induced magnetic interaction in Pd. Phys. Rev. Lett. **78**, 342–345 (1997)

150. K. Kuriyama, K. Sakai, LO phonon and plasmon coupling in NTD GaAs. Phys. Rev. B **53**, 987–989 (1996)
151. V.Ju. Baranov, (ed.), Isotopes, vol. 1 and 2 (Fizmatlit, Moscow, 2005) (in Russian)
152. T. Sekine, K. Uchinokura, E. Marzuura, Two-phonon Raman scattering in GaAs. J. Phys. Chem. Solids **38**, 1091–1096 (1977)
153. T. Kawakubo, M. Okada, Electrical and optical properties of neutron-irradiated GaP crystals. J. Appl. Phys. **67**, 3111–3116 (1990)
154. H. Ahlawadhi, R. Vogelgesang, T.P. Chin, Indirect transitions, free- and impurity-bound excitons in GaP. J. Appl. Phys. **82**(N 9), 4331–4335 (1997)
155. P. Dean, Inter-impurity recombinations in semiconductors. Prog. Solid State Chem. **8**, 1–126 (1973)
156. YuV Tarbeyev, A.K. Kaliteyevsky, V.I. Sergeyev, Scientific, engineering and metrological problems in producing pure ^{28}Si and growing single crystals. Metrologia **31**, 269–273 (1994)
157. U. Kuegens, P. Becker, X-ray interferometry and practical set-up for calibrated in the microrad range with nanorad resolution. Meas. Sci. Technol. **9**(N 8), 1072–1075 (1998)
158. A.D. Bulanov, G.G. Devyatych, A.V. Gusev et al., The highly isotopic enriched (99.9%) high-pure ^{28}Si single crystal. Cryst. Res. Technol. **35**, 1023–1026 (2000)
159. P. Becker, History and progress in the accurate determination of the Avogadro constant. Rep. Prog. Phys. **64**, 1945–2008 (2001)
160. P. Becker, The molar volume of sinle-crystal silicon. Metrologia **38**, 85–86 (2001)
161. P. Becker, M. Gläser, Avogadro constant and ion accumulation: steps towards a reditermination of the SI unit of mass. Meas. Sci. Technol. **14**, 1249–1258 (2003)
162. P. Becker, Tracing the definition of the kilogram to the Avogadro constant using a silicon single crystal. Metrologia **40**, 366–375 (2003)
163. I.M. Mills, P.J. Mohr, B.N. Taylor, Redifinition of the kilogram: a decision whose time has come. Metrologia **42**, 71–80 (2005)
164. A. Picard, Mass determination of a 1 kg silicon sphere for the Avogadro project. Metrologia **43**, 46–52 (2006)
165. P. Becker, O.N. Godisov, P. Taylor, Large-scale production of highly enriched ^{28}Si. Meas. Sci. Technol. **17**, 1854–1860 (2006)
166. P.J. Mohr, B.N. Taylor, CODATA recomended values of the fundamental physical constants: 1998. Rev. Mod. Phys. **72**, 351–495 (2000)
167. J.I. Pankove, *Optical Processes in Semiconductors* (Prentice Hall, Englewood Cliffs, 1971)
168. J.S. Blakemore, Semiconducting and other major properties of gallium arsenide. J. Appl. Phys. **53**, R123–R181 (1982)
169. M. Sze, *High Speed Devices* (Wiley, New York, 1991)
170. T. Ihn, *Semiconductors Nanostructures: Quantum States and Electronic Transport* (Oxford University Press, Oxford, 2009)
171. S. Lindsay, *Introduction to Nanosciences* (Oxford University Press, New York, 2009)
172. M.H. Devoret, R.J. Shoelkopf, Amplifying quantum signals with the single-electron transistor. Nature **406**, 1038–1046 (2000)
173. K. Goser, P. Glösekötter, J. Dienstuhl, *Nanoelectronics and Nanosystems* (Springer, Berlin, 2004)
174. M.J. Kelly, *Low-Dimensional Semiconductors* (Clarendon Press, Oxford, 1995)
175. H. Grabert (ed.) Single Charge Tunneling (Special Issue), Zs. Physik **85** (N3) (1991)
176. K. Seeger, *Semiconductor Physics* (Springer, Wien-New York, 1973)
177. K. Barnham, D. Vvedensky, *Low-Dimensional Semiconductor Structures* (Cambridge University Press, Cambridge, 2009)
178. N. Gerasimenko, Ju Parhomenko, *Silicon-Material of Nanoelectronics* (Moscow, Technosphera, 2007). (in Russian)
179. A.V. Eletskii, Mechanical properties of carbon nanostructures and related materials. Uspekhi Fiz. Nauk (Mosc.) **177**, 233–274 (2007)
180. H. Grabert, M.H. Devored (eds.), *Single Charge Tunneling: Coulomb Blockade Phenomena in Nanostructures*, NATO ASI Series B, vol. 294. (Plenum, New York, 1992)

181. S. Washburn, R.A. Webb, Quantum transport in small disordered samples from the diffuse to the ballistic regime. Rep. Prog. Phys. **55**, 1311–1383 (1992)
182. D.V. Averin, A.N. Korotkov, K.K. Likharev, Theory of single electron charging of quantum wells and dots. Phys. Rev. **44**, 6199–6211 (1991)
183. M.A. Kastner, The single electron transistor. Rev. Mod. Phys. **64**, 849–858 (1992)
184. J. Bylander, T. Duty, P. Delsing, Current measurement by real-time counting of single electrons. Nature **434**, 361–364 (2005)
185. D.V. Averin, A.A. Odintsov, S.A. Vyshenski, Ultimate accuracy of single-electron dc current standards. J. Appl. Phys. **73**, 1297–1308 (1993)
186. Y. Ono, A. Fujiwara, K. Nishiguch et al., Manipulation and detection of single electrons for future information processing. J. Appl. Phys. **97**, 031101–031119 (2005)
187. K. Thyagarajan, A.K. Ghatak (eds.), *Lasers Theory and Applications* (Plenum Press, New York, 1982)
188. O. Svelto, *Principles of Lasers*, 2nd edn. (Plenum Press, New York, 1982)
189. N.V. Karlov, *Lectures on Quantum Electronics*. (Science, Moscow, 1983) (in Russian)
190. M.S. Brodin, V. Ya. Reznitchenko, Interactions of the laser intensity radiation with A_2B_6 semiconductors, in *Physics A_2 B_6 Compounds*, ed. by A.N. Georgabiani and M.K. Sheinkman (Science, Moscow, 1986), pp. 184–225 (in Russian)
191. A.J. Taylor, D.J. Erskine, C.L. Tang, Ultrafast relaxation of photoexcited carriers in GaAs and related compounds. J. Opt. Soc. Am. (B) **2**, 663–673 (1985)
192. J.A. Kash, J.C. Tsang, in *Light Scattering in Solids*, Vol. 6, ed. by M. Cardona, G. Güntherodt (Springer, Berlin, 1991), pp. 423–467
193. W.P. Dumke, Interband transitions and maser action. Phys. Rev. **127**, 1559–1563 (1962)
194. R.E. Nahory, K.L. Shakley, R.F. Leheny, R.A. Logan, Indirect-band-gap super-radiant laser in GaP containing isoelectronic traps. Phys. Rev. Lett. **27**, 1647–1650 (1971)
195. H. Kressel, in *Laser Handbook*, Chap. B5, ed. by F.T. Arechi, E.O. Schulz-Dubois (North-Holland, Amsterdam, 1972), p. 271–319
196. F. Stern, ibid, Chap. B4
197. C. Klingshirn, Lasers processes in semiconductors, in *Spectr. Solid-State Laser Type Matter*. (Proc. Course Enrico Fermi, Erice, 1987), pp. 485–501
198. C.A. Klein, Further remarks on electron beam pumping lasers materials. Appl. Optics **5**, 1922–1924 (1966)
199. C.A. Klein, Power efficiency and quantum efficiencies of electron-beam pumped lasers, IEEE QE **4**, 186–194 (1968)
200. H. Haug, Theory of laser action involving free excitons and LO-phonon-assisted transitions. J. Appl. Phys. **39**, 4687–4696 (1968)
201. H. Haug, Nonlinear optical phenomena and bistability in semiconductors. Adv. Solid State Phys. **22**, 149–171 (1982)
202. H. Haug, S. Koch, On the theory of laser action in dense exciton systems. Phys. Stat. Solidi (b) **82**, 531–543 (1977)
203. K.C. Liu, R.L. Liboff, Criterion for exciton lasing in pure crystals. J. Appl. Phys. **54**, 5633–5637 (1983)
204. R.S. Knox, *Theory of Excitons* (Academic Press, New York, 1963)
205. E.F. Gross, Selected Papers (Science, Leningrad, 1976) (in Russian)
206. D.G. Thomas (ed.), II–VI Semiconducting Compounds (Benjamin, New York, 1967)
207. N.G. Basov, O.V. Bogdankevich, A.G. Devyatkov, Sov. Phys. JETP **20**, 1902 (1964)
208. N.G. Basov, O.V. Bogdankevich, A.G. Devyatkov Sov, Phys. Solid State **8**, 1221 (1966)
209. J.R. Packard, D.A. Campbell, W.C. Tait, Evidence for indirect annihilation of free excitons in II–VI semiconductor lasers. J. Appl. Phys. **38**, 5255–5258 (1967)
210. C. Benoit a la Guilaume, J.M. Debever, F. Salvan, in *II–VI Semiconducting Compounds*, ed. by D.G. Thomas (Benjamin, New York, 1967), p. 609
211. C. Benoit a la Guilaume, J.M. Debever, F. Salvan, Radiative recmbination in highly excited CdS. Phys. Rev. **177**, 567–580 (1969)

212. L.A. Kulevsky, A.M. Prokhorov, The nature of the laser transition in CdS vrystal at 90K with two-photon excitaion. IEEE QE **2**, 584–586 (1966)
213. M.S. Brodin, K.A. Dmitrenko, S.G. Shevel, L.V. Taranenko, The temperature dependence of laser threshold in CdS single crystals under one-photon excitation. in *Proceedings of the International Conference on Lasers?82* (STS Press, USA, 1983), pp. 287–291
214. M.S. Brodin, S.V. Zakrevski, V.S. Mashkevich, V. Ya, Reznitchenko, On mechanism of generation of laser radiation in CdS_xCdSe_{1-x} crystals in case of two-photon excitation. Sov. Phys. Semicond. **1**, 595–597 (1967)
215. V.G. Plekhanov, Fundamentals and applications of isotope effect in solids. Prog. Mater. Sci. **51**, 281–426 (2006)
216. V.G. Plekhanov, Resonant secondary emission spectra and some peculiarities of relaxation processes in crystals with self-trapping excitons, in Proceedings of the International Conference on LASERS'80 (McClean, STS, 1981), pp. 91–99
217. K. Takiyama, M.I. Abd-Elrahman, T. Fujita, T. Okada, Photolumonescence and decay kinetics of indirect free excitons in diamonds under the near-resonant laser excitation. Solid State Commun. **99**, 793–796 (1996)
218. V.G. Plekhanov, V.I. Altukhov, Free exciton luminescence and exciton-phonon interactions parameters of wide-gap insulators, in Proceedings of the International Conference on LASERS'82 (McClean, STS, 1983), pp. 292–299
219. C. Klingshirn, H. Haug, Optical properties of highly excited direct gap semiconductors. Phys. Reports **70**, 315–398 (1981)
220. V.G. Plekhanov, Wannier–Mott excitons in isotope-disordered crystals. Rep. Prog. Phys. **61**, 1045–1098 (1998)
221. V.G. Plekhanov, Comparative study of isotope and chemical effects on the exciton states in LiH crystals. Prog. Solid State Chem. **29**, 71–177 (2001)
222. V.G. Plekhanov, Changes in spectra of luminescence and Raman scattering of ithium hydride uner growth in the excitation intensity. Quantum Electron. (Mosc.) **16**, 2156–2159 (1989) (in Russian)
223. H.C. Casey, M.B. Panish, *Heterostructure Lasers* (Academic Press, New York, 1978)
224. P.S. Zoty, *Quantum Well Lasers* (Academic Press, Boston, 1993)
225. L.A. Colderen, S.W. Corzine, *Diode Lasers and Photonic Integrated Cicuits* (Wiley, New York, 1995)
226. V.M. Ustinov, A.E. Zukov, A.Y. Egorov, N.A. Maleen, *Quantum Dot Lasers* (Oxford University Press, Oxford, 2003)
227. P. Michler (ed.), Single Semiconductor Quantum Dots (Springer, Berlin, 2009)
228. N.N. Ledentsov, V.M. Ustinov, V.A. Shchukin et al., Quantum dot heterostructures: fabrication, properties, lasers. Fiz. Teh. Polup. (Phys. Tech. Semicond.) **32**, 385–410 (1998) (in Russian)
229. L. Sirigu, D.Y. Oberli, L. Deriorgi et al., Excitonic lasing in semiconductor quantum wires. Phys. Rev. **B61**, R10575–4 (2000)
230. F. Rossi, E. Molinari, Linear and nonlinear optical properties of realistic quantum-wire structures: the dominant role of Coulomb correlation. Phys. Rev. **B53**, 16462–16473 (1996)
231. F. Rossi, G. Goldoni, E. Molinari, Theory of excitonic confinement in semiconductor quantum wires. J. Phys. Condens. Matter **11**, 5969–5988 (1999)
232. D. Bimberg, M. Grundman, N.N. Ledentsov, *Quantum Dot Heterostructure* (Wiley, Chichester, 1999)
233. J.M. Martinez-Duart, R.J. Martin-Palma, F. Agullo-Rueda, *Nanotechnology for Microelectronics and Optoelectronics*, (Elsevier, Amsterdam, 2006)

Index

V.G. Plekhanov, *Isotopes in Condensed Matter*, Springer Series in Materials Science 162,
DOI: 10.1007/978-3-642-28723-7, © Springer-Verlag Berlin Heidelberg 2013